International Journal of Photoenergy

Thermal Management and Efficiency Enhancement of Solar Systems

Lead Guest Editor: Hafiz Muhammad Ali
Guest Editors: Zafar Said and Sivan Suresh

Thermal Management and Efficiency Enhancement of Solar Systems

International Journal of Photoenergy

Thermal Management and Efficiency Enhancement of Solar Systems

Lead Guest Editor: Hafiz Muhammad Ali
Guest Editors: Zafar Said and Sivan Suresh

Copyright © 2021 Hindawi Limited. All rights reserved.

This is a special issue published in "International Journal of Photoenergy." All articles are open access articles distributed under the Creative Commons Attribution License, which permits unrestricted use, distribution, and reproduction in any medium, provided the original work is properly cited.

Chief Editor

Giulia Grancini, Italy

Academic Editors

Mohamed S.A. Abdel-Mottaleb, Egypt
Angelo Albini, Italy
Mohammad Alghoul, Malaysia
Alberto Álvarez-Gallegos, Mexico
Vincenzo Augugliaro, Italy
Detlef W. Bahnemann, Germany
Simona Binetti, Italy
Fabio Bisegna, Italy
Thomas M. Brown, Italy
Joaquim Carneiro, Portugal
Yatendra S. Chaudhary, India
Kok-Keong Chong, Malaysia
Věra Cimrová, Czech Republic
Laura Clarizia, Italy
Gianluca Coccia, Italy
Daniel Tudor Cotfas, Romania
P. Davide Cozzoli, Italy
Dionysios D. Dionysiou, USA
Elisa Isabel Garcia-Lopez, Italy
Wing-Kei Ho, Hong Kong
Siamak Hoseinzadeh, Italy
Jürgen Hüpkes, Germany
Fayaz Hussain, Brunei Darussalam
Mohamed Gamal Hussien, Egypt
Adel A. Ismail, Kuwait
Chun-Sheng Jiang, USA
Zaiyong Jiang, China
Yuanzuo Li, China
Manuel Ignacio Maldonado, Spain
Santolo Meo, Italy
Claudio Minero, Italy
Regina De Fátima Peralta Muniz Moreira, Brazil
Maria da Graça P. Neves, Portugal
Tsuyoshi Ochiai, Japan
Kei Ohkubo, Japan
Umapada Pal, Mexico
Dillip K. Panda, USA
Carlo Renno, Italy
Francesco Riganti-Fulginei, Italy
Leonardo Sandrolini, Italy
Jinn Kong Sheu, Taiwan
Kishore Sridharan, India
Elias Stathatos, Greece
Jegadesan Subbiah, Australia
Chaofan Sun, China
K. R. Justin Thomas, India
Koray Ulgen, Turkey
Ahmad Umar, Saudi Arabia
Qiliang Wang, China
Xuxu Wang, China
Huiqing Wen, China
Weijie Yang, China
Jiangbo Yu, USA

Contents

Effect of Design Parameters on Fresh Water Produced from Triangular Basin and Conventional Basin Solar Still
A. Rajendra Prasad, Ravishankar Sathyamurthy, M. Sudhakar, B. Madhu, D. Mageshbabu, A. Muthu Manokar, and Ali J. Chamkha
Research Article (8 pages), Article ID 6619138, Volume 2021 (2021)

Numerical Study on the Thermal Performance of Trombe Wall for Passive Solar Building in Semiarid Climate
Maher Dhahri, Nima Khalilpoor, Hana Aouinet, Alibek Issakhov, Habib Sammouda, and Sampath Emani
Research Article (12 pages), Article ID 6630140, Volume 2021 (2021)

Efficient Topology for DC-DC Boost Converter Based on Charge Pump Capacitor for Renewable Energy System
Muhammad Zeeshan Malik, Vineet Tirth, Amjad Ali, Ajmal Farooq, Ali Algahtani, Rajesh Verma, Saiful Islam, Kashif Irshad, and Ahmed N. Abdalla
Research Article (13 pages), Article ID 6675720, Volume 2021 (2021)

Study on the Influence of Light Intensity on the Performance of Solar Cell
Zhe Li, Jian Yang, and Pouya Asareh Nejad Dezfuli
Research Article (10 pages), Article ID 6648739, Volume 2021 (2021)

Investigation of the Soan River Water Quality Using Multivariate Statistical Approach
Zakaullah and Naeem Ejaz
Research Article (15 pages), Article ID 6644796, Volume 2020 (2020)

Hindawi
International Journal of Photoenergy
Volume 2021, Article ID 6631121, 11 pages
https://doi.org/10.1155/2021/6631121

Research Article

Improvement and Nocturnal Extension of the Efficiency of a Solar Still

Benaissa Mandi,[1] Younes Menni,[1] Rachid Maouedj,[2] Giulio Lorenzini,[3] Mohammad Hossein Ahmadi,[4] and Sampath Emani[5]

[1]*Unit of Research on Materials and Renewable Energies, Department of Physics, Faculty of Sciences, Abou Bekr Belkaid University, P.B. 119-13000 Tlemcen, Algeria*
[2]*Unité de Recherche en Energies Renouvelables en Milieu Saharien (URERMS), Centre de Développement Des Energies Renouvelables (CDER), 01000 Adrar, Algeria*
[3]*Department of Engineering and Architecture, University of Parma, Parco Area delle Scienze, 181/A, Parma 43124, Italy*
[4]*Faculty of Mechanical Engineering, Shahrood University of Technology, Shahrood, Iran*
[5]*Chemical Engineering Department, Universiti Teknologi PETRONAS, 32610 Seri Iskandar, Perak D.R., Malaysia*

Correspondence should be addressed to Mohammad Hossein Ahmadi; mohammadhosein.ahmadi@gmail.com

Received 8 December 2020; Revised 12 February 2021; Accepted 13 May 2021; Published 22 July 2021

Academic Editor: Hafiz Muhammad Ali

Copyright © 2021 Benaissa Mandi et al. This is an open access article distributed under the Creative Commons Attribution License, which permits unrestricted use, distribution, and reproduction in any medium, provided the original work is properly cited.

Various studies have been made to improve the efficiency of the solar still. These studies had devoted to the combination of solar collectors with solar still. This article proposes the use of all forms of solar thermal or photovoltaic energy. In addition, photovoltaic electric storage systems convert them to thermal energy that increases the temperature of a greenhouse solar still. We investigated the possibility of improving the productivity of a greenhouse still and prolong solar distillation overnight. The proposed system is the incorporation of thermal energy produced by a parabolic-cylindrical concentrator, a greenhouse still, and photovoltaic solar energy by panels. The production at 14 pm reaches 110 L/m^2 thanks to the various thermal sources made up of the hybrid still. It has better productivity than other distillers. The distillation is extended in the evening thanks to a storage system using electric batteries. The production at 18 pm to 18 L/m^2 is reduced at 24 pm to 5 L/m^2 in the dark. The accumulated temperature decreases the negative influence of the physical parameters on the production which exceeds 100 L/m^2 per day. In the evening, the production is reached 16 L/m^2 at 22 pm, which is an advantage compared to other distillers.

1. Introduction

The increase in the volume of pollution disrupts the natural water cycle, causing drought in different areas and lack of water. The problem of water scarcity has worsened over the past centuries, due to careless and heavy consumption of water. In addition to water scarcity, supply of energy is another challenge that should be properly addressed to have better welfare level [1]. Therefore, the use of renewable energy and developing integrated systems are widely discussed and analyzed to answer these problems [2, 3]. Desalination techniques are means that produce water economically in rural and urban areas [4–7]. Research has been done to improve solar desalination (SD) techniques to produce enough water, which can reduce water scarcity. Uses of conventional solar systems, modifications of the heat utilization mechanism are suitable methods to improve the efficiency of the distillation [8]. The most common method is solar distillation [9–11]. Many studies have been done for example; Li et al. [12] used the technique of membrane distillation (MD) through an integrated system by harnessing solar thermal energy. Wang et al. [13] conducted an experimental study for a new design of a seawater distillation system for use in agricultural irrigation. Gopi et al. [14] used radiation energy for sustainable desalination. Muraleedharan et al. [15] designed an active distillation system using solar energy. The performance of this modified system has been compared with the traditional system. Parsa et al. [16]

discussed the influence of different altitudes on the efficiency of solar still. The first height is about 3964 m at the top of Mount Tochal, while the second altitude is estimated at 1171 m for the Tehran city. Miladi et al. [17] studied the technique of recycling hot cooling water, contained to condense the flow, and thus its impact on the efficiency of the vacuum MD station and on its daily production. Hejazi et al. [18] investigated the impact of intermittent operation on the performance of DM. Afzal et al. [19] gave a new system to develop the production of essential oils from plants. Alawee et al. [20–22] augmented the solar distillation yield by using different methods in various geometries. In order to avoid the disadvantages of traditional distillation systems, al-Nimr and Qananba [23] cited another distillation configuration, which relies on a combination of focused optical engineering technique and a nanofluids' spectral-splitting PV/T method. Using the solar distillation (SD) technique, Bhardwaj et al. [24] reported the total water produced with various surfaces of condensation. Kiwan et al. [25] presented a new SD model by developing a conventional power plant for a solar chimney that has the ability to produce both distilled water and electrical energy. Sharshir et al. [26] studied a solar still (SS) integrated in a solar humidification-dehumidification (HDH). The CSS and SS water production with HDH hot water outlet is 37 L/day. Omara et al. [27] analyzed a desalination system using wicks, an evacuated solar water heater, and a solar still. Water productivity has increased by 114% compared to conventional still. Tian and Zhao [28] investigated an examination of solar collectors and thermal energy storage in solar thermal applications. Three different types of concentrated solar collectors have been described and compared: heliostat field collectors, flat parabolic collectors, and trough parabolic collectors. The materials used for high temperature thermal energy storage systems were compared, and a comparison between different categories of thermal storage systems was presented. Molten salts with excellent properties are considered the ideal materials for high temperature thermal storage applications. Ayoub et al. [29] studied a SD system still with productivity. A simple amendment in the form of a slowly rotating drum is introduced allowing the formation of thin layers of water which evaporate quickly and is constantly renewed. The performance of this system was compared to a control without an introduced drum. The system was performed considerably with an average increase in daily productivity of 200%. Abdallah et al. [30] studied solar distillation using a vacuum tube coupled to a photovoltaic system. The system produced 12 L/m^2/day and gave an efficiency of over 60% for more than 5 h in daylight. Sampathkumar et al. [31] reported that many traditional and nontraditional techniques have been developed for distillation. The production is related to the thermal conductivity of coating and condensing materials, and copper has good performance because it has high thermal conductivity. Allouhi [32] studied the progress of thermoelectric solar thermal cogeneration processes and the integration of solar thermoelectric generators in solar thermal collectors. This integration provides thermal and electrical energy, which implies a good control of solar radiation. Dev and Tiwari [33] studied the characteristics of a hybrid solar still (PV-T). A hybrid solar still is a combination of a solar still and a flat plate collector integrated in a glass-to-glass photovoltaic module. It has been observed that the performance of the nonlinear characteristics is better than that of the linear characteristics. Kabeel et al. [34] have studied different types of solar still. The results show that the maximum production is obtained from a solar still with a single slope and pyramidal shape. Qin et al. [35] theoretically studied solar thermal sources of interest for hybrid solar distillation. In another study, Qin [36] provided a measure of the albedo of an urban prototype. They sequentially covered a target area with an opaque white sun mask. They simultaneously measure incident radiation and reflected radiation. Other data in different formulations and subject to distinct conditions have been recently dealt with Sharan et al. [37], Alawee et al. [38, 39], Essa et al. [40], Xiong et al. [41], and Mandi et al. [42].

In this study, we are investigating the possibility of improving productivity and extending nighttime solar distillation using a hybrid solar still and the reduction of the negative impact of weather factors on the production of the solar still. The proposed hybrid still is a coupling system between a greenhouse still, a parabolic cylindro concentrator, and an autonomous photovoltaic generator with a thermal electric converter. These various sources are temperature generators which are used to evaporate the water in the solar still.

2. System Description

Figure 1 illustrates a solar still which was combined with a photovoltaic generator and a parabolic cylindro-parabolic concentrator to have a hybrid system [42]. The operation of this system is based on passive solar energy and the conversion of thermal energy through a cylindro-parabolic concentrator and an autonomous photovoltaic system. The latter supplies converters from electrical energy to thermal energy.

The batteries store electrical energy and keep the system running, at times when the sun's rays are weak. The productivity and the operating time determine the size and the cost of the system. The hybrid system can operate during the additional hours of sunset thanks to the autonomy of the photovoltaic generator.

3. Mathematical Model

3.1. Assumptions. For the calculation of the energy balance, one poses the following:

(i) The fluid is incompressible

(ii) The parabola is symmetrical

(iii) The ambient temperature is uniform

(iv) The glass is opaque to infrared radiation

(v) The flow is one-dimensional

(vi) Temporal variations in the thickness of the absorber and the glass are negligible

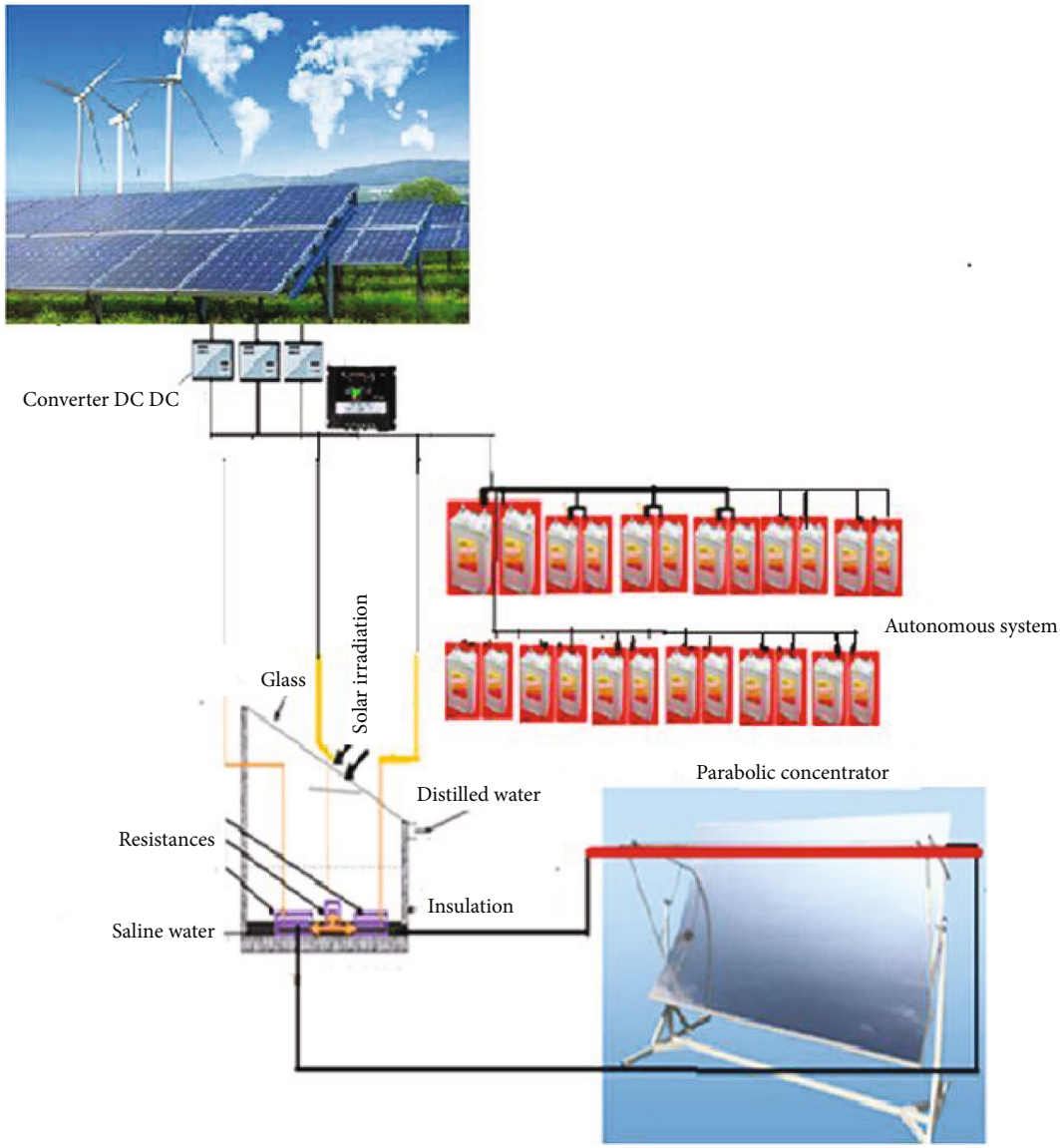

Figure 1: Thermal balance of the absorber tube of the CCP concentrator [42].

(vii) The exchange by conduction in the absorber and the glass is negligible

(viii) The effect of the shadow of the absorber tube on the mirror is negligible

(ix) The solar flux of the absorber is uniform

3.2. Cylindro-Parabolic Concentrator

3.2.1. Energy Balance for the Fluid. The energy balance of the fluid moving in the absorber is [43]

$$\frac{d}{dt}\left(\Delta Q_f(z,t)\right) = q_{\text{inl}}(z,t) - q_{\text{out}}(z+\Delta z,t)\cdot\Delta z. \quad (1)$$

The amount of heat recovered by the fluid $\Delta Q_F(z,t)$ in the interval Δz is

$$\begin{gathered}(\Delta Q_F(z,t)) = \rho_F - c_F A_{\text{internal}}\cdot\Delta z T_F(z,t),\\ A_{A,\text{internal}} = \pi\cdot D_{A,i}.\end{gathered} \quad (2)$$

The amount of heat entering and leaving the element of length Δz is

$$q_{\text{entered}}(z,t) = \rho_F C_F V' T_F(z,t),$$

$$q_{\text{entered}}(z+\Delta z,t) = \rho_F C_F V' T_F(z+\Delta z,t),$$

$$\rho_F c_F A_{A,\text{internal}}\cdot\Delta z\frac{dT_F(z,t)}{dt} = \rho_F c_F V'\cdot T_F(z,t) - \rho_F c_F V' \cdot T_F(z+\Delta z,t) + q_{\text{exit}}(z,t). \quad (3)$$

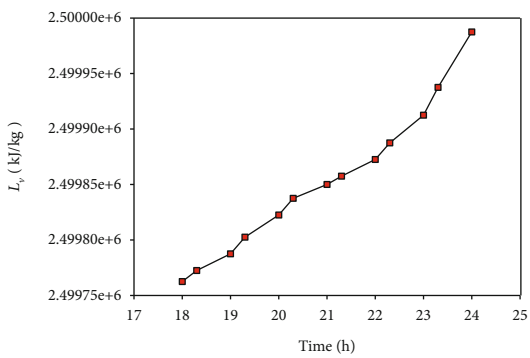

Figure 2: Temporal variation of latent heat of water.

The partial derivative with respect to the abscissa z is

$$\frac{dT_F(z,t)}{\Delta z} = \frac{dT_F(z+\Delta z,t) - T_F(z,t)}{\Delta z}. \quad (4)$$

In divisions by Δz and after substitution, we get

$$\rho_F C_F A_{A,\text{internal}} \frac{dT_F(z,t)}{dt} = -\rho_F c_F V' \cdot \frac{dT_F(z,t)}{dt} + q_{\text{useful}}(z,t). \quad (5)$$

The initial conditions and the boundary conditions are

$$\begin{aligned} T_F(0,t) &= T_{F,\text{entered}}(t) = T_{\text{amb}}(t), \\ T_F(z,0) &= T_{F,\text{initial}}(z) = T_{\text{amb}}(0). \end{aligned} \quad (6)$$

3.2.2. Between the Absorber and the Glass Envelope.

$$\begin{aligned} \frac{dz(\Delta Q_A(z,t))}{dt} &= (q_{\text{absorbed}}(t) - q_{\text{inside}}(z,t) - q_{\text{useful}}(z,t))\Delta z, \\ \Delta Q_{\text{abs}}(z,t) &= A_{\text{abs}} \cdot \rho_{\text{abs}} \cdot C_{\text{abs}} \cdot \Delta z \cdot T_{\text{abs}}(z,t). \end{aligned} \quad (7)$$

The power absorbed per unit of opening area is written as follows:

$$q_{\text{absorbed}} = I \cdot \rho \cdot \tau \cdot C \cdot \gamma. \quad (8)$$

After substitution, we get the following expression:

$$\rho_{\text{abs}} \cdot C_{\text{abs}} \cdot A_{\text{abs}} \frac{dT_{\text{abs}}}{dt} = q_{\text{absorbed}}(t) - q_{\text{inside}}(z,t) - q_{\text{useful}}(z,t). \quad (9)$$

The initial conditions are

$$T_A(z,0) = T_{A,\text{initial}}(z) = T_{\text{amb}}(0). \quad (10)$$

3.2.3. Between the Glass Envelope and the Environment.

$$\rho_v C_v A_v \frac{dT_v(z,t)}{dt} = q_{\text{internal}}(z,t) - q_{\text{external}}(z,t). \quad (11)$$

The amount of external heat between the glazing and the surrounding environment is shown.

The initial condition is as follows:

$$T_g(z,0) = T_{g,\text{initial}}(z) = T_{\text{amb}}(0). \quad (12)$$

3.3. Green House Distiller. Figure 1 (part B) illustrates the different heat exchanges that occur in a solar still. The equations, which express the heat balance at the level of each part of the still [44], are written as follows:

(i) In the cover:

(a) Outside:

$$\frac{M_g}{2} \cdot \frac{cp_g}{A_g} \cdot \frac{dT_{ge}}{dt} + q^c_{g-a} + q^r_{g-a} = \frac{\lambda_g}{e_g} \cdot (T_{gi} - T_{ge}) \quad (13)$$

(b) Inner face:

$$\frac{M_g}{2} \cdot \frac{cp_g}{A_g} \cdot \frac{dT_{gi}}{dt} + \frac{\lambda_g}{e_g} \cdot (T_{gi} - T_{ge}) = q^c_{w-g} + q^r_{w-g} + q^{ev}_{w-g} + P_g \quad (14)$$

(ii) In the brine:

$$M_w \cdot \frac{cp_w}{A_w} \cdot \frac{dT_w}{dt} + q^c_{w-g} + q^r_{w-g} + q^{ev}_{w-g} = p_w + q^c_{b-w} \quad (15)$$

(a) In the absorbent tray:

$$M_b \cdot \frac{cp_b}{A_b} \cdot \frac{dT_b}{dt} + q^c_{b-w} + q^{cd}_{b-isi} = pb \quad (16)$$

(iii) In the insulation:

To reduce heat loss through the base, we use thermal insulation. The inner side of the still receives the heat lost from the absorber and the outer side releases heat to the outside by radiation and convection, hence the equation:

(a) Inner face:

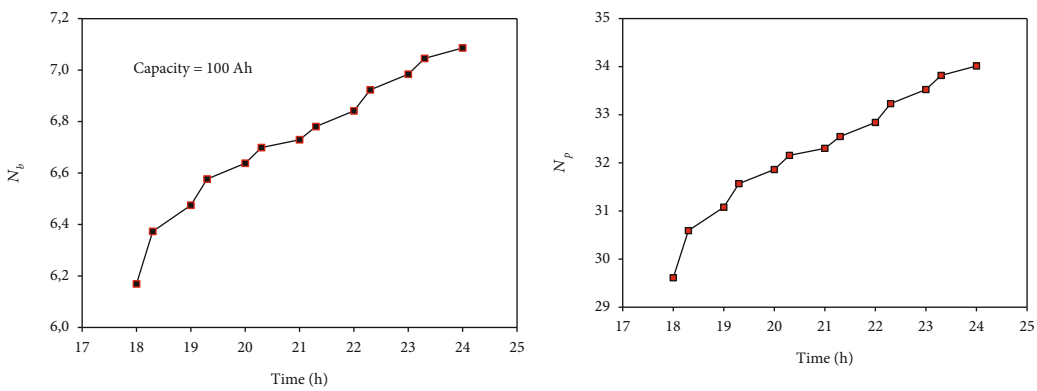

(a) (b)

Figure 3: Variation of number of (a) batteries and (b) panels as a function of time of distillation.

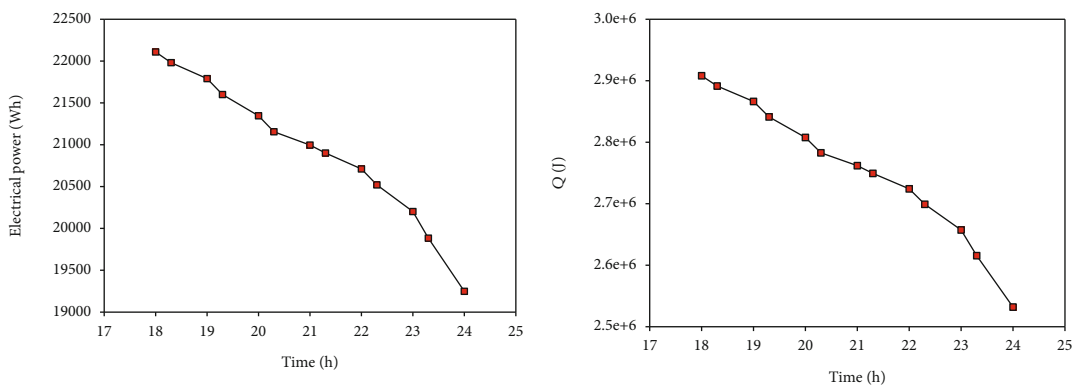

(a) (b)

Figure 4: Temporal variation of (a) electric power and (b) thermal power.

$$\frac{M_{\text{is}}}{2} \cdot \frac{cp_{\text{is}}}{A_{\text{is}}} \cdot \frac{dT_{isi}}{dt} + \frac{\lambda_{\text{is}}}{e_{\text{is}}} \cdot (T_{isi} - T_{ise}) = q_{b-isi}^{cd} \quad (17)$$

(b) Outside face:

$$\frac{M_{\text{is}}}{2} \cdot \frac{cp_{\text{is}}}{A_{\text{is}}} \cdot \frac{dT_{ise}}{dt} + q_{\text{is}-a}^{c} + q_{\text{is}-a}^{r} = \frac{\lambda_{\text{is}}}{e_{\text{is}}} \cdot (T_{isi} - T_{ise}) \quad (18)$$

3.4. Hybrid Distiller.

$$M_w \frac{cp_w}{A_w} \frac{dT_w}{dt} + q_{w-g}^{c} + q_{w-g}^{r} + q_{w-g}^{er} = p_w + mcp(T_{cc} - T_{w0}) + mcp(T_{el} - T_{w0}) + q_{b-w}^{c}. \quad (19)$$

3.5. Estimated Consumption. The power of all the devices that will be part of the installation must be determined individually, as well as the average duration of use of each of them [45]:

The alternating and direct current devices will be

$$E_{AC} = \sum P_{(AC)i} \cdot t_{di},$$
$$E_{DC} = \sum P_{(DC)i} \cdot t_{di}, \quad (20)$$
$$E_T = \frac{E_{DC}}{\eta_{\text{BAT}}} + \frac{E_{AC}}{\eta_{\text{BAT}} \cdot \eta_{\text{INV}}}.$$

3.6. Dimensioning of the Photovoltaic Generator. The total number of photovoltaic modules to be installed can be calculated from the following expression [46]:

$$N_T = \frac{E_T}{P_p G_{m\beta} P_G}. \quad (21)$$

The number of modules to be connected in series is calculated as follows:

$$N_S = \frac{V_{\text{Bat}}}{V_m}. \quad (22)$$

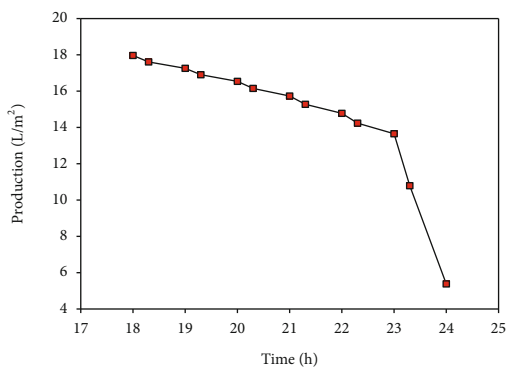

Figure 5: Temporal variation of the production of the autonomous hybrid distiller.

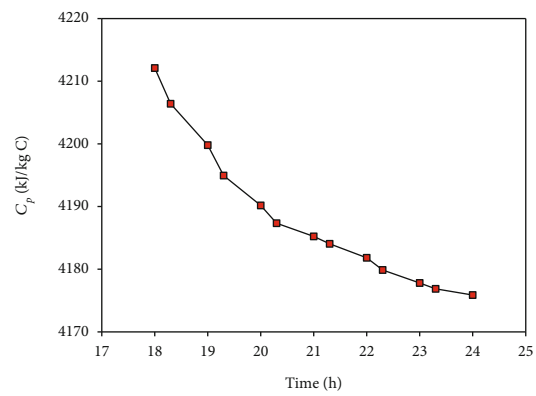

Figure 6: Temporal variation of the specific heat of water.

The number of modules connected in parallel is

$$N_S = \frac{V_{\text{Bat}}}{V_m}. \tag{23}$$

3.7. Autonomy. To define the size of the accumulator, the following parameters must be taken into account:

3.7.1. Maximum Discharge Depth. This is the maximum level of discharge that is allowed to the battery before disconnecting the regulator.

3.7.2. Autonomy Days. This is the number of consecutive days in the absence of sunlight. The accumulation system is able to respond to consumption, without exceeding the maximum depth of discharge of the battery [47].

$$\begin{aligned} C_n(Wh) &= \frac{E_T N}{P_d}, \\ C_n(Ah) &= \frac{C_n(Wh)}{V_{\text{Bat}}}. \end{aligned} \tag{24}$$

3.8. Sizing of the Regulator. The main purpose of the regulator is to obtain the maximum current that will flow through the installation. We need to calculate the current produced by the generator, the current that consumes the load. The maximum of these two currents will be at which the regulator must withstand in operation:

$$\begin{aligned} I_G &= I_R \cdot N_R, \\ I_R &= \frac{P_p \eta_m}{V_m}. \end{aligned} \tag{25}$$

The intensity consumed by the load is determined taking into account all the consumptions at the same time:

$$I_C = \frac{P_{DC}}{V_{\text{batm}}} + \frac{P_{AC}}{220}. \tag{26}$$

The regulator will have to withstand the maximum of the two currents which will be used for its election.

$$I_R = \max\left(I_G, I_C\right). \tag{27}$$

3.9. Dimensioning of the Converter. The operating characteristics that define an inverter or converter are DC-AC:

(i) Rated power

(ii) Input voltage

(iii) Rated output voltage

(iv) Operating frequency

(v) Performance

The power demanded by the AC load will be taken into account, so an inverter with a rated power slightly higher than the maximum will be chosen.

3.9.1. The Expression of the Power of the Inverter.

$$P_{Rinv} \approx P_{AC}. \tag{28}$$

3.10. Dimensioning of the Wiring. In the load power cables, there will be losses due to voltage drops. These ohmic losses must meet the restrictive of the following two conditions:

(1) The low voltage electrotechnical standards must be checked

(2) The energy loss must be less than a predefined amount

Its value can be calculated with the following expressions:

$$\begin{aligned} P_{PC} &= I^2 \cdot R_c, \\ R_c &= \frac{\rho \cdot L}{S}. \end{aligned} \tag{29}$$

3.11. Conversion of Electrical Energy to Thermal Energy. The system consists of a photovoltaic network which produces electrical energy feed heating resistors, which convert

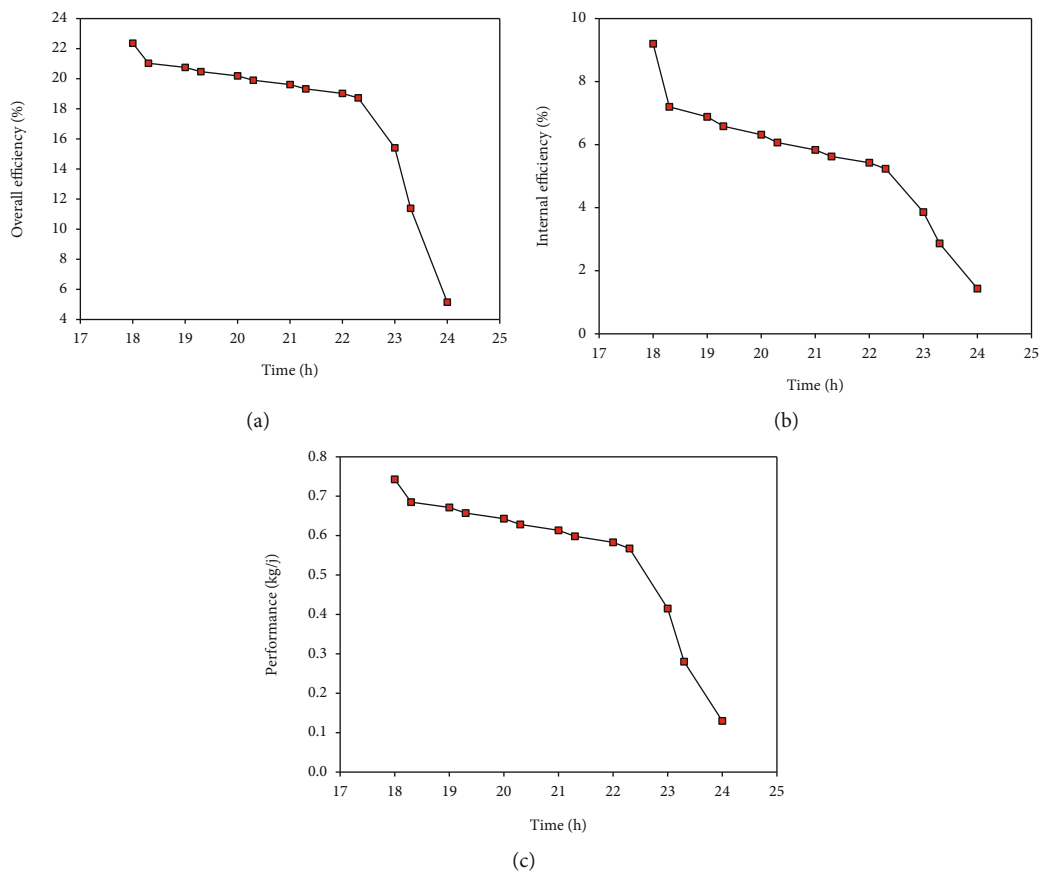

Figure 7: Temporal variation of (a) global efficiency, (b) internal efficiency, and (c) performance.

electrical energy into thermal energy.

$$Q = m \cdot Cp \cdot \Delta T,$$
$$P = V \cdot R = R \cdot I^2,$$
$$Q = P \cdot \Delta t, \tag{30}$$
$$\Delta T = \frac{P \cdot \Delta t}{m \cdot Cp}.$$

4. Results and Discussion

Figure 2 shows the temporal variation of latent heat during the evening. At 6 pm, the latent heat is at the minimum because the temperature is high, but at 24 pm, the latent heat is at the maximum because the temperature is at the minimum. It is concluded that the temperature influences the latent heat inversely.

Figures 3(a) and 3(b) show the temporal variation of the following parameters: the number of batteries and the number of panels, respectively. From 18 pm to 24 pm, the storage system produces the temperature overnight. It is noted that the number of photovoltaic elements increases, due to the temperature requested during the night.

Figures 4(a) and 4(b) show the temporal variation of thermal power and electric power, respectively. At 18 pm, thermal and electrical powers are high due to thermal storage. From 18 pm to 24 pm, they are weak because of the solar radiation, which is zero.

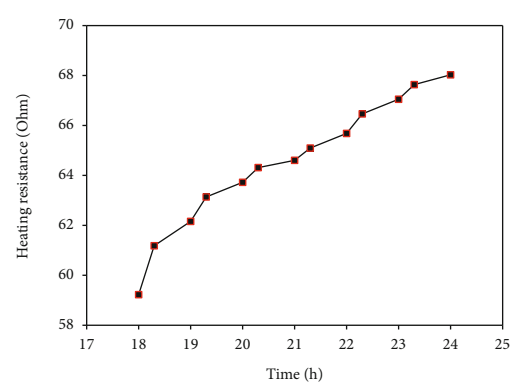

Figure 8: Temporal variation of the electrical resistance.

Figure 5 shows the variation in production over time. It is maximum at 18 pm due to the high thermal power generated by several energy sources in the system. From 18 pm to 24 pm, production decreases up to 24 h because the electrical storage is exhausted.

Figure 6 shows the temporal variation of the specific heat of water which hangs from maximum values at 18 pm, then

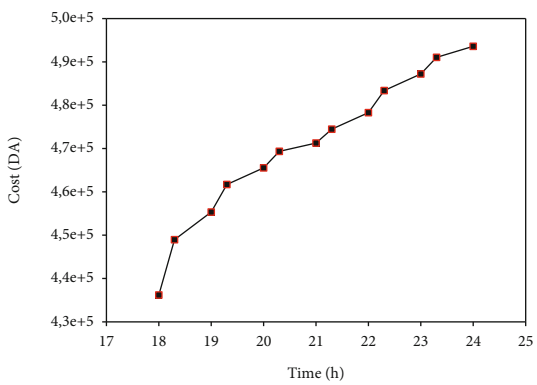

Figure 9: Variation of installation cost as a function of time.

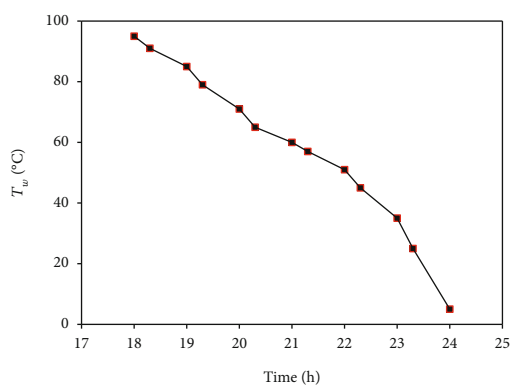

Figure 10: Variation of water temperature at sunset.

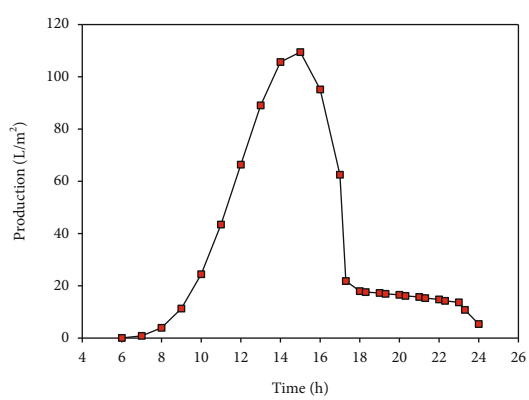

Figure 11: Temporal variation of the production of the hybrid distiller coupled with CCP and the system of autonomy.

decreases to minimum values at 24 pm, due to the temperature, which is low at 24 pm.

Figures 7(a)–7(c) show the temporal variation of the overall efficiency, internal efficiency, and performance, respectively, which hang from maximum values at 18 pm. These settings decrease slightly from 18 pm to 10 pm due to the stored temperature. From 10 pm to 24 pm, the above items decrease rapidly, as the temperature decreases to minimum values.

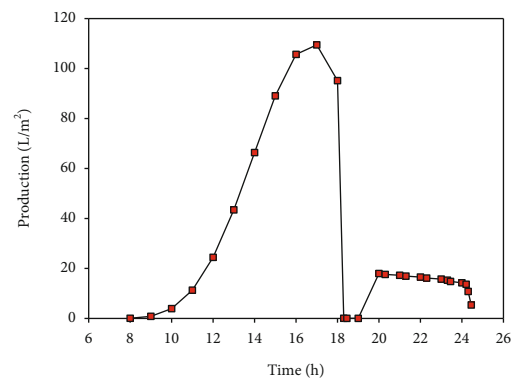

Figure 12: Effect of the delay of operation of the autonomy on the temporal variation of the production of the distiller coupled with a CCP and the autonomy.

Figure 8 shows the variation in electrical resistance which converts electrical energy stored by batteries to thermal energy overnight. A 68-ohm resistor maintains the distillation temperature for up to 24 hours. From 6 pm to midnight, we observe the evolution of the cost of distillation during the night.

Figure 9 shows that the time and amount of distillation increase the number of batteries and solar panels. In addition, the cost increases due to the number of the two previous parameters.

Figure 10 shows the temporal variation of the water temperature. At 18 pm, the temperature is high due to multiple energy sources and heat build-up. From 18 pm to 24 pm, the temperature decreases slowly thanks to the energy stored up to 24 pm.

Figure 11 shows the variation in production over time. From 12 pm to 14 pm, production reaches 100 L/m^2, because the solar radiation is powerful. At 18 pm, the production is almost 20 L/m^2 due to the absence of solar radiation. From 18 pm to 24 pm, the production is less than 20 L/m^2 during the night, due to the autonomy of the system.

Figure 12 shows the temporal variation of the production with a stop of operation of the autonomy which illustrated in the diagram from 18 h to 19 h. Then, the autonomy system begins to operate from 19 pm to midnight, which is why production grows at an average value of 16 L/m^2. At 23 pm, production slowly decreases to 0 L/m^2 at 24 pm, as the electrical energy storage is depleted.

Figure 13 shows the variation over time in the production of the following distillers: greenhouse still, hybrid still, hybrid still coupled to the CCP, and hybrid still coupled to the CCP and the autonomy system. The latter is the most efficient than the others and offers the advantage of night distillation from 18 pm to midnight.

5. Validations

Two experimental have been made on the coupling which shows that this method is effective in increasing the efficiency of solar stills. Elbar and Hassan [48] experimented with the coupling of a photovoltaic module and the integration of

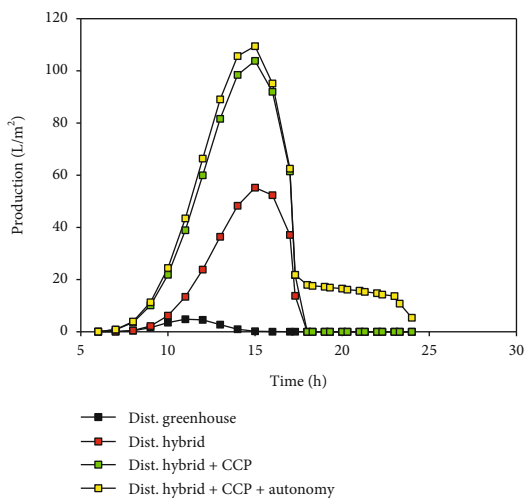

Figure 13: Temporal variation of the production of distillers.

phase change materials with the conventional solar tank (CSS). The results indicate that the combination of PV with CSS increases its production by 9%. Using the phase change pole with the PV coupled still increases their daily efficiency to 11.7%. Fathy et al. [49] experimentally studied the performance of coupling a parabolic collector with a double slope solar still. The results show that the solar still with the parabolic collector has a higher output than the conventional solar still. Freshwater production from the solar still with the parabolic collector followed about 142.3% at a saltwater depth of 20 mm in summer.

6. Conclusion

Combining several solar energy sources in one system, it improves and prolongs solar distillation at night. The coupling of concentrators or solar collectors and photovoltaic energy produces powerful thermal energy. It increases the thermal power of the passive still and improves its efficiency. The production reaches the maximum of 100 L/m^2 from noon to 14 pm, because the solar radiation is strong. From 16 pm to 18 pm, the production decreases to 20 L/m^2, due to the weak solar rays. From 18 pm to 24 pm, the production of the still takes average values thanks to the autonomy of the system. From 18 pm to 19 pm, a time difference is clearly visible in the production diagram due to an autonomy malfunction. From 19 pm to 24 pm, the autonomy system resumes operation and production increases to average values. Finally, the hybrid still, coupled with the CCP and an autonomous system, is more efficient than the other distillers proposed by various researches. In addition, it offers an advantage of distillation which lasts from 18 pm to 24 pm. The results show that the coupling of different thermal sources has several advantages for solar distillation. For example, it improves productivity, decreases the effect of meteorological factors on production, and prolongs the production time of the greenhouse still. From the study, it was noticed that thermal electrical conversion is a necessary factor that can improve still productivity to values of great interest for hybrid solar distillation.

Nomenclature

Ai: Surface of a body of index i (m^2)
C_n: Nominal battery capacity (Wh or Ah)
Cp_i: The specific heat of material of index i (J·kg^{-1}°C^{-1})
E_{AC}: Energy consumed in alternating current (Wh)
E_{DC}: Energy consumed in direct current (Wh)
e_g: Glass thickness (m)
e_{is}: Insulation thickness (mm)
E_{prod}: Produced electric energy (Wh)
E_T: Actual energy required by the system (consumption) (Wh)
g: Acceleration (m·s^{-2})
G_{mb}: Global radiation on a surface inclined at an angle b (kWh·m^{-2})
Gr: Grashof number
h_m: Nominal voltage of the modules (V)
I: Current intensity (A)
IG: Solar irradiation (W·m^{-2})
I_G: Generator current (A)
I_R: Parallel branch current of generator (A)
Kv: Coefficient of extinction of the glass (m^{-1})
L: Conductor length (m)
L_v: Latent heat of vaporization (J·kg^{-1})
m: Mass (kg)
m_A: Mass flow rate (kg·s^{-1})
M_c: Mass of the condensate (kg·s^{-1})
m_d: Mass flow rate of distillate (kg·s^{-1})
M_w: Molecular weight (g·mol^{-1})
N: Number of hours of exposure drum module (h)
N_p: Being the number of modules to be connected in parallel branches
N_R: Number of parallel branches of the generator
Ns: Number of modules in series per branch
$P^w{}_v$: Spray pressure to T_w
P_b: Solar power absorbed by the absorber (W·m^{-2})
P_c: Peak power (W)
P_d: Maximum depth of battery discharge
P_g: Solar power absorbed by the glass (W·m^{-2})
P_G: Overall loss factor (generally varies between 0.65 and 0.9)
P_i: Solar power absorbed by the body of index i (W·m^{-2})
P_p: Peak power of the module (W·m^{-2})
P_{PC}: Current flowing through the conductors (A)
Pr: Number of Prandtl
P_w: Energy absorbed by water (W·m^{-2})
$q_{absorbed}$: The amount of solar energy absorbed from thermodynamics we have (W)
$q^c{}_{b-isi}$: Heat flux between the bin and the water (W)
$q^{cd}{}_{b-isi}$: Heat flux lost by conduction from the tank (W)
$q^c{}_{g-a}$: Heat flow lost by convection through the glass to the outside (W)
$q^c{}_{is-a}$: Heat flow lost by conduction (W)
$q^c{}_{w-g}$: Heat flux by convection between the film of water and the glass (W)

Q_{E24h}: Quantity of energy entered after 24 hours (W)
Q_{ev}: Amount of heat used for evaporation per unit of time (useful gain) (W)
$q^{ev}{}_{w-g}$: Heat flux by condensation between the water film and the glass (W)
$q_{external}$: Amount of heat lost to the outside (W)
q_{inside}: The amount of energy that indicates the heat transfer between the absorber tube and the glass envelope (W)
$q_{internal}$: Quantity of internal heat in the annular space (W)
Q_{P24h}: Quantity of water produced after 24 hours (W)
$q^{r}{}_{g-a}$: Heat flux lost by the glass by radiation to the outside (W)
$q^{r}{}_{is-a}$: Heat flux by radiation between the insulation and to the outsides (W)
$q^{r}{}_{w-g}$: Heat flux by radiation (W)
q_{useful}: Heat flow exchanged by convection between the absorber and the fluid (W)
$q^{w}{}_{v}$: Spray pressure to T_w
R_C: Ohmic resistance of conductors (Ohm)
S: Conductor cross section (mm^2)
t_{di}: Daily use time (h)
T_i: Body temperature of index i (°C)
V_{Bat}: Nominal battery voltage (V)
V_m: Nominal voltage of the modules (V)
z: Tube length (mm)
α_a: Absorption coefficient of transmission
α_b: Coefficient of absorption by the basin
Δz: Element length (mm)
ε_g: Emission of the glass
ε_w: Water emissivity
λ_i: Thermal conductivity of material of index i ($W{\cdot}m^{-1}{}^{\circ}C^{-1}$)
ρ: Density $(kg{\cdot}m^{-})^3$
ρ_r: Transmission coefficient due to reflection
σ: Stefan-Boltzmann constant ($Wm^{-2}{\cdot}K^{-4}$)
τ_w: Coefficient of transmission of brine.

Data Availability

Only we can provide the results reported in the article to other researchers.

Conflicts of Interest

The authors declare that they have no conflicts of interest.

References

[1] B. Ghorbani, Z. Javadi, S. Zendehboudi, and M. Amidpour, "Energy, exergy, and economic analyses of a new integrated system for generation of power and liquid fuels using liquefied natural gas regasification and solar collectors," *Energy Conversion and Management*, vol. 219, article 112915, 2020.

[2] M. Nouri, M. Miansari, and B. Ghorbani, "Exergy and economic analyses of a novel hybrid structure for simultaneous production of liquid hydrogen and carbon dioxide using photovoltaic and electrolyzer systems," *Journal of Cleaner Production*, vol. 259, article 120862, 2020.

[3] A. Ebrahimi, B. Ghorbani, and M. Ziabasharhagh, "Introducing a novel integrated cogeneration system of power and cooling using stored liquefied natural gas as a cryogenic energy storage system," *Energy*, vol. 206, article 117982, 2020.

[4] V. S. Gupta, D. B. Singh, R. K. Mishra, S. K. Sharma, and G. N. Tiwari, "Development of characteristic equations for PVT-CPC active solar distillation system," *Desalination*, vol. 445, pp. 266–279, 2018.

[5] H. Manchanda and M. Kumar, "Performance analysis of single basin solar distillation cum drying unit with parabolic reflector," *Desalination*, vol. 416, pp. 1–9, 2017.

[6] B. Ghorbani, M. Miansari, S. Zendehboudi, and M.-H. Hamedi, "Exergetic and economic evaluation of carbon dioxide liquefaction process in a hybridized system of water desalination, power generation, and liquefied natural gas regasification," *Energy Conversion and Management*, vol. 205, article 112374, 2020.

[7] A. Ebrahimi, B. Ghorbani, M. Ziabasharhagh, and M. J. Rahimi, "Biomass gasification process integration with Stirling engine, solid oxide fuel cell, and multi-effect distillation," *Journal of Thermal Analysis and Calorimetry*, 2020.

[8] B. Ghorbani, R. Shirmohammadi, M. Amidpour, F. Inzoli, and M. Rocco, "Design and thermoeconomic analysis of a multi-effect desalination unit equipped with a cryogenic refrigeration system," *Energy Conversion and Management*, vol. 202, article 112208, 2019.

[9] F. A. Essa, W. H. Alawee, S. A. Mohammed, A. S. Abdullah, and Z. M. Omara, "Enhancement of pyramid solar distiller performance using reflectors, cooling cycle, and dangled cords of wicks," *Desalination*, vol. 50, article 115019, 2021.

[10] H. A. Dhahad, W. H. Alawee, and T. A. Mohammad, "Review on the important methods used to enhance the productivity of the solar still," *International Journal of Scientific & Engineering Research*, vol. 8, no. 7, pp. 12–18, 2017.

[11] W. H. Alawee, S. A. Mohammed, H. A. Dhahad, A. S. Abdullah, Z. M. Omara, and F. A. Essa, "Improving the performance of pyramid solar still using rotating four cylinders and three electric heaters," *Process Safety and Environmental Protection*, vol. 148, pp. 950–958, 2021.

[12] Q. Li, L.-J. Beier, J. Tan et al., "An integrated, solar-driven membrane distillation system for water purification and energy generation," *Applied Energy*, vol. 237, pp. 534–548, 2019.

[13] Q. Wang, S. Liang, Z. Zhu, G. Wu, Y. Su, and H. Zheng, "Performance of seawater-filling type planting system based on solar distillation process: numerical and experimental investigation," *Applied Energy*, vol. 250, pp. 1225–1234, 2019.

[14] G. Gopi, G. Arthanareeswaran, and A. F. Ismail, "Perspective of renewable desalination by using membrane distillation," *Chemical Engineering Research and Design*, vol. 144, pp. 520–537, 2019.

[15] M. Muraleedharan, H. Singh, M. Udayakumar, and S. Suresh, "Modified active solar distillation system employing directly absorbing Therminol 55-Al_2O_3 nano heat transfer fluid and Fresnel lens concentrator," *Desalination*, vol. 457, pp. 32–38, 2019.

[16] S. M. Parsa, D. Javadi Y, A. Rahbar et al., "Experimental assessment on passive solar distillation system on Mount Tochal at the height of 3964 m: study at high altitude," *Desalination*, vol. 466, pp. 77–88, 2019.

[17] R. Miladi, N. Frikha, A. Kheiri, and S. Gabsi, "Energetic performance analysis of seawater desalination with a solar

membrane distillation," *Energy Conversion and Management*, vol. 185, pp. 143–154, 2019.

[18] M.-A. A. Hejazi, O. A. Bamaga, M. H. Al-Beirutty, L. Gzara, and H. Abulkhair, "Effect of intermittent operation on performance of a solar-powered membrane distillation system," *Separation and Purification Technology*, vol. 220, pp. 300–308, 2019.

[19] A. Afzal, A. Munir, A. Ghafoor, and J. L. Alvarado, "Development of hybrid solar distillation system for essential oil extraction," *Renewable Energy*, vol. 113, pp. 22–29, 2017.

[20] W. H. Alawee, H. A. Dhahad, and T. A. Mohamed, "An expermental study on improving the performance of a double slope solar still," in *The 7th International Conference on Sustainable Agriculture for Food, Energy and Industry in Regional and Global Context*, pp. 1–10, Selangor, Malaysia, 2015.

[21] W. H. Alawee, "Improving the productivity of single effect double slope solar still by modification simple," *Journal of Engineering*, vol. 21, no. 8, 60 pages, 2015.

[22] W. H. Alawee, H. A. Dhahad, and K. I. Abass, "Increase the yield of simple solar distillation using the water drip method," *International Journal of Computation and Applied Sciences*, vol. 6, no. 2, pp. 437–486, 2019.

[23] M.'. A. al-Nimr and K. S. Qananba, "A solar hybrid system for power generation and water distillation," *Solar Energy*, vol. 171, pp. 92–105, 2018.

[24] R. Bhardwaj, M. V. ten Kortenaar, and R. F. Mudde, "Influence of condensation surface on solar distillation," *Desalination*, vol. 326, pp. 37–45, 2013.

[25] S. Kiwan, M.'. al-Nimr, and Q. I. Abdel Salam, "Solar chimney power-water distillation plant (SCPWDP)," *Desalination*, vol. 445, pp. 105–114, 2018.

[26] S. W. Sharshir, G. Peng, N. Yang, M. O. A. El-Samadony, and A. E. Kabeel, "A continuous desalination system using humidification - dehumidification and a solar still with an evacuated solar water heater," *Applied Thermal Engineering*, vol. 104, pp. 734–742, 2016.

[27] Z. M. Omara, M. A. Eltawil, and E. A. ElNashar, "A new hybrid desalination system using wicks/solar still and evacuated solar water heater," *Desalination*, vol. 325, pp. 56–64, 2013.

[28] Y. Tian and C. Y. Zhao, "A review of solar collectors and thermal energy storage in solar thermal applications," *Applied Energy*, vol. 104, pp. 538–553, 2013.

[29] G. M. Ayoub, M. Al-Hindi, and L. Malaeb, "A solar still desalination system with enhanced productivity," *Desalination and Water Treatment*, vol. 53, no. 12, pp. 3179–3186, 2015.

[30] S. Abdallah, M. M. Abu-Khader, and O. Badran, "Performance evaluation of solar distillation using vacuum tube coupled with photovoltaic system," *Applied Solar Energy*, vol. 45, p. 176, 2009.

[31] K. Sampathkumar, T. V. Arjunan, P. Pitchandi, and P. Senthilkumar, "Active solar distillation–a detailed review," *Renewable and Sustainable Energy Reviews*, vol. 14, no. 6, pp. 1503–1526, 2010.

[32] A. Allouhi, "Advances on solar thermal cogeneration processes based on thermoelectric devices: a review," *Solar Energy Materials & Solar Cells*, vol. 200, article 109954, 2019.

[33] R. Dev and G. N. Tiwari, "Characteristic equation of a hybrid (PV-T) active solar still," *Desalination*, vol. 254, no. 1-3, pp. 126–137, 2010.

[34] A. E. Kabeel, A. M. Hamed, and S. A. El-Agouz, "Cost analysis of different solar still configurations," *Energy*, vol. 35, pp. 2901–2908, 2010.

[35] Y. Qin, K. Tan, D. Meng, and F. Li, "Theory and procedure for measuring the solar reflectance of urban prototypes," *Energy and Buildings*, vol. 126, pp. 44–50, 2016.

[36] Y. Qin, "Pavement surface maximum temperature increases linearly with solar absorption and reciprocal thermal inertial," *International Journal of Heat and Mass Transfer*, vol. 97, pp. 391–399, 2016.

[37] P. Sharan, T. Neises, J. D. McTigue, and C. Turchi, "Cogeneration using multi-effect distillation and a solar-powered supercritical carbon dioxide Brayton cycle," *Desalination*, vol. 459, pp. 20–33, 2019.

[38] W. H. Alawee, H. A. Dhahad, I. S. Ahmed, and T. A. Mohammad, "Experimental investigation on an elevated basin solar still with integrated internal reflectors and inclined fins," *Journal of Engineering Science and Technology*, vol. 16, no. 1, pp. 762–777, 2021.

[39] W. H. Alawee, H. A. Dhahad, and T. A. Mohammad, "Enhancement of solar still productivity using absorber plate with inclined perforated rectangular fins: experimental study with economic analysis," *Desalination and Water Treatment*, vol. 213, pp. 53–63, 2021.

[40] F. A. Essa, Z. M. Omara, A. S. Abdullah et al., "Wall-suspended trays inside stepped distiller with Al_2O_3/paraffin wax mixture and vapor suction: experimental implementation," *Journal of Energy Storage*, vol. 32, article 102008, 2020.

[41] P. Y. Xiong, A. Almarashi, H. A. Dhahad et al., "Nanomaterial transportation and exergy loss modeling incorporating CVFEM," *Journal of Molecular Liquids*, vol. 330, article 115591, 2021.

[42] B. Mandi, Y. Menni, A. J. Chamkha et al., "Effect of various physical parameters on the productivity of the hybrid distiller - in the time of distillation extension at night," *European Journal of Electrical Engineering*, vol. 21, no. 3, pp. 265–271, 2019.

[43] O. García-Valladares and N. Velázquez, "Numerical simulation of parabolic trough solar collector: improvement using counter flow concentric circular heat exchangers," *International Journal of Heat and Mass Transfer*, vol. 52, pp. 597–609, 2009.

[44] V. Velmurugan, M. Gopalakrishnan, R. Raghu, and K. Srithar, "Single basin solar still with fin for enhancing productivity," *Energy Conversion and Management*, vol. 49, pp. 2602–2608, 2008.

[45] Y. Nurfaidah, I. Wibawa, B. Aprilia, C. Ekaputri, and M. Reza, "Analysis of smart house power savings with on-grid photovoltaic power system," *Journal of Physics Conference Series*, vol. 1367, article 12047, 2019.

[46] P. Sharma, H. Bojja, and P. Yemula, "Techno-economic analysis of off-grid rooftop solar PV system," in *2016 IEEE 6th International Conference on Power Systems (ICPS)*, pp. 1–5, New Delhi, India, 2016.

[47] R. Fares and M. Webber, "The impacts of storing solar energy in the home to reduce reliance on the utility," *Nature Energy*, vol. 2, article 17001, 2017.

[48] A. R. A. Elbar and H. Hassan, "Experimental investigation on the impact of thermal energy storage on the solar still performance coupled with PV module via new integration," *Solar Energy*, vol. 184, pp. 584–593, 2019.

[49] M. Fathy, H. Hassan, and M. Salem Ahmed, "Experimental study on the effect of coupling parabolic trough collector with double slope solar still on its performance," *Solar Energy*, vol. 163, pp. 54–61, 2018.

Hindawi
International Journal of Photoenergy
Volume 2021, Article ID 5546508, 13 pages
https://doi.org/10.1155/2021/5546508

Research Article

Improvement of Heat Pipe Solar Collector Thermal Efficiency Using Al_2O_3/Water and TiO_2/Water Nanofluids

Sinan Ünvar,[1] **Tayfun Menlik**,[2] **Adnan Sözen**,[2] **and Hafız Muhammad Ali**[3,4]

[1]*Ağrı İbrahim Çeçen University, Vocational School, Ağrı, Turkey*
[2]*Technology Faculty, Energy Systems Engineering, Gazi University, Teknikokullar, Ankara, Turkey*
[3]*Mechanical Engineering Department, King Fahd University of Petroleum and Minerals, Dhahran, Saudi Arabia*
[4]*Interdisciplinary Research Center for Renewable Energy and Power Systems (IRC-REPS), King Fahd University of Petroleum and Minerals, Dhahran, 31261, Saudi Arabia*

Correspondence should be addressed to Hafiz Muhammad Ali; hafiz.ali@kfupm.edu.sa

Received 11 January 2021; Accepted 18 May 2021; Published 8 June 2021

Academic Editor: Mohammad Alghoul

Copyright © 2021 Sinan Ünvar et al. This is an open access article distributed under the Creative Commons Attribution License, which permits unrestricted use, distribution, and reproduction in any medium, provided the original work is properly cited.

Heat pipe solar collectors (HPSCs) are heat exchangers that carry heat based on the phase change of the heat pipe working fluid. It is aimed to increase the operating temperature range of solar collectors by changing the phase of the working fluid in the heat pipe at low temperature. For this reason, it has become widespread to use nanofluids obtained by mixing nanosized metal oxides with the base fluid in certain proportions in order to increase both the thermal conductivity of the heat pipe working fluids and to increase the specific heat closures. The main purpose of this study, which was conducted to evaluate the performance of HPSCs, is to increase performance, and an experimental study has been conducted in this direction. For this purpose, an HPSC designed and manufactured was used. Al_2O_3-water and TiO_2-water nanofluids containing 2% nanoparticles were used in order to increase performance in the study. HPSC used in the study consists of 8 heat pipes with a length of 100 cm. The experiments were carried out for pure water and nanofluids, and their efficiency and strength were compared. The highest value of instantaneous efficiency was calculated as 48% when pure water was used as the working fluid, 58% for Al_2O_3-water nanofluid, and 64% for TiO_2-water nanofluid. The instantaneous power obtained using pure water was determined as 135.66 W, 167.96 W for Al_2O_3-water nanofluid, and 184.03 W for TiO_2-water nanofluid. The improvement in efficiency was determined as 20.8% for Al_2O_3-water nanofluid and 33.3% for TiO_2-water nanofluid. Improvement in powers was found to be 23.8% for Al_2O_3-water nanofluid and 35.6% for TiO_2-water nanofluid.

1. Introduction

Turkey is a rich country in the diversity of renewable energy sources and its current potential. Particularly, hydro, wind, solar, and geothermal energy has the potential to meet most of the energy needed. However, there are evaluations that this potential is not used effectively enough in the country [1]. The need for energy is increasing day by day in many countries, and the gap between production and consumption tends to open day by day. Among the most important reasons for this situation are as follows: factors such as population growth, technological development, industrialization, and increase in people's life comfort are at the top. For example, between 2002 and 2017, total electrical energy consumption increased from 103 TWh to 296 TWh, an increase of about three times [2]. Due to such an increase in energy use and the widening of the difference between production and consumption, the efficient use of existing energy resources has become a very important issue for every country and has made countries take some precautions. In addition to the precautions taken, the improvement works on the existing systems have become an important issue nowadays, and important steps towards the solution of the energy problem have been taken by accelerating the studies carried out in this direction. Studies are carried out in various countries to develop devices with features such as electricity generation and water heating, especially with the use of solar energy, and researchers working on these issues are also supported.

Particularly, in recent years, studies have been carried out for the use of heat pipes in solar collectors and various working fluids have been used within the scope of improving the efficiency of collectors.

Heat pipes are devices working on the principle of evaporation-condensation of the working fluid. The working fluid, which passes from the liquid phase to the vapor phase under the influence of temperature, rises under the influence of the vacuum environment and natural transport and moves its energies from one region to another [3]. The transport cycle formed in the heat pipe is completed in this way. The temperature of the working fluid, which releases its energy to the region where it rises, drops and therefore passes into the liquid phase. In other words, the heat transfer cycle is completed by making use of the phase change of the working fluid in the heat pipe. Conventional heat transfer fluids have lower thermal conductivity because they have weaker thermal properties than solids, so the use of conventional fluids in thermal systems may be insufficient to improve the performance of engineering devices and improve their compactness [4]. However, there are some ways to increase heat transfer efficiency in heat pipes. One of these ways is the addition of metallic-nonmetallic or polymeric particles to heat transfer fluids. Fluids prepared by suspending nanoparticles of 1-100 nm in size into conventional fluids are called "nanofluid," and their heat transfer properties are better than conventional fluids. The main physical events that cause the heat transfer performance of nanofluids to improve significantly can be summarized as follows [5]:

(i) The increase in the thermal conductivity of the prepared nanofluid, as the thermal conductivity of the solid metal is higher than that of the basic fluid

(ii) The increase in the thermal transfer surface area due to the increase in the thermal conductivity of the fluid

(iii) The increase in the effective thermal capacity of the fluid

(iv) Increased thermal conductivity of the liquid due to high fluid activity and turbulence volume

In recent years, many researches have been conducted on the use of nanofluids in heat pipes. Saffarian et al. conducted a numerical study based on the collector's flow direction to increase the efficiency of the flat plate solar collector. In order to examine their effects on heat transfer efficiency, they specifically examined the parameters of flow direction and the use of nanofluid in the collector and investigated their effects. Accordingly, they analyzed the geometries of structures with U-shaped, wavy, and spiral pipes of the same pipe length on a flat plate solar collector using the k-ε model. As a result of their studies, they determined that the use of wavy and spiral pipes could significantly increase the heat transfer and Nusselt number, and the increase in nanoparticle concentration could also increase the heat transfer coefficient [6]. Mercan and Yurddaş conducted a numerical study to determine the effect of using nanofluids on heat transfer in solar collectors. In this numerical study, they have chosen different fractions, different collector angles, and different mass flow rates as basic parameters for nanofluids. As a result of their studies, they determined that the use of nanofluid improved heat transfer [7]. Dehaj and Mohiabadi used magnesium oxide (MgO) and deionized water nanofluids as working fluids in the heat pipe solar collector. They experimentally examined the effects of these nanofluids on the performance they prepared in different concentrations. As a result of their studies, they found that the performance of the heat pipe solar collector increased as the rate of the refrigerant increased and the concentration of the MgO nanoparticle increased [8]. Kılıç studied the effects of fluids containing nanosized metal oxides in solar collectors on the performance of the system. In his experiments using a flat plate solar collector (FPSC), he used 2% mass alumina-water (Al_2O_3-water) and titanium dioxide (TiO_2) nanofluids. Of the nanofluids used, TiO_2-water nanofluid improved 34.43% in instantaneous efficiency compared to pure water, 32.43% improvement in power output, while Al_2O_3-water nanofluid mixture increased by 9.5% in instantaneous efficiency and 9.06% increased in power output [9]. Sözen et al. conducted a study to examine the effect of nanofluids on system performance in a heat exchanger containing a heat pipe bundle. As a result of their experiments, they determined that the use of nanofluid in the system significantly improved performance. In their tests at 6 k W heater power, they found that the maximum recovery was 37.04% [10]. Kaya et al. conducted an experimental performance assessment in an evacuated tube heat pipe using 50 nm diameter copper oxide- (CuO-) pure methanol nanofluid. Exergy values of different states were calculated, and experimental results were compared. From the data obtained as a result of the study, it was stated that the use of nanofluid provided better performance in heat pipe applications [11]. Daghigh and Zandi conducted an experimental study on the use of nanofluids in heat pipe solar collectors. In their study, they used water as the main fluid and CuO, TiO_2, and MWCNT as nanoparticles. As a result of the experiments, it was determined that the use of nanofluid provided a better thermal performance than the use of water. Compared with water, MWCNT, CuO, and TiO_2 nanofluids have been shown to perform better by 25%, 12%, and 5% in August and 25%, 15%, and 7%, respectively, in October [12]. Gürü et al. studied experimentally the effects of using a nanofluid containing bentonite in heat pipes. The particle ratios of the nanofluids used in the experiments were examined by changing 0.5%, 2%, and 4% by mass. The highest heat pipe efficiency was achieved with an increase of 37% in the parameters of 200 W heating power and 5 g/s cooling water mass flow [13]. Sözen et al. studied using fly ash and alumina nanofluids to evaluate the performance of two-phase closed thermosiphon heat pipe. In their study, they used various metal oxide containing nanoparticles such as SiO_2, TiO_2, Al_2O_3, Fe_2O_3, CaO, and MgO obtained from the cyclones of Yatağan Thermal Power Plant. Experiments were carried out at three different heating powers (200 W, 300 W, and 400W) and three different coolant flow rates (5 g/s, 7.5 g/s, and 10 g/s). It has been determined that using nanofluid instead of water at 400 W heating power and 5 g/s cooling water flow provided a 30.1% reduction in heat resistance

Figure 1: Ultrasonic bath setup.

Table 1: Properties of nanoparticles used in the study [35].

	Alumina	Titanium dioxide
Purity	99.5+	99.55+
Particle size (average)	18 nm	38 nm
Surface area	140 m^2/g	35 m^2/g
Density	3900 kg/m^3	4100 kg/m^3

Table 2: Devices and technical features used in preparing nanofluid.

Device name	Technical specifications
Ultrasonic bath (Bandelin DT 255 H)	(i) Voltage: 230 V-50/60 Hz (ii) Ultrasonic power: 160/640 W (ii) Heater power: 280 W (iv) Ultrasonic frequency: 35 kHz (v) Internal volume: 5.5 L
Precision scales (Precisa XB 320M)	(i) Precision: 0.1 mg (ii) Measuring range: 0.02-320 g

[14]. Çiftçi et al. conducted experimental studies to determine the effect of using a nanofluid containing TiO_2 in heat pipes on system improvement. For this purpose, the nanoparticle used in the experiments was mixed with 2% pure water and a nanofluid was prepared by the two-step method. As a result of the experiments conducted at various heating power and mass flow values, they found that the improvement in the highest thermal performance was 16.5% at 200 W power at 5 g/s [15]. Çakır used 2% by volume Al_2O_3 (alumina) nanoparticles in thermosiphon type heat pipe in his study. The researcher used 3 different water flows in the condenser part in his experiments and carried out the experiments at 2 different angles by giving 3 different heat inputs in the evaporator part. As a result of the experiments, it has been determined that the nanofluid used in 500 W heat input at 0.0075 kg/s mass flow and 75° heat pipe slope provided efficiency improvement of 35.7% [16]. Pise et al. investigated the working conditions and performance of a thermosiphon heat pipe with a serpentine-shaped solar collector. In their experimental study, they used 0.05%, 0.025, and 0.05% Al_2O_3 nanofluid and surfactant. They determined the angle of 50° as the optimum value among different slope angles. As a result of their studies, they found that the use of nanofluid provided better performance compared to pure water [17]. Menlik et al. produced 5% volumetric MgO/water nanofluid by direct synthesis using Triton X-100 nonionic surfactant and used it in heat pipes. In the heat pipe experimental setup they prepared, they used flat copper pipes with an inner diameter of 13 mm and wall thickness of 2 mm and 1 mm. As a result of their studies, they found that an improvement of 26% was achieved in heat pipe performance at 200 W heating power and 7.5 g/s flow [18]. Eidan et al. used acetone-based nanofluids to improve the performance of glass tube heat pipes in their study. In their study, they determined different filling rates (40%-50%-60%-70%-80%) and different collector slope angles (30°-45°-60°) as experimental parameters. As a result of their studies and experiments, they determined that the optimum performance values were at a 70% filling rate and at an angle of 45° degrees [19]. Ozturk et al. conducted an experimental study on the heat recovery system in the air recovery unit. They used TiO nanoparticles to increase performance in their studies. In their experimental study, they filled 33% of the evaporator part with working fluid. They carried out their experiments at 5 different cooling flow rates (40, 42, 45, 61, and 84 g/s) and two different heating power (3 kW and 6 kW) and between 25°C and 90°C. As a result, they detected a 50% performance increase at 3 kW heating power, 84 g/s cooling air flow, and a heat recovery system using TiO nanofluid [20]. Sözen et al. used aqueous clinoptilolite as their working fluid and carried out their studies in different working conditions to examine the performance of a heat pipe experimentally and numerically. With the use of aqueous clinoptilolite nanofluid as working fluid, it was determined that the maximum heat transfer increase and the improvement in the heat resistance of the heat pipe were 9.63% and 26.31%, respectively. In addition

Table 3: Thermophysical properties of nanofluids.

Working fluid	Density (kg/m^3)	Specific heat (kJ/kgK)	Thermal conductivity (W/mK)	Viscosity (kgm^{-1} s^{-1})			
				20°C	40°C	60°C	80°C
Pure water	998	4.18	0.607	0.98	0.64	0.45	0.35
Al_2O_3/water	1056	4.32	0.665773	1.02	0.82	0.61	0.42
TiO_2/water	1015	4.26	0.662310	1.01	0.92	0.67	0.54

to the experimental studies conducted by the researchers, the calculations made using computational fluid dynamics have been confirmed, and it has been determined that the experimental and numerical data are in harmony [21]. Tong et al. examined performance using Al_2O_3 and CuO nanofluids as working fluid in flat plate solar collectors. They found that when using Al_2O_3 nanofluid compared to water, 21.9% higher efficiency was achieved. They also evaluated the exergic efficiency of the collector using nanofluids. Accordingly, they determined that when using 1% Al_2O_3 and 0.5% CuO nanofluid, an increase of 56.9% and 49.6% was achieved, respectively [22]. Ozsoy and Corumlu synthesized silver-water nanofluids to determine the thermal efficiency of the evacuated tube solar collector. They determined the definition of this nanofluid, which can maintain its stability for a long time, by X-ray fraction, scanning electron microscope, visible spectroscopy with UV, and thermophysical analysis. As a result of their study, they found that the use of silver-water nanofluid increased the efficiency of the solar collector by 20.7% to 40% compared to pure water [23]. Su et al. conducted a literature study on the use of nanofluid in ETSCs. As a result of their studies, they advocated the view that nanofluids that will be prepared by using boron nanoparticles will have an effect on performance [24]. Zhao et al. synthesized graphene/water nanofluid and conducted an experimental study on the thermal initiation performance of the gravity-supported heat pipe. The concentrations of various graphene nanoplatelets (GNPs) were measured at different temperatures in different analyses, including the thermophysical properties-thermal conductivity and viscosity of the nanofluid. In addition, based on the operational evaluation on the start-up process of a single heat pipe, the performance of solar gravity-assisted heat pipes enriched with nanofluids using different concentrations of GNP was compared using water heating experiments. The results showed that the use of 0.05% by weight graphene/water nanofluid instead of water could lead to 15.1% and 10.7% reduction in start-up time in 30 and 60 W inlet heating conditions, respectively [25].

As can be seen from the literature review, the studies to be evaluated within the scope of passive heat improvement in recent studies for the improvement of heat transfer are directed to the use of nanometal oxides to increase the thermal conductivity of the fluid. In this context, many studies have been carried out such as heat pipes, heat recovery units that use the heat pipe as heat exchanger, cooling and heating applications. The biggest feature that distinguishes this study from others is that the heat pipe is tested not individually but in a solar energy application with experiments. Therefore, the heat gained from solar energy is to reach a temperature sufficient to cause the phase change of the working fluid in the heat pipe evaporator, and even this temperature causes the system to operate at a lower degree. For this, a comparative experimental analysis was carried out using two different nanofluids. In the study, the performances of Al_2O_3-water and TiO_2-water nanofluids were compared with that of pure water.

2. Materials and Methods

2.1. Preparation of Nanofluids. Nanofluids are not a simple solid-liquid suspension. It should also provide the following features [26]:

(i) Prepared suspension should be stable

(ii) Clumping in the particles should be negligible

(iii) The chemical properties of the fluid should not change over time

Two methods are used in nanofluid preparation:

(i) One-step method

The one-step approach is based on combining the production and dispersion processes of nanoparticles in a nanofluid in a single step. For this method, the chemical wetting method, vacuum evaporation method, and submerged nanoparticle synthesis method are widely used. In the one-step method, metal materials with high heat conduction coefficient and rapidly oxidizing are preferred. This is because when metal nanoparticles are synthesized with the fluid, their contact with air is prevented. However, one disadvantage of this method is that only low vapor pressure liquids are compatible with the process, which limits its use [27].

(ii) Two-step method

In this method, the desired nanoparticles are obtained first, and then, the nanoparticles are dispersed into the basic fluid in a way that maintains its stability and homogeneity [28]. Magnetic stirrers, ultrasonic water baths, or homogenizers are used to ensure homogeneous distribution. High surface area and surface activity tend to aggregate in nanoparticles. In the two-step method, surfactants are used to increase stability and prevent agglomeration. The two-step method is the most commonly used method in the preparation of nanofluids due to its low production cost and easy accessibility due to the industrial production of nanoparticles [29]. In addition, this method has a higher commercialization potential, since it is possible to produce large quantities of nanofluids.

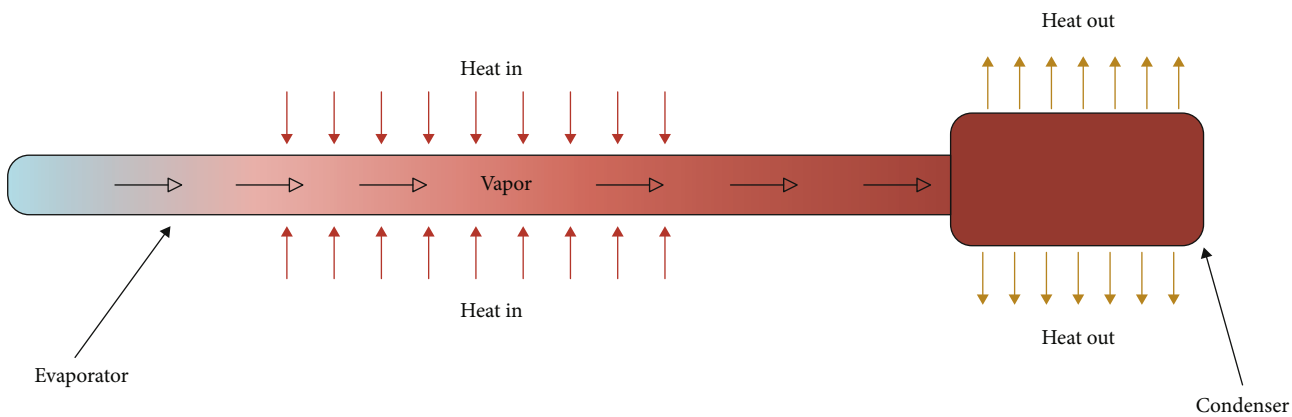

Figure 2: Schematic diagram of a basic heat pipe [37].

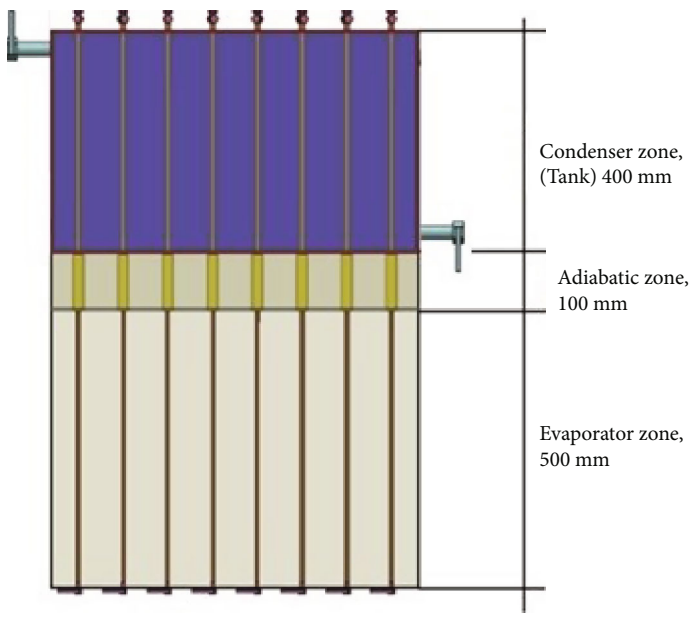

Figure 3: Parts of the heat pipe solar collector.

Table 4: Technical characteristics of the collector.

Tank	Stem	Black sheet, 2 mm
	Insulation	Rock wool, 50 mm
Safe	Stem	Galvanized sheet, 0.45 mm
	Insulation	Rock wool, 60 mm
Absorber		Copper plate, 0.5 mm
Absorber surface		Matte black
Top cover		Glass, 4 mm

The basis of the method is known as the one-step method, nanoparticle production in fluid. The two-step method is the method of suspending the particle into the basic fluid using appropriate methods. Al_2O_3 and TiO_2 nanofluids used in this study were prepared by the two-step method. In the literature, there are 3 methods used to suspend nanoparticles into the basic fluid [30].

2.1.1. Changing the pH of the Suspension. The pH value of nanofluids is related to the surface of nanoparticles, and the pH change can strongly improve the stability of unstable nanoparticles [31]. This is because the stability of the nanofluid is directly related to its electrokinetic properties. Therefore, the zeta potential can be increased or decreased by changing the pH value of the nanofluid. The pH value of a nanofluid can be increased or decreased by adding a suitable nonreactive alkaline or acidic solution [32].

2.1.2. Using Surface Activators or Diluents. The stability of the nanofluid depends on the type of nanoparticles and the basic fluid used. Nanoparticles can be hydrophobic or hydrophilic, and basic fluids can be polar or nonpolar. Hydrophilic nanoparticles such as oxide nanoparticles are easily dispersible in polar basic fluids such as water, and hydrophobic nanoparticles such as carbon nanotubes can be dispersed in nonpolar basic fluids such as oils without requiring a third component. However, surfactants need to be added to stabilize the

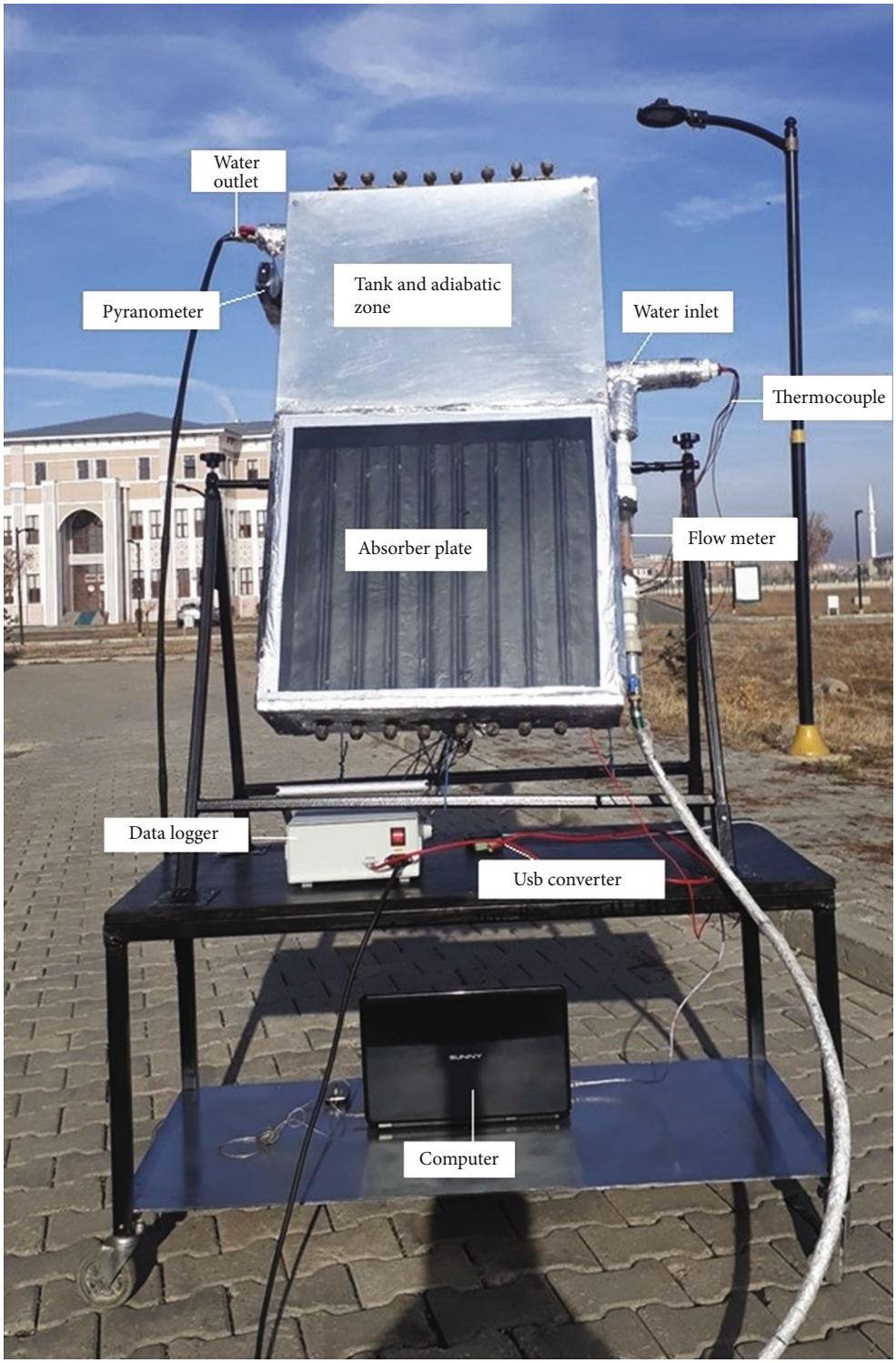

Figure 4: Experimental setup.

nanofluids if hydrophobic nanoparticles are dispersed in polar basic fluids and hydrophilic nanoparticles in nonpolar basic fluids. Surfactants act as a bridge between nanoparticles and elementary fluids and provide continuity [33, 34].

2.1.3. Applying Ultrasonic Vibrations to Particles. Ultrasonic mixing process, which is a physical method based on the use of ultrasonic waves in a fluid, is used to increase the stability of the nanofluid by breaking the gravitational force of the nanoparticles in the precipitate. There are two types of ultrasonicators: probe type and bath type. Sonication time varies according to the study. However, the sonication time should be optimized because an increase in sonication time can reduce the size of the nanoparticles.

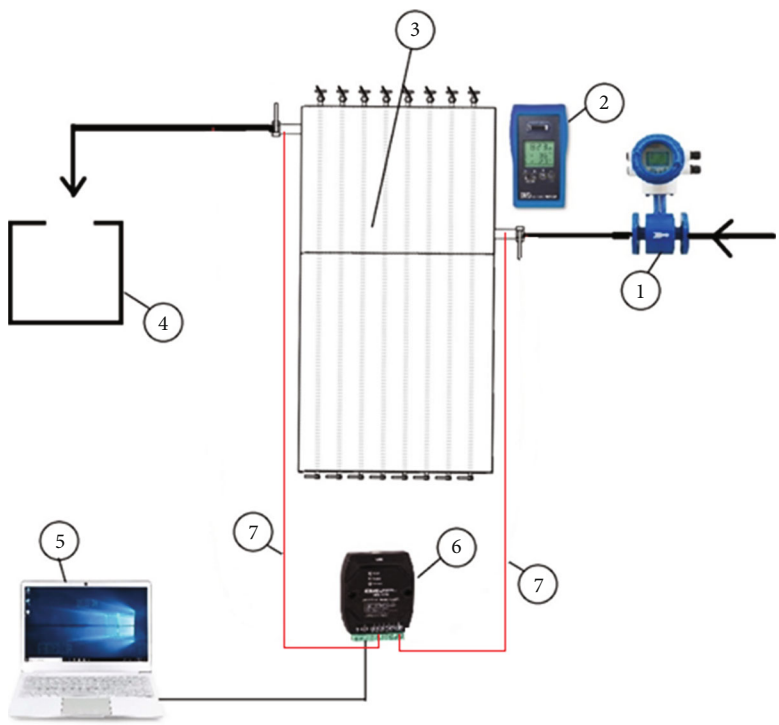

Figure 5: Scheme of the experimental setup (1: flow meter; 2: pyranometer; 3: heat pipe solar collector; 4: tanks; 5: computer; 6: data collection card; 7: thermocouple).

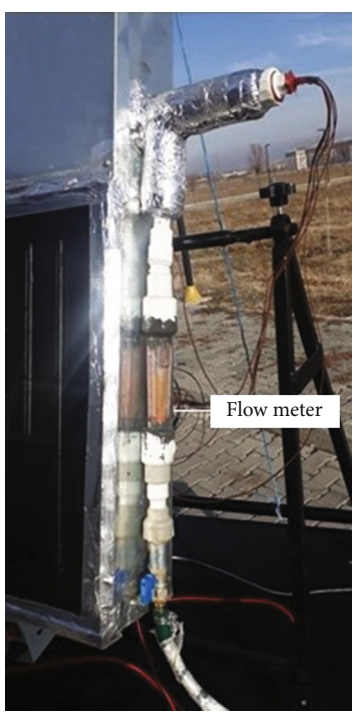

Figure 6: Connection of the flow meter to the experimental setup.

Long-term sonication can also damage surfactants found in nanofluids [34].

The Al_2O_3 and TiO_2 nanofluids to be used in the experiments are commercially available (Nanography Nano Technology), and their dimensions are on average 18 nm and 38 nm, respectively. Nanofluids were obtained by mixing Al_2O_3 and TiO_2 nanoparticles with 2% (mass/mass) distilled water. The mixing ratio of 2% was preferred because it is the optimum ratio we have achieved in previous heat pipe works [13–15, 21]. While vacuum is made in each heat pipe with the vacuum pump so that there is no air in it, the heat pipe working fluid is added on the other inlet side. The optimum heat pipe working fluid amount is 1/3 of the evaporator zone volume [13–15]. In order to prevent lumps of nanoparticles from lumpy in the mixture, 0.2% by mass Triton X-100 surfactant was added to the mixture and kept in the ultrasonic bath for 10 hours as a continuous vibration (Figure 1). During this process, the ultrasonic bath was cooled at regular intervals in order to prevent evaporation of the surfactant due to the increase of temperature in the ultrasonic bath. The properties of nanoparticles used in this study are given in Table 1.

The technical properties of the equipment used in the preparation of the nanofluids used in the study are given in Table 2.

The thermophysical properties of pure water and nanofluids used in the experiment are given in Table 3.

2.2. The Experimental Setup. The main purpose of heat pipe solar collectors (HPSCs) is to carry the solar radiation from the evaporator zone to the condenser area with the least loss. A visual including the basic working principle of a basic heat pipe is presented in Figure 2. The heat pipes used in the experiments are made of 1000 mm long, 8 mm inner diameter. and 10 mm outer diameter copper pipes. The lower 500 mm part of the heat pipes is the evaporator region, the

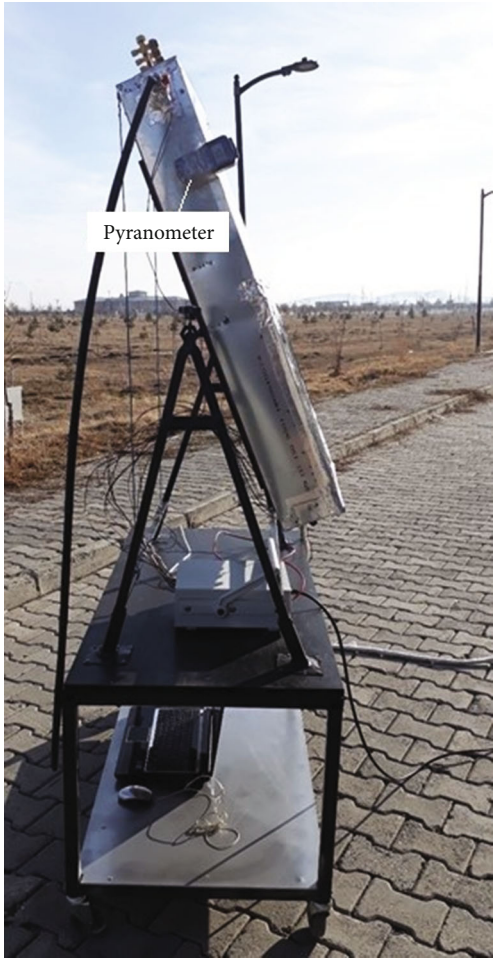

Figure 7: The position of the pyranometer on the collector.

Table 5: Technical features of the pyranometer used in the experiment.

Stability	0.1 W/m^2
Accuracy	±10 W/m^2, ±%5
Deflection	±%3/year
Temperature-induced error	±0.38 W/m^2/°C
Measuring range	1–3999 W/m^2
Sampling rate	0.25 s
Working environment	0°C–50°C, <80%RH

middle 100 mm part is the adiabatic region, and the upper 400 mm part is the condenser region. There are a total of 8 heat pipes in the heat collector solar collector. There is a tank part surrounding the heat pipes passing through the condenser region. Insulation of the adiabatic region was made using glass wool. Evaporator zone is the region where solar radiation is transferred to the heat pipe. The parts of the heat pipe solar collector used in the experiments are shown in Figure 3, and technical specifications are given in Table 4. The experiments were carried out according to the requirements of EN ISO 9806 [36], which is the reference document for determining the performance of thermal solar collectors.

Table 6: Uncertainty calculated parameters and uncertainty values.

Device name	Measuring range	Accuracy	Total uncertainty
Thermocouple T type (LZS-15)	-40/+350°C	±0.5°C	
Datalogger UDL200	-200/+400°C	±%0.2	±0.5139
Pyranometer (SM-206)	1-3999 W/m^2	±%5	
Flow meter (LZS-15)	10-100 kg/h	±%4	

The measurement devices and their properties used in the experiments have been determined according to EN ISO 9806. Radiation from the sun was measured with a handheld pyranometer model SM-206. There are thermocouple connection points at the inlet and outlet of the warehouse to measure temperatures. Thermocouples are T type, and temperatures are read with ORDEL-UDL 200 data logger and transferred to a computer with ORDEL SBA 200 data collection card and analyzed in a computer environment with dali485 software. The LZS-15 flow meter was used to measure the flow rate of the fluid entering the tank. The LZS-15 flow meter (±4%) was used for flow measurements.

Experiments were conducted in two stages to investigate the effect of nanofluids on thermal efficiency in heat pipe solar collectors. The first part experiments were done with pure water, and the second part was done with nanofluids prepared. Experiments were carried out in the month of September (2019), latitude 39°41′31.3″ north and longitude 42°59′22.2″ east coordinates of Ibrahim Chechen University Vocational School (Ağrı, Turkey) in the garden. Experiments were carried out between 09:00 and 17:00, with a collector angle of inclination of 70°, with solar beams perpendicular to the collector surface during the experiment. The experimental setup is given in Figure 4.

A schematic picture of the system is given in Figure 5 for a better understanding of the set of experiments and the connection points of the equipment used.

The flow meter used to control the water circulating in the system to be 0.02 kg/s per unit square meter [29] is mounted as shown in Figure 6.

The pyranometer used to measure global radiation was placed as shown in Figure 7. Before starting any experiment, the pyranometer was mounted in such a way that it was the same as the collector angle of inclination and measurements were made. The technical features of the pyranometer used in the measurements are given in Table 5.

2.3. Uncertainty Analysis. The method proposed by Kline and McClintock was applied to determine the uncertainty of the experimental parameters.

$$= \left[\left(\frac{\partial R}{\partial x_1} w_1 \right)^2 + \left(\frac{\partial R}{\partial x_2} w_2 \right)^2 + \cdots \left(\frac{\partial R}{\partial x_n} w_n \right)^2 \right]^{1/2}. \quad (1)$$

$w_1, w_2 \cdots w_n$ are defined as uncertainties of an independent variable. In this case, R is given as in equation (2) to give the total uncertainty of the system. According to this method,

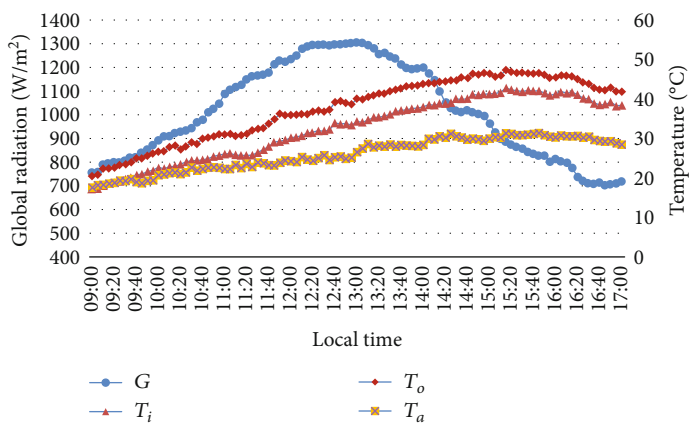

Figure 8: Solar radiation and temperature graphics for pure water.

R is the result function to be measured in the system and x_1, x_2, $x_3 \cdots x_n$ are independent variables affecting the R value [38].

In this case,

$$R = R(x_1, x_2, x_3 \cdots, x_n). \tag{2}$$

The uncertainties of the parameters (temperature, radiation, flow rate, and datalogger) in this study were calculated based on the parameters given in Table 6, indicating that the uncertainty of the experimental data is within the acceptable range.

2.4. Theoretical Analysis. In order to evaluate the thermal performance of the heat pipe solar collector, in the open experimental setup, the energy from the sun was transferred to the collector absorbent plate surface from the sun. The energy transferred to the liquid is expressed as instantaneous power. While performing experimental studies and performance calculations, it was performed in accordance with EN ISO 9806 standards. The main criteria to be followed when conducting experiments according to EN ISO 9806 standards are presented as follows:

(i) It should be an open (cloudless) atmosphere

(ii) Radiation should be more than 700 W/m^2

The heat is transferred from the heat pipes in the condenser area to the moving fluid in the tank, so the cold incoming fluid comes out by heating. The inlet and outlet temperature difference of the heat fluid received by the fluid in the condenser area is equal to the product of the mass flow of the fluid and the average specific heat values of the fluid. This equation is given in equation (3).

$$\dot{Q} = \dot{m}.c.(T_i - T_o). \tag{3}$$

In the equation above, $\dot{Q}$ is the heat transferred to the working fluid passing through the tank per unit time, ($\dot{m}$) is the flow rate of the water entering the tank (kg/s), c is the mean specific heat of water entering the tank (j/kg·°C), T_i is the temperature of water entering the tank (°C), and T_o out is the temperature of the water leaving the tank (°C).

The flow rate of the water circulating in the tank was calculated according to the following equation according to EN ISO 9806:

$$\dot{m} = 0.02\, A_G. \tag{4}$$

The instantaneous performance (η) of the collector is calculated by the ratio of the heat ($\dot{Q}$) transferred to the work fluid passing through the tank to the irradiation value (I) of the collector's openness area [39].

$$\eta = \frac{\dot{Q}}{I}. \tag{5}$$

Arrangement can be made by writing the irradiation value (I) falling in the opening area of the collector in equation (5) in $A_G.G$. Here, $A_G.G$ is the opening area of the collector and G is the radiation intensity.

$$\eta = \frac{\dot{Q}}{A_G.G}. \tag{6}$$

In this study, in evaluating the results, reduced temperature difference, instant performance of collector, and power output per instant temperature difference were used. The reduced temperature difference ($T_m{}^*$) is defined as follows [29]:

$$T_m^* = \frac{T_m - T_a}{G}, \tag{7}$$

$$T_m = T_i + \frac{\Delta T}{2} = T_i + \frac{T_o - T_i}{2}. \tag{8}$$

In equation (7), T_a refers to ambient temperature (°C); in equation (8), T_m refers to the average working fluid temperature (°C).

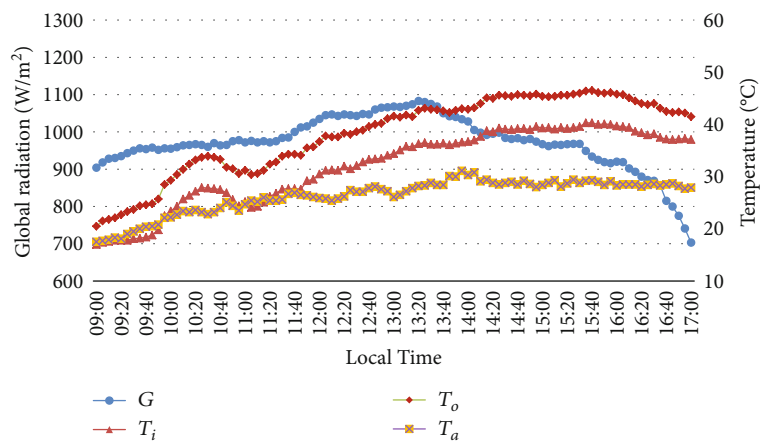

Figure 9: Solar radiation and temperature graphs for Al_2O_3-water nanofluid.

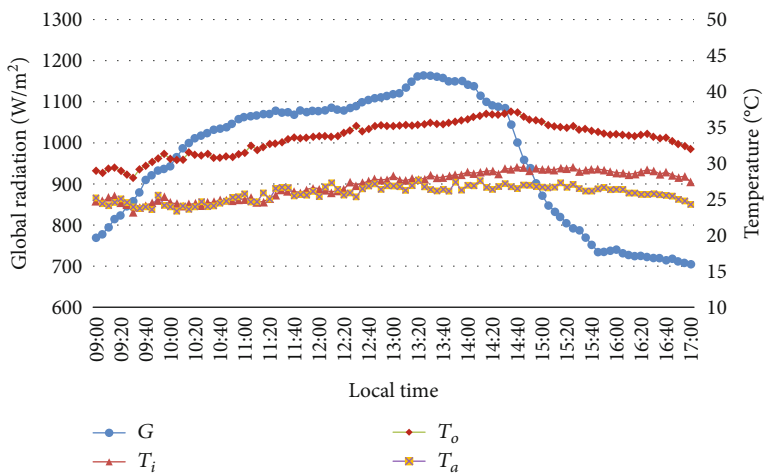

Figure 10: Solar radiation and temperature graphs for TiO_2-water nanofluid.

3. Results and Discussions

Measurements in which experimental performances of heat pipe solar collectors were tested using pure water, Al_2O_3-water, and TiO_2-water nanofluid are given in Figures 8, 9, and 10. Data were taken at 5-minute intervals. In Figure 8, the average ambient temperature of the day of the experiment with pure water was measured as 25.98°C. Since our experimental setup is an open system, the tank inlet temperature has changed depending on the temperature of the water coming from the network and the connection distance. It is seen that the storage outlet water temperature (T_o) rises until 15.00 and decreases after this time. It is seen that this decrease is due to the decrease in radiation.

In Figure 9, the average of the ambient temperature of the day on which the experiment was used Al_2O_3-water nanofluid was measured as 26.28°C. It is seen that the storage outlet water temperature (T_o) rises until 16:00 and decreases after this time. Solar irradiance values were measured at the highest values between 12:00 and 14:00. Then, the radiation started to decline. In parallel with this decrease, the water outlet temperature started to decrease.

In Figure 10, the average of the ambient temperature of the day on which the experiment was used TiO_2-water nanofluid was measured as 25.83°C. It is seen that the storage outlet water temperature (T_o) rises up to 14:00 and decreases after this time. Then, the radiation started to decline. In parallel with this decrease, the water outlet temperature started to decrease.

The performance data obtained in the application of EN ISO 9806 [29] standards have been curve fit to the 2nd-degree curves in accordance with the test conditions given that a curve fit should be made to a 2nd-degree curve. As stated here, according to the condition that the coefficient of the term x^2 in the equation is negative, a curve fit is made to a quadratic curve. Here, the x term is the $(T_m - T_a)/G$ value that represents the x-axis of the curve. Figure 11 shows the efficiency graph for pure water, Al_2O_3-water, and TiO_2-water nanofluids. Looking at the graph, the highest instantaneous efficiency is 48% for pure water, 58% for Al_2O_3-water nanofluid, and 64% for TiO_2-water nanofluid. In line with these data, Al_2O_3-water nanofluid mixture provided 20.8% higher performance than pure water; it was observed that TiO_2-water mixture provided 33.3% higher performance than pure water and 9.375% higher performance than

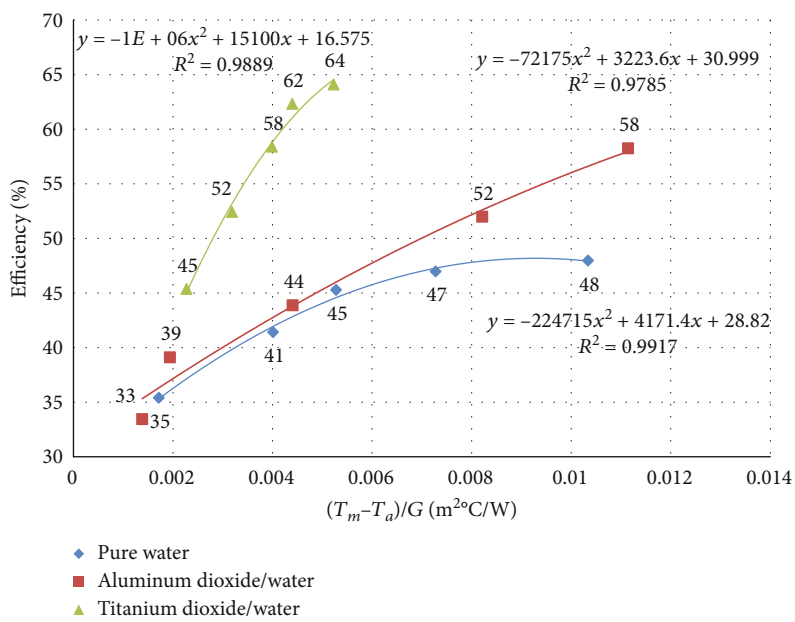

Figure 11: Efficiency chart for pure water, Al_2O_3-water, and TiO_2-water nanofluids.

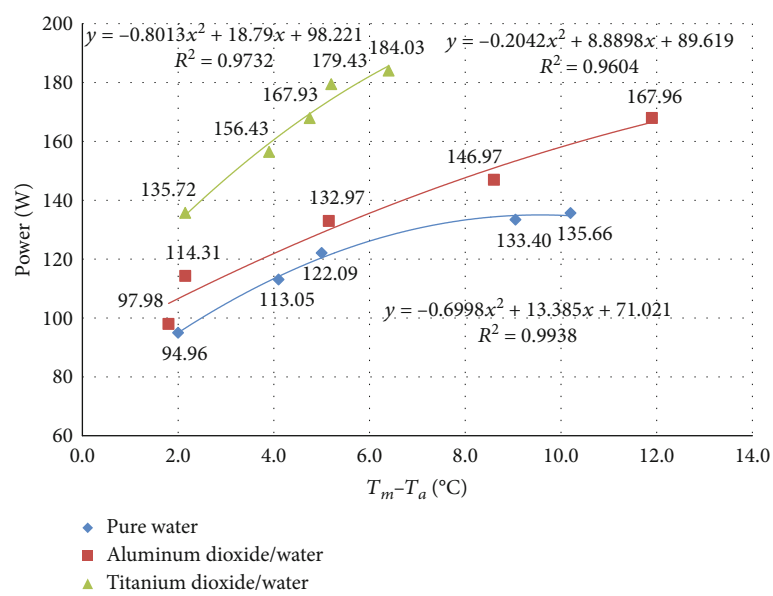

Figure 12: Power output per momentary temperature difference for pure water, Al_2O_3-water, and TiO_2-water nanofluids.

Al_2O_3-water nanofluid mixture. When curve fitting is performed for the data in the graph, the equation obtained for pure water is 48.178% of the maximum efficiency at the reduced temperature of 0.0092815 $m^{2\circ}C/W$ with accuracy of 0.9917, for Al_2O_3-water nanofluid $R^2 = 0.9785$ with an accuracy of 0.02233 $m^{2\circ}C/W$ at a reduced temperature of 66.99% of maximum efficiency, and for TiO_2-water nanofluid with $R^2 = 0.9889$ accuracy at a maximum of 0.00755 $m^{2\circ}C/W$ efficiency was determined as 73.5775%. While TiO_2-water nanofluid reached the maximum efficiency value at lower reduced temperature, Al_2O_3-water nanofluid reached the maximum efficiency value in the wider range.

Figure 12 shows the graph of power output for pure water, Al_2O_3-water, and TiO_2-water nanofluids. Looking at the graph, the highest power outputs were 135.66 W for pure water, 167.96 W for Al_2O_3-water nanofluid, and 184.03 W for TiO_2-water nanofluid. In line with these data, the Al_2O_3-water nanofluid mixture is 23.8% higher than pure water; it has been observed that TiO_2-water mixture provided 35.6% higher performance than pure water and 9.567% higher performance than Al_2O_3-water nanofluid mixture. When curve fitting is performed for the data in the graph, the equation obtained for pure water is $R^2 = 0.9938$ with an accuracy of 9.5634°C instantaneous temperature difference of 135.024 W; for Al_2O_3-water nanofluid,

$R^2 = 0.9604$ accuracy was determined as 21.7918°C instantaneous temperature-aware maximum power 186.590 W; and for TiO_2-water nanofluid, $R^2 = 0.9732$ accuracy was determined as 11.7246°C instantaneous temperature-aware maximum power 208.374 W. While the instantaneous temperature difference of TiO_2-water nanofluid reached the maximum power value at 11.7246°C, it was observed that the instantaneous temperature difference of Al_2O_3-water nanofluid reached the maximum power value of 21.7918°C.

4. Results

In this study, the effect of working fluids on the performance of the heat pipe solar collector has been investigated experimentally. In the study, pure water, Al_2O_3-water nanofluid, and TiO_2-water nanofluid are used as working fluid. The results obtained from the experiments are given follows:

(i) In the comparison of thermal performances based on the data obtained, the maximum performance was obtained from TiO_2-water nanofluid followed by Al_2O_3-water nanofluid and pure water, respectively. While the TiO_2-water nanofluid mixture improved by 33.3% compared to pure water, it was observed that the Al_2O_3-water nanofluid mixture improved by 20.8% compared to pure water. It was determined that the TiO_2-water nanofluid mixture had an improvement of 9.375% thermal performance against Al_2O_3-water nanofluid mixture

(ii) When the power output data per instant temperature difference was examined, it was seen that the results change in direct proportion to the thermal performance values. The change in power output per instant temperature was seen that the TiO_2-water nanofluid mixture improved by 35.6% compared to pure water, while the Al_2O_3-water nanofluid mixture improved by 23.8% compared to pure water. The Al_2O_3-water nanofluid mixture of TiO_2-water nanofluid mixture had an improvement in power output per instant temperature difference of 9.567%

Symbols

$\dot{Q}$: Instantaneous power (W)
$\dot{m}$: Mass flow (kg/h)
c_p: Specific heat capacity (J/kgK)
ΔT: Difference between the fluid's tank outlet and inlet temperature (K)
A_G: Collector gross area (m^2)
η: Instantaneous thermal efficiency
G: Irradiance intensity (W/m^2)
T_m: Average fluid temperature (K)
T^*_m: Reduced temperature difference on the horizontal axis (m^2K/W)
T_i: Tank inlet water temperature (K)
T_o: Tank outlet water temperature (K)
T_a: Outdoor temperature (K)
H_2O: Water
Al_2O_3: Alumina (aluminum oxide)
TiO_2: Titanium dioxide
W: Total uncertainty.

Abbreviations

HPSC: Heat pipe solar collector
TSE: Turkish Standards Institution
ISO: International Organization for Standardization
ETSCs: Evacuated tube solar collectors.

Data Availability

Data will be provided on request.

Conflicts of Interest

The authors declare that they have no conflicts of interest.

References

[1] B. Atilgan and A. Azapagic, "An integrated life cycle sustainability assessment of electricity generation in Turkey," *Energy Policy*, vol. 93, pp. 168–186, 2016.

[2] M. D. Toksari, "A hybrid algorithm of ant colony optimization (ACO) and iterated local search (ILS) for estimating electricity domestic consumption: case of Turkey," *International Journal of Electrical Power & Energy Systems*, vol. 78, pp. 776–782, 2016.

[3] E. Çiftçi, A. Sözen, and E. Karaman, "Experimental investigation of nano fluid usage including TiO_2 on the effect of heat pipe performance," *Journal of Polytechnic*, vol. 19, no. 3, pp. 367–376, 2016.

[4] E. F. Akyürek, K. Geliş, B. Şahin, and E. Manay, "Experimental analysis for heat transfer of nanofluid with wire coil turbulators in a concentric tube heat exchanger," *Results in Physics*, vol. 9, pp. 376–389, 2018.

[5] F. Kiliç, T. Menlik, and A. Sözen, "Effect of titanium dioxide/-water nanofluid use on thermal performance of the flat plate solar collector," *Solar Energy*, vol. 164, pp. 101–108, 2018.

[6] M. R. Saffarian, M. Moravej, and M. H. Doranehgard, "Heat transfer enhancement in a flat plate solar collector with different flow path shapes using nanofluid," *Renewable Energy*, vol. 146, pp. 2316–2329, 2020.

[7] M. Mercan and A. Yurddaş, "Numerical analysis of evacuated tube solar collectors using nanofluids," *Solar Energy*, vol. 191, pp. 167–179, 2019.

[8] M. S. Dehaj and M. Z. Mohiabadi, "Experimental investigation of heat pipe solar collector using MgO nanofluids," *Solar Energy Materials and Solar Cells*, vol. 191, pp. 91–99, 2019.

[9] F. Kılıç, "The impacts of fluids on performance containing nanosized metal oxide in solar collectors," *Energy Systems Engineering, [Ph.D. thesis]*, vol. 136, Gazi University, 2017.

[10] A. Sözen, A. Öztürk, M. Özalp, and E. Çiftçi, "Influences of alumina and fly ash nanofluid usage on the performance of recuperator including heat pipe bundle," *International Journal of Environmental Science and Technology*, vol. 16, no. 9, pp. 5095–5100, 2019.

[11] M. Kaya, A. E. Gürel, Ü. Ağbulut et al., "Performance analysis of using CuO-methanol nanofluid in a hybrid system with

concentrated air collector and vacuum tube heat pipe," *Energy Conversion and Management*, vol. 199, article 111936, 2019.

[12] R. Daghigh and P. Zandi, "Improving the performance of heat pipe embedded evacuated tube collector with nanofluids and auxiliary gas system," *Renewable Energy*, vol. 134, pp. 888–901, 2019.

[13] M. Gürü, A. Sözen, U. Karakaya, and E. Çiftçi, "Influences of bentonite-deionized water nanofluid utilization at different concentrations on heat pipe performance: an experimental study," *Applied Thermal Engineering*, vol. 148, pp. 632–640, 2019.

[14] A. Sözen, T. Menlik, M. Gürü et al., "A comparative investigation on the effect of fly-ash and alumina nanofluids on the thermal performance of two-phase closed thermo-syphon heat pipes," *Applied Thermal Engineering*, vol. 96, pp. 330–337, 2016.

[15] E. Çitçi, A. Sözen, and E. Karaman, "Experimental investigation of the effect of using nanofluid containing TiO2 on heat pipe performance," *Politeknik Magazine*, vol. 19, no. 3, pp. 367–376, 2016.

[16] M. Çakır, "Improving the performance of heat pipes by using nanofluid containing alimuna," *Gazi University Journal of Engineering and Architecture Faculty*, vol. 30, 2015.

[17] G. A. Pise, S. S. Salve, A. T. Pise, and A. A. Pise, "Investigation of solar heat pipe collector using nanofluid and surfactant," *Energy Procedia*, vol. 90, pp. 481–491, 2016.

[18] T. Menlik, A. Sözen, M. Gürü, and S. Öztas, "Heat transfer enhancement using MgO/water nanofluid in heat pipe," *Journal of the Energy Institute*, vol. 88, no. 3, pp. 247–257, 2015.

[19] A. A. Eidan, A. AlSahlani, A. Q. Ahmed, M. Al-fahham, and J. M. Jalil, "Improving the performance of heat pipe-evacuated tube solar collector experimentally by using Al_2O_3 and CuO/acetone nanofluids," *Solar Energy*, vol. 173, pp. 780–788, 2018.

[20] A. Ozturk, M. Ozalp, A. Sozen, and M. Guru, "Performance improvement of the heat recovery unit with sequential type heat pipes using TiO_2 nanofluid," *Thermal Science*, vol. 23, 3, Part B, pp. 1755–1764, 2019.

[21] A. Sözen, M. Gürü, A. Khanlari, and E. Çiftçi, "Experimental and numerical study on enhancement of heat transfer characteristics of a heat pipe utilizing aqueous clinoptilolite nanofluid," *Applied Thermal Engineering*, vol. 160, article 114001, 2019.

[22] Y. Tong, H. Lee, W. Kang, and H. Cho, "Energy and exergy comparison of a flat-plate solar collector using water, Al_2O_3 nanofluid, and CuO nanofluid," *Applied Thermal Engineering*, vol. 159, article 113959, 2019.

[23] A. Ozsoy and V. Corumlu, "Thermal performance of a thermosyphon heat pipe evacuated tube solar collector using silver-water nanofluid for commercial applications," *Renewable Energy*, vol. 122, pp. 26–34, 2018.

[24] U. Ö. Su, A. Sözen, and T. Menlik, "Heat pipe evacuated tubular solar collector performance improvement: application of nanofluid," *Journal of Politeknik*, vol. 22, no. 1, pp. 245–257, 2019.

[25] S. Zhao, G. Xu, W. Ning, and Z. Xiaosong, "Experimental study on the thermal start-up performance of the graphane/-water nanofluid-enhanced solar gravity heat pipe," *Nanomaterials*, vol. 8, p. 72, 2018.

[26] K. Geliş, *Investigation of heat transfer and pressure drop of nanofluids in aheat exchanger equipped with tape elements*, Ataturk University, 2013.

[27] Y. Li, J. Zhou, S. Tung, E. Schneider, and S. Xi, "A review on development of nanofluid preparation and characterization," *Powder Technology*, vol. 196, no. 2, pp. 89–101, 2009.

[28] D. K. Devendiran and V. A. Amirtham, "A review on preparation, characterization, properties and applications of nanofluids," *Renewable and Sustainable Energy Reviews*, vol. 60, pp. 21–40, 2016.

[29] N. Ali, J. A. Teixeira, and A. Addali, "A review on nanofluids: fabrication, stability, and thermophysical properties," *Journal of Nanomaterials*, vol. 2018, Article ID 6978130, 33 pages, 2018.

[30] Y. Xuan and Q. Li, "Heat transfer enhancement of nanofluids," *International Journal of Heat and Fluid Flow*, vol. 21, no. 1, pp. 58–64, 2000.

[31] R. Choudhary, D. Khurana, A. Kumar, and S. Subudhi, "Stability analysis of Al2O3/water nanofluids," *Journal of Experimental Nanoscience*, vol. 12, no. 1, pp. 140–151, 2017.

[32] R. Azizian, E. Doroodchi, and B. Moghtaderi, "Influence of controlled aggregation on thermal conductivity of nanofluids," *Journal of Heat Transfer*, vol. 138, no. 2, article 021301, 2016.

[33] S. K. S. Babita and S. M. Gupta, "Preparation and evaluation of stable nanofluids for heat transfer application: a review," *Experimantel Thermal and Fluid Science*, vol. 79, pp. 202–212, 2016.

[34] S. Hoseinzadeh, S. A. R. Sahebi, R. Ghasemiasl, and A. R. Majidian, "Experimental analysis to improving thermosyphon thermal efficiency using nanoparticles/based fluids (water)," *European Physical Journal Plus*, vol. 132, no. 197, pp. 1–8, 2017.

[35] "Nanografi Nano Technology," 2019, https://nanografi.com/.

[36] EN ISO 9806, *Solar energy - solar thermal collectors - test methods*, ISO, 2017.

[37] A. Shafieian, M. Khiadani, and A. Nosrati, "Strategies to improve the thermal performance of heat pipe solar collectors in solar systems: a review," *Energy Conversion and Management*, vol. 183, pp. 307–331, 2019.

[38] S. J. Kline and F. A. McClintock, *Describing uncertainties in single-sample experiments*, Mechanical Engineering, 1953.

[39] D. S. Sowmy, P. J. Schiavon Ara, and R. T. A. Prado, "Uncertainties associated with solar collector efficiency test using an artificial solar simulator," *Renewable Energy*, vol. 108, pp. 644–651, 2017.

Hindawi
International Journal of Photoenergy
Volume 2021, Article ID 5581081, 13 pages
https://doi.org/10.1155/2021/5581081

Research Article

Influence of Narrow Rectangular Channel (AR = 1 : 4) on Heat Transfer and Friction for V- and W-Shaped Ribs in Turbine Blade Applications

Karthik Krishnaswamy,[1] **Suresh Sivan**,[1] **and Hafiz Muhammad Ali**[2]

[1]*Mechanical Engineering, National Institute of Technology, Tiruchirappalli 620015, India*
[2]*Mechanical Engineering, King Fahd University of Petroleum and Minerals, Dhahran 31261, Saudi Arabia*

Correspondence should be addressed to Suresh Sivan; ssuresh@nitt.edu

Received 13 January 2021; Revised 8 May 2021; Accepted 17 May 2021; Published 25 May 2021

Academic Editor: Gianluca Coccia

Copyright © 2021 Karthik Krishnaswamy et al. This is an open access article distributed under the Creative Commons Attribution License, which permits unrestricted use, distribution, and reproduction in any medium, provided the original work is properly cited.

Effective cooling of blades with a nominal pressure drop is essential for performance augmentation and thermal management of gas turbines. Hence, present work is aimed at determining the heat transfer enhancement and friction for W- and V-shaped ribs inside a rectangular cooling channel having hydraulic diameter (D_h) of 0.048 m and aspect ratio (AR) 1 : 4. Ribs are fixed facing downstream with angle of attack (α) 45° on opposite walls. Pitch (P) between two successive ribs is 25 mm for both cases. Continuous V- and W-shaped ribs with height to channel hydraulic diameter ratio (e/D_h) 0.052 and 0.0416 and pitch to height ratio (P/e) 10 and 12.5, respectively, have been examined for Reynolds number (Re) range 20000-80000. Heat transfer augmentation achieved at Re 80000 is 1.94 and 1.8 times higher than Re 20000 for V- and W-shaped ribs, respectively. Streamwise and spanwise variations in local Nusselt number ratio are highest for V-shaped ribs, which are estimated to be 31% and 12%. For W-shaped ribs, variations are 17.5% and 3.5%. Nusselt number (Nu) is highest along span length $0.5w$ for V-shaped ribs due to dominance of apex induced secondary flow. For W-shaped ribs, Nusselt number along the span lengths is found to be nearly same view uniformity in secondary flow. Maximum enhancement ($\mathrm{Nu}/\mathrm{Nu}_o$) estimated for both the rib shapes is 3.9 at Re 20000. Due to increased rib height, friction losses for V-shaped ribs are higher than W-shaped ribs. Maximum friction loss increment is estimated to be 85% for V-shaped ribs and 42% for W-shaped ribs between Re 20000 and 40000. For both rib shapes, impact of ribs is found to be greatest at Re 40000. Thermohydraulic performance (THP) for W-shaped ribs is superior to V-shaped ribs. Best THP achieved for W- and V-shaped ribs are 3.7 and 3.4 at Re 20000.

1. Introduction

Gas turbine engines propel aircraft, ships, and automobiles. In addition, they are also extensively used for power generation. The efficiency and output of these engines are dependent upon the Turbine Inlet Temperature (TIT). Increase in TIT will result in increased power output. The present generation turbines are already operating closer to melting point, and therefore, any further increase in TIT is possible only through efficient thermal management. The cooling of inner and outer blade surfaces is done by withdrawing a small quantity of compressed air. Withdrawal of air impacts the output and efficiency. Hence, the aim of various cooling techniques is to attain more heat transfer with marginal drop in pressure, thereby reducing the coolant consumption. Rib cooling is one amongst the cooling techniques used for heat removal from midsection of turbine blade. For years, many researchers have examined the thermohydraulic performance generated due to ribs in turbine blade cooling channels which are generally rectangular, trapezoidal, and square in cross section. Studies have established that various geometrical parameters like channel cross section, rib height, coolant angle of attack, pitch between the ribs, rib profile, and number of walls with ribs influence the friction and heat

transfer. Results presented by few studies are discussed in succeeding paragraphs.

Goodarzi et al. [1] investigated convective heat transfer for flow inside cavity and stated that magnitude of heat transfer depends largely on effects of hydrodynamic and thermal boundary layers between the fluid and the surface. Also, majority of the studies impose constant heat flux condition on the surface to study the heat transfer phenomenon. Goodarzi et al. [2] stated that in comparison to experimental methods, computational methods are simpler, economical, and safe for understanding heat transfer and fluid flow problems. Abraham and Vedula [3] by using a converging channel examined friction and heat transfer with 45° W- and V-shaped ribs. Examination revealed that heat transfer coefficients varied more for V-shaped ribs because of cross stream flows, and performance of both rib shapes was within uncertainty limits for optimum P/e of 10. Prashant et al. [4] studied different ribs fixed in an aspect ratio 1 : 1 cooling channel for Re 19500 to 69000 and concluded that V-shaped and angled ribs at 45° to coolant flow provided greatest performance. Ghodake et al. [5] evaluated augmentations for different ribs using rectangular duct and confirmed that broken V-shaped and rectangular tape ribs with P/e of 8.3 generated higher augmentations. Heat transfer and pressure loss characteristics were investigated for AR 1 : 1 channel with high blockage ratio ribs by Yang et al. [6]. The ratio of P/e ranges from 5 to 15, and Re ranged from 1400 to 9000. Their analysis indicated that as Re increased, heat transfer coefficients and pressure losses increased. Furthermore, they concluded that symmetric arrangement ribs showed higher heat transfer and pressure losses than staggered arrangement ribs. For a revolving two pass square cross section cooling channel with staggered 45° ribs, friction and heat transfer behaviour were presented by Deng et al. [7]. The Re ranged from 20000 to 60000, and rotation number ranged 0 to 1.02. The results showed that 45° ribs with P/e ratio 10 enhanced heat transfer by 15-65% for smooth walls and 40-80% for ribbed walls. The pressure drop in ribbed channel was found 1.5-2.1 times higher than smooth channel. Further, the authors showed that when the rotation number exceeds 0.25, thermal performance considerably improved due to rotation effects. Prashant et al. [8, 9] compared the effects due to ribs on single wall and two walls of a square channel. For Re 20000, V-ribs fixed on two walls produced greater augmentation, and the trailing wall heat transfer in rotating condition was highest due to Coriolis effects. The influence on heat transfer due to 45° V-ribs in 1 : 2 aspect ratio channel for Re range 25000 to 75000 revealed that heat transfer increased in the flow direction view greater turbulent mixing, and the heat transfer was highest at the bend. Ravi et al. [10] numerically investigated four different rib profiles placed inside a square cross section channel at 45° to flow direction. The authors presented that 45° V-shaped and angled ribs exhibited best performance for the Re range 20000 to 70000.

For different aspect ratios and working conditions, impact of 45° ribs on heat transfer and flow was investigated numerically by Longfei et al. [11]. The aspect ratios of the ribbed channels studied were 1 : 2, 1 : 1, and 2 : 1, respectively. According to their findings, heat transfer area increases because of ribs, and hence, the heat transfer increases. Their evaluation revealed that heat transfer area due to ribs increased by 30%, and overall heat transfer improved by 50%. Also, the pressure loss in 1 : 2 AR channel with same hydraulic diameter as 2 : 1 AR channel was found to be 60% less. Prashant et al. [12] using an AR 1 : 1 channel studied the effect of criss-cross pattern rib turbulators positioned in an inline and staggered configurations. They concluded that heat transfer enhancement was nearly same for inline and staggered configurations; however, friction for inline configuration was lower than staggered configuration. For Re range 30000 to 60000, heat transfer enhancement ranged from 2.7 to 3.1, and thermal performance ranged from 1.2 to 1.5. Sebastian and Arbeiter [13] conducted an analysis of heat transfer and turbulent flow for V-shaped ribs with e/D_h of 0.0638 and transverse ribs with e/D_h of 0.0652 fixed on one wall. According to their findings, at Re 100000, upstream pointing V-shaped ribs produced best thermal performance and heat transfer enhancement. Effect of rib orientation on flow and thermal parameters was investigated by Liou et al. [14] inside a two pass parallelogram channel. The blockage ratio was 0.1, and P/e was 10. For Re range 5000 to 20000, thermal performance of 45° angled ribs was found to be best. Heat transfer and fluid flow due to different discrete ribs were investigated by Wang et al. [15] in a revolving rectangular channel with AR 2 : 1. The blockage ratio was 0.1, and P/e was 10. They concluded that presence of streamwise rib gap improved the heat transfer however, with increase in the gap increment in heat transfer declined. In addition, they established that the increase in spanwise rib gap reduced the pressure drop; however, heat transfer augmentation is restricted. Aghaei et al. [16] evaluated the impact of baffles on flow inside an enclosure and confirmed that entropy reduces the efficacy, and hence, it is important to establish the entropy for enhancing the efficiency of machines. Further, the authors brought out that researchers are working towards minimizing the entropy for achieving optimal performance. Patil and Borse [17] brought out that the heat transfer in turbine blade midsection is enhanced by fixing ribs inside the serpentine cooling passages. They also brought out in their review that narrow channel having AR 1 : 4 produced lower friction penalties than aspect ratios 1 : 2, 1 : 1, and 2 : 1 channels. Aboghrara et al. [18] reiterated the fact that heat transfer due to convection can be enhanced by incrementing the contact area and also by increasing the turbulent mixing by introducing roughness elements in the flow path. Omeroglu [19] evaluated the thermal enhancement inside a photovoltaic/thermal collector by using fin turbulators. The author established that with increase in Reynolds

Table 1: Details of rib geometry.

Ribs	e (mm)	P/e	e/D_h	α (°)	Recommended range in literature		
					P/e	e/D_h	α (°)
V	2.5	10	0.052	45°	5-15	0.05-0.1	30°-60°
W	2	12.5	0.0416	45°			

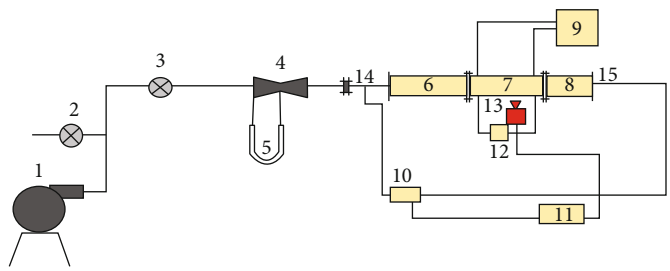

1. Centrifugal blower
2. Bypass valve
3. Inlet valve
4. Venturimeter
5. U-tube manometer
6. Developing section
7. Ribbed section
8. Exit section
9. Dc power source
10. Data logger
11. Laptop
12. Dpt
13. Infrared camera
14. Inlet thermocouple
15. Exit thermocouple

Figure 1: Illustration of experimental setup.

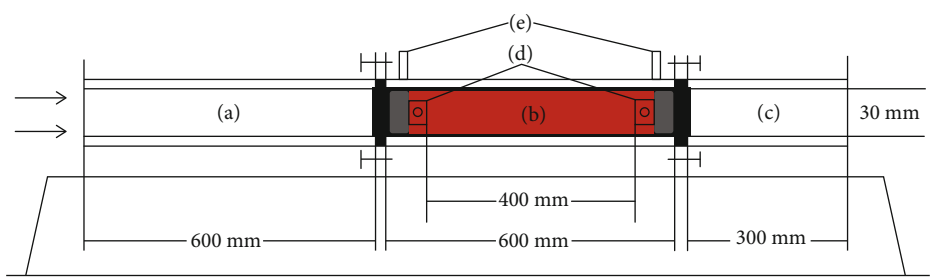

Figure 2: Schematic of (a) developing section, (b) ribbed section, and (c) exit section.

number, heat transfer increased; however, thermal performance decreased. They also concluded that the arrangement of turbulators inside enclosed spaces is an important parameter which defines the increment in heat transfer. With better arrangement of turbulators, higher heat transfer can be generated at relatively lesser flow rates. Delbari et al. [20] studied different blade profiles and established that the turbine blade aspect ratio is one of the important operational parameter, and the performance and fuel consumption depend largely on the geometry of the blade profile.

Pordanjani et al. [21] brought out that many engineering applications employ the principles of convection inside cavities. They also submitted that determination of losses and minimization of the same is considered paramount as industrial applications demand high efficiency devices. Authors Tang et al. [22] established in their work that fouling of compressor blades of a gas turbine is unavoidable, and the same has a negative effect on the overall performance and safety. Since the compressed air is used for cooling the turbine blades, it is prudent to select rib turbulators which can generate high heat transfer for low pressure drop and optimal coolant air consumption so that the inescapable reduction in overall engine performance due to fouling can be marginally compensated. Jiang et al. [23] in their research work highlighted the importance of blade cooling and selection of right alloy to prevent creep failure of rotor blades. They brought out that, in view of the rapid progression in aviation industry, necessity to operate the gas turbines at elevated temperatures for achieving higher thrust to weight ratio and performance has become inevitable. Therefore, it is of utmost importance to prevent creep failure by right selection of blade material and cooling methodology. Yousefzadeh et al. [24] researched the heat transfer inside a cavity with dissimilar areas of heat transfer. The authors concluded that by increasing fluid velocity, momentum loss increases, and in turn, pressure drop also increases due to increased collision with the surface. The authors also established that the effects of back flow reduce by increasing velocity and by decreasing the velocity, boundary layer thickness increases. Deng et al. [25] by employing 90° ribs examined the influence of three different e/D_h ratios on thermohydraulic performance inside a rotating square channel. The authors confirmed optimum performance at e/D_h ratio 0.1 for Re up to 40000. Krishnaswamy and Sivan [26] evaluated V- and W-ribs in a channel (AR = 1 : 4) and concluded that 45° V- and W-ribs with e/D_h values of 0.0729 and 0.0833 produced high thermal performances. Besides, the authors also reported that nonuniformity in heat transfer was greatest for W-ribs. Wang et al. [27] numerically investigated the cooling effectiveness of 60° inclined and V-shaped ribs in a two pass channel. They concluded by saying that under rotating condition, heat transfer increment was observed to be maximum in the trailing wall and bend regions due to rotation induced forces. Also, they established that heat transfer augmentation for V-shaped ribs was superior to angled ribs.

1.1. Novelty. Due to the airfoil shape of turbine blade, difference in height between the leading and trailing walls from the

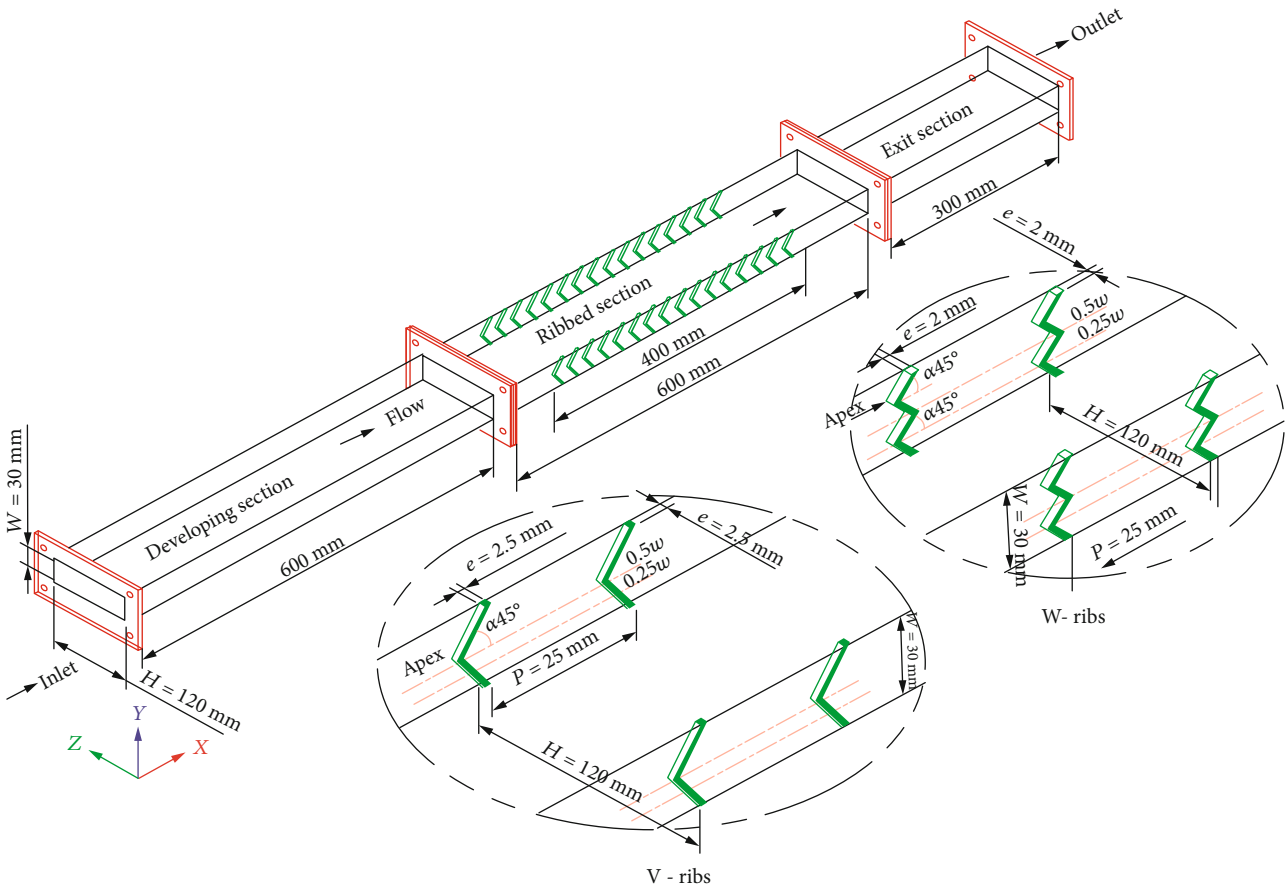

Figure 3: 3D model of test section with V- and W-shaped ribs.

Table 2: Instrument details.

Measuring device	Model and make	Accuracy	Range
Multimeter	M 3900, M/s Mastech	± 0.5%	200 mV to 1000 V
Pressure transmitter	CP 100, M/s KIMO	± 1.5%	0 to 100 Pa
Thermal camera	Ti 9, M/s Fluke	± 5°C	-20°C to 250°C
Thermocouple	*K*-type	± 0.25%	0 to 600°C
Anemometer	Testo 425	± 0.03 m/s	0 to 20 m/s

midchord increases towards the leading edge and decreases towards the trailing edge. As a result, ribbed cooling passages closer to leading edge are very narrow with aspect ratios up to 1 : 6 [26]. From the literature survey, it has been established that turbine blade aspect ratio is one of the most important operational parameter, and therefore, deployment of rib turbulators with optimal geometry is vital for optimizing the performance. Further, it is also evident that a large number of studies on blade cooling carried out till date are restricted to square and narrow ribbed cooling passages with aspect ratios up to 1 : 2, and therefore, a need is felt to assess the friction and heat transfer in narrow cooling passages adjoining the leading edge with aspect ratios lesser than 1 : 2.

Another important aspect is to effectively manage the thermal parameters near the leading edge by employing ribs that can deliver high performance. Due to high operating temperatures, thermal stresses in the areas adjoining the leading edge are exceedingly high, and hence, it is paramount to achieve maximum heat transfer with minimal friction losses and coolant consumption. As the coolant is further utilized for impingement and film cooling after exiting the ribbed passages, any effort to increase heat transfer by increasing the rib height or by reducing the rib pitch will only increase the friction losses which in turn will bring down the overall cooling effectiveness. Further, studies have concluded that the thermohydraulic performances of W- and V-shaped ribs are better than other rib profiles such as orthogonal and angled ribs because of the superiority of secondary flows produced by these ribs.

With the above background, present experimental work has been performed with an objective to maximize heat transfer and minimize pressure drop inside a ribbed passage

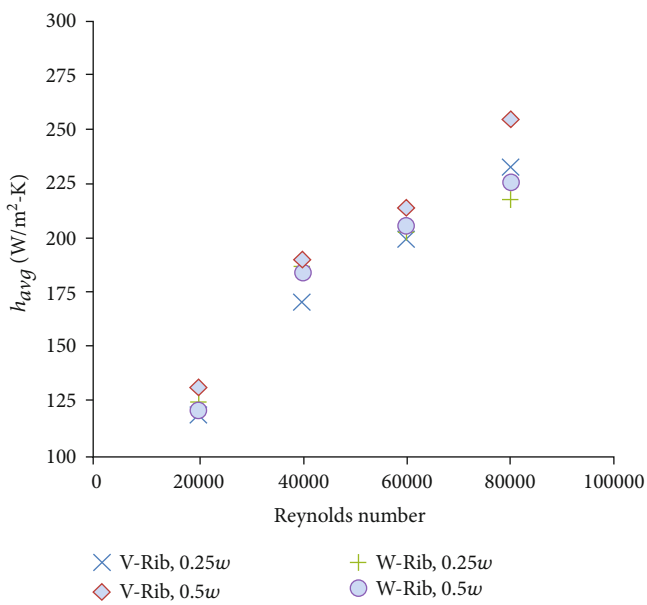

Figure 4: Variation in span averaged heat transfer coefficient (h_{avg}) with Re.

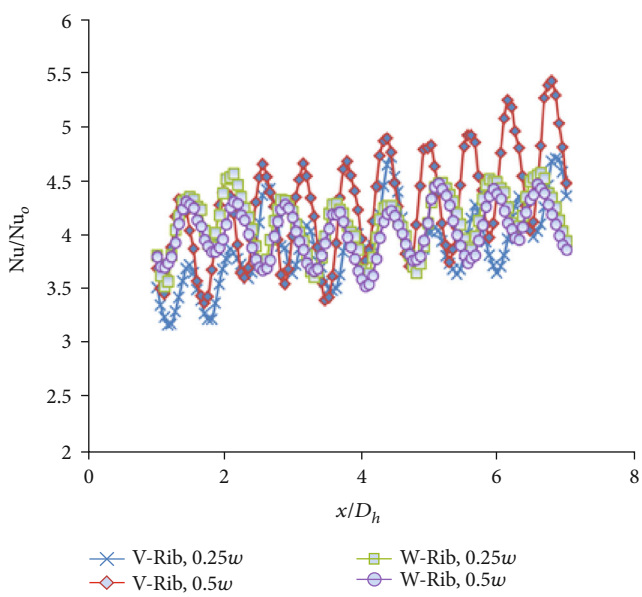

Figure 5: Streamwise variation of Nu/Nu$_o$ for Re 20000.

(AR = 1 : 4) located close to the leading edge for Re range 20000-80000. In order to achieve the objective, upstream pointing W- and V-shaped ribs are selected, and the critical geometric factors such as pitch, angle-of-attack, and rib height have been optimized. To the authors understanding and appreciation, geometry of ribs studied in the present work and same highlighted at Table 1 has been tested for the first time in a ribbed cooling passage with aspect ratio 1 : 4, and the optimized geometric parameters have provided encouraging results. Maximum and minimum thermohydraulic performances attained are 3.7 and 1.7 for Re 20000 and 80000, respectively. Considering the superior thermal performance, it can be concluded that the ribs and geometric parameters selected are ideal for effective thermal management in cooling passages near the leading edge.

2. Materials and Methods

A fabricated setup installed in the lab is illustrated in Figure 1. The atmospheric air is supplied to the system by the centrifugal blower with a maximum capacity of 1500 CFM. The discharge of the blower is passed through a calibrated venturimeter and controlled using a ball valve. Excess air is released to atmosphere through bleed valve. The flow rate is determined by the pressure head difference in the water manometer connected with the venturimeter. The venturimeter outlet is connected to test section through a 1 m pipe which houses two calibrated thermocouples (K-type) to measure inlet bulk air temperature.

Schematic of the three sections is represented in Figure 2. Test section is manufactured using a 12 mm thick acrylic sheet which is also commercially available under the brand names Plexiglas, Lucite, Perspex, and Crystallite. In the present case, acrylic material is preferred as they can withstand operating temperatures up to 120°C, possesses adequate strength and very low thermal conductivity. The test section height is 120mm, width is 30 mm, and full length is 1500 mm. The test section consists of three sections namely developing, ribbed, and exit sections. Developing section is 12.5 D_h in length to ensure the flow is developed completely prior to ribbed section, which is connected downstream. The ribbed section is also 12.5 D_h consisting of ribs on two walls. For measuring the pressure drop across ribbed section, either end of the ribbed section is provided with a pressure tap. A differential pressure transmitter (DPT) is connected to the pressure taps by using a flexible transparent hose for measuring the pressure drop. To avoid change in parameters in view of sudden expansion of air to the atmosphere, exit section of

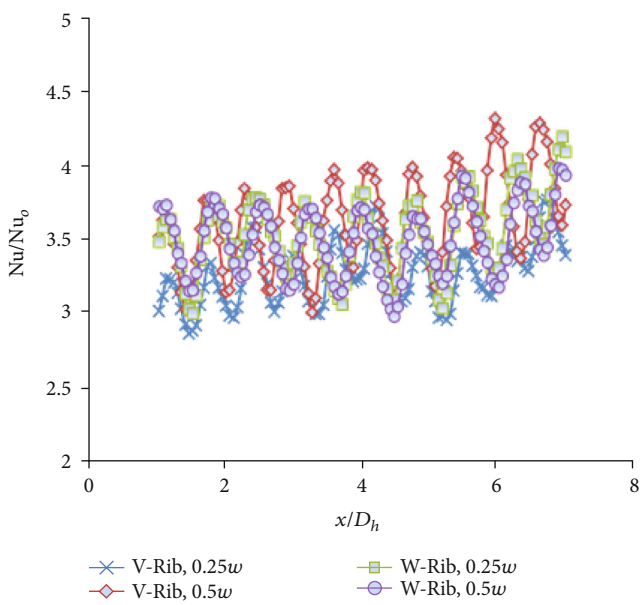

Figure 6: Streamwise variation of Nu/Nu$_o$ for Re 40000.

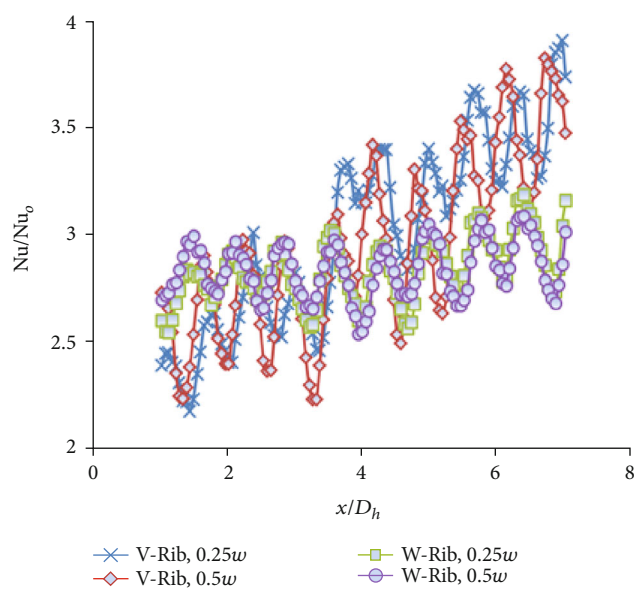

Figure 7: Streamwise variation of Nu/Nu$_o$ for Re 60000.

6.25 D_h is connected to downstream end of ribbed section. Sudden variation in velocity will influence the friction and heat transfer behaviours in ribbed section; therefore, exit section is considered important. The exit section houses two calibrated thermocouples (K-type) for measurement of exit bulk air temperature.

The two opposite ribbed walls measuring 460 mm in length and 40 mm in width are prepared using 0.2 mm thickness stainless steel sheet. Two copper blocks each of size 25 mm × 30 mm × 3 mm consisting of a brass stud at the center are soldered to either end of the sheet. After reinforcement, the effective ribbed surface area is 400 mm × 30 mm. The power is supplied to the stainless steel foil through the copper blocks. The resistance of each foil is as low as 0.0355 Ω. As

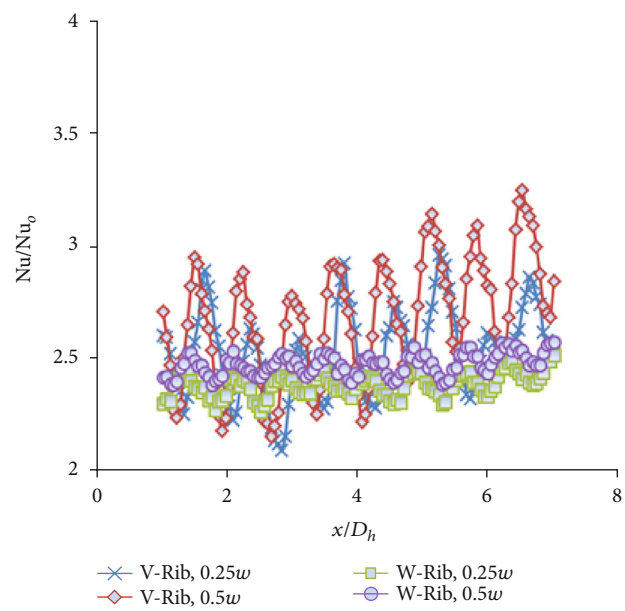

Figure 8: Streamwise variation of Nu/Nu$_o$ for Re 80000.

the thickness of the foil is very less, temperature variation between inner and outer surfaces is insignificant, and therefore, the effect due to lateral conduction has not been considered. A DC source with a maximum capacity of 1200 W (150 A and 8 V) is used to provide the required power.

The ribs under study are square in cross section and made from 2.5 mm and 2 mm balsa wood, respectively. Balsa material has been chosen as it possesses very low density, high strength to weight ratio, and widely used in studies related to aero-modeling and internal cooling of turbine blades using ribs [3]. The V-shaped ribs consist two arms which are joined along the centerline, and the W-shaped ribs consist of four arms made into two V-shapes and joined together along the centerline. Anabond silicone sealant is used to position the ribs on the foil inner surface. Subsequently, both the ribbed foils are secured to the acrylic sheet. After securing, high temperature heat resistant silicone tape is used additionally to bond the foils with the acrylic sheet. While bonding, due care is exercised to avoid air gap between the surfaces. The outer surface of the foils is painted with matt black paint for high emissivity. A thermal imaging camera has been used to measure the ribbed wall temperatures. A 3D model of test section with rib shapes is shown in Figure 3 for better appreciation.

The coolant flow rate is adjusted to achieve the differential pressure head corresponding to Reynolds number under examination. After stabilization of flow inside the test section, power source is switched on and after 30 minutes; critical parameters such as ribbed wall temperatures, pressure drop across ribbed section, inlet/exit bulk air temperatures, voltage drop across the copper blocks, and coolant velocity are recorded. Subsequently, using the infrared camera, ribbed wall images are captured and then processed to determine the wall temperatures locally. Friction factor and Nusselt number have been calculated by using the equations referred in literature.

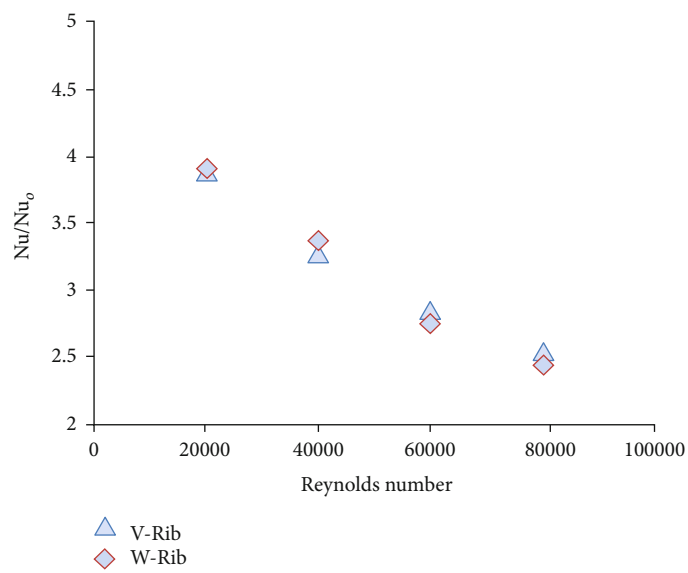

Figure 9: Variation of area averaged Nusselt number ratio with Re.

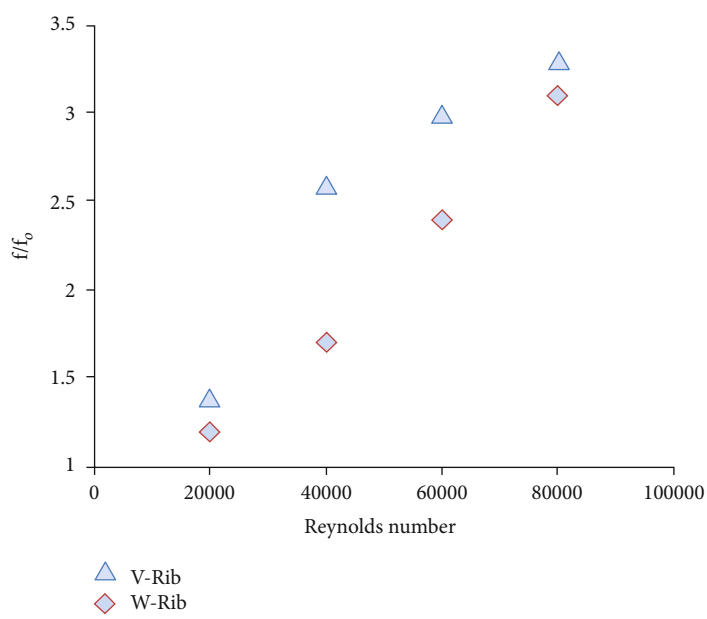

Figure 10: Normalized friction factor ratio.

The Re is determined using Eq. (1) referred in Krishnaswamy and Sivan [26].

$$\mathrm{Re} = \frac{\rho v D_h}{\mu}. \tag{1}$$

Heat input is given by Eq. (2) referred in Abraham and Vedula [3] and Deng et al. [25].

$$Q_{\mathrm{input}} = VI. \tag{2}$$

Heat loss due to radiation and natural convection adds up to the total heat loss and the same expressed at Eq. (3) and referred in Krishnaswamy and Sivan [26]. Maximum heat loss has been found to be 10.5% of power input at Re 20000.

$$Q_{\mathrm{loss}} = Q_{\mathrm{rad}} + Q_{\mathrm{conv}}. \tag{3}$$

Equation (4) referred by Abraham and Vedula [3] and Deng et al. [25] gives the net heat input.

$$Q_{\mathrm{net}} = Q_{\mathrm{input}} - Q_{\mathrm{loss}}. \tag{4}$$

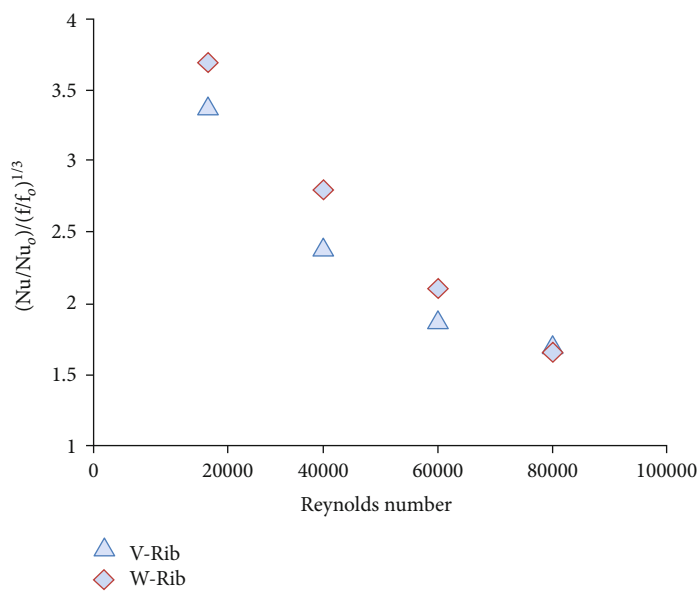

Figure 11: Thermohydraulic performance.

Table 3: Nu/Nu_o comparison.

	Ribs	e/D_h	P/e	α (°)	Re	Nu/Nu_o
Present study	V-ribs	0.052	10	45°	20000/40000/60000	3.9/3.3/2.8
Present study	W-ribs	0.0416	12.5	45°		3.9/3.4/2.7
Abraham and Vedula [3]	V-ribs	0.08	10	45°	20000/35000	2.4/2.1
Abraham and Vedula [3]	W-ribs	0.08	10	45°		2.45/2.3
Prashant et al. [4]	V-ribs	0.125	16	45°	20000/40000/60000	3.0/2.75/2.5
Prashant et al. [4]	W-ribs	0.125	16	45°		2.5/2.4/2.1
Ravi et al. [10]	Angled ribs	0.125	16	45°	20000/40000/60000	2.25/2.2/2.15
Ravi et al. [10]	M-ribs	0.125	16	45°		1.8/1.75/1.7
Deng et al. [25]	Orthogonal ribs	0.1	—	90°	20000	3

After calculating, net heat input the energy balance is obtained from Eq. (5) used by Abraham and Vedula [3] and Deng et al. [25].

$$Q_{\text{net}} = \dot{m}c_p(T_{\text{bin}} - T_{\text{bout}}). \tag{5}$$

Inlet and exit bulk air temperatures are linearly interpolated for determining the localized bulk temperature of air. The localized bulk temperature in spanwise direction is assumed to be constant. Equation (6) referred in Deng et al. [25] is used to estimate the local heat transfer coefficient.

$$h = \frac{Q_{\text{net}}}{A(T_{\text{wall}} - T_{\text{bulk}})}. \tag{6}$$

Expression used by Omeroglu [19] and Deng et al. [25] to evaluate area averaged Nusselt number is shown in

$$\text{Nu} = \frac{\bar{h}D_h}{k}. \tag{7}$$

Equation (8) represents the Dittus-Boelter Correlation for a smooth circular pipe referred in Deng et al. [25].

$$\text{Nu}_o = 0.023\ \text{Re}^{0.8}\ \text{Pr}^{0.4}. \tag{8}$$

Nusselt number ratio used by Omeroglu [19] and Deng et al. [25] for evaluating the augmentation is represented in

$$\frac{\text{Nu}}{\text{Nu}_o}. \tag{9}$$

Ribbed wall friction factor is determined by using Eq. (10) referred in Deng et al. [25].

$$f = \frac{\Delta P D_h}{2\rho L v^2}. \tag{10}$$

Blasius equation for Turbulent Friction factor in smooth circular pipe is denoted by Eq. (11) and the same referred in

Omeroglu [19] and Deng et al. [25].

$$f_o = 0.079\ \mathrm{Re}^{-1/4}. \tag{11}$$

For constant pumping power, thermohydraulic performance is determined from Eq. (12) used by Omeroglu [19] and Deng et al. [25].

$$\mathrm{THP}\,(\eta) = \frac{(\mathrm{Nu}/\mathrm{Nu}_o)}{(f/f_o)^{1/3}}. \tag{12}$$

2.1. Validation. In the current work, uncertainties in heat transfer and friction measurements are mainly because of errors noticed in measurement of coolant flow rate and ribbed wall temperatures. Hot wire anemometer and calibrated thermocouple (K-type) have been used to validate the coolant flow rate and ribbed wall temperatures measured by the venturimeter and thermal imaging camera, respectively. The coolant velocity is estimated from the static differential head across the U-tube water manometer connected to the venturimeter. The velocity of coolant thus measured is corroborated with the velocity measured by the anemometer. For the experimented range of Re, error observed in coolant velocity ranged from 0.55 m/s to 1.25 m/s. To evaluate error in wall temperature measurement, calibrated thermocouple is fixed to a stainless steel metal sheet (0.2 mm, grade 304) coated with matt finish black paint used for painting the ribbed walls also. Thereafter, by using the DC power source, stainless steel sheet is energised gradually in steps up to 80°C. The steady state temperatures are then recorded simultaneously by the thermocouple and thermal camera. Between the camera and thermocouple measurements, a maximum error of 4°C at 80°C is observed. Thermocouples used for measurement are calibrated by using thermo water bath. The errors are found to be within ±0.05°C. The accurancy and range of measuring instruments utilized in this work are highlighted in Table 2. Using the methodology proposed by Moffat [28], maximum uncertainty in estimation of friction and Nusselt number are 8.5% and 11.5% at Reynolds number 20000.

3. Results and Discussion

The present study is aimed at evaluating thermohydraulic performance of continuous W- and V-ribs. Nusselt number ratios ($\mathrm{Nu}/\mathrm{Nu}_o$) for both rib shapes have been determined along span lengths $0.25w$ and $0.5w$. Also, friction factor across the ribbed walls has been determined to evaluate the thermohydraulic performance.

3.1. Span Averaged Heat Transfer Coefficient. Figure 4 depicts variation in span averaged heat transfer coefficients. The values improved as the Reynolds number increased and are highest along the centerline ($0.5w$) for V-shaped ribs because of dominant nature of rib generated flow separation and reattachment. For V-shaped ribs, averaged heat transfer coefficient along $0.5w$ at Re 80000 is found to be 1.94 times higher than the value measured at Re 20000. For W-shaped ribs, magnitude of averaged heat transfer coefficient along $0.25w$ is noticed to be highest for Re 20000 and 40000 and along $0.5w$ for Re 60000 and 80000. The value at Re 80000 is 1.8 times higher than that measured at Re 20000. Comparison of increment in values between two successive Re shows that increment is highest at 45% between the Re 20000 and 40000 for V-shaped ribs and 50% for W-shaped ribs. For Re range 40000-80000, extent of augmentation in heat transfer reduced and is noticed to be in the range of 15-18% for V-shaped ribs and 8-10% for W-shaped ribs. Reduction in increment beyond Re 40000 is due to decline in magnitude of secondary flow in the direction of stream due to coolant diversion along rib arms. The primary reason for coolant diversion is the decrease in velocity boundary layer thickness at higher Re. In addition, it is also speculated that, for the selected blockage ratio and pitch, impact induced by the ribs on flow is highest at Re 40000.

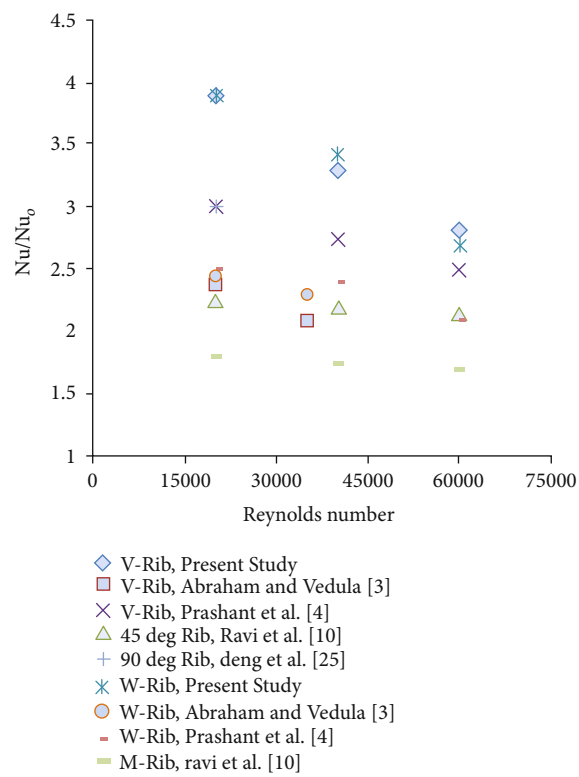

Figure 12: Comparison of $\mathrm{Nu}/\mathrm{Nu}_o$ with published data.

3.2. Streamwise and Spanwise Variations in Nusselt Number Ratio. In the direction of stream, heat transfer is predominantly influenced by the secondary flow generated as a result of flow separation at the rib. Along rib arms, magnitude of heat transfer depends upon the strength of counter rotating vortices generated as a result of coolant flow along the arms. In general, intensity of secondary flows is primarily influenced by the factors such as rib pitch, profile, angle-of-attack, and rib height. Nusselt numbers along the stream are highest at the reattachment zone due to very low wall temperatures produced by the high impingement velocity of the coolant. At the separation zone, Nusselt numbers are found to be relatively lower than reattachment zone. This is because,

Table 4: THP comparison.

	Ribs	e/D_h	P/e	α (°)	Re	THP
Present study	V-ribs	0.052	10	45°	20000/40000/60000	3.4/2.4/1.9
Present study	W-ribs	0.0416	12.5	45°		3.7/2.8/2.1
Abraham and Vedula [3]	V-ribs	0.08	10	45°	20000/35000	1.45/1.3
Abraham and Vedula [3]	W-ribs	0.08	10	45°		1.3/1.2
Prashant et al. [4]	V-ribs	0.125	16	45°	20000/40000/60000	1.6/1.45/1.25
Prashant et al. [4]	W-ribs	0.125	16	45°		1.45/1.2/1.05
Ravi et al. [10]	Angled ribs	0.125	16	45°	20000/40000/60000	1.15/1.1/1.05
Ravi et al. [10]	M-ribs	0.125	16	45°		0.95/0.85/0.8
Deng et al. [25]	Orthogonal ribs	0.1	—	90°	20000	1.8

magnitude of secondary flow generated in the stream direction is relatively higher than that of counter rotating vortices induced by the rib arms. After the reattachment zone, capability of the coolant to withdraw heat gradually reduces due to the development of boundary layer. This phenomenon in turn leads to a decline in extent of heat transfer in the direction of stream. Due to above phenomenon, the magnitude of Nusselt number between the two successive ribs varies along the stream in a sinusoidal manner, with maximum heat transfer at the reattachment zone and minimum heat transfer at the separation zone.

Figures 5–8 show the streamwise variations in local Nusselt number ratio along span lengths $0.25w$ and $0.5w$ for both the ribs. The variations for V-shaped ribs are 31% and 26% at Re 20000 and 80000, respectively. For W-shaped ribs, variations are 17.5% and 7% at Re 20000 and 80000, respectively. Increased height of V-shaped ribs influenced the boundary layer separation and reattachment more thereby leading to large variation in Nusselt number ratio. Further, streamwise variations are found to be greatest at lesser Re for both ribs due to dissimilarities in magnitude of heat transfer observed between the separation and reattachment zones. At higher Re , the variation reduced due to effect of stronger secondary flows along the span induced by the diverted coolant. Nusselt number ratio slowly increased in the streamwise direction because of increased turbulent mixing. The increasing trend is prominent for V-shaped rib view increased height of the rib. Also, an abrupt increase in Nusselt number ratio closer to exit of ribbed section is observed due to turbulence generated by the coolant while leaving the section.

The spanwise variation in local Nusselt number ratio for both rib shapes has also been analyzed. For experimented Re range, maximum spanwise variation for V-shaped ribs is 12%, and W-shaped ribs is 3.5%. Low variation for W-shaped ribs is because of the uniformity generated in view of turbulent mixing of secondary flow induced by two apexes. Also, due to the presence of additional rib arms, magnitude of counter rotating vortices generated by W-shaped ribs along the rib arms is superior in comparison to the vortices generated by V-shaped ribs. In addition, due to shorter length of rib arms, coolant is less warm, and hence, its capacity to extract heat is more for W-shaped ribs. In view of the above reasons, spanwise variations are lowest for W-shaped ribs.

3.3. Area Averaged Normalized Nusselt Number. Figure 9 depicts variation of area averaged Nusselt number ratio. Maximum difference between W- and V-shaped ribs is 3.5% at Reynolds number 80000, which is within the uncertainty limits. Low variation is because of the fact that secondary flow strength along stream for V-shaped ribs having 25% greater rib height is higher than the magnitude of secondary flow along the stream induced by W-shaped ribs. The higher strength of secondary flow along the stream for V-shaped ribs compensated for the increased strength of counter rotating vortices generated by W-shaped ribs, which in turn resulted in low variation. Nu/Nu_o for the rib profiles decreased as the Re increased. For V-shaped ribs, values are observed to be 3.9 and 2.5 corresponding to Re 20000 and 80000, respectively. At Re 40000, the Nu/Nu_o is estimated as 3.3, and at Re 60000, the value is 2.8. For W-shaped ribs, Nu/Nu_o values for Re 20000 and 80000 are estimated to be 3.9 and 2.4, respectively. For the Re 40000 and 60000, the respective values are 3.4 and 2.7. In general, Nu/Nu_o for both the rib profiles are observed to be high which is attributed to greater strength of secondary flows produced by the ribs deployed inside the narrow cooling passage. Also, to enhance the power and performance of the engine, high and uniform heat transfer augmentations are desired. While both the configurations are recommended for deployment in regions exposed to extreme temperatures, W-shaped ribs are preferred over V-shaped ribs in view of low heat transfer variations in the direction of stream and span.

3.4. Normalized Friction Factor. In a ribbed cooling passage, magnitude of friction loss is primarily dependent on the pressure drop generated by ribs. Figure 10 depicts variations in friction factor ratio. For Re range, investigated friction factor ratios for V-shaped ribs ranged from 1.4 to 3.3, and for W-shaped ribs, it ranged from 1.2 to 3.1. Friction factor ratio increased with increase in Re. Friction factor ratios are highest for V-shaped ribs due to a 25% greater height-to-channel hydraulic diameter ratio. Highest and lowest differences between friction factor ratios of the ribs are 53% and 6.5% corresponding to Re 40000 and 80000. Normalized friction factor for both ribs has been independently examined, and a maximum increase of 85% for V-shaped ribs and 42% for W-shaped ribs has been observed between Re 20000 and 40000. For both rib shapes, increment in friction factor ratio

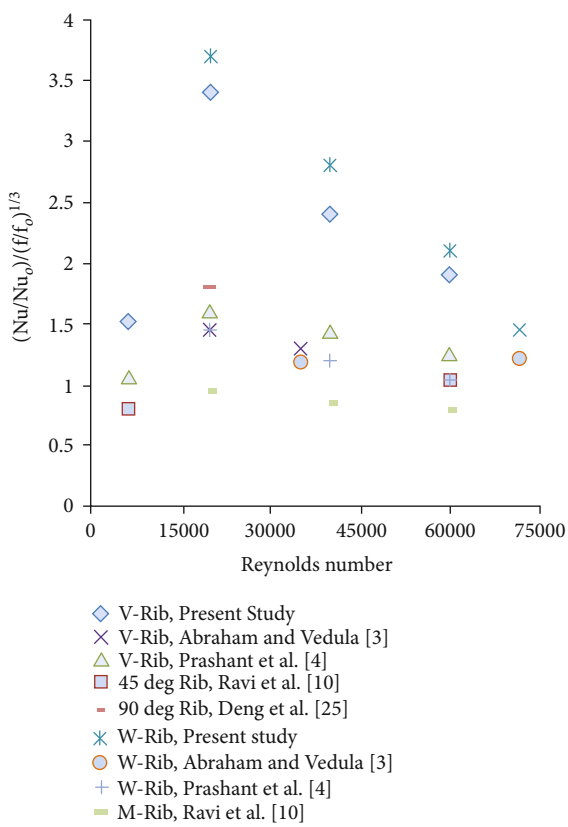

Figure 13: Comparison of THP with published data.

between successive Re beyond Re 40000 reduced due to surge in flow of coolant towards side walls owing to diversion, which consecutively decreased the overall pressure drop. In comparison to V-shaped ribs, reduction in increment is found to be lower for W-shaped ribs because the diverted coolant resulted to a surge in concentration of coolant along the centerline due to the converging rib arms, which generated a reasonable pressure drop. Despite the above phenomenon, overall pressure drop due to V-shaped ribs continued to remain higher than W-shaped ribs due to greater rib height.

3.5. Thermohydraulic Performance. Figure 11 illustrates variation in thermohydraulic performances of W- and V-shaped ribs. THP values for W-shaped ribs are higher than V-shaped ribs for Re range 20000-60000. Variation in THP is 8.8%, 16.6%, and 10.5% for Re 20000, 40000, and 60000, respectively. As it can be seen, despite low variation (3.5%) in heat transfer enhancements estimated for both rib shapes, variation in THP estimated at Re 40000 is highest owing to high pressure drop generated by the V-shaped ribs. Beyond Re 40000, variation starts reducing due to the overall decline in pressure drop owing to coolant diversion. At Re 80000, THP of V-shaped ribs is 2.5% greater than W-shaped ribs.

3.6. Comparative Study. Normalized Nusselt numbers of the rib shapes under study are compared with the published results in Table 3 and the same represented in Figure 12. Nu/Nu_o values estimated for V-shaped ribs ($e/D_h = 0.052$) at Re 20000 and 35000 are 60-66% higher than V-ribs ($e/D_h = 0.08$) placed inside a converging duct studied by Abraham and Vedula [3]. In comparison to the results presented for V-ribs ($e/D_h = 0.125$) in an aspect ratio 1 : 1 channel by Prashant et al. [4], Nu/Nu_o values for V-shaped ribs having blockage ratio 0.052 are 12-30% higher for the range of Re 20000 to 60000. Compared to Nu/Nu_o values estimated by Ravi et al. [10] for 45° angled ribs ($e/D_h = 0.125$) in a channel having aspect ratio 1 : 1, V-shaped ribs used in this work generated 30-73% higher enhancement for Re range 20000 to 60000. The enhancement reported by Deng et al. [25] for orthogonal ribs ($e/D_h = 0.1$) in an aspect ratio 1 : 1 channel is found to be 30% less than the enhancement estimated at Re 20000 for V-shaped ribs. Similar to V-shaped ribs, Nu/Nu_o values of W-shaped ribs are also noticed to be higher than that presented in literature. As compared with the enhancement predicted by Abraham and Vedula [3] for Re 20000 and 35000 for W-ribs ($e/D_h = 0.08$) inside a converging channel, enhancement due to W-shaped ribs ($e/D_h = 0.0416$) in the current work is found to be 48-60% higher. Further, when compared with the predictions of Prashant et al. [4] for continuous W-ribs for the Re 20000-60000, Nu/Nu_o values estimated for W-shaped ribs in this work are 30-56% higher. Besides, the enhancements due to W-shaped ribs are found to be higher by 60-100% than that predicted by Ravi et al. [10] for continuous M-ribs ($e/D_h = 0.125$). As compared with the enhancement predicted by Deng et al. [25] for 90° ribs ($e/D_h = 0.1$) in a aspect ratio 1 : 1 channel, enhancement due to W-shaped ribs at Re 20000 is noticed to be 30% higher. Thermohydraulic performance values of V-shaped ribs and W-shaped ribs have been compared with different rib configurations, and the same are shown in Table 4 and Figure 13. For the experimented Re, the THP values of V- and W-shaped ribs used in this work are 50% to 200% greater than that presented for different rib configurations such as V-ribs, W-ribs, M-ribs, and angled ribs inside cooling channels. In addition, THP value of V- and W-shaped ribs observed at Re 20000 is 90% higher than that predicted at Re 20000 by Deng et al. [25] for 90° ribs inside a square channel with higher blockage ratio. Hence, from the comparative study, it can be concluded that the overall thermal performance due to W- and V-shaped ribs with low e/D_h ratio is superior to other configurations due to high heat transfer generated by the ribs for low friction losses. Therefore, rib configurations are recommended for deployment in regions adjacent to leading edge for enhancing the heat transfer with no major effect on friction loss.

4. Conclusions

The present experimental work has been performed with an objective to maximize heat transfer and minimize pressure drop inside a ribbed passage (AR = 1 : 4) located close to the leading edge for Re range 20000-80000 using V- and W-shaped ribs. Nusselt number ratio (Nu/Nu_o) and thermohydraulic performance (THP) values for the experimented Re are found to reasonably good for both the rib profiles. The following are concluded based on the analysis of results.

(1) For increase in Reynolds number, friction factor ratio increased, and Nusselt number ratio decreased

(2) In case of V-shaped ribs, extent of heat transfer at Re 20000 is 94% higher than *Re* 80000. For W-shaped ribs, the increase is 80%

(3) Maximum difference in area averaged Nusselt number ratio between both ribs is 3.5%, which is within the uncertainty limits

(4) Maximum streamwise variation in local Nusselt number ratio of V-shaped ribs is 31% at Re 20000. For W-shaped ribs, variation is 17.5% at same Re

(5) Maximum spanwise variation in local Nusselt number ratio of V-shaped ribs is 12%. For W-shaped ribs, variation estimated is 3.5

(6) Friction losses for V-shaped ribs are greater than W-shaped ribs for Re range investigated

(7) Minimum and maximum differences between the friction factor ratios of the rib shapes are 6.5% and 53% corresponding to Re 80000 and 40000

(8) For both the rib shapes, impact of ribs on friction and heat transfer is noticed to be greatest at Re 40000

(9) Highest and lowest THP values achieved with V-ribs are 3.4 and 1.7 at Re 20000 and 80000. For W-ribs, values are 3.7 and 1.65

4.1. Recommendation. In a turbine blade, large variations in heat transfer coefficient will lead to formation of hotspots and failure of the blade subsequently due to thermal stresses. Further, increase in weight of the blade due to ribs will reduce the power-to-weight ratio. While both the rib profiles generated reasonably good Nu/Nu_o and THP values, based on above conclusions, W-shaped rib which generated higher THP, lower heat transfer coefficient variations, and 25% lesser height is recommended for effective thermal management and improvised engine performance.

Nomenclature

α: Angle of attack, degree (°)
P: Rib pitch, mm
e: Height of the rib, mm
D_h: Hydraulic diameter of test section, m
W: Width of the test section, mm
H: Height of the test section, mm
v: Velocity of air, m/s
w: Width of the ribbed wall, mm
$\dot{m}$: Mass flow rate, kg/s
h: Local heat transfer coefficient, W/m^2-K
h_{avg}: Span averaged heat transfer coefficient, W/m^2-K
$\bar{h}$: Area averaged heat transfer coefficient for ribbed wall, W/m^2-K
Nu: Area averaged Nusselt number
Nu_o: Nusselt number for smooth circular pipes (Dittus-Boelter correlation)
Pr: Prandtl number
v: Streamwise air velocity, m/s
ρ: Density of air, kg/m^3
μ: Dynamic viscosity of air, N s/m^2
k: Thermal conductivity of air, W/m-K
Q_{input}: Heat input, W
Q_{loss}: Heat loss, W
Q_{net}: Net heat input, W
Q_{conv}: Heat loss due to natural convection, W
Q_{rad}: Heat loss due to radiation, W
A: Effective surface area of ribbed wall, m^2
L: Length between the pressure taps, m
T_{bulkv}: Bulk air temperature, K
T_{bin}: Bulk air inlet temperature, K
T_{bout}: Bulk air outlet temperature, K
T_{wall}: Wall temperature, K
c_p: Specific heat of air, J/kg K
I: Current, ampere (A)
V: Voltage, volt (V)
f: Friction factor
f_o: Friction factor in smooth circular pipe (Blasius friction factor)
η: Thermohydraulic performance
ΔP: Pressure drop across the ribbed section, N/m^2
A: Ampere
V: Volt
Ω: Ohms
W: Watt
Pa: Pascal.

Abbreviations

CFM: Cubic feet per minute
DC: Direct current
DPT: Differential pressure transmitter.

Data Availability

Data will be made available on request made to corresponding author.

Conflicts of Interest

The authors declare that there is no conflict of interest regarding the publication of this paper.

References

[1] M. Goodarzi, M. R. Safaei, K. Vafai et al., "Investigation of nanofluid mixed convection in a shallow cavity using a two-phase mixture model," *International Journal of Thermal Sciences*, vol. 75, pp. 204–220, 2014.

[2] M. Goodarzi, M. R. Safaei, A. Karimipour et al., "Comparison of the Finite Volume and Lattice Boltzmann Methods for Solving Natural Convection Heat Transfer Problems inside Cavities and Enclosures," *Abstract and Applied Analysis*, vol. 2014, Article ID 762184, 15 pages, 2014.

[3] S. Abraham and R. P. Vedula, "Heat transfer and pressure drop measurements in a square cross-section converging

Channel with V and W rib turbulators," *Experimental Thermal and Fluid Science*, vol. 70, pp. 208–219, 2016.

[4] P. Singh, B. V. Ravi, and S. V. Ekkad, "Experimental and numerical study of heat transfer due to developing flow in a two-pass rib roughened square duct," *International Journal of Heat and Mass Transfer*, vol. 102, pp. 1245–1256, 2016.

[5] N. G. Ghodake, C. Rao, and R. R. Arakerimath, "Flow and heat transfer analysis of various ribs for forced convection heat transfer," *Journal of Emerging Technologies and Innovative Research*, vol. 3, no. 7, pp. 42–47, 2016.

[6] W. Yang, S. Xue, Y. He, and W. Li, "Experimental study on the heat transfer characteristics of high blockage ribs channel," *Experimental Thermal and Fluid Science*, vol. 83, pp. 248–259, 2017.

[7] H. Deng, Y. Li, Z. Tao, G. Xu, and S. Tian, "Pressure drop and heat transfer performance in a rotating two-pass channel with staggered 45-deg ribs," *International Journal of Heat and Mass Transfer*, vol. 108, pp. 2273–2282, 2017.

[8] P. Singh, W. Li, S. V. Ekkad, and J. Ren, "A new cooling design for rib roughened two-pass channel having positive effects of rotation on heat transfer enhancement on both pressure and suction side internal walls of a gas turbine blade," *International Journal of Heat and Mass Transfer*, vol. 115, pp. 6–20, 2017.

[9] P. Singh, W. Li, S. V. Ekkad, and J. Ren, "Experimental and numerical investigation of heat transfer inside two-pass rib roughened duct (AR = 1:2) under rotating and stationary conditions," *International Journal of Heat and Mass Transfer*, vol. 113, pp. 384–398, 2017.

[10] B. V. Ravi, P. Singh, and S. V. Ekkad, "Numerical investigation of turbulent flow and heat transfer in two-pass ribbed channels," *International Journal of Thermal Sciences*, vol. 112, pp. 31–43, 2017.

[11] L. Wang, S. Wang, X. Zhou, F. Wen, and Z. Wang, "Numerical prediction of 45 ° angled ribs effects on U-shaped channels heat transfer and flow under multi conditions," *International Journal of Turbo & Jet-Engines*, vol. 37, no. 1, pp. 41–59, 2017.

[12] P. Singh, Y. Ji, and S. V. Ekkad, "Experimental and numerical investigation of heat and fluid flow in a square duct featuring criss-cross rib patterns," *Applied Thermal Engineering*, vol. 128, pp. 415–425, 2018.

[13] S. Ruck and F. Arbeiter, "Detached eddy simulation of turbulent flow and heat transfer in cooling channels roughened by variously shaped ribs on one wall," *International Journal of Heat and Mass Transfer*, vol. 118, pp. 388–401, 2018.

[14] T. M. Liou, S. W. Chang, and S. P. Chan, "Effect of rib orientation on thermal and fluid-flow features in a two-pass parallelogram channel with abrupt entrance," *International Journal of Heat and Mass Transfer*, vol. 116, pp. 152–165, 2018.

[15] J. Wang, J. Liu, L. Wang, B. Sundén, and S. Wang, "Numerical investigation of heat transfer and fluid flow in a rotating rectangular channel with variously-shaped discrete ribs," *Applied Thermal Engineering*, vol. 129, pp. 1369–1381, 2018.

[16] A. Aghaei, G. A. Sheikhzadeh, M. Goodarzi, H. Hasani, H. Damirchi, and M. Afrand, "Effect of horizontal and vertical elliptic baffles inside an enclosure on the mixed convection of a MWCNTs-water nanofluid and its entropy generation," *European Physical Journal Plus*, vol. 133, no. 11, article 12278, 2018.

[17] P. S. Patil, "Recent studies in internal cooling of gas turbine blade : a review," *International Journal of Applied Engineering Research*, vol. 13, no. 9, pp. 7131–7141, 2018.

[18] A. M. Aboghrara, M. A. Alghoul, B. T. H. T. Baharudin et al., "Parametric study on the thermal performance and optimal design elements of solar air heater enhanced with jet impingement on a corrugated absorber plate," *International Journal of Photoenergy*, vol. 2018, Article ID 1469385, 21 pages, 2018.

[19] G. Ömeroğlu, "CFD analysis and electrical efficiency improvement of a hybrid PV/T panel cooled by forced air circulation," *International Journal of Photoenergy*, vol. 2018, Article ID 9139683, 11 pages, 2018.

[20] S. H. Delbari, A. Nejat, M. H. Ahmadi, A. Khaleghi, and M. Goodarzi, "Numerical modeling of aeroacoustic characteristics of different savonius blade profiles," *International Journal of Numerical Methods for Heat and Fluid Flow*, vol. 30, no. 6, pp. 3349–3369, 2019.

[21] A. Hajatzadeh Pordanjani, S. Aghakhani, A. Karimipour, M. Afrand, and M. Goodarzi, "Investigation of free convection heat transfer and entropy generation of nanofluid flow inside a cavity affected by magnetic field and thermal radiation," *Journal of Thermal Analysis and Calorimetry*, vol. 137, no. 3, article 7982, pp. 997–1019, 2019.

[22] J. Tang, D. Gao, L. Wang, and J. Huo, "Experimental study on the distribution trends of fouling on a compressor blade," *International Journal of Photoenergy*, vol. 2020, Article ID 8885737, 7 pages, 2020.

[23] L. Jiang, X. Dou, and M. Wu, "Effect of stress on creep behavior of single crystal alloy IC6SX at 980°C," *International Journal of Photoenergy*, vol. 2020, Article ID 8844874, 5 pages, 2020.

[24] S. Yousefzadeh, H. Rajabi, N. Ghajari, M. M. Sarafraz, O. A. Akbari, and M. Goodarzi, "Numerical investigation of mixed convection heat transfer behavior of nanofluid in a cavity with different heat transfer areas," *Journal of Thermal Analysis and Calorimetry*, vol. 140, no. 6, article 9018, pp. 2779–2803, 2019.

[25] H. Deng, H. Li, Z. Tao, L. Qiu, and J. Zhu, "Effect of blockage ratio on heat transfer and pressure drop in rotating ribbed channels at high rotation numbers," *Journal of Thermal Science*, vol. 30, no. 3, article 1275, pp. 902–913, 2021.

[26] K. Krishnaswamy and S. Sivan, "Improvement in thermal hydraulic performance by using continuous V and W-shaped rib turbulators in gas turbine blade cooling application," *Case Studies in Thermal Engineering*, vol. 24, article 100857, 2021.

[27] X. Wang, H. Xu, J. Wang, W. Song, and L. Wang, "High pressure turbine blade internal cooling in a realistic rib roughened two-pass channel," *International Journal of Heat and Mass Transfer*, vol. 170, article 121019, 2021.

[28] R. Moffat, "Describing the uncertainties in experimental results," *Experimental Thermal and Fluid Science*, vol. 1, no. 1, pp. 3–17, 1988.

Hindawi
International Journal of Photoenergy
Volume 2021, Article ID 6692598, 10 pages
https://doi.org/10.1155/2021/6692598

Research Article

On the Determination of the Output Power in Mono/Multicrystalline Photovoltaic Cells

Xia Liu,[1] Yongqiu Liu,[1] and Mohammad Eslami[2]

[1]*School of Electrical and Mechanical Engineering, Guangdong University of Science and Technology, Dongguan 523083, China*
[2]*Department of Electrical and Computer Engineering, Chabahar Branch, Islamic Azad University, Chabahar, Iran*

Correspondence should be addressed to Yongqiu Liu; banbianqiu@126.com and Mohammad Eslami; m.eslami@iauzah.ac.ir

Received 3 January 2021; Revised 11 February 2021; Accepted 17 April 2021; Published 8 May 2021

Academic Editor: Hafiz Muhammad Ali

Copyright © 2021 Xia Liu et al. This is an open access article distributed under the Creative Commons Attribution License, which permits unrestricted use, distribution, and reproduction in any medium, provided the original work is properly cited.

In the present work, two artificial intelligence-based models were proposed to determine the output power of two types of photovoltaic cells including multicrystalline (multi-) and monocrystalline (mono-). Adaptive neuro-fuzzy inference system (ANFIS) and Least-squares support vector machine (LSSVM) are applied for the output power calculations. The estimation results are very close to the actual data based on graphical and statistical analysis. The coefficients of determination (R^2) of monocrystalline cell output power for LSSVM and ANFIS models are as 0.997 and 0.962, respectively. Additionally, multicells have R^2 values of 0.999 and 0.995 for LSSVM and ANFIS, respectively. The acceptable values for R^2 and various error parameters prove the accuracy of suggested models. The visualization of these comparisons clarifies the accuracy of suggested models. Additionally, the proposed models are compared with previously published machine learning methods. The accurate performance of proposed models in comparison with others showed that our models can be helpful tools for the estimation of output power. Moreover, a sensitivity analysis for the effects of inputs parameters on output power has been employed. The sensitivity output shows that light intensity has more on output power. The outcomes of this study provide interesting tools which have potential to apply in different parts of renewable energy industries.

1. Introduction

Photovoltaic (PV) cell power generation as a renewable energy source has vital importance, because it is not only used to overcome the present energy problems but also is environment-friendly to overcome the present environmental problems [1–3]. The development and studies in renewable energy technology can reduce the global warming problem and other environmental problems [4]. In the literature, there are some valuable studies on renewable energy topics such as experimental investigation on the effect on the mass flow rate of the nanofluid, volume fraction of the nanofluid, and volume of the storage tank on the inlet-outlet water temperature difference and the energy efficiency of an evacuated tube solar collector. Additionally, three machine learning approaches called gene-expression programming, model tree, and multivariate adaptive regression spline were developed for prediction of these target parameters [5]. Sadeghi et al. developed a modeling investigation on the evacuated tube solar collector. In their work, the gene-expression programming was used to simulate evacuated tube solar collector in various volumes of the thermal storage tanks and solar radiation intensities [6]. Akhter et al. evaluated the performance of three PV technologies including thin-film, monocrystalline, and poly-crystalline technologies based on eleven different performance parameters [7].

The device temperature and material and solar radiation intensity are effective parameters on the output power of PV cells. For instance, multicrystalline, monocrystalline, and amorphous crystalline silicon solar PV cells have different behaviors in the operational conditions. Therefore, an accurate predictive tool for determination of PV power supply and home power demand is highly required to save costs and time [8–10]. Among all predictive tools, the artificial intelligence (AI) approaches have a vital place for the determination of power because the AI approaches because of the ability of AI models in the prediction of the behavior of nonlinear dynamic systems [11]. In the AI approaches,

there is no need to employ any physics-based derivations or specific analytical formulations [12]. They do not require complex calculations or high amount of tuning parameters, and also, they have better performance than the multiple linear regression models in nonlinear systems [13, 14]. Overall, a dynamic system can be simulated by feeding a comprehensive dataset into an organized network. This network is trained until an acceptable degree of accuracy is obtained [15].

According to the successful background of intelligence methods in the prediction of different industrial parameters [16–18], in this work, two intelligence models based on adaptive neuro-fuzzy inference system (ANFIS) and Least-squares support vector machine (LSSVM) were suggested to determine the output power of two types of photovoltaic cells including multicrystalline and monocrystalline. Various comparisons have been carried out to investigate the performance of these models. Additionally, an interesting sensitivity analysis is employed to identify the impact of temperature and light intensity on output power.

2. Methodology

2.1. Experimental Databank. To train the aforementioned models, a comprehensive experimental databank was gathered from dependable sources in the literature. The experimental setup and conditions which were used to obtain these data points can be described as follows.

The utilized monocrystalline and multicrystalline PV cells have a size of 2.8 cm × 2.5 cm which was produced by QS Solar Company. For data acquisition, the PV testing system with number SAC which produced in Chengdu ZKY Instrument Company Xenon light source is used for the simulated sunlight. A six tranches toggle switch adjusts the intensity of the incident light. The light intensities of these tranches are around 1100, 1000, 900, 800, 700, and 600 W/m^2, respectively. A semiconductor refrigeration device was used for the temperature control room of an experimental sample.

The maximum output powers (MOP) and current-voltage curves were measured in temperatures of 40, 35, 30, 27, 25, 20, 15, 10, 5, 0, -5, and -10°C, respectively. Thus, each light intensity tranch has twelve measurement conditions. For instance, the experimental conditions of temperature and light intensity are -10°C and 6th tranche, -5°C and 6th tranche, 0°C and 6th tranche, 5°C and 6th tranche, 10°C and 6th tranche, 15°C and 6th tranche, 20°C and 6th tranche, 25°C and 6th tranche, 27°C and 6th tranche, 30°C and 6th tranche, 35°C and 6th tranche, and 40°C and 6th tranche. A total number of 72 actual points were collected, 62 of them were used as training data points, and 10 data points were used in the testing phase for evaluating the performance of models in unseen conditions [10].

2.2. Adaptive Neuro-Fuzzy Inference System. Fuzzy logic (FL) includes the inference strategy and cognitive uncertainties. On the other hand, artificial neural networks have parallel scattered structures which can be adapted quickly with different types of problems. Referring to these characteristics, the combination of these structures created neuro-fuzzy method. This method was employed by Takagi first time; after that, Jang proposed ANFIS. This model employed the abilities of both fuzzy and ANN structures to improve its performance [19]. In other words, this model combines fuzzy structure characteristic and adaptive system. The schematic structure of the ANFIS model is demonstrated in Figure 1. In this demonstration, fuzzy rules of the first-order Sugeno are expressed as follows: if $X_1 = A_i$ and $X_2 = B_j$ are acceptable, $f_i = m_i X_1 + n_i X_2 + r_i$ is assumed. In which, r_i, m_i, and n_i are obtained in the process of training. The below figure gives information about the layered structure of this model [20]:

Layer 1: in this layer, adaptive nodes exist. These nodes can be considered as counterparts of linguistic terms, in which outputs have a relationship with membership function (MF) as follows:

$$O_i^1 = \beta(X) = \exp^{\left(-(1/2)\left((X-Z)^2/\sigma^2\right)\right)}. \quad (1)$$

In this formulation, σ, Z, and O are the variances, Gaussian membership function center, and output, respectively.

Layer 2: this layer includes multiplying entrance signals to determine the fire strength:

$$O_i^2 = W_i = \beta_{Ai}(X).\beta_{Bi}(X). \quad (2)$$

Layer 3: this layer contains some firm nodes. The nodes determine the ratio of firing strength to the sum of all firing strength. The final outputs of this layer can be defined as follows:

$$O_i^3 = \frac{W_i}{\sum W_i}. \quad (3)$$

Layer 4: available adaptive nodes in this layer are used to calculate normalized firing strength as following:

$$O_i^4 = \overline{W_i} f_i = \overline{W_i}(m_i X_1 + n_i X_2 + r_i). \quad (4)$$

Layer 5: the final layer includes a node that sums the outputs of the fourth layer [21, 22]:

$$O_i^5 = Y = \sum_i \overline{W_i} f_i = \overline{W_1} f_1 + \overline{W_2} f_2 = \frac{\sum W_i f_i}{\sum W_i}. \quad (5)$$

2.3. Least-Squares Support Vector Machine. The cornerstone of support vector machine (SVM) is structural risk minimization and machine learning concepts. This algorithm can detect various patterns of available data and investigation of them based on a suitable way [23]. Seykens et al. upgraded SVM algorithm and called it least squares SVM (LSSVM). The significant point of the new algorithm is the fact that uses a linear equation system to solve the problem. This point makes it faster than the

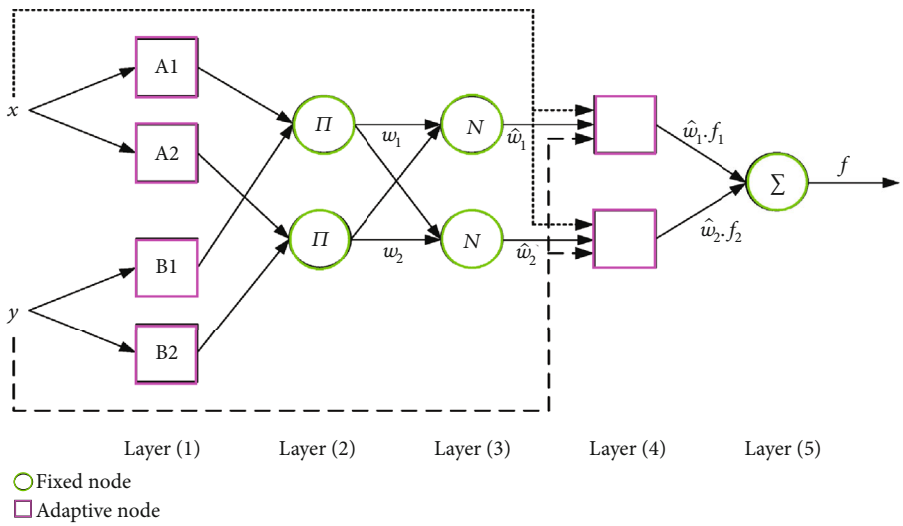

Figure 1: Structure of a typical ANFIS approach.

SVM algorithm. The below formulation describes the cost function of LSSVM method [24]:

$$\min_{\omega, b, e} J(\omega, e) = \frac{1}{2}\omega^T\omega + \frac{1}{2}\gamma\sum_{k=1}^{N} e_k^2. \quad (6)$$

The following constrain is defined for the cost function:

$$y_k = \omega^T\varphi(x_k) + b + e_k, k = 1, 2, \cdots, N. \quad (7)$$

In which, b and w are the bias and linear regression slope values, respectively. Υ stands for the regularization parameter. x and y stand for the input and output. T and φ are the transpose matrix and feature map. In the following, the Lagrange equation is defined:

$$L(\omega, b, e, \alpha) = J(\omega, e) - \sum_{k=1}^{N}\alpha_k\{\omega^T\varphi(x_k) + b + e_k - y_k\}. \quad (8)$$

In which, α_k is the Lagrangian multiplier which is estimated based on partial differentiation concept:

$$\begin{aligned}
&\frac{\partial L(\omega, b, e, \alpha)}{\partial \omega} = 0 \longrightarrow \omega = \sum_{k=1}^{N}\alpha_k\varphi(x_k),\\
&\frac{\partial L(\omega, b, e, \alpha)}{\partial b} = 0 \longrightarrow \sum_{k=1}^{N}\alpha_k = 0,\\
&\frac{\partial L(\omega, b, e, \alpha)}{\partial e_k} = 0 \longrightarrow \alpha_k = \gamma e_k, k = 1, 2, \cdots, N,\\
&\frac{\partial L(\omega, b, e, \alpha)}{\partial \alpha_k} = 0 \longrightarrow y_k = \omega^T\varphi(x_k) + b + e_k\, k = 1, 2, \cdots, N,
\end{aligned} \quad (9)$$

In which, $y = [y_1 \cdots y_N]^T$, $\alpha = [\alpha_1 \cdots \alpha_N]^T$, $1_N = [1 \cdots 1]^T$, and I is the identity matrix. Ω_{kl} stands for $\varphi(x_k)^T\varphi(x_l) = K(x_k, x_l)$.

$$\begin{bmatrix} 0 & 1_v^T \\ 1_v & \Omega + \gamma^{-1}I \end{bmatrix}\begin{bmatrix} b \\ \alpha \end{bmatrix} = \begin{bmatrix} 0 \\ y \end{bmatrix}. \quad (10)$$

The LSSVM theory can be arranged in the other form:

$$y(x) = \sum_{k=1}^{N}\alpha_k K(x, x_k) + b. \quad (11)$$

In which, $K(x, x_k)$ is the kernel function that is in the form of radial basis function:

$$K(x_i, x_j) = e^{\left(-\left(\left(\|x_i - x_j\|^2\right)/\sigma^2\right)\right)}, \quad (12)$$

which σ^2 stands for radial basis width which is calculated during the training process. The process of determination of tuning parameters is shown in Figure 2[25]. The particle swarm optimization (PSO) is used for the determination of these parameters.

2.4. Particle Swarm Optimization. For the first time, the PSO algorithm was developed by Eberhart [26]. The main end of this approach is the determination of best conditions for nonlinear and complex problems. The motion of particles is the fundamental of finding global optimum in this method. Each particle stands for possible answers. During the optimization, the location and velocity of the particle are used. g_{best} is known as the optimum solution from this algorithm, and p_{best} is the best location of the particle in the defined domain. The below formulations

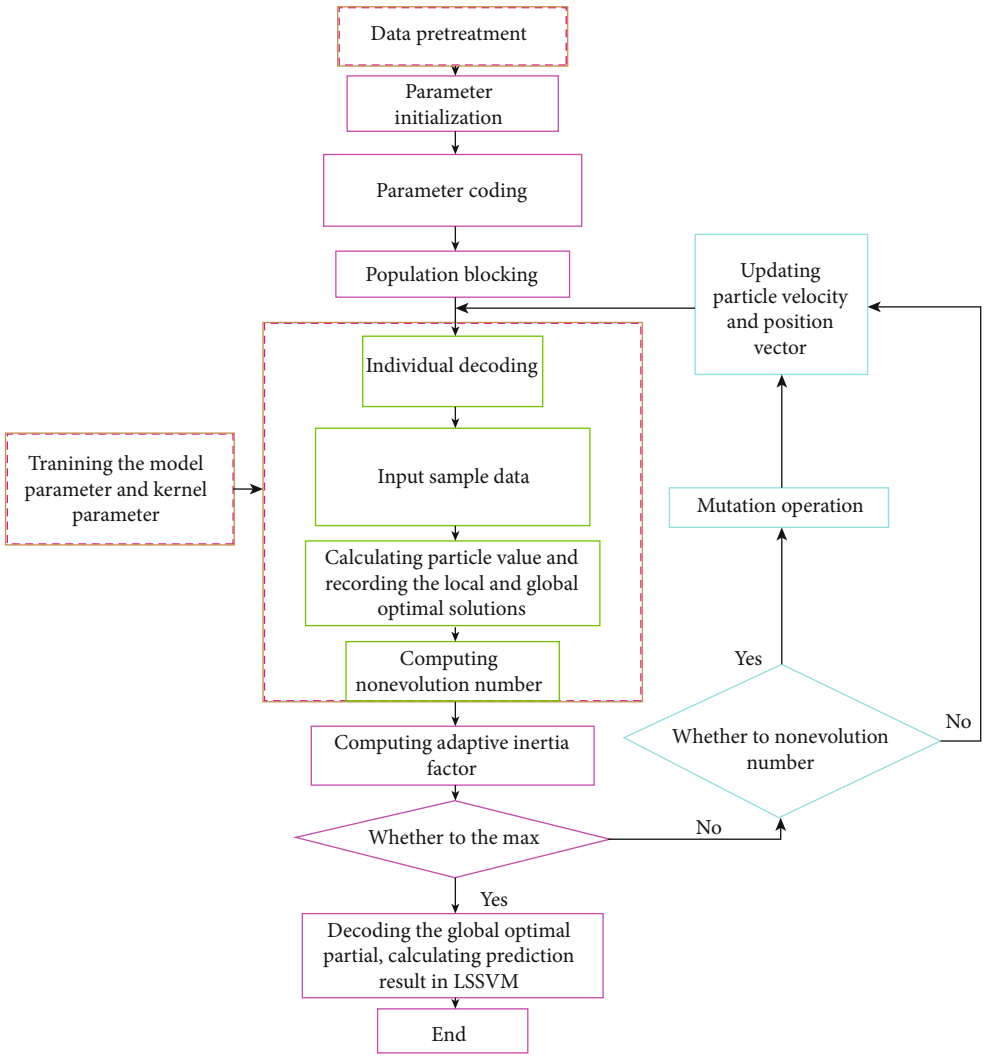

Figure 2: Structure LSSVM-PSO approach.

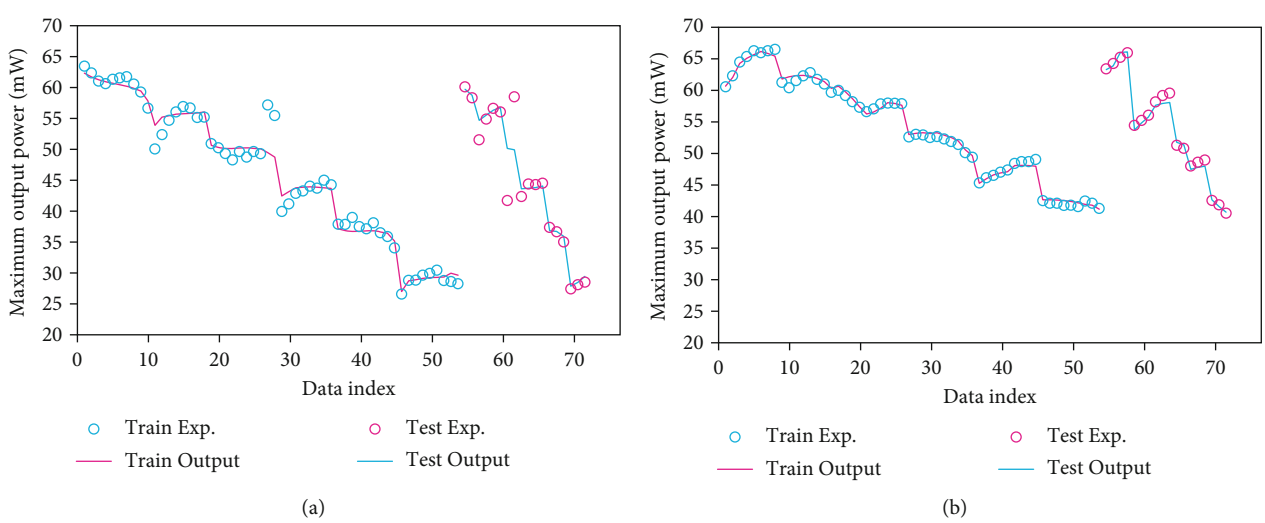

Figure 3: The predicted maximum output power by ANFIS for (a) monocells and (b) multicells.

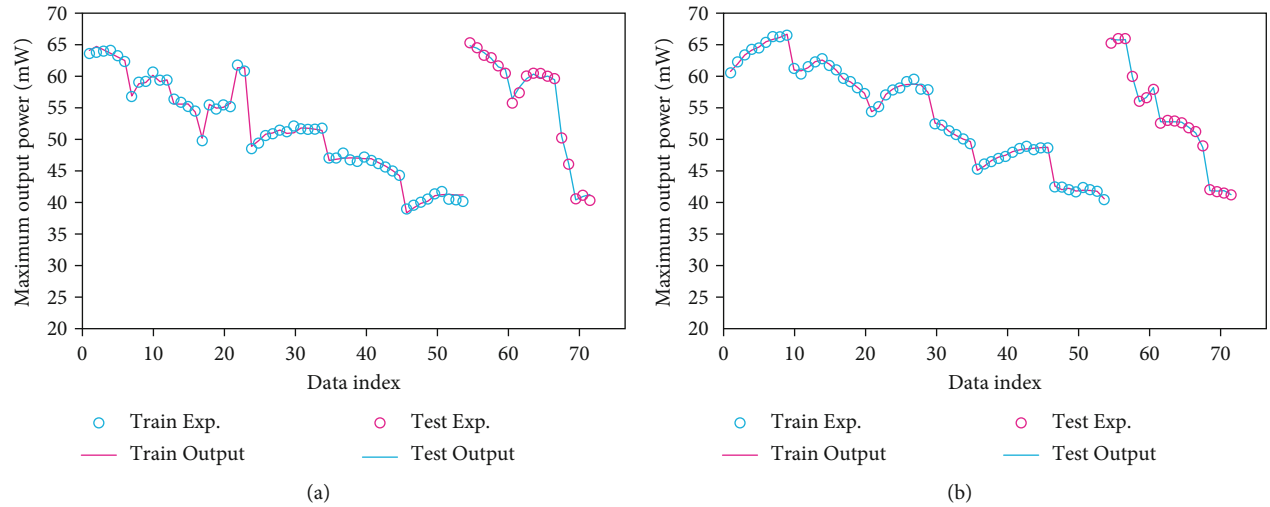

Figure 4: The predicted maximum output power by LSSVM for (a) monocells and (b) multicells.

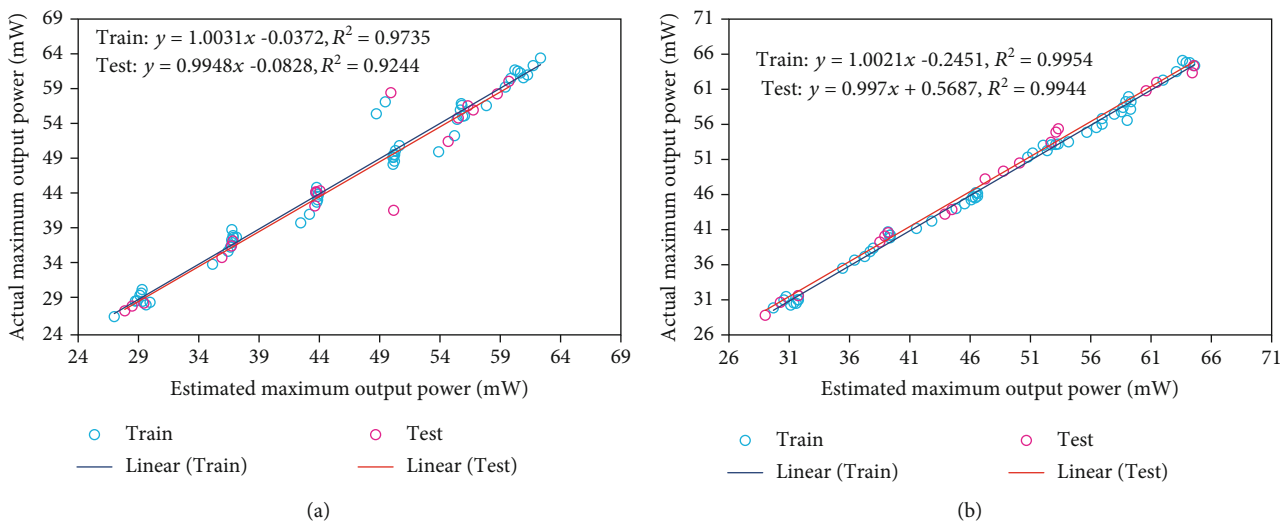

Figure 5: The cross plot of experimental and predicted maximum output power by ANFIS for (a) monocells and (b) multicells.

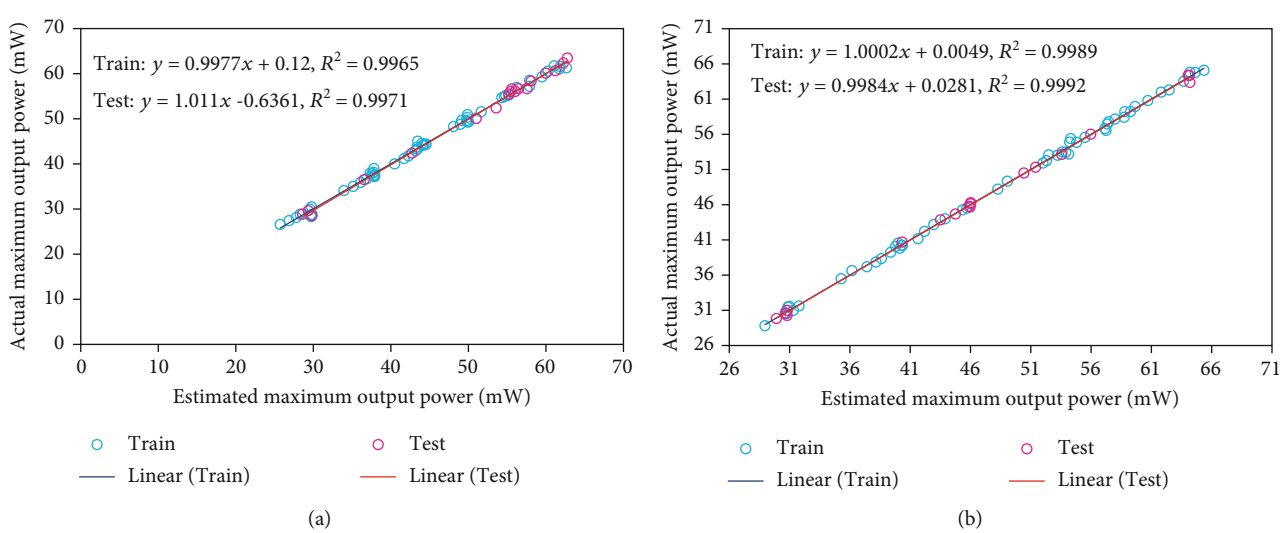

Figure 6: The cross plot of experimental and predicted maximum output power by LSSVM for (a) monocells and (b) multicells.

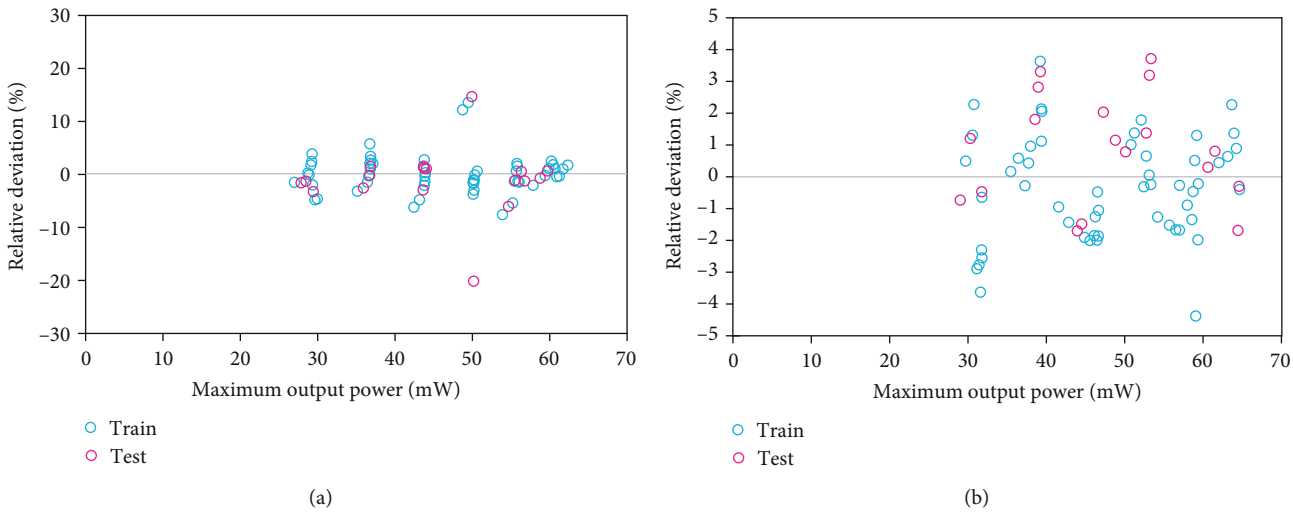

Figure 7: The relative deviation between experimental and predicted maximum output power by ANFIS for (a) monocells and (b) multicells.

show the ways that particle location and velocity are determined:

$$X_{\text{pd}}^{\text{iter}+1} = X_{\text{pd}}^{\text{iter}} + V_{\text{pd}}^{\text{iter}+1},$$

$$v_{\text{id}}(t+1) = wv_{\text{id}}(t) + c_1 r_1 \left(p_{\text{best,id}}(t) - X_{\text{iid}}(t)\right) + c_2 r_2 \left(g_{\text{best},d}(t) - X_{\text{id}}(t)\right). \quad (13)$$

$Vi(t)$ and $Xi(t)$ stand for the velocity and position of the particle, respectively. c_1 and c_2 show the learning terms which can control the speed of the particle. w is used as a connection between previous velocity and current value. r_1 and r_2 are random values between 0 and 1 [27, 28]. There are other optimization algorithms in the literature. Genetic algorithm (GA) and hybrid of GA and PSO (HGAPSO) are well-known algorithms which can be used for optimization of LSSVM and ANFIS algorithms. Their combinations with these predictive tools create great models for the prediction of different processes in the industries [24, 25].

3. Results and Discussion

In the present part, the outputs of models and experimental output powers for these two types of cells are compared to ensure the accuracy and ability of models. To this end, graphical and statistical comparisons are carried. First, for graphical comparison, the simultaneous illustrations of predicted and actual output power for monocells and multicells are shown in Figures 3 and 4 for ANFIS and LSSVM models, respectively. These comparisons show that models outputs have an agreement with experimental values.

The cross plots for these models are depicted in Figures 5 and 6. The regression lines for monocells and multicells show that they have similar equations to $y = x$ line. The coefficients of determination parameters for these lines are near one. Therefore, the accuracy of proposed models in the determination of output power is acceptable. The details of discussing lines are shown in Figures 5 and 6. The compaction of output power data points near the bisector shows that models have enough accuracy in the determination of output power.

The relative deviation between predicted and experimental values for ANFIS and LSSVM models is shown in Figures 7 and 8. The concentration of relative deviations around the x-axis line shows that the proposed models have great accuracy in the wide range of output powers. As a noticeable point, the trained models have better accuracy in the prediction of output power values for multicells. The best performance belongs to the LSSVM algorithm for the prediction of multicell with a relative error lower than 2 percent.

The coefficients of determination (R^2), mean relative error (MRE), mean squared errors (MSEs), relative mean squared errors (RMSEs), and Standard deviations (STDs) are formulated as below [29–31]:

$$R^2 = 1 - \frac{\sum_{i=1}^{N}\left(X_i^{\text{actual}} - X_i^{\text{predicted}}\right)^2}{\sum_{i=1}^{N}\left(X_i^{\text{actual}} - \overline{X^{\text{actual}}}\right)^2},$$

$$\text{MRE} = \frac{100}{N}\sum_{i=1}^{N}\left|X_i^{\text{predicted}} - X_i^{\text{actual}}\right|,$$

$$\text{MSE} = \frac{100}{N}\sum_{i=1}^{N}\left(X_i^{\text{actual}} - X_i^{\text{predicted}}\right)^2, \quad (14)$$

$$\text{RMSE} = \sqrt{\frac{100}{N}\sum_{i=1}^{N}\left(X_i^{\text{actual}} - X_i^{\text{predicted}}\right)^2},$$

$$\text{STD}_{\text{error}} = \left(\frac{1}{N-1}\sum_{i=1}^{N}\left(\text{error} - \overline{\text{error}}\right)\right)^{0.5}.$$

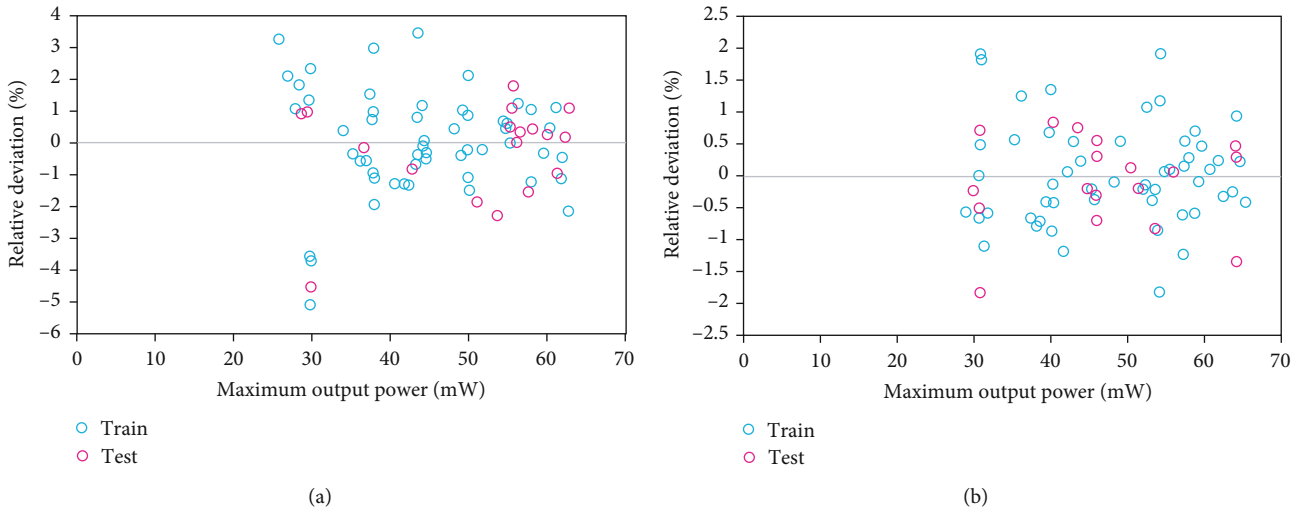

Figure 8: The relative deviation between experimental and predicted maximum output power by LSSVM for (a) monocells and (b) multicells.

Table 1: Statistical evaluations of models.

			R^2	MRE (%)	MSE	RMSE	STD
Monocell	LSSVM	Train	0.997	1.232	0.37366882	0.6113	0.3621
		Test	0.997	1.097	0.413593905	0.6431	0.4053
		Total	0.997	1.198	0.383650091	0.6431	0.3705
Multicell		Train	0.999	0.617	0.131896651	0.3632	0.2304
		Test	0.999	0.570	0.104762187	0.3237	0.2049
		Total	0.999	0.605	0.125113035	0.3237	0.2232
Monocell	ANFIS	Train	0.973	2.496	3.282398807	1.8117	1.4126
		Test	0.924	3.460	8.918576686	2.9864	2.5967
		Total	0.962	2.737	4.691443277	2.9864	1.7726
Multicell		Train	0.995	1.370	0.573499732	0.7573	0.4360
		Test	0.994	1.603	0.860051592	0.9274	0.5437
		Total	0.995	1.428	0.645137697	0.9274	0.4652

Determination of above parameters shows the accuracy of models in the prediction of the output power of photovoltaic cells. The calculated parameters are inserted in Table 1.

As can be seen, the LSSVM model has better accuracy in comparison with the ANFIS model. The determined R^2 values for monocell and multicell are 0.997 and 0.999 for LSSVM, respectively. The calculated R^2 values of ANFIS model are reported 0.962 and 0.995 for monocell and multicell, respectively. Moreover, the MSE values of LSSVM are 0.3836 and 0.1251 for monocell and multicell, respectively. The MSE values of 4.6914 and 0.6451 are reported for monocell and multicell, respectively. Furthermore, the other error parameters are very low for the LSSVM model. Therefore, the accuracy and performance of this algorithm are acceptable for the estimation of the output power of photovoltaic cells. Xiao et al. used the different structure of ANN algorithms for the estimation of output power. The best predictive structures for their work had 8 and 9 hidden layer unit with an average correlation coefficient of 0.97 and 0.988 for monocrystalline and multicrystalline. Our proposed models have better performance than these ANN-based methods [10].

One of the well-known analyses which are carried in this study is the estimation of the relevancy factor for inputs. The relevancy factor describes the impacts of the considered input parameter on the output power of photovoltaic cells. This factor can be formulated as below [25, 32]:

$$r = \frac{\sum_{i=1}^{n}\left(X_{k,i} - \overline{X_k}\right)\left(Y_i - \bar{Y}\right)}{\sqrt{\sum_{i=1}^{n}\left(X_{k,i} - \overline{X_k}\right)^2 \sum_{i=1}^{n}\left(Y_i - \bar{Y}\right)^2}}. \quad (15)$$

Herein, Y_i, $\bar{Y}$, $X_{k,i}$, and $\overline{X_k}$ stand for the "i" th output, output average, kth of input, and average of inputs [21]. The estimated relevancy factor for each input is demonstrated in Figure 9 which shows that the most effective parameter on the output power of cells is light intensity with r value of

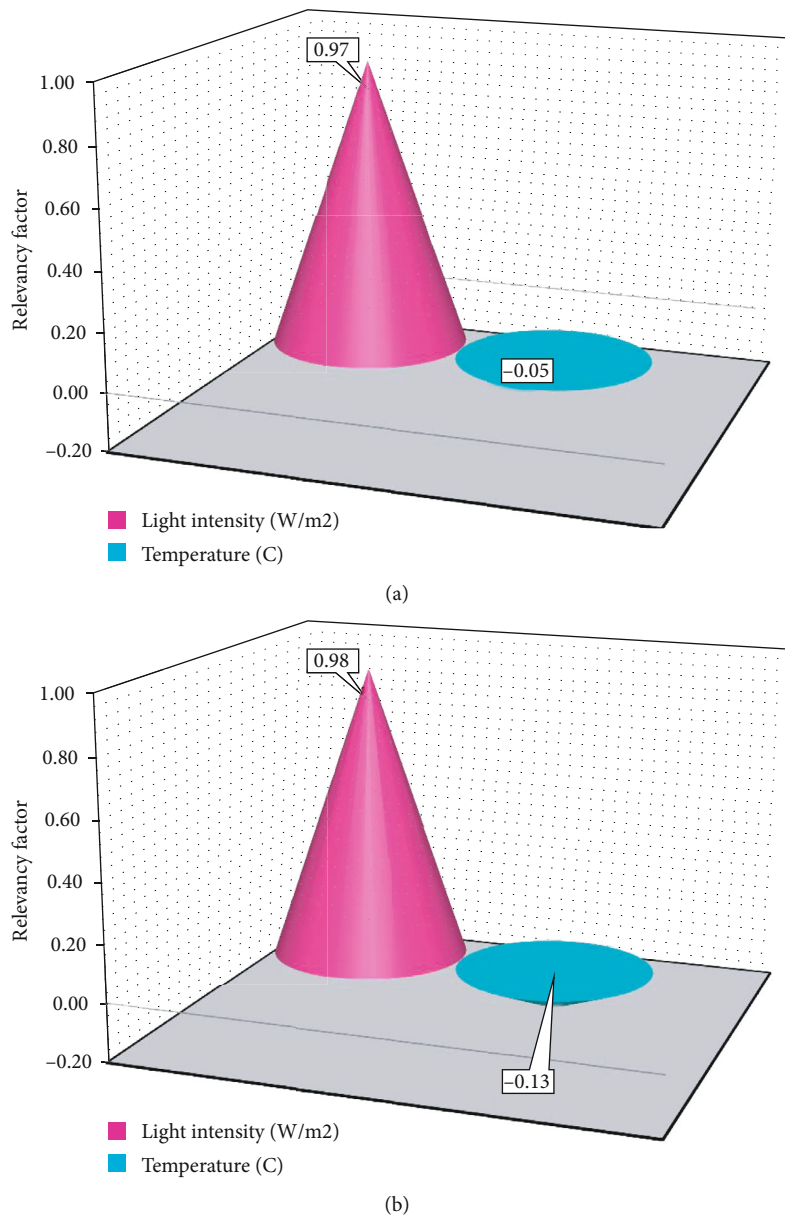

Figure 9: Impacts of input parameters on output power of (a) monocells and (b) multicells.

0.97. Additionally, the values of output power will increase if light intensity increases. On the other hand, the negative values of the relevancy factor for temperature show that there is a reverse relationship between temperature and output power.

4. Conclusions

In this work, two artificial intelligence methods based on ANFIS-PSO and LSSVM-PSO have been developed to determine the output power of two types of photovoltaic cells. The employed models show great accuracy in graphical and statistical comparisons. The coefficients of determination (R^2) of monocrystalline cell output power for LSSVM and ANFIS models are determined as 0.997 and 0.962, respectively. Additionally, multicells have R^2 values of 0.999 and 0.995 for LSSVM and ANFIS, respectively. The lower error values show that the present models have great accuracy in the prediction of cell output power. The graphical comparisons are also employed to the better demonstration of agreement between predicted and actual output power values. After that, a sensitivity analysis has been carried out to show the relationship of input parameters and output power of these cells. According to the obtained results, the present work provides useful information about the determination of output power for different types of cells. The suggested models can determine this parameter by consuming the least time and cost. The main limitation of these methods is that they need a comprehensive dataset for training models and obtaining tuning parameters. If a limited number of experimental data points are used in the training phase, the performance of the model in determination of unseen conditions will be limited.

According to this fact, a comprehensive and large experimental databank which covers a wide range of operational conditions should be provided.

Data Availability

The data that support the findings of this study are available from the corresponding author, upon reasonable request.

Conflicts of Interest

The authors declare no conflicts of interest.

Acknowledgments

The study is financially supported by the Key research project of Guangdong University of Science & Technology in 2020: Algorithm Research on smart Grid Power Supply Restoration (GKY-2020KYZDK-3).

References

[1] X. Hu, Y. Zou, and Y. Yang, "Greener plug-in hybrid electric vehicles incorporating renewable energy and rapid system optimization," *Energy*, vol. 111, pp. 971–980, 2016.

[2] J.-T. Liu, X.-H. Deng, W. Yang, and J. Li, "Perfect light trapping in nanoscale thickness semiconductor films with a resonant back reflector and spectrum-splitting structures," *Physical Chemistry Chemical Physics*, vol. 17, no. 5, pp. 3303–3308, 2015.

[3] G. K. Singh, "Solar power generation by PV (photovoltaic) technology: a review," *Energy*, vol. 53, pp. 1–13, 2013.

[4] M. N. Akhter, S. Mekhilef, H. Mokhlis, and N. M. Shah, "Review on forecasting of photovoltaic power generation based on machine learning and metaheuristic techniques," *IET Renewable Power Generation*, vol. 13, no. 7, pp. 1009–1023, 2019.

[5] G. Sadeghi, M. Najafzadeh, and M. Ameri, "Thermal characteristics of evacuated tube solar collectors with coil inside: an experimental study and evolutionary algorithms," *Renewable Energy*, vol. 151, pp. 575–588, 2020.

[6] G. Sadeghi, M. Najafzadeh, and H. Safarzadeh, "Utilizing gene-expression programming in modelling the thermal performance of evacuated tube solar collectors," *Journal of Energy Storage*, vol. 30, p. 101546, 2020.

[7] M. N. Akhter, S. Mekhilef, H. Mokhlis, L. Olatomiwa, and M. A. Muhammad, "Performance assessment of three grid-connected photovoltaic systems with combined capacity of 6.575 kW_p in Malaysia," *Journal of Cleaner Production*, vol. 277, 2020.

[8] K. Gajowniczek and T. Ząbkowski, "Electricity forecasting on the individual household level enhanced based on activity patterns," *PLoS One*, vol. 12, no. 4, 2017.

[9] X. Wu, X. Hu, S. Moura, X. Yin, and V. Pickert, "Stochastic control of smart home energy management with plug-in electric vehicle battery energy storage and photovoltaic array," *Journal of Power Sources*, vol. 333, pp. 203–212, 2016.

[10] W. Xiao, G. Nazario, H. Wu, H. Zhang, and F. Cheng, "A neural network based computational model to predict the output power of different types of photovoltaic cells," *PLoS One*, vol. 12, no. 9, 2017.

[11] A. Mellit and S. A. Kalogirou, "Artificial intelligence techniques for photovoltaic applications: a review," *Progress in Energy and Combustion Science*, vol. 34, no. 5, pp. 574–632, 2008.

[12] Z. Lei, W. Zhenpo, H. Xiaosong, and D. G. Dorrell, "Residual capacity estimation for ultracapacitors in electric vehicles using artificial neural network," *IFAC Proceedings Volumes*, vol. 47, no. 3, pp. 3899–3904, 2014.

[13] D. A. Fadare, "Modelling of solar energy potential in Nigeria using an artificial neural network model," *Applied Energy*, vol. 86, no. 9, pp. 1410–1422, 2009.

[14] E. Izgi, A. Öztopal, B. Yerli, M. K. Kaymak, and A. D. Şahin, "Short–mid-term solar power prediction by using artificial neural networks," *Solar Energy*, vol. 86, no. 2, pp. 725–733, 2012.

[15] E. F. Fernández, F. Almonacid, N. Sarmah, P. Rodrigo, T. K. Mallick, and P. Pérez-Higueras, "A model based on artificial neuronal network for the prediction of the maximum power of a low concentration photovoltaic module for building integration," *Solar Energy*, vol. 100, pp. 148–158, 2014.

[16] M. Najafzadeh and H. M. Azamathulla, "Neuro-fuzzy GMDH to predict the scour pile groups due to waves," *Journal of Computing in Civil Engineering*, vol. 29, no. 5, 2015.

[17] M. Najafzadeh, A. Etemad-Shahidi, and S. Y. Lim, "Scour prediction in long contractions using ANFIS and SVM," *Ocean Engineering*, vol. 111, pp. 128–135, 2016.

[18] M. Najafzadeh and A. Zahiri, "Neuro-fuzzy GMDH-based evolutionary algorithms to predict flow discharge in straight compound channels," *Journal of Hydrologic Engineering*, vol. 20, no. 12, 2015.

[19] J.-S. R. Jang, C.-T. Sun, and E. Mizutani, "Neuro-fuzzy and soft computing-a computational approach to learning and machine intelligence [book review]," *IEEE Transactions on Automatic Control*, vol. 42, no. 10, pp. 1482–1484, 1997.

[20] J.-S. R. Jang, "ANFIS: adaptive-network-based fuzzy inference system," *IEEE Transactions on Systems, Man, and Cybernetics*, vol. 23, no. 3, pp. 665–685, 1993.

[21] A. Bemani, A. Baghban, and A. H. Mohammadi, "An insight into the modeling of sulfur content of sour gases in supercritical region," *Journal of Petroleum Science and Engineering*, vol. 184, p. 106459, 2020.

[22] R. Daneshfar, A. Bemani, M. Hadipoor et al., "Estimating the heat capacity of non-Newtonian ionanofluid systems using ANN, ANFIS, and SGB tree algorithms," *Applied Sciences*, vol. 10, no. 18, p. 6432, 2020.

[23] K. Pelckmans, J. A. Suykens, T. Van Gestel et al., "LS-SVMlab: a matlab/c toolbox for least squares support vector machines," in *Tutorial*, KULeuven-ESAT, Leuven, Belgium, 2002.

[24] A. Bemani, Q. Xiong, A. Baghban, S. Habibzadeh, A. H. Mohammadi, and M. H. Doranehgard, "Modeling of cetane number of biodiesel from fatty acid methyl ester (FAME) information using GA-, PSO-, and HGAPSO- LSSVM models," *Renewable Energy*, vol. 150, pp. 924–934, 2020.

[25] R. Razavi, A. Bemani, A. Baghban, and A. H. Mohammadi, "Modeling ofCO2absorption capabilities of amino acid solutions using a computational scheme," *Environmental Progress & Sustainable Energy*, vol. 39, no. 6, 2020.

[26] R. Eberhart and J. Kennedy, "A new optimizer using particle swarm theory, MHS'95," *Proceedings of the Sixth International Symposium on Micro Machine and Human Science*, 1995, pp. 39–43, Nagoya, Japan, 1995.

[27] J.-S. Chiou, S.-H. Tsai, and M.-T. Liu, "A PSO-based adaptive fuzzy PID-controllers," *Simulation Modelling Practice and Theory*, vol. 26, pp. 49–59, 2012.

[28] Y. Shi and R. Eberhart, "A modified particle swarm optimizer," in *1998 IEEE International Conference on Evolutionary Computation Proceedings. IEEE World Congress on Computational Intelligence (Cat. No.98TH8360)*, pp. 69–73, Anchorage, AK, USA, 1998.

[29] M. Najafzadeh and F. Saberi-Movahed, "GMDH-GEP to predict free span expansion rates below pipelines under waves," *Marine Georesources & Geotechnology*, vol. 37, no. 3, pp. 375–392, 2019.

[30] M. Najafzadeh, F. Saberi-Movahed, and S. Sarkamaryan, "NF-GMDH-based self-organized systems to predict bridge pier scour depth under debris flow effects," *Marine Georesources & Geotechnology*, vol. 36, no. 5, pp. 589–602, 2018.

[31] F. Saberi-Movahed, M. Najafzadeh, and A. Mehrpooya, "Receiving more accurate predictions for longitudinal dispersion coefficients in water pipelines: training group method of data handling using extreme learning machine conceptions," *Water Resources Management*, vol. 34, no. 2, pp. 529–561, 2020.

[32] E. Khamehchi and A. Bemani, "Prediction of pressure in different two-phase flow conditions: machine learning applications," *Measurement*, vol. 173, 2021.

Hindawi
International Journal of Photoenergy
Volume 2021, Article ID 5512679, 15 pages
https://doi.org/10.1155/2021/5512679

Research Article

Numerical Performance Investigation of Parabolic Dish Solar-Assisted Cogeneration Plant Using Different Heat Transfer Fluids

Muhammad Sajid Khan,[1,2] Muhammad Abid,[3] Khuram Pervez Amber,[2] Hafiz Muhammad Ali,[4] Mi Yan,[1] and Samina Javed[5]

[1]*Institute of Energy and Power Engineering, Zhejiang University of Technology, Hangzhou, Zhejiang 310014, China*
[2]*Department of Mechanical Engineering, Mirpur University of Science and Technology (MUST), Mirpur 10250 (AJK), Pakistan*
[3]*Department of Energy Systems Engineering, Faculty of Integrated Technologies, Universiti Brunei Darussalam, Jalan Tungku Link BE 1410, Bandar Seri Begawan, Brunei Darussalam*
[4]*Mechanical Engineering Department, King Fahd University of Petroleum & Minerals (KFUPM), Dhahran 31261, Saudi Arabia*
[5]*Department of Mechanical Engineering, University of Engineering and Technology, Taxila 47050, Pakistan*

Correspondence should be addressed to Hafiz Muhammad Ali; hafiz.ali@kfupm.edu.sa

Received 6 February 2021; Revised 27 March 2021; Accepted 13 April 2021; Published 28 April 2021

Academic Editor: Regina De Fátima Peralta Muniz Moreira

Copyright © 2021 Muhammad Sajid Khan et al. This is an open access article distributed under the Creative Commons Attribution License, which permits unrestricted use, distribution, and reproduction in any medium, provided the original work is properly cited.

Parabolic dish solar collectors gain higher solar to thermal conversion efficiency due to their maximum concentration ratio. The present research focuses by integrating the parabolic dish solar collector to the steam cycle producing power and rate of process heating. Pressurized water, therminol VP1, and supercritical carbon dioxide are the examined working fluids in the parabolic dish solar collector. The aim of the current research is to observe the optimal operating conditions for each heat transfer fluid by varying inlet temperature and flow rate of the working fluid in the parabolic dish solar collector, and combination of these parameters is predicted to lead to the maximum energy and exergy efficiencies of the collector. The operating parameters are varied to investigate the overall system efficiencies, work output, and process heating rate. Findings of the study declare that water is an efficient heat transfer fluid at low temperature levels, whereas therminol VP1 is effective for a higher temperature range. The integrated system efficiencies are higher at maximum flow rates and low inlet temperatures. The efficiency map of solar collector is located at the end of study, and it shows that maximum exergy efficiency gains at inlet temperature of 750 K and it is observed to be 37.75%.

1. Introduction

Renewable energy resources are considered the best alternative solutions to address the severe ecological problems created due to the consumption of fossil fuels [1]. Although there are various types of renewable energy resources (geothermal, solar, and wind etc.), solar energy is a unique choice as it is available abundantly [2]. Concentrating solar systems, also known as concentrated solar power (CSP) technologies, gain more interest due to their useful heat production at elevated temperatures. Particularly, dish solar collectors are an efficient source that converts solar energy into useful thermal energy and also attain maximum thermal efficiency due to higher concentration ratio [3]. Its operation relies on the concentration of solar radiations onto a small receiver where it exchanges heat with the working fluid. The application of the cavity receiver has been noticed to be a very useful technique as solar radiations are properly centered on parabolic solar dishes [4]. The useful heat gain from solar dish collectors can be used as an input source for dryers, hydrogen production systems, and Rankine and Brayton cycles [5, 6].

The literature consists of both numerical and experimental works regarding parabolic dish cavity receivers. Daabo et al. [7] performed numerical analysis of various parabolic dish cavity receivers to investigate their optical performance. Results indicated that the conical shaped receiver received and absorbed maximum solar radiations per unit area as compared to the others with optical efficiency near to

75.3%. The optimization of the receiver employing optimal methods and CFDs was conducted to examine the most suitable position of the solar receiver on a concentrator collector by Przenzak et al. [8]. The optimized value of fluid flow was calculated to be 0.6 m/s without any overheating of the receiver body, and it also decreased the convection and radiation heat losses. Jilte et al. [9] investigated the dish collector with different cavity shapes mathematically, and research was performed for five inclinations and three different isothermal wall temperatures. The conical cavity receiver showed the lowest convective heat losses as compared to the other investigated receivers. Kaushika and Reddy [10] suggested a method for design and development of a low-cost steam generation system integrated with a parabolic dish (PD) system. Solar to steam conversion efficiency was to found be 70 to 80% at 723 K. Parabolic dish using cavity receiver was numerically modeled and thermally optimized by Loni et al. [11].

Experimental work has been performed to analyze the energetic and exergetic performances of the SK-14 cylindrical cavity solar dish system [12]. Heat loss factor was observed to be 4.6 W/K with 52% optical efficiency under higher solar insulations. Mohammad [13] designed and developed a parabolic dish solar (PDS) water heater for domestic usage. Thermal efficiencies were between 52% and 56% that showed the reliability of the designed system. Reddy et al. [14] carried out an experimental work on a 20 m^2 prototype fuzzy focal dish receiver. Madadi et al. [15] theoretically and experimentally analyzed the energetic and exergetic performances of PDSC. Two different cavity receivers, namely, cylindrical and conical, were taken into account with different parameters. It was observed that almost 35% to 60% of the exergy destroyed was due to the heat transfer from the sun to the receiver. The cylindrical cavity receiver showed better results than the counterpart did.

Furthermore, utilization of heat transfer fluid (HTF) has an immense impact on the efficiency of solar collectors. The most used HTFs in concentrated solar power (CSP) technologies are oil-based, while molten salts are also tested by researchers [16, 17]. Loni et al. [18] conducted a study using different cavity receivers of PDC utilizing water and Behran oil as heat transfer fluids. Another study was conducted by Loni et al. [19] using air as a HTF in a dish collector integrated with organic Rankine cycle (ORC). Khan et al. [20] examined numerically a PD cavity receiver with three different nanofluids, and the dish system was coupled with sCO_2 Brayton cycle to generate electricity. Abid et al. [21] performed an analysis of different sCO_2 recompression Brayton cycles. The heat source was a parabolic dish solar collector using pressurized water. Abid et al. [22] performed another study using different nanofluids and molten salts in parabolic trough and parabolic dish collectors to power a steam cycle.

The other HTFs utilized in the solar collector are the gasses (air, helium, nitrogen, and CO_2) and argon [23]. Supercritical carbon dioxide has attracted a lot of attention due to its extraordinary thermophysical properties. Its critical point is quite low (305 K and 7.8 MPa) that assists properties to enhance in the region adjacent to the triple point. Numerous studies proposed and recommended sCO_2 as a heat transfer medium for higher temperature solar thermal applications [24–27].

Furthermore, the use of nanofluids in the solar collector enhances the rate of heat transfer that also raises the convective heat transfer coefficient, useful heat gain, and thermal efficiency of the solar collector. Mebarek-Oudina [28] numerically investigated laminar stationary natural convection heat transfer of different nanofluids contained in a cylindrical annulus using a discrete heat source. The objective was to investigate the effect of volume fraction, Rayleigh number, and base fluid type on the heat transfer rate. It was concluded that Raileigh number and volume fraction of nanoparticles has an influence on the thermal efficiency and growth rate of the heat transfer. Mebarek-Oudina [29] conducted a numerical investigation of natural convection heat transfer stability in vertical annulus using different heat source lengths. It was observed that heat transfer rates for smaller heater length are higher; however, heat transfer rate decreases by increasing the heater length. Kherbeet et al. [30] reported a numerical study of nanofluid flow and heat transfer of laminar convection flow adjacent to a horizontal and three-dimensional microscale forward facing step. It showed that the forward facing step increased the heat transfer, while Nusselt number also enhanced with rise in step height. Abbassi et al. [31] carried out a parametric investigation of a nanofluid-filled incinerator with a rectangular hot block on the bottom to evaluate the influence of different parameters (nanoparticle volume fraction, Rayleigh number, external magnetic intensity, etc.). It was concluded that increasing the width and height of the heater also enhanced the entropy generation but it has been reduced by increasing the Hartmann number. Goodarazi et al. [32] performed a study on the non-Newtonian nanofluid flow of carboxymethyl cellulose-aluminum oxide in a microtube. The aim was to explore the presence of nanoparticles and phenomenon of slip and temperature jump. Olia et al. [33] stated the modern developments on the applications of nanofluids for heat transfer fluid in parabolic trough solar collectors. It was concluded that nanofluids not only enhance the exergy efficiency, energy efficiency, and convective heat transfer coefficient but also mitigate the entropy generation of the system.

Gheynani et al. [34] examined the influence of nanoparticle concentration and diameter on the different heat transfer properties of non-Newtonian carboxymethyl cellulose/CuO fluid in a microtube using numerical simulation with the finite volume method. Taner [35] presented a bulgur drying plant based on the bulgur mass, temperature, and moisture for optimum production. Uncertainty analysis was carried out for data accuracy. The drying process energy and exergy efficiencies were found to be 24.95% and 44.05%, respectively. Taner [36] carried out an experimental optimization of a PEM fuel cell to enhance the efficiency and development of the simulations and modeling of PEM fuel cell. The first and second law efficiencies were almost 47.6% and 50.4%, respectively.

Topal et al. [37] performed a thermodynamic analysis of a trigeneration system that converted a single-fuel source into power, heating, and cooling and concentrated on the

simulation of such systems to a direct cocombustion of poultry wastes. It was found that cocombustion of poultry waste was the best environment-friendly remedy to put away wastes. Topal et al. [38] conducted a thermodynamic analysis of a can circulating fluidized bed power plant cofired with olive pits and to check the effect on exergy destruction and carbon dioxide emissions. Total exergy destruction of the plant was found to be 295 MW with 31.26% exergy efficiency. Taner and Sivrioglu [39] developed a general model for technoeconomic and cost analysis of a turbine power plant. Simple payback period and unit cost for turbine power plant were calculated as 4.32 years and 3.142 $/kW, respectively.

It is presented that there are many studies about the performance investigation of parabolic dish solar collector but there is lack of studies where both liquid and gas phase substances are evaluated simultaneously for their first and second law analyses. The aim of the present research is to examine in detail the energy and exergy efficiencies of PDSC using therminol VP1, pressurized water, and sCO_2 as heat transfer fluids. The thermal energy produced by the collector is further utilized to power a regenerative steam cycle for the purpose of electricity generation and rate of process heat. Therminol VP1 is a eutectic mixture of diphenyl oxide (DPO) and biphenyl. It can be used as a liquid heat transfer fluid or as a boiling-condensing heat transfer medium up to its maximum temperature. Various inlet temperature levels and mass flow rates are investigated to evaluate the work output, process heat rate, integrated efficiencies, and collector efficiencies of the solar integrated cogeneration plant. Different combinations of temperature and flow rate are tested for each heat transfer fluid, and at the end, a unique method of solar efficiency map is presented to depict the efficiencies of the solar receiver. The map shows the optimal conditions for the three HTFs exergetically and thermally with different operating temperature levels.

1.1. System Description. The proposed parabolic solar dish-integrated Rankine cycle producing electricity and rate of process heat is presented in Figure 1. Solar radiations from the sun and incidences on the aperture are reflected to the cavity receiver. The HTFs circulating inside the receiver takes the collected heat from the receiver. The high-temperature fluid at about 650 K moves to the boiler of steam cycle (point 9). The heated fluid transfers its heat to the water entering the boiler (point 5), circulating to the collector at relatively low temperature (point 10). Steam at higher pressure and higher temperature expands after passing through the turbine of a cogeneration plant (point 6). A small fraction ($1/4^{th}$) of steam is extracted from the turbine (point 7) for process heating, while the remaining enters into the turbine to be expanded in the turbine (state point 8). The state of the liquid at the exit of the condenser is saturated, is pressurized using pump 1, and enters into the feed water heater (FWH) at higher pressure. A fraction of the steam after process heater (point 3) merges with the pressurized water in the feed water heater (FWH) and the mixture is pumped again towards the boiler for further process.

2. Methodology and Thermodynamic Analysis

The present section of the work is related to the mathematical equations, used for the thermodynamic modeling of PD solar receiver and regenerative Rankine cycle. Table 1 shows the input design parameters for the above said systems. A validated numerical mathematical model is developed with the help of the engineering equation solver (EES) [40]. The parabolic dish system presented in the present research is taken from Abid et al. [41], whereas Rankine cycle is adopted from [42]. The complete detail of both the systems can be found in the respective references.

2.1. First and Second Law Analyses of Solar Parabolic Dish Collector. The performance of the solar collector has an important role, and it is closely associated with the useful heat gain by the collector. The useful energy can be calculated using the following two equations:

$$\dot{Q}_u = \dot{m}C_p(T_{\text{out}} - T_{\text{in}}), \tag{1}$$

$$\dot{Q}_u = hA_{ri}\left(T_r - T_{fm}\right). \tag{2}$$

Amount of the solar energy available to the collector can be determined by

$$\dot{Q}_{\text{sun}} = G_b A_a. \tag{3}$$

The heat transfer coefficient (h) between the working fluid in the solar collector and the receiver tube in equation (2) can be calculated using Nusselt number:

$$N_u = \frac{h.D_h}{k}. \tag{4}$$

Reynolds number is given by.

$$R_e = \frac{4\,\dot{m}}{\mu\,\pi D_{ri}}. \tag{5}$$

Gnielinski's correlation [43] for turbulent flow ($3000 \le R_e \le 5 \times 10^6$ and $0.5 \le P_r \le 2000$) is

$$N_U = \frac{(R_e - 1000)P_r(f_r/8)}{1 + 12.8\left(\sqrt{(f_r/8)}\right)\left(P_r^{0.68} - 1\right)}. \tag{6}$$

The Prandtl number [44] and friction factor are evaluated as

$$P_r = \frac{\mu\,C_p}{k}, \qquad f_r = (0.790\ \ln - 1.64)^{-2}. \tag{7}$$

The energy efficiency of the dish collector is given by

$$\eta_{\text{en,PDSC}} = \frac{\dot{Q}_u}{\dot{Q}_{\text{sun}}}. \tag{8}$$

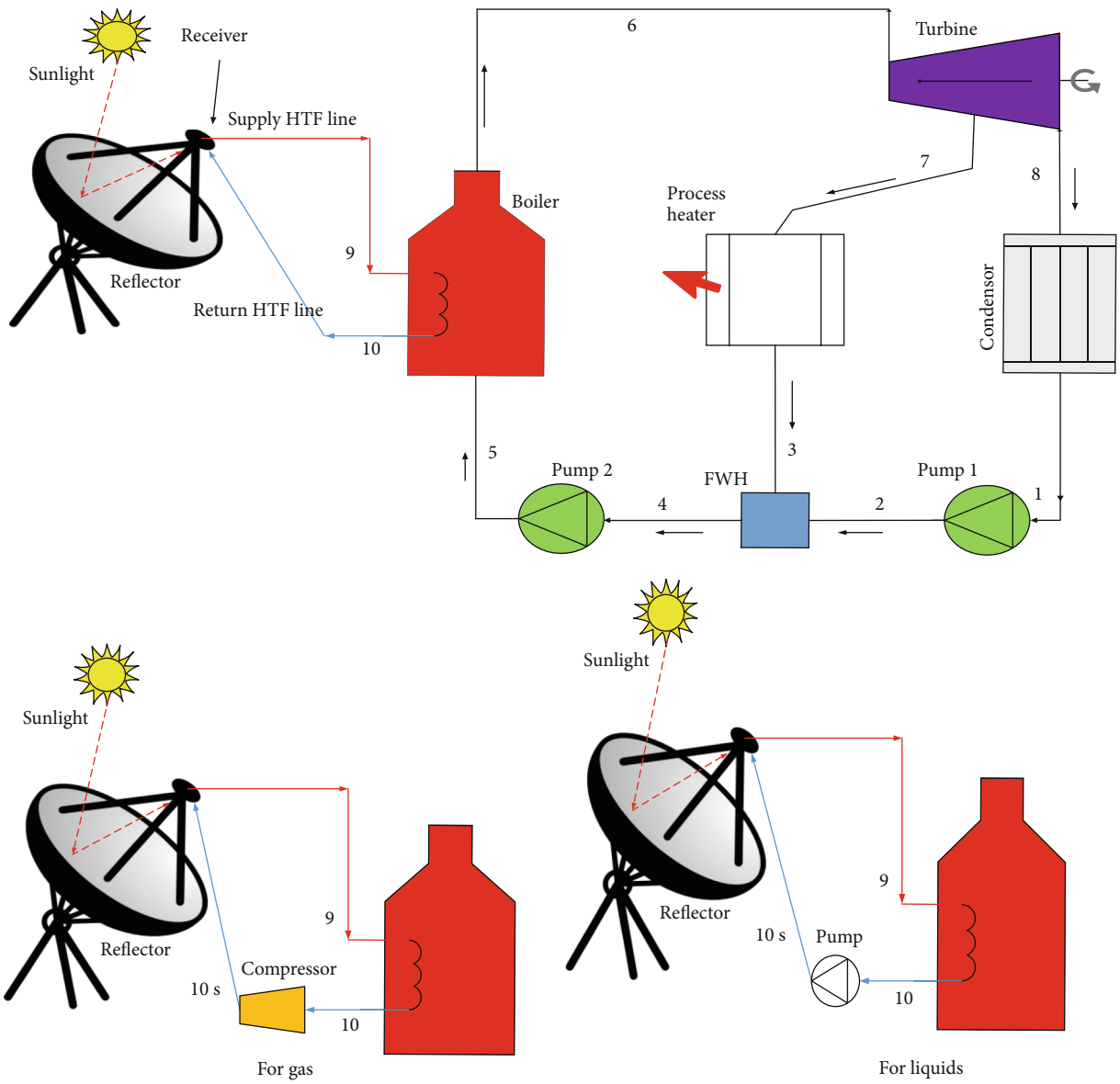

Figure 1: Schematic diagram of the proposed parabolic dish solar integrated cogeneration plant.

Another crucial parameter that is required to be determined is the output exergy of the solar receiver that is presented in equation (9). Exergy is the maximum possible work available from any process [45]. Equation (9) considers different parameters such as useful heat available, pressure losses, mass flow rate, and temperature [46].

$$\dot{E}_{x,u} = \dot{Q}_u - \dot{m}C_p T_{\text{amb}} \ln\left[\frac{T_{\text{out}}}{T_{\text{in}}}\right] - \dot{m}T_{\text{amb}} \frac{\Delta P}{\rho_{fm} T_{fm}}. \tag{9}$$

The Petela model is the most established model to calculate the rate of solar exergy.

$$E_{x,\text{sun}} = G_b A_a \eta_{\text{pet}},$$
$$\eta_{\text{pet}} = \left[1 - \frac{4T_0}{3T_{\text{sun}}} + \frac{1}{3}\left(\frac{T_0}{T_{\text{sun}}}\right)^4\right]. \tag{10}$$

Finally, exergy efficiency is found using exergy ratio between useful exergy and exergy of the sun.

$$\eta_{\text{Ex,PDSC}} = \frac{\dot{E}_{x,u}}{E_{x,sun}}. \tag{11}$$

The receiver's exergy destruction can be found using the below relation.

Table 1: Investigated system characteristics [41, 42].

η_o	85%
ε_r	90%
$\dot{m}$ (in solar collector)	0.02 kg/sec
G_b	1000 W/m^2
T_{in}	350 K
T_r	540 K
V_{air}	1 m/sec
T_a=T_0	300 K
Outer and inner diameters of receiver tube	0.15 m & 0.015 m
Radius of dish, R	1.33 m
L	15 m
T_s	5700 K
A_{ap}	5.56 m^2
C_{rat}	337
Insulation thickness	0.02 m
Steam mass flow rate through Rankine cycle	1 kg/sec
$\eta_{\text{tur}} = \eta_{\text{pump}}$	0.8
T_{TIT} & P_{TIT}	773 K & 4000 kPa
Temperature and pressure of sCO$_2$ in collector	314-673 K & 10,000 kPa

$$\dot{\psi}_{x,\text{des},\Delta_p} = T_a \frac{\dot{m}\Delta_p}{p} \frac{\ln\left(T_{\text{out}}/T_{\text{in}}\right)}{T_{\text{out}} - T_{\text{in}}} \tag{12}$$

The heat gain of solar system is determined by the famous Hottel-Whillier equation [47].

$$\dot{Q}_u = F_r A_r \left[\left(S - \frac{A_r}{A_a}\right) U_L((T_{\text{in}} - T_a)\right], \tag{13}$$

whereas heat removal factor and collector efficiency factor are summarized as

$$F_R = \frac{\dot{\text{m}}C_P}{A_r U_L}\left[1 - \exp\left(\frac{-A_r U_L F_1}{\dot{\text{m}}C_P}\right)\right], \quad F_1 = \frac{U_0}{U_L}. \tag{14}$$

2.2. Energetic and Exergetic Analyses of Rankine Cycle. Enthalpy is one of the most important parameters for steam cycle analysis. It is necessary to first calculate the enthalpy at each state of the system to calculate the rest of the output parameters. The efficiency of turbines is given as

$$\eta_{\text{tur}} = \frac{h_6 - h_7}{h_6 - h_{s,7}}, \quad \eta_{\text{tur}} = \frac{h_6 - h_8}{h_6 - h_{s,8}}. \tag{15}$$

Table 2: Comparison table for three HTFs at three inlet temperature levels.

T_a = 300 K T_{in} = 350 K $\dot{m}_r$ = 0.02 kg/sec	sCO$_2$	Water	Therminol VP1
$\dot{Q}_u$ (kW)	3898	4091	4013
W_{net} (kW)	1104	1159	1137
$\dot{Q}_{\text{pr,heat}}$ (kW)	719.2	754.8	740.4
T_a = 300 K T_{in} = 550 K $\dot{m}_r$ = 0.02 kg/sec	sCO$_2$	Water	Therminol VP1
$\dot{Q}_u$ (kW)	3510	3599	3610
W_{net} (kW)	994.3	1020	1023
$\dot{Q}_{\text{pr,heat}}$ (kW)	647.6	664	666.1
T_a = 300 K T_{in} = 750 K $\dot{m}_r$ = 0.02 kg/sec	sCO$_2$	Water	Therminol VP1
$\dot{Q}_u$ (kW)	3101	3170	3186
W_{net} (kW)	878.5	898	902.5
$\dot{Q}_{\text{pr,heat}}$ (kW)	572.1	585	587.8

Work consumed by the pumps, to increase and circulate the pressure of working fluid, is given as

$$W_{p1} = v_1 \frac{[P_2 - P_1]}{\eta_{\text{pump}}}, \quad W_{p2} = v_4 \frac{[5 - P_4]}{\eta_{\text{pump}}}. \tag{16}$$

Work done by the turbine is given as

$$W_{\text{Tur,out}} = \dot{m}_6(h_6 - h_7) + \dot{m}_8(h_7 - h_8). \tag{17}$$

Heat input rate to the boiler and heat rejected by the condenser can be determined as [41]

$$Q_{\text{in}} = \dot{m}_5.(h_6 - h_5), \quad Q_{\text{out}} = \dot{m}_8.(h_8 - h_1). \tag{18}$$

The thermal energy for the process heater can be evaluated as

$$Q_{\text{proc,heat}} = \dot{m}_7.(h_7 - h_3). \tag{19}$$

The net power output of the cycle can be computed as

$$W_{\text{net,cycle}} = W_{\text{Tur,out}} - \left[W_{p1} + W_{p2}\right]. \tag{20}$$

The thermal or energy efficiency of the steam cycle is

Table 3: Thermodynamic properties of regenerative Rankine cycle.

State points	Enthalpy, h (kJ/kg)	Pressure, P (kPa)	Temperature, T (K)	Entropy, s (kJ/kg)	Mass flow rate (kg/sec)	Exergy, Ex (kJ)
1	191.8	10	319	0.649	0.75	1.73
2	193.5	1200	319.1	0.650	0.75	2.65
3	798.3	1200	461.1	2.216	0.25	34.7
4	344.7	1200	355.2	1.1	1	20.09
5	348.8	4000	355.7	1.10	1	23.17
6	3446	4000	773	7.09	1	1323
7	3080	1200	588.8	7.09	0.25	239.5
8	2247	10	319	7.09	0.75	93.33

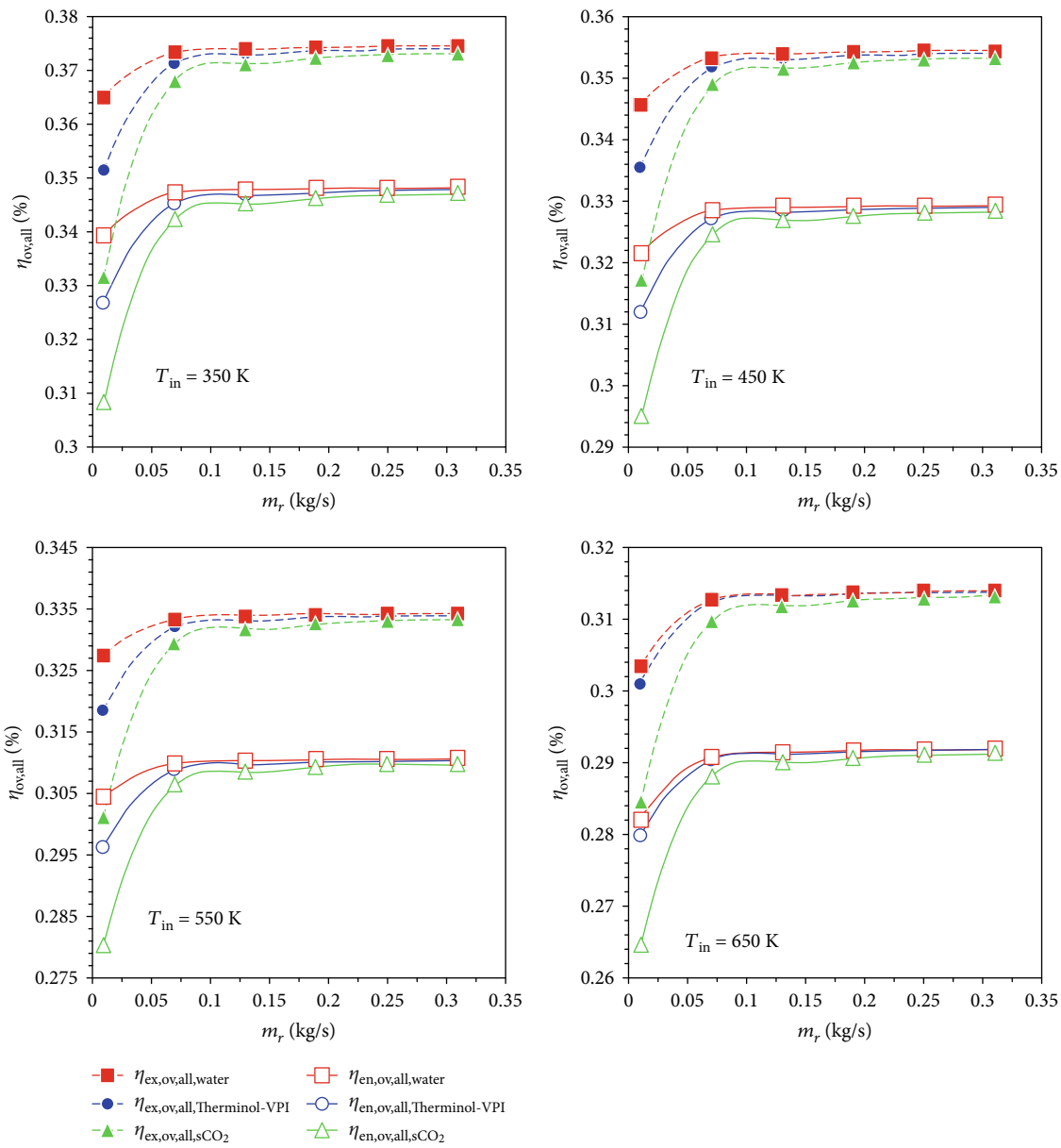

Figure 2: Effect of the mass flow rate on system-integrated efficiencies for various inlet temperature levels.

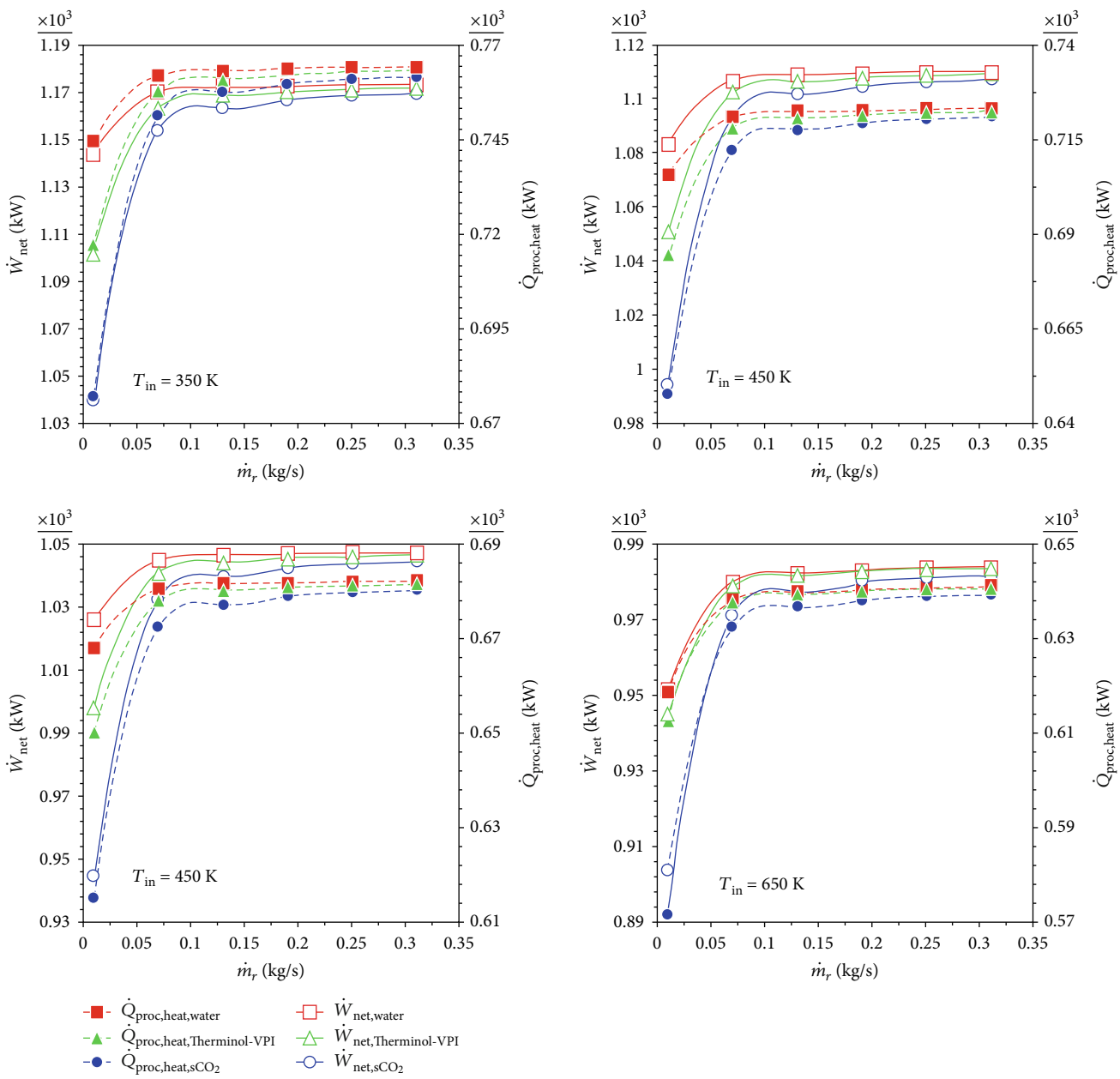

Figure 3: Effect of mass flow rate on net work and process heating for various inlet temperature levels.

determined as

$$\eta_{\text{th}} = \frac{W_{\text{net,cycle}} + Q_{\text{proc,heat}}}{Q_{\text{in}}} \tag{21}$$

Exergy values at all the points of the examined system are required to be determined in order to calculate the exergy destruction rate. Equation (22) gives the relation for exergy at relevant points.

$$\dot{E}_x = \dot{m}(h - h_0) - T_o(s - s_o). \tag{22}$$

The exergy supplied to the boiler and condenser is measured as

$$\begin{aligned} \dot{E}x_{\text{th},b} &= \left[1 - \frac{T_0}{T_b}\right].\dot{Q}_b, \\ \dot{E}x_{\text{th},c} &= \left[1 - \frac{T_0}{T_c}\right].\dot{Q}_c. \end{aligned} \tag{23}$$

Finally, exergy efficiency of the steam cycle and system-integrated efficiencies are given as

$$\eta_X = \frac{W_{\text{net,cycle}} + Q_{\text{proc,heat}}}{\dot{E}x_{\text{th},b}}, \tag{24}$$

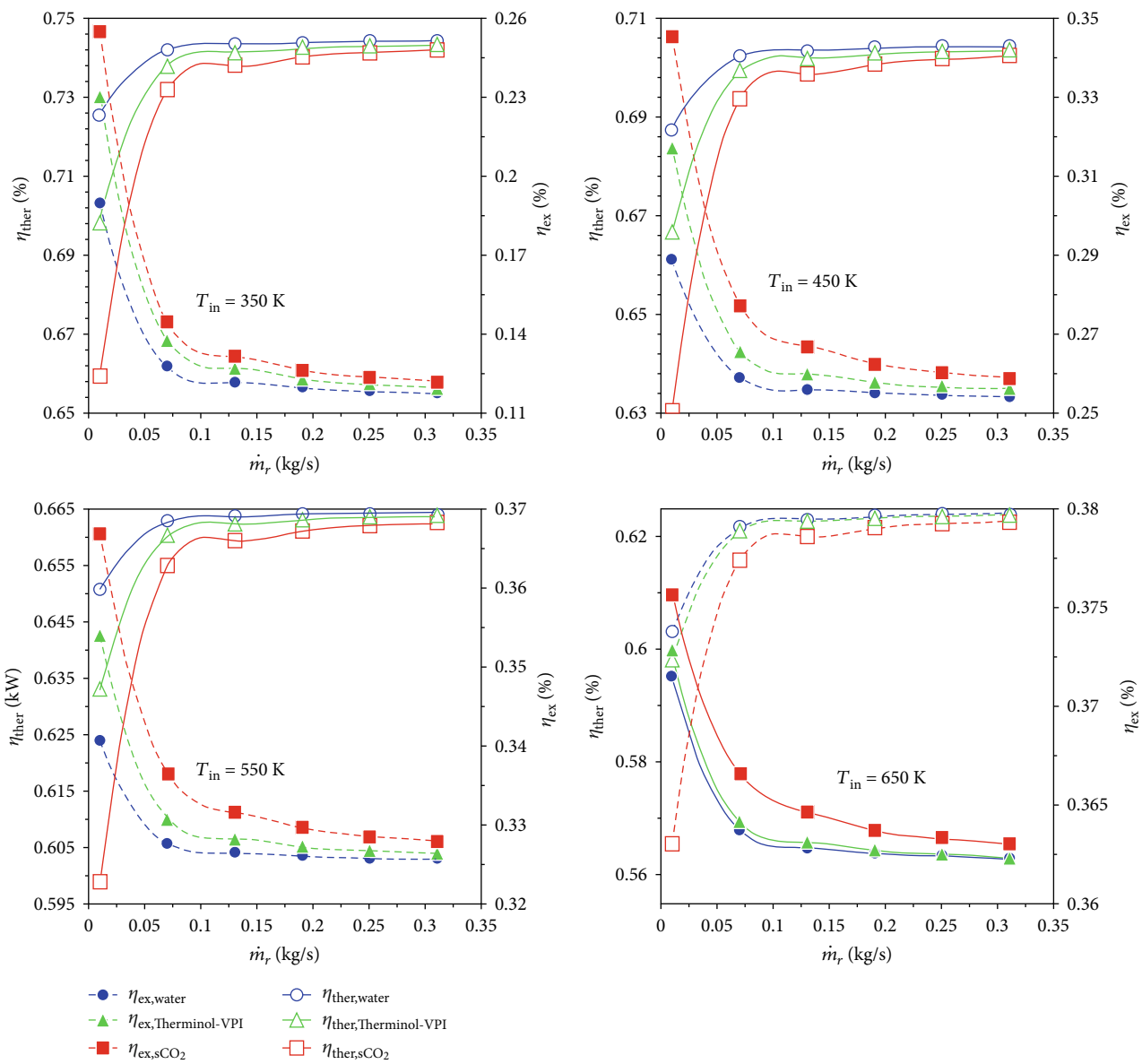

FIGURE 4: Effect of mass flow rate on the thermal and exergy efficiencies for various inlet temperature levels.

$$\eta_{en,ovall} = \frac{W_{net,cycle} + Q_{proc,heat}}{\dot{Q}_{solar}}, \quad (25)$$

$$\eta_{ex,ovall} = \frac{W_{net,cycle} + Q_{proc,heat}}{\dot{E}x_{solar}}. \quad (26)$$

3. Results and Discussion

This study concentrates on the integration of the parabolic dish solar collector utilizing three different HTFs, namely, sCO_2, therminol VP1, and pressurized water with regenerative Rankine cycle, generating electricity and process heat. The present section discusses the findings of the investigated system in details. The change in mass flow rate at different inlet temperature levels of three heat transfer fluids in the solar collector is examined. The performance parameters considered in the study are overall energetic and exergetic efficiencies, power output and rate of process heat, receiver thermal and exergy efficiencies, and convective heat transfer coefficient. The steam Rankine cycle produces 875 kW of electricity and 570 kW heat for processing, and its thermal and exergy efficiencies are found to be 46.7% and 76.3%, respectively. Table 2 below shows the useful heat gain by the solar collector, net power produced, and process heat rate for the examined HTFs at three different inlet temperature levels. It is evident from the table that for lower inlet temperature, water is a better working fluid; however its effectiveness becomes less at higher temperatures. The performance of therminol VP1 gets better at elevated temperatures of above 550 K, while sCO_2 also performs well at upper temperature levels. Thermodynamic properties of regenerative Rankine cycle are presented in Table 3.

Figure 2 illustrates the variation of system-integrated efficiencies for a range of inlet temperature from 350 K to 650 K.

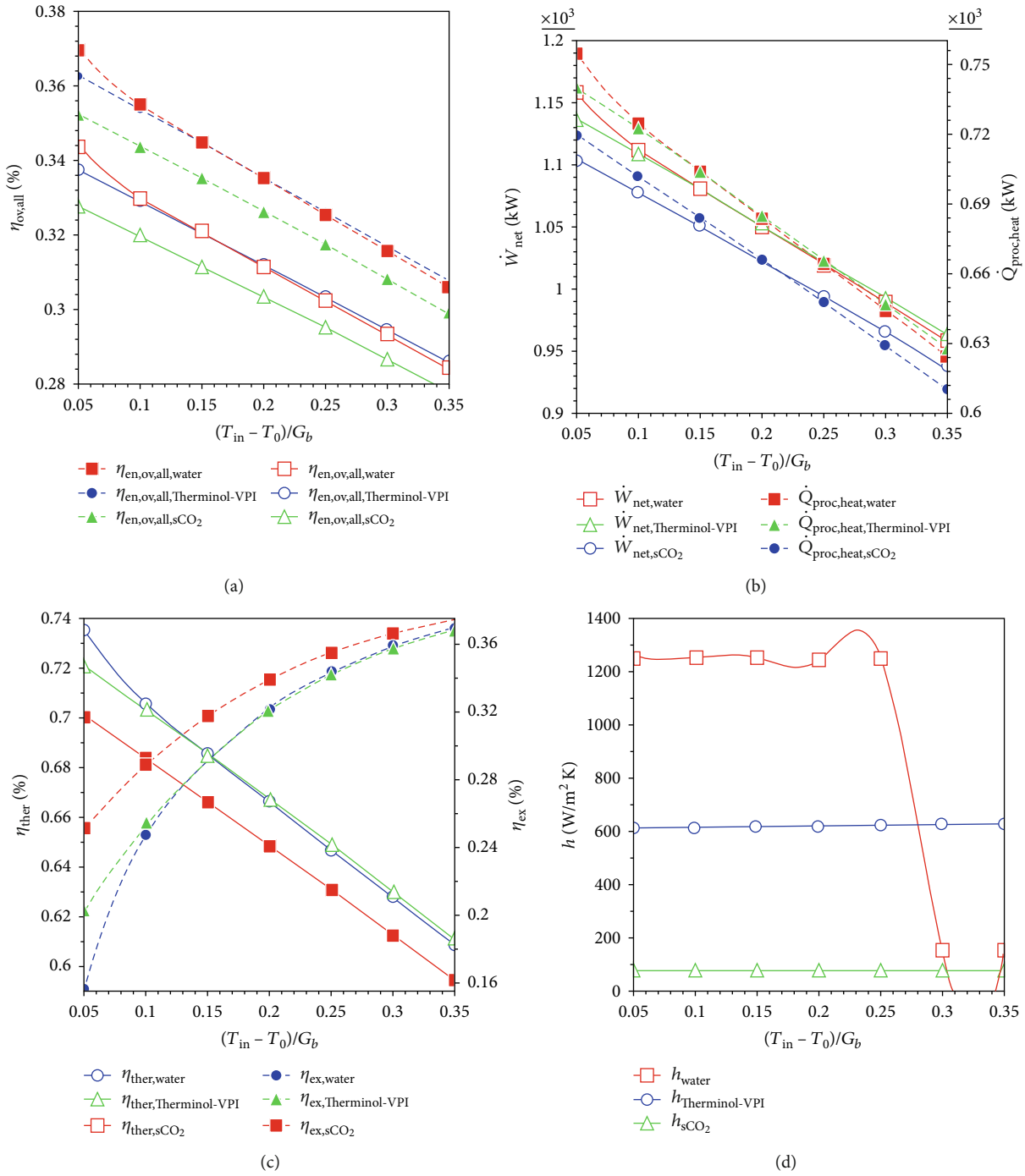

Figure 5: Effect on Inlet temperature on (a) integrated efficiencies, (b) net work output and process heating, (c) thermal and exergy efficiencies, and (d) heat transfer coefficient.

These graphs can be explained in many ways. It can be seen that higher flow rate and lower temperature gives maximum overall energy and exergy efficiencies for the investigated HTFs. However, for a mass flow rate of above 0.15 kg/sec, the variation in the properties becomes stagnant, meaning that there is no reason for employing higher mass flow rate from a thermal point of view. According to equation (25), overall energy efficiency of the integrated system is the ratio of work output from turbine and process heat rate of the process heater to the energy of the solar. Furthermore, higher value of the numerator depends on higher amount of useful heat by the solar collector according to equation (1).

Furthermore, for all the inlet temperature levels, integrated efficiencies of pressurized water are the highest as compared to the other investigated fluids. The maximum difference in efficiency values of HTFs is seen at nearly 0.01 kg/sec, but after that, this difference reduces continuously. At a mass flow rate of 0.3 kg/sec, the efficiency of all

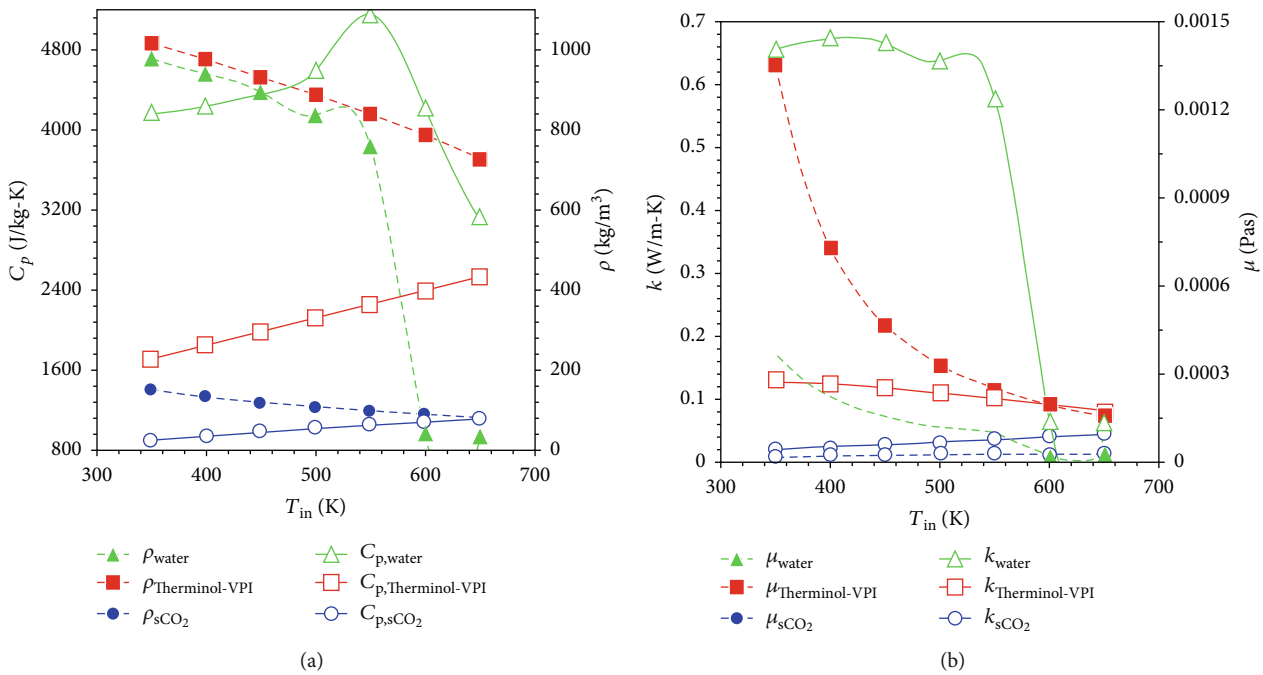

Figure 6: Comparison of properties (a) density and specific heat capacity and (b) thermal conductivity and viscosity.

the investigated fluids converges on the same point. At inlet temperature of 650 K, efficiency of therminol VP1 approaches very near to water values because the performance of water becomes less efficient after 600 K [24]. Pressurized water is witnessed to have 3.85% and 10% higher efficiency than the therminol VP1- and sCO_2-based HTFs, respectively, at a mass flow rate of 0.01 kg/sec. However, these values are reduced to 0.11% and 0.31% at higher mass flow rate of 0.3 kg/sec.

Figure 3 is related to the variation of mass flow rate and its influence on net power produced and rate of process heat at four different inlet temperature levels. Both the performance parameters increase sharply between 0.01 and 0.15 kg/sec and after that remain constant until 0.3 kg/sec. It is evident from Figure 3 that higher values are obtained at lower inlet temperature, and pressurized water is observed to have the highest rate of process heat and work output than the other two investigated HTFs. Net power output utilizing pressurized water in the collector loop is increased to 2.44% for a range of flow rate from 0.01 and 0.15 kg/sec; however, after 0.15 to 0.3 kg/sec, the increment is found to be as low as 0.17%. Therminol VP1 and sCO_2 has 6% and 11.9% increase for 0.01 to 0.15 kg/sec but very less increment in work output (0.17% and 0.51%, respectively). Further rise in mass flow rate clearly indicates that after a certain point, increase in mass flow rate has no importance for thermal enhancement. The highest variation is seen for sCO_2 values at all inlet temperatures due to its behavior near critical region [20]. Highest amount of work produced and rate of process heat is obtained for pressurized water at 350 K that is 1173 kW and 764 kW, respectively. For higher inlet temperature of 650 K, almost 19% reduction is found for both performance parameters.

Figure 4 depicts the influence of the mass flow rate on the thermal and exergetic efficiencies of the parabolic dish receiver at four inlet temperature levels. Thermal efficiency of all investigated fluids has the same trend as discussed above for other performance parameters but exergy efficiency behaves in an opposite way with the rise in mass flow rate. PD collector with water as a HTF has the highest thermal efficiency (74.43%) at 350 K and at a mass flow rate of 0.3 kg/sec, while lowest value has been found for sCO_2 (74.2%). From the exergetic point of view, sCO_2 has a dominant feature as compared to the other HTFs and highest exergy efficiency (37.56%) is noticed at higher temperature (650 K) and lower flow rate (0.01 kg/sec). The highest exergy efficiency value of sCO_2 is due to its lower specific heat capacity as compared to therminol VP1 and pressurized water [23]. Exergy efficiency is the ratio of collector useful exergy to the exergy available from solar [22] and higher inlet temperature of fluid in the receiver will deliver maximum exergy but solar exergy is independent of the inlet temperature and remains the same for all the values of the temperature. The collector exergy depends on useful heat gain from collector, mass flow rate, and temperatures of fluid as followed by equation (9).

Figures 5(a)–5(d) represent the simulation results of integrated system efficiencies, work output, and process heat rate and collect performance as well as the heat transfer coefficient with respect to the inlet temperature. The operational parameter$(T_{in} - T_0)/G_b$ is a parameter expressing the collector efficiency. It reflects the inlet temperature of HTFs as direct normal irradiation, and ambient temperature remained constant during the simulation. The obtained results are considered at ambient temperature of 300 K, DNI of 1000 W/m^2, and flow rate of 0.02 kg/sec. The inlet temperature increases between 350 K and 650 K with a step

Table 4: Optimum operating conditions for the three examined HTFs at different inlet temperatures.

T_{in} (K)	$\dot{m}_{in,op}$ (kg/sec)	η_{th}			η_{ex}		
		sCO_2	Water	Therminol VP1	sCO_2	Water	Therminol VP1
350	0.07	0.7319	0.7421	0.7381	0.1683	0.1275	0.1447
450	0.07	0.6936	0.7023	0.6993	0.2773	0.2588	0.2657
550	0.20	0.661	0.6642	0.6632	0.3296	0.326	0.3272
650	0.30	0.6228	0.6241	0.6239	0.363	0.3622	0.3623
750	0.30	0.5829	0.5837	0.5839	0.3776	0.3775	0.3775
850	0.30	0.543	0.5438	0.5439	0.33	0.3265	0.3276

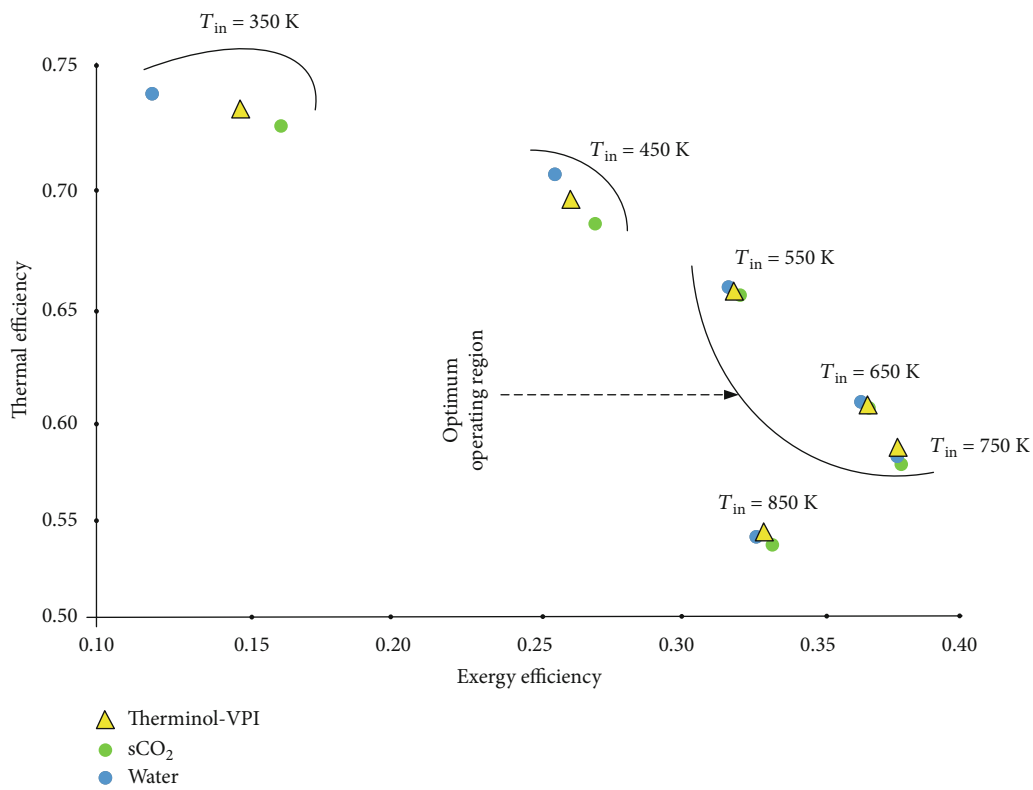

Figure 7: Efficiency map of PDSC for the three investigated fluids at various inlet temperature levels.

50 K. Higher values of inlet temperature offers greater temperature of the receiver surface that results in maximum heat losses from the receiver surface. Higher heat losses decreases the useful heat production from the collector which eventually results in lowering the net power produced and process heat rate of the system.

In Figure 5(a), overall energy and exergy efficiencies of the integrated system employing water reduce from 34.4% to 28.5% and 37% to 30.6%, respectively, and it shows reduction of almost 20.8%. The same trend is noticed for the therminol VP1- and sCO_2-based integrated systems with decrease of nearly 17.93% and 17.87%, accordingly. Pressurized water was found to be 1.95% and 4.95% efficient than the systems operated with therminol VP1 and sCO_2, respectively, at 350 K. However, after 500 K, the performance of the system using water as HTF reduces, and at 650 K, therminol VP1 was found to be 0.52% better than water. Similarly, Figure 5(b) has a very similar trend as described above; therminol VP1 has a dominant role at elevated temperatures. Collector thermal efficiency presented in Figure 5(c) has a very similar behavior to the work output and integrated efficiencies, i.e., higher thermal efficiency is found at lower temperature of 350 K. However, for exergy efficiency, sCO_2-based collector has the highest value among the other compared HTFs. Maximum value is recorded for sCO_2, therminol VP1, and water with 37.37%, 36.86%, and 36.98%, respectively, at 650 K. Figure 5(d) shows the graphical representation of the convective heat transfer coefficient of the absorber and investigated HTFs. It is clear that sCO_2 has the lowest value of h as compared to the other HTFs. The heat transfer coefficient (h) of therminol VP1 is more stable at all the temperature levels, while for water, h is constant at lower temperatures and after 500 K, and it drops dramatically due to evaporation.

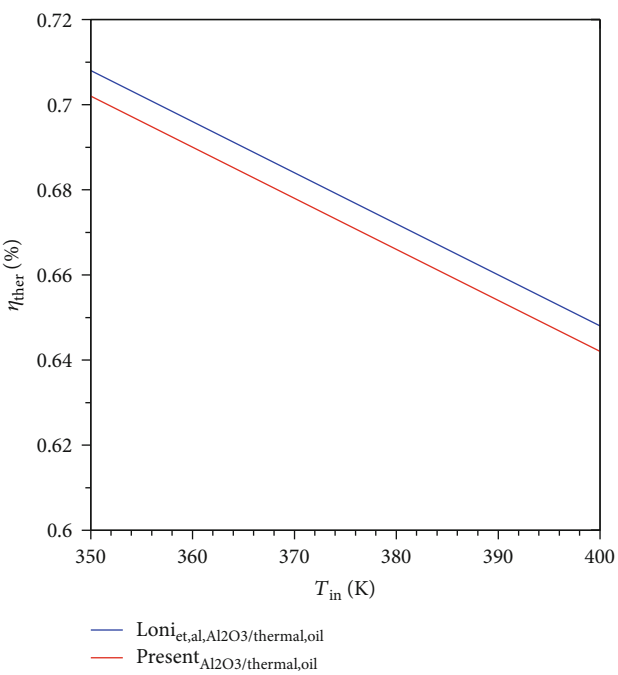

Figure 8: Validation of solar dish collector model with Loni et al. [48].

Figure 6(a) is the portrayal of density and heat capacity of three investigated fluids. The C_p values of pressurized water have an upward trend at low temperatures; however, a sudden decrease is observed after 550 K, while sCO_2 has shown an increment of nearly 23.3%. The synthetic oil is found to have better thermophysical properties, as C_p of the therminol increases by 48.5 with a rise in temperature. A decrease in the density of all HTFs is found with the rise in temperature. Maximum value of density can be seen for oil at lower temperature, and a constant fall is found for sCO_2 as well, while water depicts a dramatic change after 550 K [41]. Thermal conductivity values in Figure 6(b) shows the similar tendency to that of viscosity; maximum k value can be seen at 400 K for water and a reduction can be observed afterwards. Thermal conductivity of oil reduces to 61.5%, while a small increase for sCO_2 is noticed.

The following section provides the optimum operating conditions for the investigated heat transfer fluids in solar dish collector at various inlet temperature levels. The combinations of mass flow rate and inlet temperature of the working fluid in the receiver that lead to higher thermal and exergy efficiency will be assumed the optimum conditions. Table 4 and Figure 7 consist of the outcomes for optimal values against all levels of inlet temperatures. For low-temperature levels of up to 450 K, the optimum flow rate is 0.07 kg/sec and corresponding efficiency values are tabulated in front of them. At 550 K, the optimum value of the mass flow rate can be seen to be 0.20 kg/sec, while higher inlet temperatures have optimum features at 0.30 kg/sec. The highest value of the exergetic efficiency for all the three investigated fluids is obtained at 750 K with flow rate of 0.30 kg/sec; however, a higher value of thermal efficiency is witnessed at 350 K and 0.07 kg/sec. This table also proves that the highest exergy performance does not associate with the higher thermal efficiency, and hence, the optimal operating scenario can be selected by taking both energy and exergy into consideration. The efficiency map of the collector is very useful and is an innovative tool to evaluate the collector performance under different criteria. Furthermore, validation of the parabolic dish receiver has been conducted by comparing the thermal efficiency of the collector using Al_2O_3/thermal oil as a HTF with the model presented by Loni et al. [48] in Figure 8. The proposed model shows a discrepancy of 0.85% in efficiency in comparison to the reference model when evaluated against inlet temperature.

4. Conclusions

Thermodynamic performance investigation of PD solar-assisted cogeneration plant is presented in this study. Three working fluids/HTFs, namely, sCO_2, pressurized water, and therminol VP1, are used to collect the heat produced by the solar collector. The collected heat is further used to drive the regenerative steam Rankine cycle producing power and process heat simultaneously. Firstly, PDSC is thermodynamically modeled by considering three HTFs (sCO_2, pressurized water, and therminol VP1) and those modeling results are further utilized to evaluate the performance of integrated system. Different combinations of flow rates and inlet temperatures have been tested and an optimal scenario is presented that leads to maximum energy and exergy efficiencies of the solar collector. The major outcomes are presented as follows:

(i) Higher flow rate and lower temperature offer maximum overall energy and exergy efficiencies for the investigated HTFs. Pressurized water is observed to have an integrated efficiency of 10% and 3.85% higher than sCO_2- and therminol VP1-based HTFs, respectively, at a flow rate of 0.01 kg/sec. However, these values are reduced to 0.11% and 0.31% at a higher flow rate of 0.3 kg/sec

(ii) Net power output of the proposed integrated system for water as a HTF in the collector loop is increased to 2.44% for flow rate from 0.01 to 0.15 kg/sec; however, after 0.15 to 0.3 kg/sec, this increment is as low as 0.17%. Therminol VP1 and sCO_2 has 6% and 11.9% increase for flow rate between 0.01 and 0.15 kg/sec but very less increment in work output values (0.17% and 0.51%, respectively) for further rise in the mass flow rate. Highest amount of net power produced (1173 kW) and the rate of process heat (764 kW) are obtained for pressurized water at 350 K, respectively. For higher inlet temperature of 650 K, almost 19% reduction is found for both performance parameters

(iii) The PD collector with water as a HTF has the highest thermal efficiency (74.43%) at 350 K and at a flow rate of 0.3 kg/sec, while lowest value has been found for sCO_2 (74.2%). From the exergetic point of view, the sCO_2 outperforms the other heat transfer fluids

(iv) Pressurized water was found to be 1.95% and 4.95% more efficient than the systems operating with therminol VP1 and sCO_2, working fluids at a temperature of 350 K. However, the performance of the system using water as HTF starts to decrease with rise in temperature, and at 650 K, therminol VP1 is observed to surpass water with 0.52% better efficiency

(v) An innovative solar efficiency map is proposed with an aim to find out the optimal operating region with respect to collector energy and exergy efficiencies. The maximum exergy efficiency of 37.75% is observed at a temperature of 750 K and at a flow rate of 0.3 kg/sec

Nomenclature

Acronyms

CSP: Concentrated solar power
CFD: Computational fluid dynamics
FWH: Feed water heater
HTFs: Heat transfer fluids
PDC: Parabolic dish collector
sCO_2: Supercritical carbon dioxide.

Symbols

A_a: Area of aperture (m^2)
A_{ri}: Area of receiver (m^2)
C_p: Specific heat capacity (J/kg-K)
D_h: Hydraulic diameter (m)
$\dot{E}_{x,u}$: Useful exergy
f_r: Friction factor
F_r: Heat removal factor
F_1: Collector efficiency factor
G_b: Solar radiation (W/m^2)
h: Enthalpy (kJ/kg)
k: Thermal conductivity (W/m-K)
$\dot{m}$: Mass flow rate (kg/sec)
P_r: Prandtl number
$\dot{Q}_u$: Useful heat (kW)
$\dot{Q}_b$: Heat rate of boiler (kW)
T_{fm}: Mean fluid temperature (K)
U_L: Coefficient of heat loss (W/m^2 K).

Greek Letters

η_{pump}: Pump efficiency (%)
η_{tur}: Turbine efficiency (%)
ρ: Density (kg/m^3)
η_{pet}: Petela efficiency
η_{en}: Energy efficiency (%)
$\dot{\psi}$: Rate of exergy destruction (kW).

Data Availability

Data will be provided on request.

Conflicts of Interest

The authors declare that they have no conflicts of interest.

Acknowledgments

The authors wish to express their great appreciation for the financial support from the National International Cooperation Project, China (2016YFE0202000 and 2017YFE0107600), National Natural Science Foundation of China (51976196), and International Cooperation Project of Zhejiang Province (2019C04026).

References

[1] I. M. Yusri, R. Mamat, G. Najafi et al., "Alcohol based automotive fuels from first four alcohol family in compression and spark ignition engine: a review on engine performance and exhaust emissions," *Renewable and Sustainable Energy Reviews*, vol. 77, pp. 169–181, 2017.

[2] A. R. Keeley and K. I. Matsumoto, "Investors' perspective on determinants of foreign direct investment in wind and solar energy in developing economies - Review and expert opinions," *Journal of Cleaner Production*, vol. 179, pp. 132–142, 2018.

[3] S. Pavlovic, A. M. Daabo, E. Bellos, V. Stefanovic, S. Mahmoud, and R. K. Al-Dadah, "Experimental and numerical investigation on the optical and thermal performance of solar parabolic dish and corrugated spiral cavity receiver," *Journal of Cleaner Production*, vol. 150, pp. 75–92, 2017.

[4] M. Abid, M. S. Khan, and T. A. H. Ratlamwala, "Comparative energy, exergy and exergo-economic analysis of solar driven supercritical carbon dioxide power and hydrogen generation cycle," *International Journal of Hydrogen Energy*, vol. 45, no. 9, pp. 5653–5667, 2020.

[5] M. S. Khan, K. P. Amber, H. M. Ali, M. Abid, T. A. Ratlamwala, and S. Javed, "Performance analysis of solar assisted multigenerational system using therminol VP1 based nanofluids: a comparative study," *Thermal Science*, vol. 24, no. 2 Part A, pp. 865–878, 2020.

[6] J. Coventry and C. Andraka, "Dish systems for CSP," *Solar Energy*, vol. 152, pp. 140–170, 2017.

[7] A. M. Daabo, S. Mahmoud, and R. K. Al-Dadah, "The effect of receiver geometry on the optical performance of a small-scale solar cavity receiver for parabolic dish applications," *Energy*, vol. 114, pp. 513–525, 2016.

[8] E. Przenzak, M. Szubel, and M. Filipowicz, "The numerical model of the high temperature receiver for concentrated solar radiation," *Energy Conversion and Management*, vol. 125, pp. 97–106, 2016.

[9] R. D. Jilte, S. B. Kedare, and J. K. Nayak, "Investigation on convective heat losses from solar cavities under wind conditions," *Energy Procedia*, vol. 57, pp. 437–446, 2014.

[10] N. D. Kaushika and K. S. Reddy, "Performance of a low cost solar paraboloidal dish steam generating system," *Energy Conversion and Management*, vol. 41, no. 7, pp. 713–726, 2000.

[11] R. Loni, A. B. Kasaeian, E. A. Asli-Ardeh, B. Ghobadian, and W. G. Le Roux, "Performance study of a solar-assisted organic Rankine cycle using a dish- mounted rectangular-cavity tubular solar receiver," *Applied Thermal Engineering*, vol. 108, pp. 1298–1309, 2016.

[12] A. Mawire and S. H. Taole, "Experimental energy and exergy performance of a solar receiver for a domestic parabolic dish concentrator for teaching purposes," *Energy for Sustainable Development*, vol. 19, pp. 162–169, 2014.

[13] I. L. Mohammed, "Design and development of a parabolic dish solar water heater," *International Journal of Engineering Research and Applications*, vol. 2, no. 1, pp. 822–830, 2012.

[14] K. S. Reddy, S. K. Natarajan, and G. Veershetty, "Experimental performance investigation of modified cavity receiver with fuzzy focal solar dish concentrator," *Renewable Energy*, vol. 74, pp. 148–157, 2015.

[15] V. Madadi, T. Tavakoli, and A. Rahimi, "First and second thermodynamic law analyses applied to a solar dish collector," *Journal of Non-Equilibrium Thermodynamics*, vol. 39, no. 4, pp. 183–197, 2014.

[16] E. Bellos, C. Tzivanidis, and K. A. Antonopoulos, "A detailed working fluid investigation for solar parabolic trough collectors," *Applied Thermal Engineering*, vol. 114, pp. 374–386, 2017.

[17] M. Abid, T. A. H. Ratlamwala, and U. Atikol, "Performance assessment of parabolic dish and parabolic trough solar thermal power plant using nanofluids and molten salts," *International Journal of Energy Research*, vol. 40, no. 4, pp. 550–563, 2016.

[18] R. Loni, E. A. Asli-Ardeh, B. Ghobadian, E. Bellos, and W. G. Le Roux, "Numerical comparison of a solar dish concentrator with different cavity receivers and working fluids," *Journal of Cleaner Production*, vol. 198, pp. 1013–1030, 2018.

[19] R. Loni, A. B. Kasaeian, E. A. Asli-Ardeh, and B. Ghobadian, "Optimizing the efficiency of a solar receiver with tubular cylindrical cavity for a solar-powered organic Rankine cycle," *Energy*, vol. 112, pp. 1259–1272, 2016.

[20] M. S. Khan, M. Abid, H. M. Ali, K. P. Amber, M. A. Bashir, and S. Javed, "Comparative performance assessment of solar dish assisted s-CO2 Brayton cycle using nanofluids," *Applied Thermal Engineering*, vol. 148, pp. 295–306, 2019.

[21] M. Abid, M. S. Khan, and T. A. Ratlamwala, "Techno-environmental analysis of a parabolic dish assisted recompression with and without reheat s-CO<SUB align="right">2 Brayton cycle," *International Journal of Exergy*, vol. 27, no. 4, pp. 527–552, 2018.

[22] M. Abid, T. A. Ratlamwala, and U. Atikol, "Solar assisted multi-generation system using nanofluids: a comparative analysis," *International Journal of Hydrogen Energy*, vol. 42, no. 33, pp. 21429–21442, 2017.

[23] E. Bellos, C. Tzivanidis, K. A. Antonopoulos, and I. Daniil, "The use of gas working fluids in parabolic trough collectors–an energetic and exergetic analysis," *Applied Thermal Engineering*, vol. 109, pp. 1–14, 2016.

[24] E. C. Okonkwo, M. Abid, and T. A. Ratlamwala, "Numerical analysis of heat transfer enhancement in a parabolic trough collector based on geometry modifications and working fluid usage," *Journal of Solar Energy Engineering*, vol. 140, no. 5, article 051009, 2018.

[25] M. Atif and F. A. Al-Sulaiman, "Energy and exergy analyses of solar tower power plant driven supercritical carbon dioxide recompression cycles for six different locations," *Renewable and Sustainable Energy Reviews*, vol. 68, pp. 153–167, 2017.

[26] Y. Qiu, M. J. Li, Y. L. He, and W. Q. Tao, "Thermal performance analysis of a parabolic trough solar collector using supercritical CO2 as heat transfer fluid under non-uniform solar flux," *Applied Thermal Engineering*, vol. 115, pp. 1255–1265, 2017.

[27] R. Aguilar, L. Valenzuela, A. L. Avila-Marin, and P. L. Garcia-Ybarra, "Simplified heat transfer model for parabolic trough solar collectors using supercritical CO2," *Energy Conversion and Management*, vol. 196, pp. 807–820, 2019.

[28] F. Mebarek-Oudina, "Convective heat transfer of Titania nanofluids of different base fluids in cylindrical annulus with discrete heat source," *Heat Transfer - Asian Research*, vol. 48, no. 1, pp. 135–147, 2019.

[29] F. Mebarek-Oudina, "Numerical modeling of the hydrodynamic stability in vertical annulus with heat source of different lengths," *Engineering science and technology, an international journal*, vol. 20, no. 4, pp. 1324–1333, 2017.

[30] A. S. Kherbeet, H. A. Mohammed, H. E. Ahmed et al., "Mixed convection nanofluid flow over microscale forward-facing step—effect of inclination and step heights," *International Communications in Heat and Mass Transfer*, vol. 78, pp. 145–154, 2016.

[31] M. A. Abbassi, M. R. Safaei, R. Djebali, K. Guedri, B. Zeghmati, and A. A. Alrashed, "LBM simulation of free convection in a nanofluid filled incinerator containing a hot block," *International Journal of Mechanical Sciences*, vol. 144, pp. 172–185, 2018.

[32] M. Goodarzi, S. Javid, A. Sajadifar et al., "Slip velocity and temperature jump of a non-Newtonian nanofluid, aqueous solution of carboxy-methyl cellulose/aluminum oxide nanoparticles, through a microtube," *International Journal of Numerical Methods for Heat and Fluid Flow*, vol. 29, no. 5, pp. 1606–1628, 2019.

[33] H. Olia, M. Torabi, M. Bahiraei, M. H. Ahmadi, M. Goodarzi, and M. R. Safaei, "Application of nanofluids in thermal performance enhancement of parabolic trough solar collector: state-of-the-art," *Applied Sciences*, vol. 9, no. 3, p. 463, 2019.

[34] A. R. Gheynani, O. A. Akbari, M. Zarringhalam et al., "Investigating the effect of nanoparticles diameter on turbulent flow and heat transfer properties of non-Newtonian carboxymethyl cellulose/CuO fluid in a microtube," *International Journal of Numerical Methods for Heat and Fluid Flow*, vol. 29, no. 5, pp. 1699–1723, 2019.

[35] T. Taner, "Optimisation processes of energy efficiency for a drying plant: a case of study for Turkey," *Applied Thermal Engineering*, vol. 80, pp. 247–260, 2015.

[36] T. Taner, "Energy and exergy analyze of PEM fuel cell: a case study of modeling and simulations," *Energy*, vol. 143, pp. 284–294, 2018.

[37] H. Topal, T. Taner, Y. Altıncı, and E. Amirabedin, "Application of trigeneration with direct co-combustion of poultry waste and coal: a case study in the poultry industry from Turkey," *Thermal Science*, vol. 22, no. 6 Part B, pp. 3073–3082, 2018.

[38] H. Topal, T. Taner, S. A. H. Naqvi, Y. Altınsoy, E. Amirabedin, and M. Ozkaymak, "Exergy analysis of a circulating fluidized bed power plant co-firing with olive pits: a case study of power plant in Turkey," *Energy*, vol. 140, pp. 40–46, 2017.

[39] T. Taner and M. Sivrioglu, "A techno-economic & cost analysis of a turbine power plant: a case study for sugar plant," *Renewable and Sustainable Energy Reviews*, vol. 78, pp. 722–730, 2017.

[40] S. A. Klein, *Engineering equation solver, v8.411*, F-Chart Software, Madison, Wisconsin, 2009.

[41] M. Abid, M. S. Khan, T. A. H. Ratlamwala, and K. P. Amber, "Thermo-environmental investigation of solar parabolic dish-assisted multi-generation plant using different working fluids," *International Journal of Energy Research*, vol. 44, no. 15, pp. 12376–12394, 2020.

[42] A. Cengel Younus and M. A. Boles, *Thermodynamics: An Engineering Approach*, McGraw-Hill, New York, NY, USA, 7th edition, 2017, in SI units.

[43] V. Gnielinski, "New equations for heat and mass transfer in turbulent pipe and channel flow," *International Chemical Engineering*, vol. 16, no. 2, pp. 359–368, 1976.

[44] T. L. Bergman, A. S. Lavine, F. P. Incropera, and D. P. Dewitt, *Fundamentals of Heat and Mass Transfer*, John Wiley & Sons, 2011.

[45] I. Dincer and T. A. H. Ratlamwala, "Importance of exergy for analysis, improvement, design, and assessment," *Wiley Interdisciplinary Reviews: Energy and Environment*, vol. 2, no. 3, pp. 335–349, 2013.

[46] J. Yazdanpanahi, F. Sarhaddi, and M. M. Adeli, "Experimental investigation of exergy efficiency of a solar photovoltaic thermal (PVT) water collector based on exergy losses," *Solar Energy*, vol. 118, pp. 197–208, 2015.

[47] L. C. Ngo, *Exergetic analysis and optimization of a parabolic dish collector for low power application, Centre for Renewable and Sustainable Energy Studies*, University of Pretoria, 2013.

[48] R. Loni, A. Kasaeian, K. Shahverdi, E. A. Asli-Ardeh, B. Ghobadian, and M. H. Ahmadi, "ANN model to predict the performance of parabolic dish collector with tubular cavity receiver," *Mechanics & Industry*, vol. 18, no. 4, p. 408, 2017.

Hindawi
International Journal of Photoenergy
Volume 2021, Article ID 6675236, 13 pages
https://doi.org/10.1155/2021/6675236

Research Article

Effect of Reflecting Material on CPC to Improve the Performance of Hybrid Groundwater Solar Desalination System

S. A. Kedar,[1] A. K. Bewoor,[2] G. Murali,[1] Ravinder Kumar,[3] Milad Sadeghzadeh,[4] and Alibek Issakhov[5]

[1]*Department of Mechanical Engineering, Koneru Lakshmaiah Education Foundation, Green Fields, Vaddeswaram, Guntur 522502, India*
[2]*Department of Mechanical Engineering, MKSSS's Cummins College of Engineering for Women, Pune, 411052, India*
[3]*Lovely Professional University, Phagwara, 144411 Punjab, India*
[4]*Department of Renewable Energy and Environmental Engineering, University of Tehran, Tehran, Iran*
[5]*Department of Mathematical and Computer Modelling, Faculty of Mechanics and Mathematics, Al-Farabi Kazakh National University, Almaty, Kazakhstan*

Correspondence should be addressed to G. Murali; muralinitt@gmail.com, Ravinder Kumar; rav.chauhan@yahoo.co.in, and Milad Sadeghzadeh; milad.sadeghzadeh@gmail.com

Received 23 November 2020; Revised 21 February 2021; Accepted 25 March 2021; Published 7 April 2021

Academic Editor: Hafiz Muhammad Ali

Copyright © 2021 S. A. Kedar et al. This is an open access article distributed under the Creative Commons Attribution License, which permits unrestricted use, distribution, and reproduction in any medium, provided the original work is properly cited.

Water-energy nexus is a crucial and challenging concern that addressing it is noteworthy for the future of human beings. In addition, freshwater production is a highly energy-intensive procedure. Therefore, developing a suitable solution for this problem is of importance. In the present scenario, solar energy is one of the suitable options for desalination because solar energy is available at a low cost, is clean for the environment, and is widely available. Generally, solar collectors such as flat plate collectors (FPC) and evacuated tube collectors were experimented for desalination applications. This work presents an experimental investigation of a single-stage hybrid (ETC-CPC) groundwater solar desalination system. A compound parabolic concentrator (CPC) is placed below the evacuated tube collector (ETC) for collecting solar radiations to transfer heat to evacuated tubes which improves performance in the case of different weather conditions of Pune city in India. Experimental results show that the hybrid solar groundwater desalination system, by maintaining the optimum distance of 20 mm between ETC and CPC with Mylar as the reflecting material, could offer a drinking water production rate of up to 3.4 l/(m^{2}h)/day. However, the proposed single-stage hybrid (ETC+CPC) groundwater solar desalination system with aluminum foil as a reflecting material could generate 1.9 liters of soft water per day. Further, the use of Mylar as a reflecting material could generate 3.5 liters of soft water per day.

1. Introduction

The current demand for solar energy is continuously increasing for electricity generation and other useful work in the world. The world population is continuously increasing day-by-day, and the need for freshwater for drinking application and the electricity demand to fulfill their need are the biggest issues in the world [1, 2]. The lack of freshwater in the rural areas makes it very difficult for human beings because of the less amount of freshwater available and less amount of electricity. Solar energy is one of the options especially in rural areas for making the maximum amount of drinkable water with low cost [3]. In the world scenario, approximately 97% of water is seawater and the remaining water is found in various sources such as lakes, rivers, and groundwater. Some amount of that water is in the form of ice, and the remaining 1% or less of that freshwater will be utilized for humans and animals [4]. In the world, supply of freshwater to urban and rural areas is the main issue. Various engineers and scientists had developed various desalination technologies such as RO, ED, and VP, but the major drawbacks of these methods include large energy

consumption and maximum use of fossil fuels which will impact the environment [5]. Kedar et al. had theoretically studied the solar desalination system using ETC and CPC; as per their primary studies, there is a wide scope in research in the field of solar desalination system [6]. Moungar et al. [7] had experimentally studied immersed fins which will have influence on the double slope still production. Their results show that to achieve better soft water production using a double slope solar still, the authors had planned the whole study for south Algeria for various climatic and environmental conditions. Using a sand heat energy storage technology, Sathyamurthy et al. [8] developed a conventional solar still. Their experimental results show high heat storage capacity in the solar still whereas Morad et al. [9] worked on thermal performance improvement in the solar still. Bhambare et al. [10] presented various desalination systems that are available in Oman. Kedar et al. [11–13] mainly developed an evacuated tube collector and compound parabolic concentrator using a single-effect boiling method. The authors had done extensive experimental work for a hybrid solar desalination system. Grosu et al. [14] carried out an exergy-based optimization on solar thermal collectors. Sadeghzadeh et al. [15] applied smart models based on machine learning approaches to predict the efficiency of flat-plate solar collectors. Olia et al. [16] discussed the possible application of using nanofluids to improve the performance of the solar parabolic collectors. Loni et al. [17] estimated the performance of parabolic dish collectors with tubular cavity receivers. Jilte et al. [18] investigated the integration of a biomass gasifier with a solar heat pipe. Rafiei et al. [19] performed a novel sensitivity analysis and monitored the working parameters of a parabolic trough collector under defined circumstances. Sampathkumar et al. [20] had performed a detailed review for active solar distillation, and their detailed review shows the future of research in the field of composite materials. Siddiqui et al. [21] had made a study using a solar air heater to study the thermal performance of the desalination system, and their results show that the observed productivity increased to 72% as well as gained output ratio (GOR) increased up to 57%. Kabeel and El-Said [22] mainly reviewed various desalination systems and developed water desalination systems using HDH technology. Sapre et al. [23] worked on a desalination system with a parabolic concentrator through the collector; they mainly developed an absorber as a thin pressure wall vessel useful for the absorption process. Zheng et al. [24] had experimentally developed multieffect tubular solar desalination devices; through their experimentation, the authors mainly focused on the performance analysis of the multieffect devices.

Khalil et al. [25] had developed a solar desalination system with HDH technology; they had developed an air bubble column humidifier. Ahmed et al. [26] had developed an evacuated tube solar desalination system; they had studied the multistage characteristics of ETC in solar distillation. Wu et al. [27] have made an effective study on the heat and mass transfer in vacuum membrane distillation based on air bubbling, whereas Jahangiri et al. [28] had performed an experiment using solar energy to assess the performance of thermosyphon heat pipes as well as vacuum glass. Dwivedi and Tiwari [29] conducted a comparison study on internal heat transfer coefficients in a passive solar still by different thermal models. Rahbar and Esfahani [30] used a thermoelectric module and heat pipe to perform an experimental study on a novel portable solar still. Kargar Sharif Abad et al. [31] studied a novel integrated solar desalination system with a pulsating heat pipe whereas Dimri et al. [32] observed the performance of a condensing cover material concerning the yield of an active solar still.

Chandrashekara and Yadav [33] had reviewed various articles related to a water desalination system using solar heat; their studies show that there is a need for the development of a new hybrid desalination system. Zuo et al. [34, 35] had an experimental study on solar chimneys which are progressively coupled with seawater desalination whereas Ming et al. [36] and Bacha [37] prepared a water desalination prototype for the dynamic modeling by solar energy and made an experimental validation on the same. Li et al. [38] conducted an experimental study of desalination systems at both the humidification and dehumidification stages of the solar air heater. Cao et al. [39] had conducted an experimental study of the desalination system at both the humidification and dehumidification phases which are combined with chimneys whereas Murali et al. [40–42] had worked on solar still productivity enhancement by PCM and made a serious investigation on the performance of a solar aluminum can air heater in the case of latent heat storage and also in the absence of latent heat storage. They argued that a phase change material (PCM) is required for solar still productivity improvement. Al-Nimr et al. [43] had worked on a hybrid solar-wind desalination system. Their study shows that soft water of 0.5296 l per day was obtained for the climatic conditions of Irbid, Jordan. Kedar et al. [44–46] investigated the hybrid ETC+CPC solar system for desalination application.

Panchal et al. [47] reviewed possible techniques to improve freshwater production from a tubular solar still. In an experimental study, Panchal et al. [48] investigated the effect of fin inclination in solar stills. It has been found that vertical and inclined fins enhanced the output yield of the solar still.

With regard to the literature and expert discussions in light of solar desalination systems, it is analyzed that most of the studies were carried out in multistage flash, multieffect boiling, and reverse osmosis. This attempt is the elongation of the recent study of a single-stage hybrid (ETC-CPC) groundwater solar desalination system. This paper presents the investigation for four different materials, viz., aluminum foil, Mylar, chrome vinyl silver wrap, and white paint, as reflecting material used over a compound parabolic concentrator to enhance the rate of heat transfer. Therefore, solar desalination is expected at higher rates. All the experiments are carried out for different atmospheric conditions of Pune city. Effects of few parameters such as material, the intensity of the solar radiation, and distance between ETC and CPC on the production rate are thoroughly inspected.

2. Details of the Experimental Setup

The whole sum of experiments was carried out in Pune city, Maharashtra, India. Precisely, the location of Pune is at

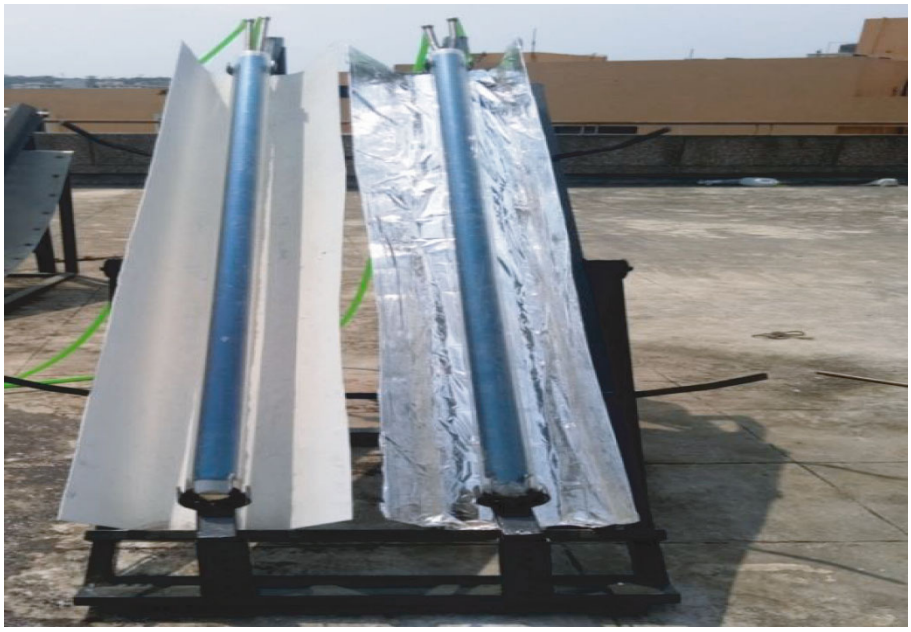

Figure 1: Experimental setup.

Figure 2: CPC with aluminum foil and chrome mirror silver vinyl wrap.

latitude 18.6° (18° 36′ North), longitude 74.15° (74.9′ East), and an altitude of 560 m above mean sea level. The hybrid solar desalination system is categorized into two different parts. The first part was an evacuated tube collector of size 1500 mm long; a copper tube was added in the ETC for flowing the water from one side and heat/steam from another side. The main purpose of using copper tubes in ETC is to enhance the rate of heat transfer. The second part was a compound parabolic concentrator which will be placed exactly below the evacuated tubes for avoiding solar radiation loss. Different materials are studied and used over the compound parabolic concentrator such as aluminum foil, reflective white paint, chrome mirror silver vinyl wrap, and Mylar. All the experiments are conducted from morning 7 AM to evening 6 PM. A schematic of the experimental setup is demonstrated in Figures 1–3, which shows CPC with aluminum foil and chrome mirror sliver vinyl wrapped and CPC with aluminum foil and Mylar. Various technical parameters and detailed dimensions are gathered in Table 1.

3. Instrumentation Used for Experimentations

In the case of Pune city, about 60% of solar heat is reached between 10:00 AM and 3:00 PM. All the experimentations

Figure 3: CPC with aluminum foil and Mylar.

were carried out from the period January to May for the entire months in the year 2018. For the observations in the entire experimentations, ambient temperature (T_a), outside evacuated tube temperature, outlet water temperature (T_{out}), and the temperature of the CPC ($CPC_{temp.}$) were measured with the help of thermocouples and a noncontact type of thermometer model IRL-380. The intensity of solar radiation was measured by pyranometer KM-SPM530. The flow rate of water is measured by a standard water flowmeter. Wind velocity is measured by an anemometer with model KM-910. Finally, desalinated water is collected in a bottle with 10 mL resolution.

3.1. Uncertainty Analysis. During the experimentation, an infrared thermometer instrument was used for the measurement of temperature with model IRL-380 and range available -50 to 380°C. The anemometer instrument was used for the measurement of wind velocity with model KM-910 and range 0–45 m/sec. The pyranometer instrument is used for the measurement of the intensity of solar radiation with model KM-SPM-530 and range 0 to 2000 W/m^2. Water flow rate is used for the measurement of water flow with range 0.01 to 100 lpm. On an approximation, the uncertainty of daily performance efficiency and amount of soft water (liters) were recorded as ±2% and ±4%, respectively.

4. Results and Discussion

4.1. Effect of Rate of Generation of Freshwater. During the experimentation, the continuous monitoring of the hourly change of the measured parameters such as ambient temperature, outside evacuated tube temperature, outlet water temperature, temperature of the CPC along with the intensity of the solar radiation, wind velocity, and rate of the generation of freshwater on one of the experiments since May 2018 are shown in Table 2.

Table 1: Technical parameters and dimensions for a desalination system.

Sr. no.	Technical parameters	Symbol	Dimensions
01	Evacuated tube diameter	D	65 mm
02	Distance between tubes	b	116 mm
03	Length of evacuated tube	L_{ETC}	1500 mm
04	Length of CPC	L_{CPC}	1500 mm
05	Length of copper tube	L_{cu}	1600 mm
06	Number of copper tube	N_{cu}	02
07	Diameter of copper tube	d_{cu}	20 mm
08	Absorber area	$A_{abs.}$	1.6 m^2
09	ETC glass tube thickness	t	1.6 mm
10	Refractive index	N	1.5

In this experiment, the material used for CPC is aluminum foil with a thickness of 2 mm. The intensity of the solar radiation, wind velocity, and rate of soft water desalination are shown in Table 2. It is noted that the rate of generation of soft water increases when the intensity of solar radiation increases. In the morning time of the experiment, water in the evacuated tube is not warm sufficiently; due to this reason, a lower rate of gaining heat from solar radiation and the rate of generation of freshwater are very low. After a

Table 2: Hourly variations of measured parameters in May 2018 with Al foil material of CPC.

Time	The intensity of solar radiation (I_g)	Ambient temp. (T_{amb})	Outside ETC temp.	Outlet water temp.	Temp. of CPC (°C)	Wind velocity (m/sec)	Rate of soft water (kg/m^2/h)
07:00	220	22.7	27.5	29.4	27.9	3.20	0.01
08:00	250	22.9	31.8	33.6	32.9	3.52	0.05
09:00	278	23.7	36.9	40.2	37.8	3.53	0.09
10:00	345	24.8	43.5	43.7	44.3	4.32	0.12
11:00	487	25.7	55.3	60.3	57.4	4.50	0.17
12:00	620	31.6	62.8	65.3	65.3	5.00	0.20
13:00	735	32.5	67.9	69.4	69.4	5.03	0.25
14:00	875	34.7	76.8	79.4	79.5	5.42	0.27
15:00	930	35.2	85.4	87.4	87.3	4.83	0.35
16:00	810	32.5	71.3	75.4	73.4	4.20	0.27
17:00	573	28.7	56.2	60.3	59.4	4.01	0.20
18:00	245	25.5	45.1	47.5	47.4	3.82	0.15

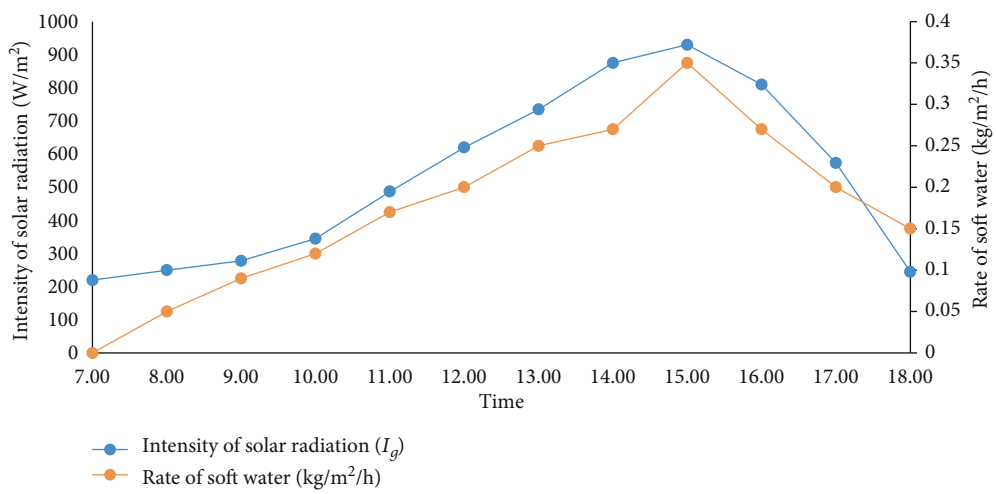

Figure 4: Rate of generation and solar intensity versus time (Al foil on CPC).

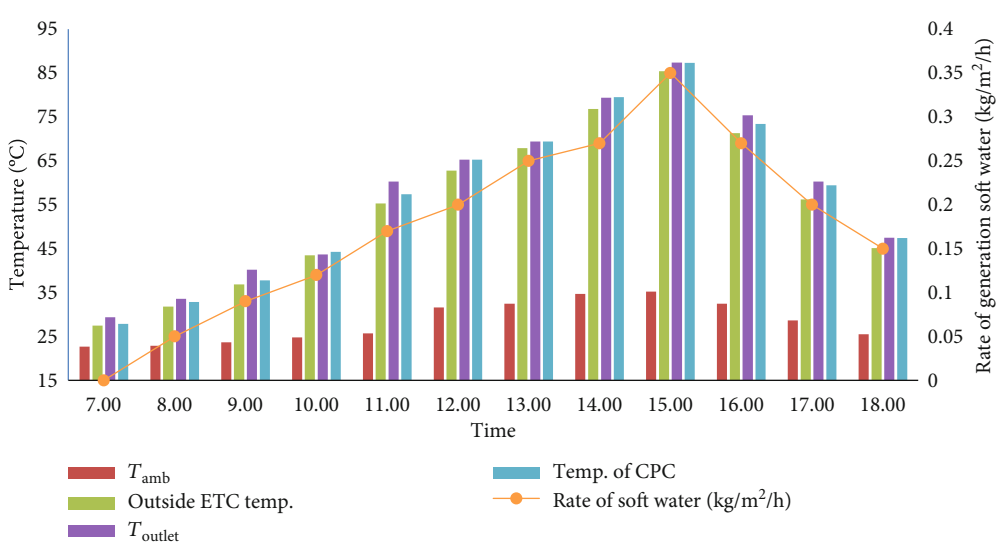

Figure 5: Variations of the rate of generation and measuring temperatures versus time (aluminum foil).

Table 3: Hourly variations of measured parameters in May 2018 with reflective white paint of CPC.

Time	The intensity of solar radiation (I_g)	Ambient temp. (T_{amb})	Outside ETC temp.	Outlet water temp.	Temp. of CPC	Wind velocity (m/sec)	Rate of soft water (kg/m^2/h)
07:00	220	22.7	27.5	29.4	27.9	3.20	0.00
08:00	250	22.9	31.8	33.6	32.9	3.52	0.05
09:00	278	23.7	36.9	40.2	37.8	3.53	0.09
10:00	345	24.8	43.5	43.7	44.3	4.32	0.12
11:00	487	25.7	55.3	60.3	57.4	4.50	0.17
12:00	620	31.6	62.8	65.3	65.3	5.00	0.20
13:00	735	32.5	67.9	69.4	69.4	5.03	0.25
14:00	875	34.7	76.8	79.4	79.5	5.42	0.27
15:00	930	35.2	85.4	87.4	87.3	4.83	0.35
16:00	810	32.5	71.3	75.4	73.4	4.20	0.27
17:00	573	28.7	56.2	60.3	59.4	4.01	0.20
18:00	245	25.5	45.1	47.5	47.4	3.82	0.15

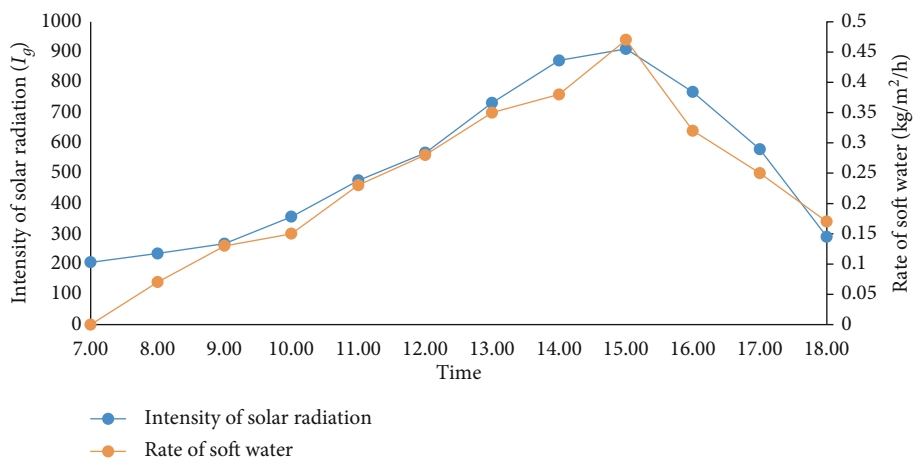

Figure 6: Rate of soft water generation and solar intensity versus time (reflective white paint on CPC).

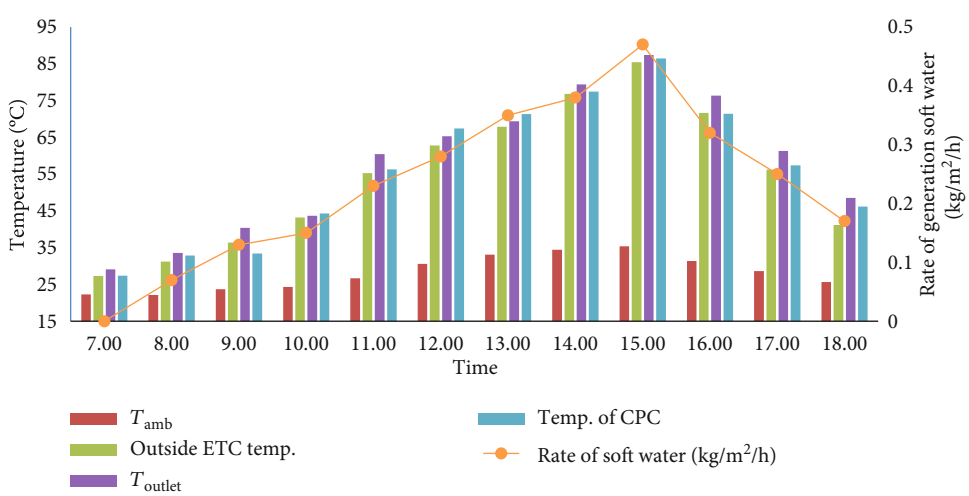

Figure 7: Variations of the rate of generation and measuring temperatures versus time (reflective white paint).

Table 4: Hourly variations of measured parameters in May 2018 with chrome mirror silver vinyl wrap material of CPC.

Time	The intensity of solar radiation (I_g)	Ambient temp. (T_{amb})	Outside ETC tempt	Outlet water temp.	Temp. of CPC	Wind velocity (m/sec)	Rate of soft water (kg/m^2/h)
07:00	220	22.7	27.5	29.4	27.9	3.20	0.00
08:00	250	22.9	31.8	33.6	32.9	3.52	0.05
09:00	278	23.7	36.9	40.2	37.8	3.53	0.09
10:00	345	24.8	43.5	43.7	44.3	4.32	0.12
11:00	487	25.7	55.3	60.3	57.4	4.50	0.17
12:00	620	31.6	62.8	65.3	65.3	5.00	0.20
13:00	735	32.5	67.9	69.4	69.4	5.03	0.25
14:00	875	34.7	76.8	79.4	79.5	5.42	0.27
15:00	930	35.2	85.4	87.4	87.3	4.83	0.35
16:00	810	32.5	71.3	75.4	73.4	4.20	0.27
17:00	573	28.7	56.2	60.3	59.4	4.01	0.20
18:00	245	25.5	45.1	47.5	47.4	3.82	0.15

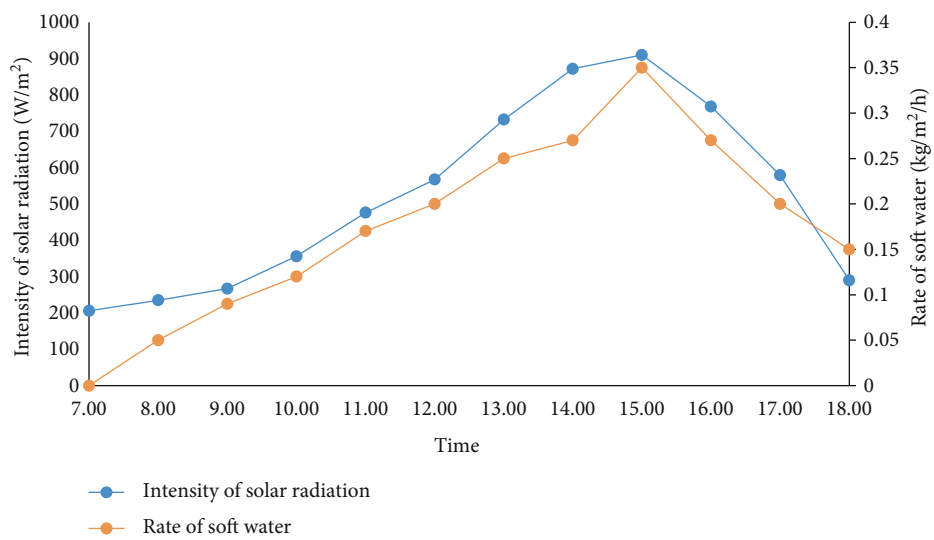

Figure 8: Rate of generation and solar intensity versus time (chrome mirror silver vinyl wrap on CPC).

certain time, the temperature of the water inside the ETC tube continuously increases which will be useful for the formation of steam; due to the effect of the formation of bubbles on the surface condenser, distilled water droplets are formed which will be collected in a bottle. Due to the continuous increase in solar radiation from 10:00 AM to 4:00 PM, the rate of generation of soft water will be increased and reaches its higher values of 1.5 kg/h at 3:00 PM, and finally, the rate of generation of soft water at the end of the day is 1.7 kg/h at 6:00 PM. Figure 4 shows the effect of the rate of generation and intensity of solar radiation with time as Al foil material was used on the compound parabolic concentrator. Figure 5 represents the study of the rate of soft water generation along with ambient temperature, outside ETC temperature, outlet temperature, and temperature of CPC with time. Result shows that the maximum temperature (85-90°C) was reached at 15:00 hours and 0.35 kg/m^2/h soft water got generated (using Al foil material used in CPC).

During the experimentation, the hourly changes continuously monitored and parameters that are measured were the ambient temperature, outside evacuated tube temperature, outlet water temperature, temperature of the CPC intensity of the solar radiation, wind velocity, and rate of the generation of freshwater, and the experiments conducted by CPC are painted with reflective white paint (as shown in Table 3).

Figure 6 shows the condition where reflective white paint material is painted on the compound parabolic concentrator, and the relationship between the intensity of solar radiation and the time effect of the rate of soft water generation. Figure 7 shows the relationship of the rate of soft water generation along with ambient temperature, outside ETC temperature, outlet temperature, and temperature of CPC with time. As the result shows, at 15:00 hours, maximum temperature (90-95°C) was reached with 0.45 kg/m^2/h soft water generated (using reflective white paint material used in CPC). In the afternoon time, the maximum intensity of solar

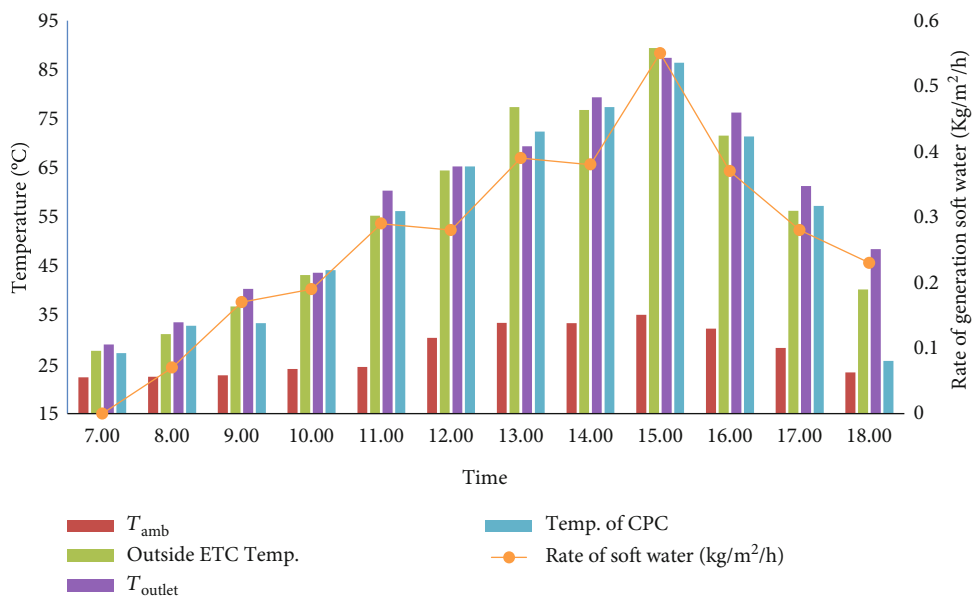

Figure 9: Variations of the rate of generation and measuring temperatures versus time (chrome mirror silver vinyl wrap).

Table 5: Hourly variations of measured parameters in May 2018 with Mylar material of CPC.

Time	The intensity of solar radiation (I_g)	Ambient temp. (T_{amb})	Outside ETC temp.	Outlet water temp.	Tempt. of CPC	Wind velocity (m/sec)	Rate of soft water (kg/m^2/h)
07:00	220	22.7	27.5	29.4	27.9	3.20	0.00
08:00	250	22.9	31.8	33.6	32.9	3.52	0.05
09:00	278	23.7	36.9	40.2	37.8	3.53	0.09
10:00	345	24.8	43.5	43.7	44.3	4.32	0.12
11:00	487	25.7	55.3	60.3	57.4	4.50	0.17
12:00	620	31.6	62.8	65.3	65.3	5.00	0.20
13:00	735	32.5	67.9	69.4	69.4	5.03	0.25
14:00	875	34.7	76.8	79.4	79.5	5.42	0.27
15:00	930	35.2	85.4	87.4	87.3	4.83	0.35
16:00	810	32.5	71.3	75.4	73.4	4.20	0.27
17:00	573	28.7	56.2	60.3	59.4	4.01	0.20
18:00	245	25.5	45.1	47.5	47.4	3.82	0.15

radiation (800-930 W/m^2) was achieved using reflective white paint on CPC.During the experimentation, continuous monitoring of the hourly change of the measured parameters such as the ambient temperature, outside evacuated tube temperature, outlet water temperature, temperature of the CPC along with the intensity of the solar radiation, wind velocity, and rate of the generation of freshwater of one of the experiments since May 2018 with reflective white paint of CPC is shown in Table 4.

During the experimentation, continuous monitoring of the hourly change of the measured parameters such as the ambient temperature, outside evacuated tube temperature, outlet water temperature, temperature of the CPC along with the intensity of the solar radiation, wind velocity, and rate of the generation of freshwater of one of the experiments since May 2018 with chrome mirror silver vinyl wrap of CPC is shown in Table 4.Figure 8 shows the effect of the rate of soft water generation and the intensity of solar radiation when mirror silver vinyl material was wrapped on the compound parabolic concentrator. Figure 9 shows the study of the rate of soft water generation along with ambient temperature, outside ETC temperature, outlet temperature, and temperature of CPC with time. The result also shows that at 15:00 hours, maximum temperature (90-93°C) with 0.53 kg/m^2/h soft water was generated when chrome mirror silver vinyl material was wrapped on CPC. In the afternoon time, the maximum intensity of solar radiation (800-930 W/m^2) was achieved using chrome mirror silver vinyl wrap on CPC.

During this experimentation, the hourly changed parameters that were monitored and measured were the ambient temperature, outside evacuated tube temperature, outlet water temperature, temperature of the CPC, intensity of the solar radiation, wind velocity, and rate of the generation of freshwater (with Mylar of CPC shown in Table 5).

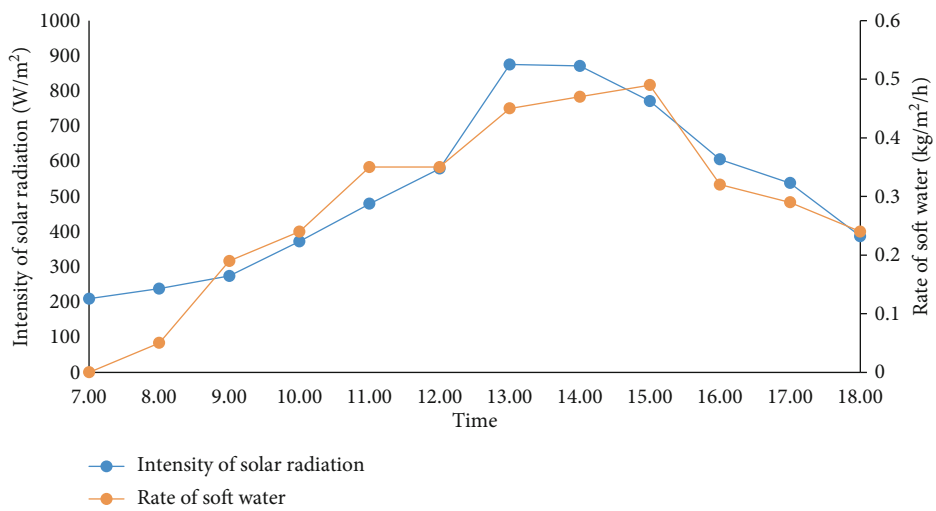

Figure 10: Rate of generation and solar intensity versus time (Mylar on CPC).

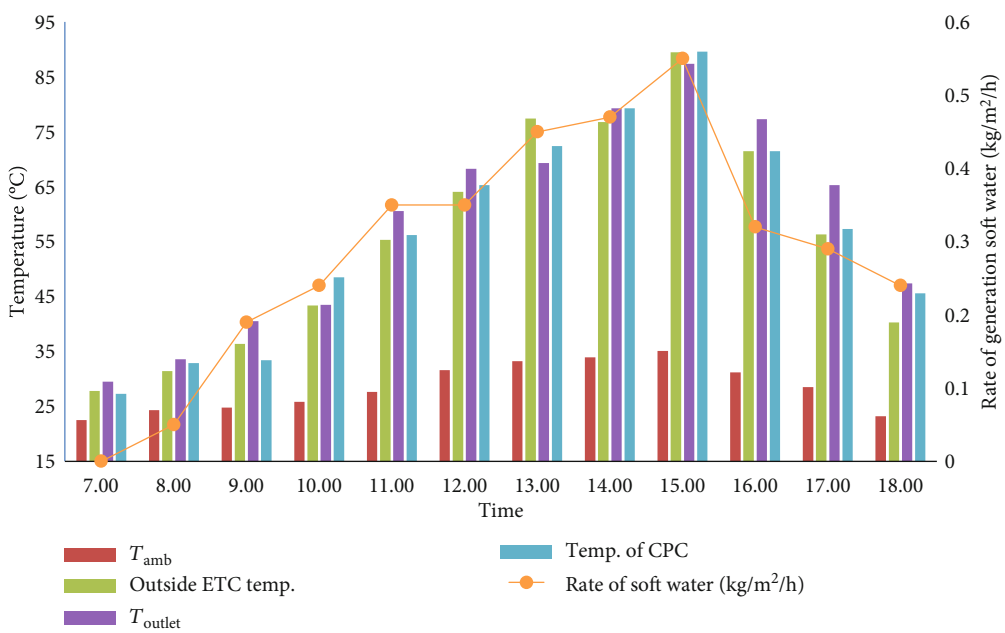

Figure 11: Variations of the rate of generation and measuring temperatures versus time (Mylar).

Figure 10 shows the relationship between the rate of generation and the intensity of solar radiation with time when Mylar material is used on the compound parabolic concentrator. Figure 11 shows the relationship of the rate of soft water generation along with the ambient temperature, outside ETC temperature, outlet temperature, and temperature of CPC with time. As the result shows, at 15:00 hours, a maximum temperature (90-93°C) with 0.55 kg/m^2/h soft water was generated using the Mylar material used in CPC. In the afternoon time, maximum intensity of solar radiation (750-890 W/m^2) was achieved while using Mylar on CPC.

From the tables, it is observed that there is a time lag of about an hour between the maximum point of the curvature part and the maximum intensity of solar radiation because

Table 6: Various materials used on CPC with reflectivity and rate of generation of soft water.

Sr. no.	Material on CPC	Reflectivity	Rate of generation of soft water in liter/day
01	Aluminum foil	90%	2.15
02	Reflective white paint	94%	2.80
03	Chrome mirror silver vinyl wrap	95%	3.20
04	Mylar	98%	3.50

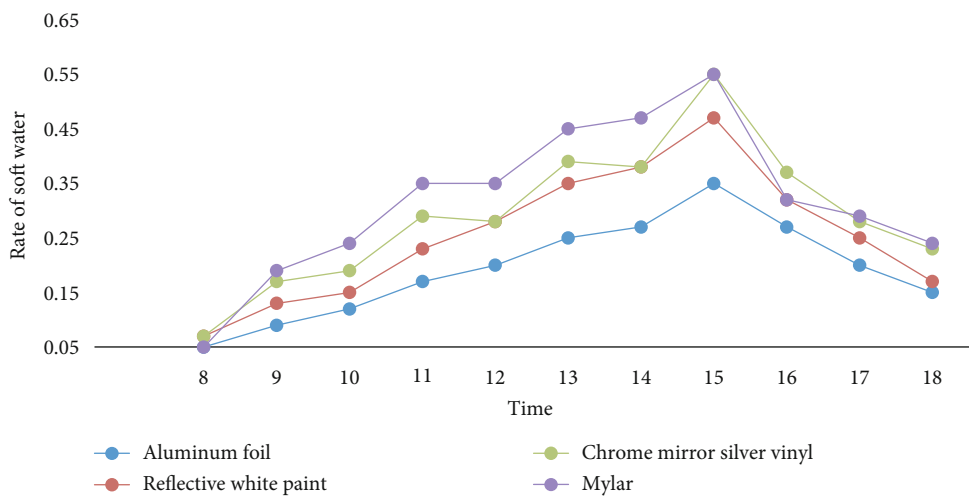

Figure 12: Comparison of various materials on CPC with the rate of generation of soft water.

there is good agreement between time and intensity of solar radiation, which will positively impact the maximum generation of freshwater. The variations of the rate of generation and various temperatures with respect to time is shown in Figure 11. It is observed that there is also good agreement between temperatures and the generation of the freshwater. This is an acceptable fact due to the continuously increasing CPC temperature with good reflecting materials. The rates of generation of freshwater of some previous research works and those of the present study were compared in above figures. It is observed that there was a significant increase in the rate of generation of freshwater per day.

4.2. Effect of Material on CPC. In the hybrid solar groundwater desalination process, the reflectivity of the compound parabolic concentrator plays an important role because of the absorption of solar radiation and reflection of the evacuated tube. During the entire experimentation, four different materials are used such as aluminum foil, reflective white paint, chrome mirror silver vinyl wrap, and Mylar. Table 6 shows that various materials are used on CPC with reflectivity and rate of generation of soft water.

Therefore, to reconstruct this hypothesis, four different CPC made up of different materials (aluminum foil, reflective white paint, chrome mirror silver vinyl wrap, and Mylar) were employed. As per the prediction, the desalination rates were expected to be unmatched for all the different CPC materials. The highest results were obtained from the Mylar material that gives 3.30 kg/h/day.

Figure 12 shows the comparison of various materials on CPC with the rate of generation of soft water. The Mylar material offers the highest rate of soft water (0.55 kg/m^2/h).

4.2.1. Effects of Aluminum Foil Material on CPC. Aluminum foil is one of the lightweight materials with a reflectivity of 90%. It is suitable for ultraviolet reflecting radiations. The aluminum foil has a thickness of less than 0.2 mm which will be measured through a micrometer. The thin foils are sometimes laminated with plastics. The shiny side of the aluminum foil is strongly pasted over the compound parabolic aluminum sheet to get the maximum reflectivity. The reflectivity of the bright aluminum foil is in the range of 88-90%. The result shows that to improve the rate of generation of soft water, approximately 2.15 liters of soft water per day must be obtained.

4.2.2. Effect of Reflective White Paint Material on CPC. Reflective white paints have been widely available and have been used to reflect the heat component of incident sunlight. Reflective white paint is used on the compound parabolic concentrator to get the maximum reflection of solar radiation towards the evacuated tube for maximum heat transfer. The reflectivity of the bright aluminum foil is in the range of 93-94%. The results show that to improve the rate of generation of soft water, approximately 2.80 liters of soft water per day must be obtained.

4.2.3. Effect of Chrome Mirror Silver Vinyl Wrap Material on CPC. Chrome mirror silver vinyl wrap material has a mirror-like finish which has higher reflectivity in the range of 94-95%. The material should be lightweight and easily repositioned and stretched for the exact filament. When solar radiation is impacted to the CPC with chrome mirror silver vinyl wrap, it should be reflected within less time toward the evacuated tube collector. The results show that to improve the rate of generation of soft water, approximately 3.20 liters of soft water per day must be obtained.

4.2.4. Effect of Mylar Material on CPC. Mylar is one of the materials named for stretched polyester resin which will be a clear, thin plastic. The thickness of the said material is 0.01 micrometers. Its higher reflective insulation on CPC will work on the entire process of heat transfer. The Mylar polyester film has the advantage of retaining good physical properties between the temperature range of −70°C and 150°C and which will be more suitable for CPC. As the main effect on Mylar on CPC due to higher reflectivity, 98% maximum solar radiation-reflected evacuated tubes will be useful for water heating within less time. The results show that approximately 3.50 liters of soft water is obtained per day.

4.3. Effect of Distance between ETC and CPC. The distance between ETC and CPC is the focusing parameter that seriously affects the performance of the hybrid solar desalination system. The effect of the distance between ETC and CPC on the hybrid desalination system generation of soft water has also been investigated in this study. In this contrast, three heights were preselected between ETC and CPC to the experiment. The maximum generation of freshwater obtained in a hybrid solar desalination system is 2 cm. Continuously increasing the distance will get a little amount of freshwater, and very near/close ETC-CPC distance also gets the same results. This is due to the maximum solar radiation loss observed in ETC-CPC. A consequence is that the effective distance of ETC-CPC should be considered. In this experiment, the optimum value for distance is 2 cm. Along with it, it is observed that the rate of generation of freshwater is very smooth after 4:00 PM because the intensity of solar radiation decreases after 3:00-4:00 PM; also, temperature withstands fast dropdown in the timing of 3:00 to 6:00 PM. From a comparison point of view, it was seen that Al-Nimr et al. [43] could obtain 0.5296 liters of soft water per day for the climatic conditions of Irbid, Jordan, by using their developed hybrid solar wind water desalination system. However, the proposed single-stage hybrid (ETC+CPC) groundwater solar desalination system with aluminum foil as a reflecting material could generate 1.9 liters of soft water per day. Further, the use of Mylar as a reflecting material could generate 3.5 liters of soft water per day.

5. Conclusion

A single-stage hybrid (ETC+CPC) groundwater solar desalination system consisting of the hard water tank, ETC, CPC, surface condenser, and collecting water bottle was investigated experimentally. The performance of the hybrid groundwater solar desalination system was evaluated by using different CPC made up of layers of aluminum foil, reflective white paint, chrome mirror silver vinyl wrap, and Mylar.

Concluding remarks can be briefly expressed as follows:

(i) Experimental results concluded that Mylar was the best CPC material for the maximum generation of freshwater throughout the day

(ii) Using an optimum distance between ETC and CPC will get a good agreement for the generation of freshwater

(iii) The proposed single-stage hybrid (ETC+CPC) groundwater solar desalination system with aluminum foil as a reflecting material could generate 1.9 l soft water per day

(iv) The use of Mylar as a reflecting material could generate 3.4 l soft water per day

Data Availability

The data used to support the findings of this study are included within the article.

Conflicts of Interest

The authors declare that there is no conflict of interest regarding the publication of this paper.

Acknowledgments

The authors would like to acknowledge Cummins College of Engineering for Women, Pune, 411052 Maharashtra, India, for providing facilities to conduct pilot experiments and the Board of College and University Development, Savitribai Phule Pune University (SPPU), Pune, under Grant No. 15ENG000570 for the financial support.

References

[1] B. Ghorbani, M. Mehrpooya, and M. Sadeghzadeh, "Developing a tri-generation system of power, heating, and freshwater (for an industrial town) by using solar flat plate collectors, multi-stage desalination unit, and Kalina power generation cycle," *Energy Conversion and Management*, vol. 165, pp. 113–126, 2018.

[2] A. B. Baci, M. Salmi, Y. Menni, S. Ghafourian, M. Sadeghzadeh, and M. Ghalandari, "A new configuration of vertically connecting solar cells: solar tree," *International Journal of Photoenergy*, vol. 2020, Article ID 8817440, 8 pages, 2020.

[3] M. H. Ahmadi, H. Sayyaadi, A. H. Mohammadi, and M. A. Barranco-Jimenez, "Thermo-economic multi-objective optimization of solar dish-Stirling engine by implementing evolutionary algorithm," *Energy Conversion and Management*, vol. 73, pp. 370–380, 2013.

[4] S. A. Kalogirou, "Seawater desalination using renewable energy sources," *Progress in Energy and Combustion Science*, vol. 31, no. 3, pp. 242–281, 2005.

[5] M. T. Ali, H. E. S. Fath, and P. R. Armstrong, "A comprehensive techno-economical review of indirect solar desalination," *Renewable and Sustainable Energy Reviews*, vol. 15, no. 8, pp. 4187–4199, 2011.

[6] S. A. Kedar, A. K. Bewoor, and S. Madhusudan, "Solar desalination system using evacuated tube collector and compound parabolic concentrator - theoretical approach," *National Conference Advance Electrical Engineering Energy Science*, pp. 30–62, 2016.

[7] H. Moungar, A. Ahmed, S. Youcef, and H. Aabdelkrim, "Immersed fins influence on the double slope solar still production in south Algeria climatic condition," *International Journal of Heat and Technology*, vol. 35, no. 4, pp. 1065–1071, 2017.

[8] R. Sathyamurthy, P. Nagarajan, M. Edwin et al., "Experimental investigations on conventional solar still with sand heat energy storage," *International Journal of Heat and Technology*, vol. 34, no. 4, pp. 597–603, 2016.

[9] M. M. Morad, H. A. M. El-Maghawry, and K. I. Wasfy, "Improving the double slope solar still performance by using flat-plate solar collector and cooling glass cover," *Desalination*, vol. 373, pp. 1–9, 2015.

[10] P. S. Bhambare, M. C. Majumder, and C. V. Sudhir, "Solar thermal desalination: a sustainable alternative for Sultanate of Oman," *International Journal of Renewable Energy Resources*, vol. 8, pp. 733–751, 2018.

[11] S. A. Kedar, K. A. Raj, and A. K. Bewoor, "Thermal analysis of solar desalination system using evacuated tube collector," *AIP Conference Proceedings*, vol. 2039, p. 20061, 2018.

[12] S. A. Kedar, K. Arul Raj, and A. Bewoor, "Design and analysis of solar desalination system using compound parabolic concentrator," *IOP Conference Series: Materials Science and Engineering*, vol. 455, p. 12063, 2018.

[13] S. A. Kedar, K. A. Raj, and A. K. Bewoor, "Performance analysis of hybrid solar desalination system using ETC and CPC," *SN Applied Sciences*, vol. 1, no. 9, p. 965, 2019.

[14] L. Grosu, A. Mathieu, P. Rochelle, M. Feidt, M. H. Ahmadi, and M. Sadeghzadeh, "Steady state operation exergy-based optimization for solar thermal collectors," *Environmental Progress & Sustainable Energy*, vol. 39, no. 3, 2020.

[15] M. Sadeghzadeh, M. H. Ahmadi, M. Kahani, H. Sakhaeinia, H. Chaji, and L. Chen, "Smart modeling by using artificial intelligent techniques on thermal performance of flat-plate solar collector using nanofluid," *Energy Science & Engineering*, vol. 7, no. 5, pp. 1649–1658, 2019.

[16] H. Olia, M. Torabi, M. Bahiraei, M. H. Ahmadi, M. Goodarzi, and M. R. Safaei, "Application of nanofluids in thermal performance enhancement of parabolic trough solar collector: state-of-the-art," *Applied Sciences*, vol. 9, no. 3, p. 463, 2019.

[17] R. Loni, A. Kasaeian, K. Shahverdi, E. Askari Asli-Ardeh, B. Ghobadian, and M. H. Ahmadi, "ANN model to predict the performance of parabolic dish collector with tubular cavity receiver," *Mechanics & Industry*, vol. 18, no. 4, p. 408, 2017.

[18] R. Jilte, M. H. Ahmadi, V. Kalamkar, and R. Kumar, "Solar flux distribution study in heat pipe cavity receiver integrated with biomass gasifier," *International Journal of Energy Research*, vol. 44, no. 9, pp. 7698–7712, 2020.

[19] A. Rafiei, R. Loni, M. H. Ahmadi et al., "Sensitivity analysis of a parabolic trough concentrator with linear V-shape cavity," *Energy Science & Engineering*, vol. 8, no. 10, pp. 3544–3560, 2020.

[20] K. Sampathkumar, T. V. Arjunan, P. Pitchandi, and P. Senthilkumar, "Active solar distillation–a detailed review," *Renewable and Sustainable Energy Reviews*, vol. 14, no. 6, pp. 1503–1526, 2010.

[21] F. R. Siddiqui, N. A. S. Elminshawy, and M. F. Addas, "Design and performance improvement of a solar desalination system by using solar air heater: experimental and theoretical approach," *Desalination*, vol. 399, pp. 78–87, 2016.

[22] A. E. Kabeel and E. M. S. El-Said, "A hybrid solar desalination system of air humidification, dehumidification and water flashing evaporation: part II. Experimental investigation," *Experimental Investigation. Desalination*, vol. 341, pp. 50–60, 2014.

[23] M. Sapre, A. Auti, and T. Singh, "Design and manufacturing of absorber for solar desalination system," *Applied Mechanics and Materials*, vol. 446-447, pp. 716–720, 2013.

[24] H. Zheng, Z. Chang, Z. Chen, G. Xie, and H. Wang, "Experimental investigation and performance analysis on a group of multi-effect tubular solar desalination devices," *Desalination*, vol. 311, pp. 62–68, 2013.

[25] A. Khalil, S. A. El-Agouz, Y. A. F. El-Samadony, and A. Abdo, "Solar water desalination using an air bubble column humidifier," *Desalination*, vol. 372, pp. 7–16, 2015.

[26] M. I. Ahmed, M. Hrairi, and A. F. Ismail, "On the characteristics of multistage evacuated solar distillation," *Renewable Energy*, vol. 34, no. 6, pp. 1471–1478, 2009.

[27] C. Wu, Z. Li, J. Zhang, Y. Jia, Q. Gao, and X. Lu, "Study on the heat and mass transfer in air-bubbling enhanced vacuum membrane distillation," *Desalination*, vol. 373, pp. 16–26, 2015.

[28] S. Jahangiri Mamouri, H. Gholami Derami, M. Ghiasi, M. B. Shafii, and Z. Shiee, "Experimental investigation of the effect of using thermosyphon heat pipes and vacuum glass on the performance of solar still," *Energy*, vol. 75, pp. 501–507, 2014.

[29] V. K. Dwivedi and G. N. Tiwari, "Comparison of internal heat transfer coefficients in passive solar stills by different thermal models: an experimental validation," *Desalination*, vol. 246, no. 1-3, pp. 304–318, 2009.

[30] N. Rahbar and J. Esfahani, "Experimental study of a novel portable solar still by utilizing the heatpipe and thermoelectric module," *Desalination*, vol. 284, pp. 55–61, 2012.

[31] H. Kargar Sharif Abad, M. Ghiasi, S. Jahangiri Mamouri, and M. B. Shafii, "A novel integrated solar desalination system with a pulsating heat pipe," *Desalination*, vol. 311, pp. 206–210, 2013.

[32] V. Dimri, B. Sarkar, U. Singh, and G. N. Tiwari, "Effect of condensing cover material on yield of an active solar still: an experimental validation," *Desalination*, vol. 227, no. 1-3, pp. 178–189, 2008.

[33] C. M and A. Yadav, "Water desalination system using solar heat: a review," *Renewable and Sustainable Energy Reviews*, vol. 67, pp. 1308–1330, 2017.

[34] L. Zuo, Y. Yuan, Z. Li, and Y. Zheng, "Experimental research on solar chimneys integrated with seawater desalination under practical weather condition," *Desalination*, vol. 298, pp. 22–33, 2012.

[35] L. Zuo, Y. Zheng, Z. Li, and Y. Sha, "Solar chimneys integrated with sea water desalination," *Desalination*, vol. 276, no. 1-3, pp. 207–213, 2011.

[36] T. Ming, T. Gong, R. K. de Richter, C. Cai, and S. A. Sherif, "Numerical analysis of seawater desalination based on a solar chimney power plant," *Applied Energy*, vol. 208, pp. 1258–1273, 2017.

[37] H. B. Bacha, "Dynamic modeling and experimental validation of a water desalination prototype by solar energy using humidification dehumidification process," *Desalination*, vol. 322, pp. 182–208, 2013.

[38] X. Li, G. F. Yuan, Z. Wang, H. Li, and Z. Xu, "Experimental study on a humidification and dehumidification desalination system of solar air heater with evacuated tubes," *Desalination*, vol. 351, pp. 1–8, 2014.

[39] F. Cao, Q. Liu, and H. Xiao, "Experimental Study of a Humidification-Dehumidification Seawater Desalination System Combined with the Chimney," *International Journal of Photoenergy*, vol. 2020, Article ID 1937040, 9 pages, 2020.

[40] G. Murali, M. Sankeerthana, A. Srinath, and C. Sivakandhan, "Solar still productivity enhancement by PCM and nano-PCM composites as energy storage," *Test Engineering and Management*, vol. 83, pp. 9579–9587, 2020.

[41] G. Murali, A. T. M. Sundari, S. Raviteja, S. Chanukyachakravarthi, and M. Tejpraneeth, "Experimental study of thermal performance of solar aluminium cane air heater with and without fins," *Materials Today Proceedings*, vol. 21, pp. 223–230, 2020.

[42] G. Murali, G. Sandeep, N. Hari, M. Praveen, and B. Neeraj, "Experimental studies on solar aluminium can air heater with and without latent heat storage," *International Journal of*

Mechanical Engineering and Technology, vol. 9, no. 4, pp. 145–155, 2018.

[43] M.'. A. al-Nimr, S. M. Kiwan, and S. Talafha, "Hybrid solar-wind water distillation system," *Desalination*, vol. 395, pp. 33–40, 2016.

[44] S. A. Kedar, A. R. Kumaravel, and A. K. Bewoor, "Experimental investigation of solar desalination system using evacuated tube collector," *International Journal of Heat and Technology*, vol. 37, no. 2, pp. 527–532, 2019.

[45] S. A. Kedar, G. Murali, and A. K. Bewoor, "Effective hybrid solar groundwater desalination in rural areas," *International Transaction Journal of Engineering, Management & Applied Sciences & Technologies*, vol. 12, no. 3, pp. 1–10, 2021.

[46] S. A. Kedar and A. K. Bewoor, "Patent on "solar desalination system" ref. no.201921032482," *The Patent office Journal*, vol. 7/2021, p. 7767, 2019.

[47] H. Panchal, K. K. Sadasivuni, M. Israr, and N. Thakar, "Various techniques to enhance distillate output of tubular solar still: a review," *Groundwater for Sustainable Development*, vol. 9, article 100268, 2019.

[48] H. Panchal, D. Mevada, K. K. Sadasivuni, F. A. Essa, S. Shanmugan, and M. Khalid, "Experimental and water quality analysis of solar stills with vertical and inclined fins," *Groundwater for Sustainable Development*, vol. 11, article 100410, 2020.

Hindawi
International Journal of Photoenergy
Volume 2021, Article ID 6681084, 11 pages
https://doi.org/10.1155/2021/6681084

Research Article

Technoeconomic Performance Analysis of Solar Tracking Methods for Roof-Type Solar Power Plants and Electric Vehicle Charging Stations

Tahsin Boyekin [1] **and İsmail Kıyak** [2]

[1] *Department of Electrical and Electronics Engineering, Institute of Pure and Applied Sciences, Marmara University, Istanbul, Turkey*
[2] *Department of Electrical and Electronics Engineering, Faculty of the Technology, Marmara University, Istanbul, Turkey*

Correspondence should be addressed to Tahsin Boyekin; tahsinboyekin@marun.edu.tr

Received 13 November 2020; Revised 8 March 2021; Accepted 11 March 2021; Published 7 April 2021

Academic Editor: Hafiz Muhammad Ali

Copyright © 2021 Tahsin Boyekin and İsmail Kıyak. This is an open access article distributed under the Creative Commons Attribution License, which permits unrestricted use, distribution, and reproduction in any medium, provided the original work is properly cited.

In building integrated photovoltaic (BIPV) solar energy projects, cost effectiveness, durability, and long-term reliability are among the criteria that should be taken into consideration as well as the gain in electricity generation efficiency. Also, in a study, it is stated that a dual-axis solar tracking system occupies approximately 100% more space than a single-axis system and 160% more than a fixed-angle system. It has been observed that most of the studies that are mounted on the building and include a tracking system are small-scale experimental studies. The aim of this article is to present a systematic analysis with a low investment cost, a low operating cost, and high reliability, in a real application especially for roof applications in buildings. Three buildings in the same location and with the same roof area were selected. Photovoltaic power plants with 23.68 kW power were installed; these panels had three types: fixed-angle, manually controlled, and single-axis solar tracking systems. The energy generation system is connected to the network with a double-sided meter, and there is a double-sided energy flow. The energy produced is used to meet the energy needs of the vehicle charging station and common areas of the buildings. Although the single-axis tracking system is 27.85% more efficient than other energy generation methods, the manually adjusted method has proven to have the shortest amortization time. The study also presents shading, which is a serious problem in large-scale roof projects, and the area covered by the module per unit watt produced.

1. Introduction

Solar power plants (SPPs) convert sunlight into electrical energy. The intensity of solar power outside the atmosphere is approximately 1370 W/m^2. However, much of this is lost due to the atmosphere, and the intensity of the solar power that reaches the Earth's surface varies between 0 and 1100 W/m^2 [1]. However, even a small portion of the remaining energy is considerably higher than the existing energy requirements [2]. Studies on solar energy have accelerated since the 1970s; photovoltaic (PV) technology is now widespread, offering increased efficiency and decreased production costs relative to fossil fuels [3]. Solar energy is also unlimited, making it better able to meet the increasing demands for energy [4–6]. Solar cells form modules with a certain number of serial or parallel connections. These modules make up arrays (also with a certain number of serial or parallel connections), and these arrays in turn comprise SPPs. There are many types of cells in PV modules [7–12]:

(i) Crystalline and multicrystalline silicon solar cells

(ii) Thin-film solar cells (a-Si, cadmium telluride, and CIS)

(iii) Nanotechnology-based solar cells (tandem, super tandem, and intermediate-band solar cells, etc.)

The most frequently used types are crystalline silicon, cadmium telluride, and CIS/CIGS cells [3]. The types of SPPs vary according to their structure. Each has various applications,

including single-axis and dual-axis solar tracking systems; roof, field, and facade applications; and grid-tied and off-grid connections [13–20]. Grid-tied SPPs can be high-power (>1-MW) systems, but their use as low-power systems in buildings is also common. These grid-tied systems can receive energy from the grid when required and can also provide excess energy to feed the grid [21]. Grid-tied systems do not need energy storage; it is sufficient to convert direct current (DC) electricity into alternating current (AC) electricity with the help of an inverter so as to conform to the [22–25]. However, nonlinear voltage waves and harmonics occur in such systems. The mathematical form of these nonlinear waves is determined using Fourier series.

Solar energy is used to generate electricity in all areas where electricity is available. PV modules are sometimes utilized for visual comfort and for the shade that they provide, in addition to their energy production [26–29]. Building-based applications were used in this project. SPPs that are usually installed on the roofs of buildings can also be installed on facades. In one developing technology, semitransparent solar modules can be installed instead of glass in some applications, although these modules have low efficiency [30–34]. Furthermore, some solar panels can be used in place of shutters; energy production can be increased by adding a solar-tracking system to these shutters [5].

Shading is the most important consideration in projections for rooftop SPPs. The amount of shade that can appear on the part of the building where the SPP will be installed should be analysed. Other building that are close to the SPP (especially taller ones) and other rooftop structures should also accounted for [35]. The shading analysis involves modelling these structures using a simulation program such as PVSyst or PV*SOL [36]. The results describe the percentage shade for each module. The modules with high shading should be replaced with modules that would be exposed to more light. In this project, these analyses were performed using the PV*SOL program [37–41].

The basic criteria to be considered in building-integrated solar energy systems can be listed as follows: solar tracking system cost, installation cost, logistics cost, space usage, operation and maintenance cost, tracking system power consumption, performance and energy gain, tracking method's solar tracking accuracy, service life, and resistance to wind and other natural abrasives. In a study where the system was installed at a latitude angle of 36.25°N, it was determined that a dual-axis solar tracking system was able to generate approximately 30% more energy than a fixed-angle system, but the area covered was approximately 100% more than a single-axis tracker and approximately 160% more than a fixed-angle system [42]. The results of another experimental study show that the total energy consumption of the single-axis tracking system is approximately 2-8% of the energy produced by the grid-connected PV system and approximately 5-12% in the dual-axis solar tracking system [43]. In this respect, when compared to building-mounted solar energy generation systems ground projects, it can be stated that project logistics, installation cost, operating cost, overall efficiency, and service life are the factors that should be paid more attention to. The aim of this study is to perform analysis on a real-time project with optimal efficiency that adopts low investment and operating costs that can be applied on building roofs, as opposed to tracking systems using various solar tracking methods including double-axis (two axis of rotation for better efficiency), hybrid model (includes both sensors and data/time to analyse the best position), polar-aligned single-axis (the tilted axis is aligned to the polar star), and azimuth/tilt roll mechanism (the ground is called azimuth axis) [22].

The main contributions of this study to the literature are as follows:

(1) In an area of approximately 1000 m^2, three different methods have been tested. This is the first academic study to be carried with a roof this size

(2) This is the most innovative approach that presents detailed cost analysis and depreciation periods among the large-scale rooftop projects

(3) This is an original study in terms of the application of minimum shading and maximum use of space among roof-mounted applications

(4) The study also provides the instantaneous monitoring of the theoretical and application performances of the system and the control of its economic feasibility

Other chapters of this paper are organized as follows: Section 2 presents a theoretical model analysis. Section 3 presents the details of the project that was implemented. Design components, energy production/consumption estimates, and application information are explained in detail. Section 4 presents the electrical system performance and cost analysis. And lastly, Section 5 provides study results and recommendations.

2. Literature Overview

In Ref. [44], researchers have compared the thermal energy produced at a specific solar position with the energy demanded and implemented a solar tracking system that determines the solar position for the new state. In Ref. [22] review study, various solar tracking system methods including single-axis, dual-axis, polar-axis, open-loop, closed-loop, hybrid model, and azimuth/tilt roll mechanism were discussed and compared with existing solar tracking methods. In Ref. [45], a dual-axis solar tracking system was designed by using the sensor information and control technologies of the solar cell to increase the overall efficiency of the PV system. In Ref. [46], three angles to the sun were estimated by predicting the position of the sun during the day. In practice, when well-calibrated, results showing an improvement between 5 and 7% were obtained.

In Ref. [47], a review of the properties and functions of systems such as building-integrated concentrating photovoltaics (BICPV), building-integrated concentrating solar thermal (BICST), and building-integrated concentrating solar daylighting (BICSD), and BICPV/T, BICPV/D, BICST/D, and BICPV/T/D are presented. In Ref. [48], a PV system was

integrated into the facade of a high-rise building and Honeybee and Ladybug were used for the first time in this study as control logic, and 354734.7 kWh/year energy was produced. In Ref. [43], using the single-axis PV tracking system, it was determined that the total energy production increased up to 30.3% for a sunny day and 15.2% in average weather conditions. In Ref. [42], the study reports a design and industrial prototype of a large-scale dual-axis solar tracker consisting of a vertical axis moving platform and multirow elevation structures. In Ref. [49], the design options for PV structural cell types are investigated and the analysis of design options for BIPV systems using an electrical-module layout with additional interlayers are presented. In Ref. [50], although the choice of trackers depended mainly on the physical characteristics of the terrain, overall, this system has proven to be more efficient and advantageous than its single-axis and fixed counterparts.

In Ref. [51], the results show that the BIPV model can estimate the average daily energy efficiency of 6.2% and the temperature behind the module with an average difference of 1.74°C. In Ref. [52], a four-position controlled vertical axis method was used and it was observed that the overall efficiency increased by 2% in the experimental solar tracking prototype study. In Ref. [53], it was observed that the solar panel production efficiency increased up to 40% in the experimental application with 4 LDR sensors and Arduino controlled application. In Ref. [54], analyses with and without thermal absorbers were performed by using a three-dimensional combined heat transfer model to increase the efficiency of the PV module.

3. Background Theory

This section gives detailed analysis of PV modules' electrical performance, irradiation modeling, and array sizing.

3.1. PV Module Analysis and Irradiance Modelling. In this section, evaluations about the electrical components of a PV module are made. Some of these parameters can be represented as short-circuit current, open-circuit current under distinct radiation conditions, and array temperature. PV cell operating temperature is different from ambient temperature and also defines open-circuit voltage. Since the cell operating temperature changes depending on the ambient temperature and solar radiation, it can be calculated using Equation (1). Equations (3), (4), and (5) are used to predict PV open-circuit voltage, current, and power, respectively [55].

$$T_{\mathrm{c}} = T_{\mathrm{a}} + 0.03.H_T, \tag{1}$$

$$H_T = H_b R_b + H_d R_d + (H_b + H_d) R_r, \tag{2}$$

$$V_{\mathrm{oc}} = V_{\mathrm{oc},0} + \left(-\frac{2.3\mathrm{mV}}{C}\right)(T_{\mathrm{c}} - T_{\mathrm{a}}), \tag{3}$$

$$I = I_{\mathrm{PV}} - I_0\left[e^{\left(\frac{V+R_s.I}{\alpha V_t}\right)} - 1\right] - \frac{V + R_s.I}{R_p}, \tag{4}$$

$$P_{\mathrm{PV}} = k_1 H_T A\left[1 + k_2\left(T_{\mathrm{a}} - T'_{\mathrm{a}}\right)\right], \tag{5}$$

where T_c is the cell operating temperature, T_a is the ambient temperature, I_{PV} is the PV current, I_0 is the reverse current, α is a diode constant, V_{t} is the thermal voltage, R_{p} and R_{s} are the parallel and series equivalent resistances of the module, ε is the PV conversion rate, A is the PV surface area, H_t is the hourly PV power output (kWh/m^2), H_{b} is the beam radiation, H_{d} is the scattered radiation, and R_{b}, R_{d}, and R_{r} are the tilt elements for the beam, scattered, and reflected irradiation; k_1 refers to the typical distribution of modules and relevant data for a panel is included 0.095 to 0.105; and $k_2 = -0.47\%/°\mathrm{C}$.

Irradiance collected on a photovoltaic panel surface, I_t (W/m^2), can be expressed as

$$I_t = I_{\mathrm{f}} + I_{\mathrm{r}}, \tag{6}$$

where I_{f} (W/m^2) and I_{r} (W/m^2) is the expression that gives the radiation reaching the front and rear parts of the photovoltaic panel, respectively. I_{r} is included in the formulation only when bifacial modules are used. I_{f} can be explained as

$$I_{\mathrm{f}} = I_{\mathrm{dir,f}} + I_{\mathrm{dif,f}} + I_{\mathrm{gnd,f}}, \tag{7}$$

where $I_{\mathrm{dir,f}}$ (W/m^2),$I_{\mathrm{dif,f}}$ (W/m^2), and$I_{\mathrm{gnd,f}}$ (W/m^2) is the expression that gives the sum of the direct, scattered, and reflected radiation reaching the front of the photovoltaic panel. Expressions can be defined as

$$I_{\mathrm{dir,f}} = \mathrm{DNI}.\cos\left(A0I_{\mathrm{f}}\right), \tag{8}$$

where DNI (W/m^2) is the linear irradiance and $(A0I_{\mathrm{f}})$ (°) is the angel of ratio between DNI and the normal of the photovoltaic panel front surface.

$$I_{\mathrm{dif,f}} = \mathrm{DHI}.\left[(1 - F_1).\frac{1 + \cos(\theta_m)}{2} + F_1.\frac{a'}{c'} + |F_2.\sin(\theta_m)|\right], \tag{9}$$

where DHI (W/m^2) is the scattered horizontal irradiance, (θ_m) (°) is the module tilt angle F_1, F_2, a' and c' are parameter characterize in following the Perez model [54]. This approach explains the celestial hemisphere in three different parts, the sky (as the first part), circumsolar (as the second part), and horizon (as the third part) can be obtain from Equation (9).

$$I_{\mathrm{gnd,f}} = \mathrm{GHI}.\rho.\frac{1 - \cos(\theta_m)}{2}. \tag{10}$$

Equation (10) expresses the addition of irradiation reflected from the ground according to the isotropic model. At the same time, the stated ratio will increase with GHI (W/m^2) and ground albedo, ρ during periods of high spherical horizontal radiation, as this will add to the total radiation reflected from the ground [54].

3.2. PV Array Sizing. A PV array consists of photovoltaic panels with series and parallel connected photovoltaic cells, DC to DC converters, controllers, and batteries.

The main purpose of the solar energy project is to feed the system without the need for an electricity grid. PV array calculation that will produce energy equal to feeding power is important in system designs. When calculating system leaks, it should be accepted as the ratio of daily load demand to the product of the efficiency of all units in the system. As in Equation (11), the total solar energy array (E_r) must meet the daily energy requirement.

$$E_r = \frac{E_{\text{demand}}}{\eta_{\text{sys}}}, \tag{11}$$

where E_{demand} is the required demand energy (Wh) and η_{sys} is the entire structure performance. It is necessary to make calculations in order to meet the daily energy need in the most efficient way. This value can be determined by dividing the power generation system location by the average daily sunshine duration for the region.

$$P_{\text{peak}} = \frac{E_r}{T_{\min}}, \tag{12}$$

where P_{peak} is the peak energy produced from the planned photovoltaic arrays (W) and $T_{\min}$ is the least sunshine time (hours). The terms given indicate the technical characteristics of the photovoltaic array designed: module power (P_{unit}), open-circuit voltage (V_{oc}), short-circuit current (I_{sc}), maximum power point voltage (V_{mpp}), and current (I_{mpp}). The sum of photovoltaic modules (n_{PV}) can be calculated from Equation (13).

$$n_{\text{PV}} = \frac{P_{\text{peak}}}{P_{\text{unit}}}, \tag{13}$$

where n_{PV} is the sum of photovoltaic arrays andP_{unit} is the part power. The sum of photovoltaic modules includes series and sections made up of strings [54, 55]. The sum of series and strings parts can be determined from these equations:

$$\begin{aligned} n_{\text{PV(s)}} &= \frac{V_{\text{DC}}}{V_{\text{mpp}}}, \\ n_{\text{PV(p)}} &= \frac{n_{\text{PV}}}{n_{\text{PV(s)}}}, \end{aligned} \tag{14}$$

where $n_{\text{PV(s)}}$ is the sum of series parts, $n_{\text{PV(p)}}$ is the sum string of series parts, and V_{DC} is the DC link value. Most of solar projects relate to the "tilt angle" or "tilt" of a PV array or all collectors from a horizontal plane [54]. The tilt angle of a tracker plate and the tracker altitude angle are involved by the equation:

$$\text{TiltAngle} = |90\ \text{deg} - \theta_{\text{TE}}|. \tag{15}$$

The azimuth/elevation trackers work with two free cycle axes: the first is in azimuth around a vertical axis and the second is in height around a horizontal axis. The tracer azimuth can be regarded as a moving shaft at certain angles that can be geographically defined in the range of (0 degrees, 360 degrees) [56].

The SPPs shown in Figure 1 are connected to the grid and are designed to feed the charging station.

This system was designed such that the people who work in the building could charge their vehicles to full capacity during their work hours. The station's energy requirements would be continuously met with solar energy during these hours, and if needed, additional energy would be drawn from the grid.

4. System Description

The project was carried out in three buildings with the same roof sizes in Istanbul/Başakşehir, and analyses were performed using a different solar tracking system for each building. The use of the produced energy was realized with the systematic below:

(i) The designed roof-type PV energy system is connected to the grid and the energy that is produced but cannot be consumed instantaneously will be sold to the national electricity network with a bidirectional meter or it draws energy from the grid in energy requirements

(ii) The designed roof-type PV energy system primarily feeds the electric vehicle charging station

(iii) The surplus energy from the charging station is used for the lighting, ventilation, and common area energy requirements of the buildings

In this project, PV plants with 23.68 kW of DC power were installed on the roofs of three buildings with similar features in the same location. The PV plants that were mounted on these buildings comprised a fixed-angle, an adjustable-angle, and an automatic solar tracking system, each of which was realized with 320 W polycrystalline PV panels (16.5% efficiency). These systems were then monitored via energy-production data for 1 year. The projects were then compared in technical and economic terms, particularly with respect to investment and operating costs.

4.1. Annual Energy Production. Each SPP in this project was installed on the roof of a workplace in the Başakşehir District of Istanbul. The plants were installed on three separate but similar buildings in a single complex; the systems operated independently but under the same conditions and at equal power (20-kW AC output). Therefore, for the electrical project, only one of these plants will be discussed. Polycrystalline PV modules with 320 W of power and 16.5% efficiency were used in the project. A rooftop SPP with 23.68 kW of DC power and an inverter with 20 kW of AC output power were used; the system had a total of 74 modules. This power plant fueled two EV charging stations—one for big cars and one for small cars—in the building's parking lot. The system was also connected to the grid.

As can be seen in Figure 2, the actual production data are very close to the estimated production data made using PVsyst and PV*SOL software. The values in this table belong

Figure 1: The roof type SPP and its PV panels.

to SPP with fixed construction. Actual production data consists of data recorded using an inverter datalogger.

4.2. Project Layout. The project's general connection form is summarized in Figure 3. The modules convert sunlight into DC electricity, which the inverter then converts into AC at the appropriate voltage and frequency, before delivering the AC energy to the distribution panel. The panel is also connected to the grid, the building's electrical system, and EV charging station. After the panel has met the energy needs of the building and the charging station with the energy from the solar module, it transmits any surplus energy to the grid. When the solar module is insufficient (such as when there is no sunlight), the building and charging station draw power from the grid [57–67].

4.3. Power System Project. The modules were serially interconnected to form arrays. One positive output and one negative output from these arrays were then connected to the inverter. The inverter used in this project has two MPPTs (maximum power point tracker), each of which works independently. Thus, arrays of various voltage levels were connected to distinct MPPT inputs. For one MPPT input, two arrays, each with 18 modules connected in series, were connected to the inverter. For the other, two arrays, each with 19 modules connected in series, were connected to the inverter. Thus, the 74 modules (320 W) produced 23.68 kW of DC power. The output of the inverter was set to 20 kW AC. The total harmonic distortion at the output of the inverter was less than 3%.

4.4. Power Line Calculations. A TEDAŞ regulation was taken into account when calculating the inverter's compatibility with the module array; according to this regulation, the maximum cell temperature and the minimum cell temperature were 70°C and −10°C, respectively. Equations (6) and (7) were used in these calculations.

Table 1 shows the calculations for the DC voltage drop, power dissipation, and current; a 4 mm^2 cable meets all of the requirements. The k_1 and k_2 coefficients used in these calculations are the correction factors for the cables used in the project (according to the cable-laying method and the temperature). These factors were used to calculate the current that the cable can carry.

According to the regulations, 2% DC and 3% AC voltage drops are allowed. Table 2 shows the calculations for the AC voltage drop, power dissipation, and current; the chosen cables met all the requirements.

4.5. Installation Stages. Using the data from the project's implementation stages, Figure 4 shows the aluminum construction (in an unfinished state) and the SPP (once it was ready for electricity production).

An applied ergonomics analysis of the final project's solar tracking systems was also performed for use in subsequent applications. In this context, three roof-type SPPs of the same power level but with distinct tracking systems were installed. These three projects (Figure 5) had the same conditions and were part of the same building complex, and the same number and power of modules and inverters were used.

This system has higher operating and maintenance costs than the other systems because it involves rotating parts and an engine. In addition, although faults are quite rare in the other systems, engine breakdowns are common with this system. Based on tests performed by the relevant distribution company and TEDAŞ, the stations work smoothly. A grounding measurement was also performed, with a result of 1.52 Ω.

5. Results and Discussion

The results of the application project are presented and discussed below, under two headings: Electrical System Performance and Cost Analysis.

5.1. Electrical System Performance. Two different strings were formed from PV modules as 18 panels connected in series and 19 also connected in series. A total of 74 320 W PV modules were used by connecting 2 strings of 18 and 2 of 19 strings in parallel for each power plant. Strings with different voltage were connected to different MPPT inputs. This means that losses due to voltage difference were prevented and the system worked more efficiently. Simply connecting strings with the same number of serial panels to MPPT inputs is not enough to achieve this. Arrays should be created according to the similarity of the technical data in the Flash Testing Report, by looking at the serial number of the PV modules. It was observed that many applications did not pay attention to the voltage differences while creating the arrays. The researchers paid attention to this issue in this project. Furthermore, the length of the cable used in the

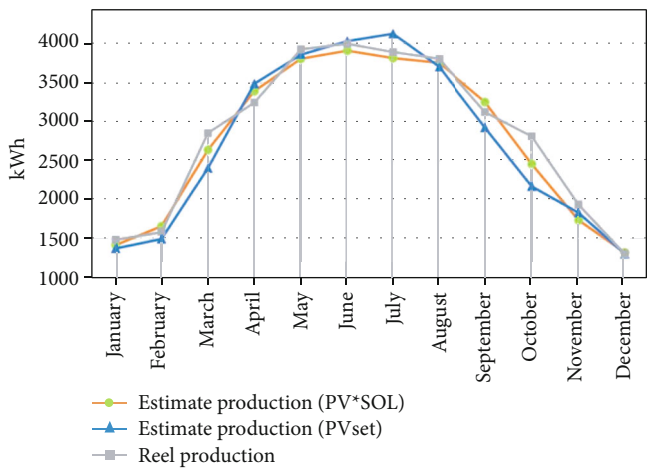

Figure 2: Estimated graph of energy injected into grid.

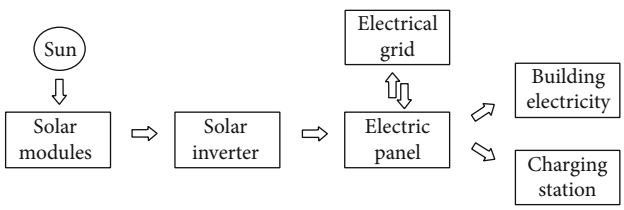

Figure 3: Project block diagram of the general arrangement.

Table 1: Calculations for the DC voltage drop (E), power dissipation, and current.

String no	L_{sum} (m)	k_1	k_2	I_o (A)	I_d (A)	P (Wp)	S (mm^2)	$\Delta v, \Delta P$ (%)
S 01	32	0.45	0.76	55	18.81	5760	4	0.188
S 02	25	0.45	0.76	55	18.81	6080	4	0.139
S 03	36	0.45	0.76	55	18.81	6080	4	0.200
S 04	60	0.45	0.76	55	18.81	5760	4	0.352

connection of the strings to the inverter is also important. The voltage drop will be different in different sizes and sections.

The total PV module power of each power plant is 23.68 kW, and the inverter output power is 20 kW. Thanks to two separate EV charging stations, each with a power of 22 kW, and a system connected to the building main panel, energy transmission losses are minimized by consuming energy on the location where it is produced. Additionally, since the power plants are connected to the grid through the building's main panel, the surplus can be transmitted to the city electricity grid. This transmission can be done smoothly with the inverters operating at the frequency and voltage compatible with the grid.

For the region where the project was conducted, data from October are roughly average with respect to sunshine and production. Accordingly, October was examined separately; Figure 6 shows the production data for the three types of power plants. The SPP with the solar tracking system produced the most energy: The fixed-angle system produced 2830.5 kWh per month, the adjustable-angle system produced 3050.4 kWh per month, and the solar-tracking system produced 3351.95 kWh per month. Based on these data, the plants with the adjustable-angle and solar tracking systems produced approximately 8% and 18% more energy, respectively, than the fixed-angle system.

There are many issues to be considered in the project implementation stages for SPPs. For example, equal numbers of voltage arrays should be connected to each MPPT when connecting the arrays to the inverter. These modules should also have test values that are as close to equal as possible so as to avoid mismatches. Attention should be paid to many factors, including the number of adjacent cables, the ambient temperature, and the method of laying the cables. The current should be determined according to these factors, and an appropriate section should be selected. Furthermore, this section should be checked for voltage drops and power dissipation. When estimating the power plants' production, attention should also be paid to time-dependent efficiency loss in the modules, as this is a general problem for semiconductors. Module manufacturers usually guarantee 80% to 85% efficiency at the end of 25 years.

A graph of the annual production data for the analysed systems (solar tracking, adjustable-angle, and fixed-angle) is presented in Figure 7.

5.2. Cost Analysis. Table 3 presents the cost of the power plants, the amount of energy production, and the return on investment, comparatively. As can be seen, the fixed system has the lowest investment and operation and maintenance cost. However, at the same time, energy generation is the lowest with this power plant. The manually adjusted system ranks second in terms of low investment cost. However, the return on investment in this power plant is observed to be the shortest. Trackers are the plants with the highest investment and operation and maintenance cost. They also achieve the highest production. However, they are still the worst plants in terms of return time. One of the reasons why the manually adjusted system works well is that technical personnel are always present at the location of the plant. This allows more frequent angle changes for the unit. Therefore, the efficiency increases by frequently adjusting the angle to the optimum. According to the results we have obtained here, the manually adjusted system is economically better. Of course, the tracker system is technically superior. The costs are gradually decreasing in the tracker system, so it will be a better choice both economically and technically in the future. If the lowest investment and operation and maintenance cost is to be preferred, a fixed system must be installed. Today, this system is more preferable due to its low cost.

Figure 8 presents the comparison of power plant production data and consumption of EV charging stations connected to this power plant. As can be seen, the power plant meets approximately 85% of the annual total consumption of the two EV charging stations. According to the EV charging station load curve used in the project, each station achieves an average of 3 hours/day EV charge annually. This demand varies depending on the number of EVs. Since the number of EVs will increase with the developing technology,

Table 2: Calculations for the AC voltage drop, power dissipation, and current.

	L (m)	S (mm^2)	k_1	k_2	k_3	I_o (A)	I_d (A)	P (We)	$\Delta v, \Delta P$ (%)
INV-R. E. panel	5	5×25	0.79	0.90	0.84	106	63.307	20000	0.045
R. E. panel-E. panel	100	5×25	0.79	0.90	0.84	106	63.307	20000	0.893
E. panel-EV 1	30	5×25	0.79	0.90	0.84	106	63.307	22170	0.297
E. panel-EV 2	25	5×16	0.79	0.90	0.84	79	47.182	11085	0.193

Figure 4: Project installation stages.

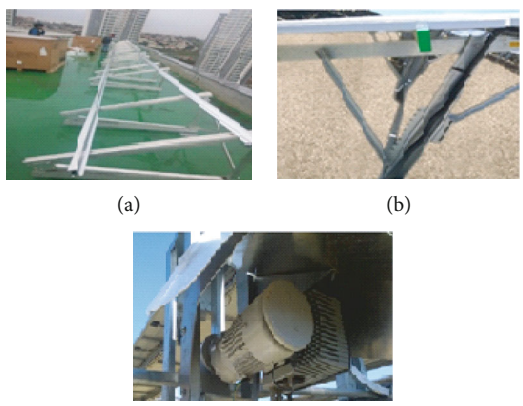

(a) (b) (c)

Figure 5: (a) PV panels for the fixed-angle, (b) manually adjustable-angle, and (c) solar tracking SPPs.

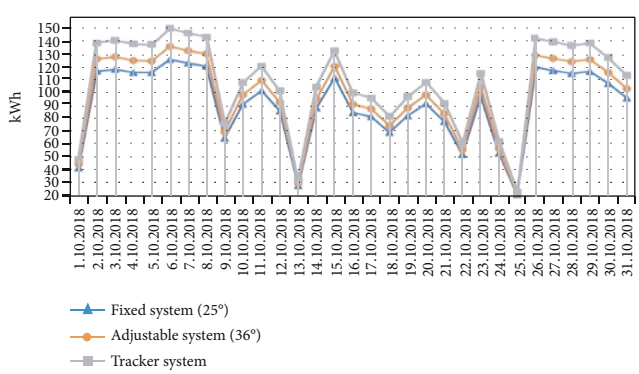

Figure 6: Comparison of October production data.

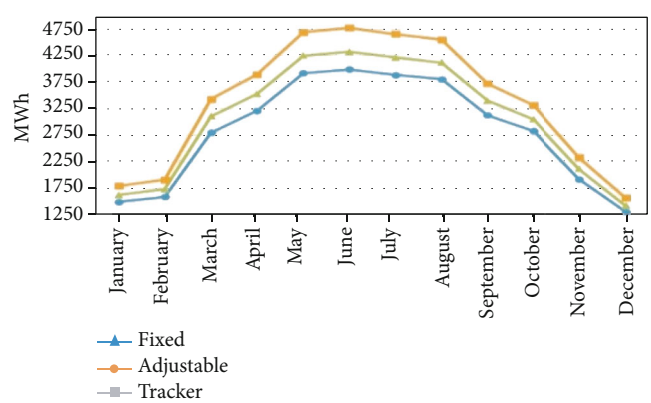

Figure 7: Graph of comparison of solar-tracking system applications according to monthly production data.

SPP power should be made as high as possible in such projects. This way, the EV charge will be achieved with clean energy as much as possible and energy transmission line losses will be minimized. Also, there may be network electrical infrastructure problems encountered, when EV charging stations draw power from the same network at the same time. To avoid this, it is recommended to install the EV charging station and SPP together just as the project in this article.

Table 3: Production costs and profits.

	Fixed	Adjustable	Tracker
Solar module	$ 7,500.00	$ 7,500.00	$ 7,500.00
Inverter	$ 2,500.00	$ 2,500.00	$ 2,500.00
DC cable	$ 200.00	$ 200.00	$ 200.00
AC cable	$ 250.00	$ 250.00	$ 250.00
Electric panel	$ 900.00	$ 900.00	$ 900.00
Workmanship	$ 2,100.00	$ 2,100.00	$ 2,100.00
Official transaction	$ 1,100.00	$ 1,100.00	$ 1,100.00
Project design	$ 2,250.00	$ 2,250.00	$ 2,250.00
Construction	$ 3,000.00	$ 4,000.00	$ 7,500.00
Other materials	$ 1,200.00	$ 1,200.00	$ 1,200.00
Unpredictable expense	$ 1,000.00	$ 1,000.00	$ 1,000.00
Total investment	$ 22,000.00	$ 23,000.00	$ 26.500.00
Produced energy	33.9 MWh/year	36.9 MWh/year	40.7 MWh/year
Annual energy sales amount	$ 4,507.89	$ 4,907.54	$ 5,409.70
Annual operation and maintenance expenses	$ 400.00	$ 500.00	$ 1,000.00
Annual yield loss	1.2%	1.2%	1.3%
Amortization time	5.75 years	5.60 years	6.31 years
10-year forecast profit	$ 16,720.91	$ 18,508.40	$ 14,539.61

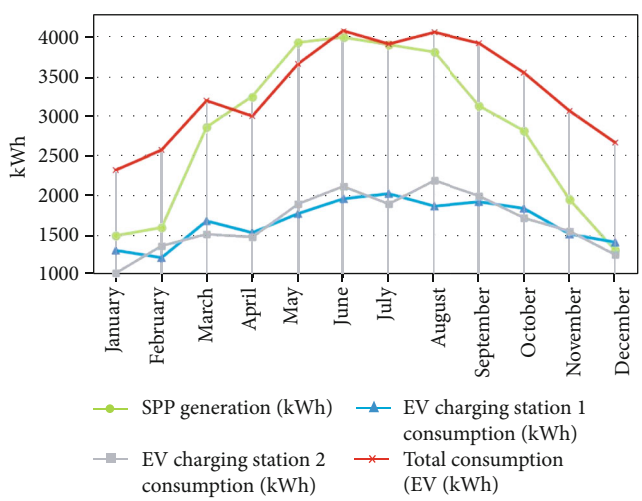

Figure 8: Graph of power plant production data and consumption of EV charging stations connected to this power plant.

According to Table 3, when accounting for the 10% loss in module efficiency over 10 years, the SPP with the fixed-angle system results in a profit of $16,720 if the electricity is sold only to the grid. This SPP does no harm to the environment because it yields profit and is a renewable energy source; it also decreases loss due to leakage because it reduces the need to transport energy to EV charging stations, as these stations can be fed without the need for an extra transmission line.

System life is 30 years, and the PV module, one of the main components used in the system, has an 80% performance guarantee at the end of 25 years. The whole system has a 10-year product and energy sale guarantee for connection to the grid. Taking into account the system life and performance loss, this power plant will save approximately 280 tons of CO_2 emission in 30 years with the energy it produces. While calculating these savings, CO_2 emissions that occur directly or indirectly during the production of all materials used and the emissions during the system's network integration are taken into account. Emission savings calculations are based on the IEA list/Turkey.

6. Conclusion

According to the annual production data for SPPs, systems with adjustable angles produced 8.4% more energy than those with fixed angles. This advantage can be further increased by changing the angle more frequently. In this project, the angles were changed four times per year. The solar tracking system also produced 19.8% more energy than the fixed-angle system. The SPPs with the solar tracking systems have higher investment, operating, and maintenance costs than the other systems, which makes the solar tracking systems less popular. The adjustable-angle and fixed-angle systems have similar costs; however, the former has much better energy production. Of the three SPPs, the one with the adjustable-angle system ranks first in terms of amortization time and 10-year earnings. With the produced power, the charge station provided energy for electric cars: either 16-A or 32-A Mode 3 alternating current. According to the EV charging station load curve used in the project, each station achieves an average of 3 hours/day EV charge annually. This demand varies depending on the number of EVs. Since the number of EVs will increase with the developing technology, SPP power should be made as high as possible in such projects.

The main purpose of this article was to demonstrate, using a real application, an optimal efficiency system analysis with low investment cost, low operating cost, and high

reliability, especially for roof applications in buildings. It was also aimed at exploring a new approach to energy-saving based on net energy gain. The main findings can be summarized as follows:

(i) In terms of energy generation, manual adjustment and single-axis solar tracking methods are the best options in the spring equinox. The E-W tracking single-axis tracking system becomes more efficient as the slope and height of the sun increase

(ii) In addition to approaches based on net energy generation, the system is also more applicable in terms of logistics, installation/operating costs, resistance to meteorological conditions, and system life

(iii) The energy consumed by the single-axis tracking system corresponds to 9.2% of the energy produced. Systems consisting of multiple components with complex designs are not always the right options

(iv) Although the single-axis tracking system is 27% more efficient than other methods of energy generation, the manually adjusted method has the shortest depreciation period

The data obtained in similar studies and the data in this project show similarities. What distinguishes this project from others is the manually adjusted system. Furthermore, projects with 3 different constructions of the same power, built using the same technical equipment at the same location, were compared. This is a guiding study for researchers who will carry out similar applications, conducted by comparing real production data and 2 different production-forecasting software estimates. Therefore, the results from this study are not only scientific work but also valuable for the green building concept, engineering, and construction (EPC) companies to make better decisions about what type of solar tracking method to use based on project details.

Nomenclature

V: Cell voltage (Volt)
V_{oc}: Cell open-circuit voltage
I_d: Reverse saturation current at the T_c temperature
I_{ph}: Photogenerated current
I_{sh}: Parallel resistor current
R_s: Series resistance
R_{sh}: Shunt resistance
T_c: Cell temperature (Kelvin)
q: Electron charge = $1.6^{*}10^{-19}$ Coulomb
K: Boltzmann constant (1.38×10^{-23} j/K)
N: Diode ideality factor
N_p: Cells in parallel
N_s: Cells in series
k_{Voc}: Temperature-dependent voltage coefficient
k_{Isc}: Temperature-dependent current coefficient
k_{Pmax}: Temperature-dependent power coefficient
t: Instantaneous cell temperature
t_{st}: Cell temperature under standard test conditions.

Data Availability

Datasets used to support the findings of this study are included within the article.

Conflicts of Interest

The authors declare that they have no conflicts of interest.

Supplementary Materials

Graphical abstract: the system was connected to the grid and electric vehicle charging station with a bidirectional energy meter to transfer the generated energy or provide the required energy. With regard to the energy production values, the automatic solar tracking system generated 10% more energy than the manually controlled system and 20% more energy than the fixed-angle system. *(Supplementary Materials)*

References

[1] S. Akshya, A. Ravindran, A. S. Srinidhi, S. Panda, and A. G. Kumar, "Grid integration for electric vehicle and photovoltaic panel for a smart home," in *Proceedings of IEEE International Conference on Circuit, Power and Computing Technologies, ICCPCT 2017*, Kollam, India, 2017.

[2] A. H. Yazdavar, M. A. Azzouz, and E. F. El-Saadany, "Modeling and simulation of standalone photovoltaic charging stations for electric vehicles," *International Journal of Computer and Information Engineering*, vol. 9, no. 1, pp. 72–80, 2015.

[3] T. Boyekin and İ. Kıyak, "Rooftop solar power plant based electric vehicle charging station," in *6. European Conference On Renewable Energy Systems (ECRES)*, Istanbul, Turkey, 2018.

[4] U. K. Das, K. S. Tey, M. Seyedmahmoudian et al., "Forecasting of photovoltaic power generation and model optimization: a review," *Renewable and Sustainable Energy Reviews*, vol. 81, Part 1, pp. 912–928, 2018.

[5] H. Kang, T. Hong, S. Jung, and M. Lee, "Techno-economic performance analysis of the smart solar photovoltaic blinds considering the photovoltaic panel type and the solar tracking method," *Energy & Buildings*, vol. 193, pp. 1–14, 2019.

[6] B. Parida, S. Iniyan, and R. Goic, "A review of solar photovoltaic technologies," *Renewable and Sustainable Energy Reviews*, vol. 15, no. 3, pp. 1625–1636, 2011.

[7] H. Hemza, C. Abdeslam, M. P. Rachid, and D. Barakel, "Tracing current-voltage curve of solar panel based on LabVIEW Arduino interfacing," *Journal of Bilişim Teknolojileri Dergisi*, vol. 8, no. 3, pp. 117–123, 2015.

[8] A. Chialastri and M. Isaacson, "Performance and optimization of a BIPV/T solar air collector for building fenestration applications," *Energy and Buildings*, vol. 150, no. 1, pp. 200–210, 2017.

[9] T. Ibn-Mohammed, S. C. L. Koh, I. M. Reaney et al., "Perovskite solar cells: an integrated hybrid lifecycle assessment and review in comparison with other photovoltaic technologies," *Renewable and Sustainable Energy Reviews*, vol. 80, pp. 1321–1344, 2017.

[10] T. D. Lee and A. U. Ebong, "A review of thin film solar cell technologies and challenges," *Renewable and Sustainable Energy Reviews*, vol. 70, pp. 1286–1297, 2017.

[11] A. C. Martins, V. Chapuis, F. Sculati-Meillaud, A. Virtuani, and C. Ballif, "Light and durable: composite structures for building-integrated photovoltaic modules," *Progress in Photovoltaics: Research and Applications*, vol. 26, no. 9, pp. 718–729, 2018.

[12] V. Ciocia, A. Boicea, A. Dematteis, P. D. Leo, F. Giordano, and F. Spertino, "PV system integration in buildings: an energy and economic case study," in *2017 10th International Symposium on Advanced Topics in Electrical Engineering (ATEE)*, Bucharest, Romania, 2017.

[13] M. Brito, S. Freitas, S. Guimarães, C. Catita, and P. Redweik, "The importance of facades for the solar PV potential of a Mediterranean city using LiDAR data," *Renewable Energy*, vol. 111, pp. 85–94, 2017.

[14] W. Bahr, "A comprehensive assessment methodology of the building integrated photovoltaic blind system," *Energy and Buildings*, vol. 82, pp. 703–708, 2014.

[15] A. Z. Hafez, A. M. Yousef, and N. M. Harag, "Solar tracking systems: technologies and trackers drive types - a review," *Renewable and Sustainable Energy Reviews*, vol. 91, pp. 754–782, 2018.

[16] S. Heslop and I. MacGill, "Comparative analysis of the variability of fixed and tracking photovoltaic systems," *Solar Energy*, vol. 107, pp. 351–364, 2017.

[17] N. AL-Rousan, N. A. M. Isa, and M. K. M. Desa, "Advances in solar photovoltaic tracking systems: a review," *Renewable and Sustainable Energy Reviews*, vol. 82, no. 3, pp. 2548–2569, 2018.

[18] M. Sorgato, K. Schneider, and R. Rüther, "Technical and economic evaluation of thin-film CdTe building-integrated photovoltaics (BIPV) replacing façade and rooftop materials in office buildings in a warm and sunny climate," *Renewable Energy*, vol. 118, pp. 84–98, 2018.

[19] A. Vulkan, I. Kloog, M. Dorman, and E. Erell, "Modeling the potential for PV installation in residential buildings in dense urban areas," *Energy and Buildings*, vol. 169, pp. 97–109, 2018.

[20] A. K. Athienitis, G. Barone, A. Buonomano, and A. Palombo, "Assessing active and passive effects of façade building integrated photovoltaics/thermal systems: dynamic modelling and simulation," *Applied Energy*, vol. 209, pp. 355–382, 2018.

[21] A. Yushchenko, A. de Bono, B. Chatenoux, M. K. Patel, and N. Ray, "GIS-based assessment of photovoltaic (PV) and concentrated solar power (CSP) generation potential in West Africa," *Renewable and Sustainable Energy Reviews*, vol. 81, no. 2, pp. 2088–2103, 2018.

[22] R. Singh, S. Kumar, A. Gehlot, and R. Pachauri, "An imperative role of sun trackers in photovoltaic technology: a review," *Renewable and Sustainable Energy Reviews*, vol. 82, no. 3, pp. 3263–3278, 2018.

[23] M. Tripathy, P. Sadhu, and S. Panda, "A critical review on building integrated photovoltaic products and their applications," *Renewable and Sustainable Energy Reviews*, vol. 61, pp. 451–465, 2016.

[24] J.-Y. Kim, G.-Y. Jeon, and W.-H. Hong, "The performance and economical analysis of grid-connected photovoltaic systems in Daegu, Korea," *Applied Energy*, vol. 86, no. 2, pp. 265–272, 2009.

[25] Y. Kim, H. Cha, B.-M. Song, and K. Y. Lee, "Design and control of a grid-connected three-phase 3-level NPC inverter for building integrated photovoltaic systems," in *PES Innovative Smart Grid Technologies (ISGT)*, Washington, DC, USA, 2012.

[26] M. Mandalaki, T. Tsoutsos, and N. Papamanolis, "Integrated PV in shading systems for Mediterranean countries: balance between energy production and visual comfort," *Energy and Buildings*, vol. 77, pp. 445–456, 2014.

[27] W. Zhang, L. Lu, and J. Peng, "Evaluation of potential benefits of solar photovoltaic shadings in Hong Kong," *Energy*, vol. 137, pp. 1152–1158, 2017.

[28] M. Mandalaki, S. Papantoniou, and T. Tsoutsos, "Assessment of energy production from photovoltaic modules integrated in typical shading devices," *Sustainable Cities and Society*, vol. 10, pp. 222–231, 2014.

[29] C. Vassiliades, A. Michael, A. Savvides, and S. Kalogirou, "Improvement of passive behaviour of existing buildings through the integration of active solar energy systems," *Energy*, vol. 163, pp. 1178–1192, 2018.

[30] C. Breyer, D. Bogdanov, A. Gulagi et al., "On the role of solar photovoltaics in global energy transition scenarios," *Progress in Photovoltaics: Research and Applications*, vol. 25, no. 8, pp. 727–745, 2017.

[31] J. Oh, C. Koo, T. Hong, K. Jeong, and M. Lee, "An economic impact analysis of residential progressive electricity tariffs in implementing the building-integrated photovoltaic blind using an advanced finite element model," *Applied Energy*, vol. 202, pp. 259–274, 2017.

[32] Y. Chen, P. Xu, J. Gu, F. Schmidt, and W. Li, "Measures to improve energy demand flexibility in buildings for demand response (DR): a review," *Energy and Buildings*, vol. 177, pp. 125–139, 2018.

[33] N. X. Truong, N. L. Tung, N. Q. Hung, and B. Delinchant, "Grid-connected PV system design option for nearly zero energy building in reference building in Hanoi," in *International Conference on Sustainable Energy Technologies (ICSET)*, Hanoi, Vietnam, 2016.

[34] A. Chub, O. Korkh, R. Kosenko, and D. Vinnikov, "Novel approach immune to partial shading for photovoltaic energy harvesting from building integrated PV (BIPV) solar roofs," in *20th European Conference on Power Electronics and Applications (EPE'18 ECCE Europe)*, Riga, Latvia, 2018.

[35] İ. Kıyak, B. Oral, and V. Topuz, "Smart indoor LED lighting design powered by hybrid renewable energy systems," *Energy and Buildings*, vol. 148, pp. 342–347, 2017.

[36] TEDAŞ, *Turkey electricity distribution company*, Technical Report, Turkey, 2018.

[37] BEDAŞ, *Boğaziçi electricity distribution company*, Technical Report, Istanbul, Turkey, 2018.

[38] K. Jeong, T. Hong, C. Koo, J. Oh, M. Lee, and J. Kim, "A prototype design and development of the smart photovoltaic system blind considering the photovoltaic panel, tracking system, and monitoring system," *Applied Sciences*, vol. 7, no. 10, p. 1077, 2017.

[39] E. Taveres-Cachat, K. Bøe, G. Lobaccaro, F. Goia, and S. Grynning, "Balancing competing parameters in search of optimal configurations for a fix louvre blade system with integrated PV," *Energy Procedia*, vol. 122, pp. 607–612, 2017.

[40] C. Koo, T. Hong, K. Jeong, C. Ban, and J. Oh, "Development of the smart photovoltaic system blind and its impact on net-zero energy solar buildings using technical-economic-political analyses," *Energy*, vol. 124, pp. 382–396, 2017.

[41] M. Macellari, U. Grasselli, and L. Schirone, "Modular MPPT converter with series-connection for PV installations embedded in the urban environment," in *IECON 2013-39th Annual*

Conference of the IEEE Industrial Electronics Society, Vienna, Austria, 2013.

[42] B. H. Lim, C. S. Lim, H. Li et al., "Industrial design and implementation of a large-scale dual-axis sun tracker with a vertical-axis-rotating-platform and multiple-row-elevation structures," *Solar Energy*, vol. 199, pp. 596–616, 2020.

[43] X. C. Ngo, T. H. Nguyen, N. Y. Do et al., "Grid-connected photovoltaic systems with single-axis sun tracker: case study for Central Vietnam," *Energies*, vol. 13, no. 6, article 1457, 2020.

[44] O. Achkari, A. El Fadar, I. Amlal, A. Haddi, M. Hamidoun, and S. Hamdoune, "A new sun-tracking approach for energy saving," *Renewable Energy*, vol. 169, pp. 820–835, 2021.

[45] H. Allamehzadeh, "An update on solar energy and sun tracker technology with a dual axis sun tracker application," in *2019 IEEE 46th Photovoltaic Specialists Conference (PVSC)*, Chicago, IL, USA, 2019.

[46] M. G. Satué, F. Castaño, M. G. Ortega, and F. R. Rubio, "Autocalibration method for high concentration sun trackers," *Solar Energy*, vol. 198, pp. 311–323, 2020.

[47] G. Li, Q. Xuan, M. W. Akram, Y. G. Akhlaghi, H. Liu, and S. Shittu, "Building integrated solar concentrating systems: a review," *Applied Energy*, vol. 260, article 114288, 2020.

[48] P. Hoseinzadeh, M. K. Assadi, S. Heidari et al., "Energy performance of building integrated photovoltaic high-rise building: case study, Tehran, Iran," *Energy and Buildings*, vol. 235, article 110707, 2021.

[49] T. E. Kuhn, C. Erban, M. Heinrich, J. Eisenlohr, F. Ensslen, and D. H. Neuhaus, "Review of technological design options for building integrated photovoltaics (BIPV)," *Energy and Buildings*, vol. 231, article 110381, 2021.

[50] A. Awasthi, A. K. Shukla, S. R. Murali Manohar et al., "Review on sun tracking technology in solar PV system," *Energy Reports*, vol. 6, pp. 392–405, 2020.

[51] J. E. Gonçalves, T. van Hooff, and D. Saelens, "Simulating building integrated photovoltaic facades: comparison to experimental data and evaluation of modelling complexity," *Applied Energy*, vol. 281, p. 116032, 2021.

[52] S. Abdallah and O. O. Badran, "Sun tracking system for productivity enhancement of solar still," *Desalination*, vol. 220, no. 1-3, pp. 669–676, 2008.

[53] I. H. Rosma, J. Asmawi, S. Darmawan, B. Anand, N. D. Ali, and B. Anto, "The implementation and analysis of dual axis sun tracker system to increase energy gain of solar photovoltaic," in *2018 2nd International Conference on Electrical Engineering and Informatics (ICon EEI)*, Batam, Indonesia, 2018.

[54] T. F. Megahed and A. Radwan, "Performance investigation of zero-building-integrated photovoltaic roof system: a case study in Egypt," *Alexandria Engineering Journal*, vol. 59, no. 6, pp. 5053–5067, 2020.

[55] C. D. Rodríguez-Gallegos, O. Gandhi, S. K. Panda, and T. Reindl, "On the PV tracker performance: tracking the sun versus tracking the best orientation," *IEEE Journal of Photovoltaics*, vol. 10, no. 5, pp. 1474–1480, 2020.

[56] D. Riley and C. Hansen, "Sun-relative pointing for dual-axis solar trackers employing azimuth and elevation rotations," *Journal of Solar Energy Engineering*, vol. 137, no. 3, article 031008, 2015.

[57] X. Jiang, J. Wang, Y. Han, and Q. Zhao, "Coordination dispatch of electric vehicles charging/discharging and renewable energy resources power in microgrid," *Procedia Computer Science*, vol. 107, pp. 157–163, 2017.

[58] M. Clemente, M. P. Fanti, and W. Ukovich, "Smart management of electric vehicles charging operations: the vehicle-to-charging station assignment problem," in *19th World Congress The International Federation of Automatic Control*, Cape Town, South Africa, 2014.

[59] W. Shengjun, X. Qingshan, L. Qun, Y. Xiaodong, and C. Bing, "Optimal EV charging control strategy based on DC microgrid," *Energy Procedia*, vol. 100, pp. 243–247, 2016.

[60] Ö. Polat, K. Yumak, M. S. Sezgin, G. Yumurtaci, and Ö. Gül, "Elektrikli Araç Ve Şarj İstasyonlarının Türkiye'deki Güncel Durumu," in *VI. Energy Efficiency, Quality Symposium and Exhibition, EVK'2015*, Kocaeli, Turkey, 2015.

[61] S o A, *Engineers, SAE J1772- Electric Vehicle and Plug in Hybrid Electric Vehicle Conductive Charge Coupler*, 2012.

[62] IE Commission, *IEC 61851-1- Electric Vehicle Conductive Charging System - Part 1: General Requirements*, 2011.

[63] C Association, *Technical Specifications of Quick Charger for the Electric Vehicle*, 2011.

[64] B. Yağcıtekin, M. Uzunoğlu, and A. Karakaş, "A new deployment method for electric vehicle charging infrastructure," *Turkish Journal of Electrical Engineering and Computer Sciences*, vol. 24, no. 3, pp. 1292–1305, 2016.

[65] M. Brenna, M. Longo, and W. Yaïci, "Modelling and simulation of electric vehicle fast charging stations driven by high speed railway systems," *Energies*, vol. 10, no. 9, p. 1268, 2017.

[66] B. Zhao, M. Hu, X. Ao et al., "A novel strategy for a building-integrated diurnal photovoltaic and all-day radiative cooling system," *Energy*, vol. 183, pp. 892–900, 2019.

[67] C. Ghenai and M. Bettayeb, "Modelling and performance analysis of a stand-alone hybrid solar PV/fuel cell/diesel generator power system for university building," *Energy*, vol. 171, pp. 180–189, 2019.

Hindawi
International Journal of Photoenergy
Volume 2021, Article ID 6668325, 8 pages
https://doi.org/10.1155/2021/6668325

Research Article

Energy, Exergy Analysis, and Optimizations of Collector Cover Thickness of a Solar Still in El Oued Climate, Algeria

Abderrahmane Khechekhouche,[1] A. Muthu Manokar,[2] Ravishankar Sathyamurthy,[3] Fadl A. Essa,[4] Milad Sadeghzadeh,[5] and Alibek Issakhov[6]

[1]*Faculty of Technology, El Oued University, Algeria*
[2]*Department of Mechanical Engineering, B.S. Abdur Rahman Crescent Institute of Science and Technology, Chennai 600 048, India*
[3]*Department of Mechanical Engineering, KPR Institute of Engineering and Technology, Arasur, Coimbatore, 641407 Tamil Nadu, India*
[4]*Mechanical Engineering Department, Faculty of Engineering, Kafrelsheikh University, Kafrelsheikh, Egypt*
[5]*Department of Renewable Energies and Environment, Faculty of New Sciences & Technologies, University of Tehran, Tehran, Iran*
[6]*Faculty of Mechanics and Mathematics, Department of Mathematical and Computer Modelling, Al-Farabi Kazakh National University, Almaty, Kazakhstan*

Correspondence should be addressed to Milad Sadeghzadeh; milad.sadeghzadeh@gmail.com

Received 29 November 2020; Accepted 28 February 2021; Published 13 March 2021

Academic Editor: Hafiz Muhammad Ali

Copyright © 2021 Abderrahmane Khechekhouche et al. This is an open access article distributed under the Creative Commons Attribution License, which permits unrestricted use, distribution, and reproduction in any medium, provided the original work is properly cited.

Researches in many laboratories on solar still desalination are concerned with increasing efficiency using only solar energy. One of the techniques is the difference in the thickness of the glass cover of the distiller. In order to see the influence of this parameter on efficiency, three similar stills with three different glass coverings were investigated. The flow of heat goes through the cover, and higher glass temperature leads to solar still productivity becoming lower. This paper presents an optimization of glass thickness (G_t) of a conventional solar still (CSS) in El Oued climate, Algeria. Based on the experimental results, the distilled water production rate, energy, and energy efficiency of the CSS have been discussed. The results showed that the suitable G_t of the CSS was 3 mm. The distilled water of around 3.15, 2.02, and 1.13 kg was produced by the CSS at energy efficiency of 30.71, 19.02, and 11.44% with the G_t of 3, 5, and 6 mm, respectively. The daily average exergy efficiency of 2.46, 1.38, and 0.84% was calculated for the CSS at G_t of 3, 5, and 6 mm, respectively.

1. Introduction

Solar distillation is one of the simplest, economical, and environmental solutions with no emission of toxic or dangerous gas [1–3]. This technique is used in many countries around the world, especially in the isolated areas. As its name indicates, it is based on solar energy which is renewable and free energy [4–7]. The solar distiller works according to the laws of heat and mass transfer [8]. Improving the productivity of pure water from a conventional solar distiller is the subject of research in several laboratories [9, 10]. This improvement is based on two main parameters, solar radiation and the gradient of temperature between water and glazing. In addition, exergy, energy, and technoeconomic assessments have been widely carried out to monitor the performance of solar-based conversion systems such as solar distillers to demonstrate their feasibility [11–18]. To prove the first parameter, an experiment was performed in the summer season and in the winter season to see the effect of solar radiation on traditional distillation production; the results show 89.44% increase in productivity during the summer season [19]. Another experiment used reflectors to focus the solar radiation that passes through the still's glass; the rate of improvement was approximately 30% [20].

The lenses were also used to increase a traditional solar still's performance, and the result obtained was 638% [21].

To prove the second parameter, double glazing was used in a solar still to reduce temperature gradient, and the results show 55.7% reduction in productivity [22]. There have also been many studies on the glazing itself, for example, a study which tested the cooling of glass evaluated the productivity of the solar stills. The experimental results revealed that the pure water productivity is 10.06 L/m^2·day [23]. Another study shows that efficiency of solar distiller glass with water cooling was 11.81% more efficient than the solar still without water cooling [24].

According to an experimental study, cooling of glass covers can also be achieved by flowing air over the glass cover [25]. The use of partial shading on a CSS gave 12% improvement in productivity, a result confirmed by an experimental study carried out in southern Algeria [26]. Some researchers have tried to adjust the glazing angle to maximize pure water production; they have found that the best angles vary between 20° and 30°. The best glazing angle was 30° with an output of 3517 kg/m^2 in the autumn season and 3633 kg/m^2 in the winter; the best inclination was 20° with a yield of 5224 kg/m^2 in the spring season and 4527 kg/m^{2}in the summer season [27].

The variation of 3 different glazing thicknesses (4, 6, and 8 mm) was published by Panchal and Shah [28]. The outcome of the study indicates that the best pure water production corresponds to the 4 mm thickness. The results of an experiment revealed that while the thickness of the glass cover of a solar still reduces to 3.5 mm, the average output of pure water from the still was 31.13% higher than that from a solar still with a 4 mm thick glass cover [29]. Several experiments were reported on the effect of different glass covers thickness on a solar still performance [30–32].

A theoretical and experimental study was done on three different cover thicknesses to determine the optimum thickness of the solar still glass cover. The results obtained show that a glass cover thickness of 4 mm and 5 mm has 27 and 12% higher production as compared to a thickness of 6 mm [33]. Two solar stills with two glass lids with different thicknesses of 4 mm and 6 mm were tested; the best productivity of 1.60 liters from the still with the 4 mm glazing and 1.55 liters from the still with the 6 mm glazing was reported [34, 35]. The heat flow through the glass of a CSS has been studied recently [36]. In another study, 5 glass covers were tested (2, 6, 10, 14, and 18 mm); the result indicates that optimum thickness that offers the highest pure water productivity is 6 mm [37]. The influence of a large glazing thickness on the performance of a solar still was studied by Khechekhouche et al. [38]. The cover consists of two 3 mm thick glass plates separated by a 100 mm air layer, forming an air chamber isolated from the sides. The results show that this technique minimizes the efficiency of the distiller by 56.52% compared to the CSS [38].

From the detailed literature, it has been identified that only few works have been reported on the effect of glass thickness on energy and exergy efficiencies of a solar still. Hence, the present work consists of making an experiment with three conventional solar stills, and each still has a glazing with a thickness that differs from the other distillers for the climatic condition of the El Oued climate, Algeria. The objective is to optimize the thickness in order to obtain the best productivity in pure water. In this work, calculation of energy, exergy efficiency, and fractional exergy of evaporation and convection between $T_{s.w}$ and $T_{c.c}$ is a novelty of the present study.

Table 1: Meteorological conditions.

Sun lever	5:41
Sunset	19:19
Ambient temperature	35 (°C)
Humidity	25%

2. Experimental Set-Up and Methodology

2.1. Protocol of the Experiment. The city of El Oued southeast of Algeria's geographical coordinates is 33.3676° north latitude and 6.8516° longitude. The experiment was carried out several times, and since the results obtained are the same, one sunny day (25th May 2018) was considered. K-1-type thermocouples were placed on solar stills and precisely in the water, below and above the glass cover, and in the open place to measure the ambient temperature. The glass side of the two stills faces south for maximum exposure to solar radiation. The quantities of distilled water produced were measured manually every hour by a graduated cup. Temperatures were measured every hour from 9:00 AM to 4:00 PM. The meteorological condition of the experimental day is shown in Table 1.

2.2. Solar Distiller Description. Figure 1 shows the schematic of the CSS with location of thermocouples. This system helps to purify polluted water and restore it to pure water. It is a very simple technique which uses energy from solar radiation. Nevertheless, this type of system is distinguished from other desalination devices by its relatively low efficiency. This distiller has a very simple construction with a low investment cost. The distiller used in our experiment consists basically of a square wooden box of 0.5 × 0.5 m, a transparent glass cover of 0.55 × 0.55 m, a thickness of 0.003 m, a PVC recovery tube of 0.60 m in length and 0.025 m in diameter situated in the lower part of the distillery, and finally a pure-water storage tank.

2.3. Treatment Data. The experiment was performed in the climate of El Oued region, in southeast Algeria, on 25th May 2018. Three separate solar stills have the same size with the same inclination angle (20° with the horizontal). At the same time, all the three distillers (CSS with the G_t of 3, 5, and 6 mm) are exposed to the sun on the same experiential day with similar water quality and quantity. Each distiller has a thickness covering that differs from other distillers as shown in Figure 2.

3. Results and Discussion

3.1. Hourly Variations of Solar Intensity and Ambient Temperature. Figure 3 shows the hourly variations of solar

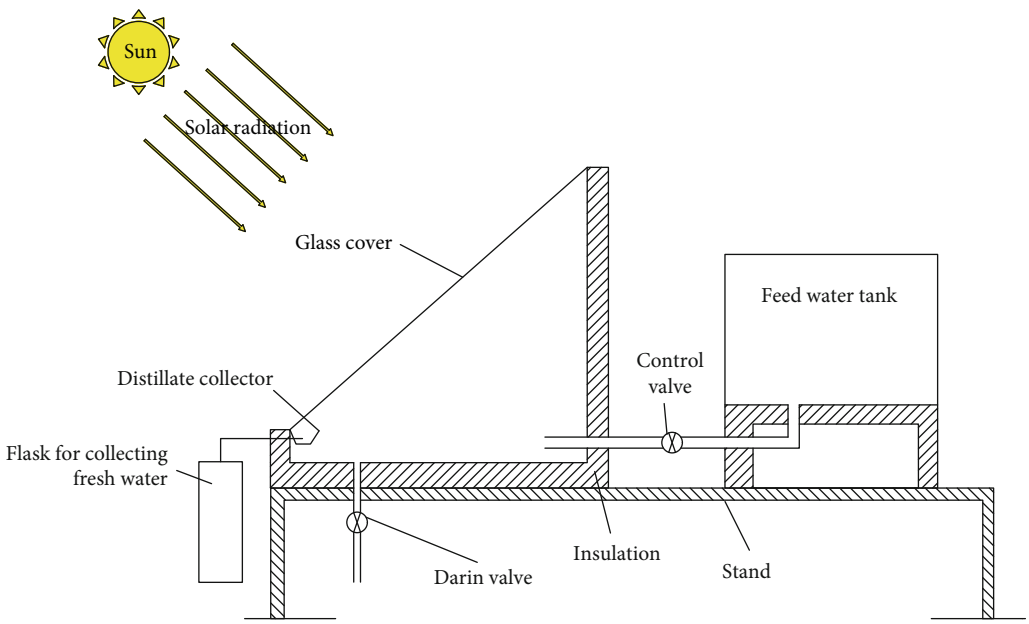

Figure 1: Location of the thermocouples.

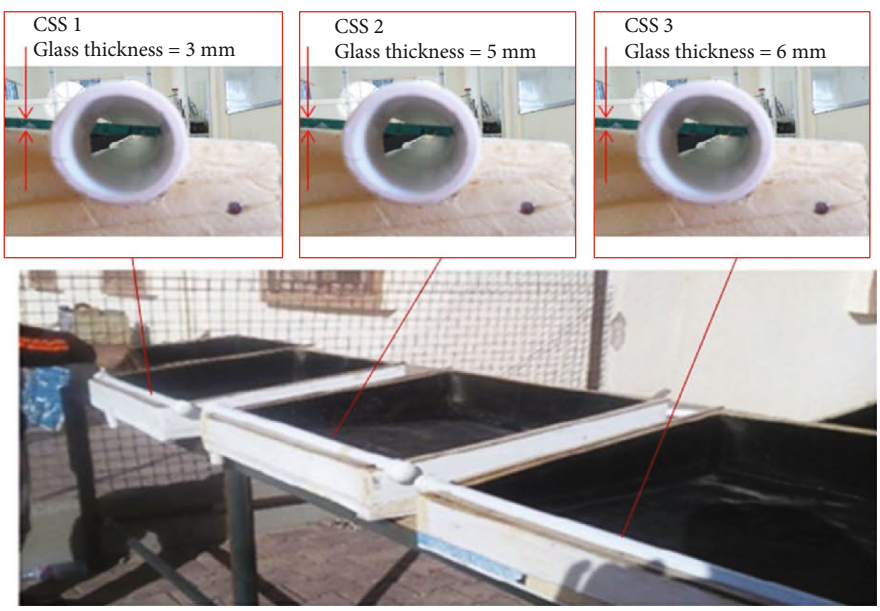

Figure 2: Photographic view of the experimental set-up.

intensity and ambient temperature. From the graph, it is clear that both the values increase linearly and reached the maximum value at 1 PM, and after 1 PM, it has decreased. The maximum solar intensity and an ambient temperature of 1005 W/m^2 and 36°C has been recorded. The daily average solar intensity and ambient temperature during the testing have been recorded as 754.38 W/m^2 and 32.25°C, respectively. During the testing, the sky was very clear and there were no clouds.

3.2. Hourly Variations of Water Temperature. Figure 4 shows the hourly variations of water temperature (T_W) for the CSS at G_t of 3, 5, and 6 mm. T_W has a similar curve like solar intensity and ambient temperature since the water temperature is directly proportional to the solar intensity. The maximum T_W of 60, 58, and 55°C has been recorded for the CSS at G_t of 3, 5, and 6 mm, respectively. The daily average T_W of 49.5, 47.88, and 46°C has been calculated for the CSS at G_t of 3, 5, and 6 mm, respectively. From the experimentation of the CSS at different G_t, the maximum T_W obtained for the G_t of 3 mm is found. The CSS at G_t of 5 and 6 mm reduces the daily average T_W by 3.28% and 7.07%, respectively, as compared to the CSS at G_t of 3 mm. Compared to the other two stills,

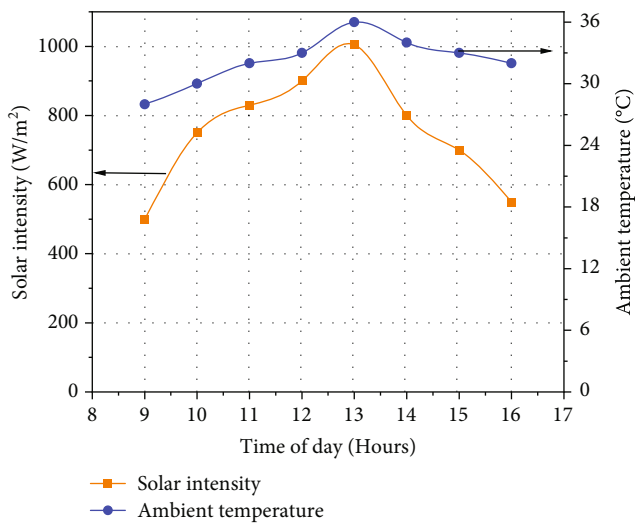

Figure 3: Time-wise fluctuation of solar intensity and ambient temperature.

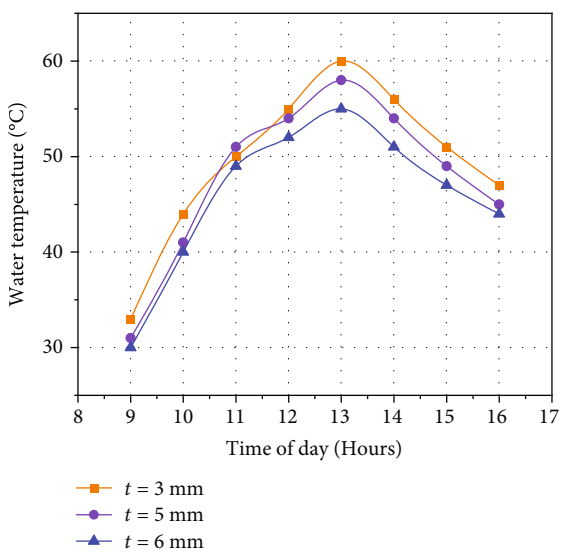

Figure 4: Time-wise fluctuation of T_W.

the water temperature in the CSS at G_t of 3 mm is highest, and it is known that any rise in the water temperature causes an increase in evaporation.

3.3. Hourly Variations of Glass Temperature. Figure 5 shows the hourly variations of glass temperature (T_G) for the CSS at G_t of 3, 5, and 6 mm. T_G also has a similar curve like solar intensity. The maximum T_G of 49, 51, and 54°C has been recorded for the CSS at G_t of 3, 5, and 6 mm, respectively. The daily average T_G of 42.25, 44.25, and 46.13°C has been calculated for the CSS at G_t of 3, 5, and 6 mm, respectively. From the experimentation of the CSS at different G_t, it is found that the CSS at G_t of 3 mm has minimum T_G as compared to the CSS at G_t of 5 and 6 mm. The CSS at G_t of 5 and 6 mm increases the daily average T_G by 4.52% and 8.4%, respectively, as compared to the CSS at the G_t of 3 mm. From graphs 3 and 4, it is found that the CSS at G_t of 3 mm has the

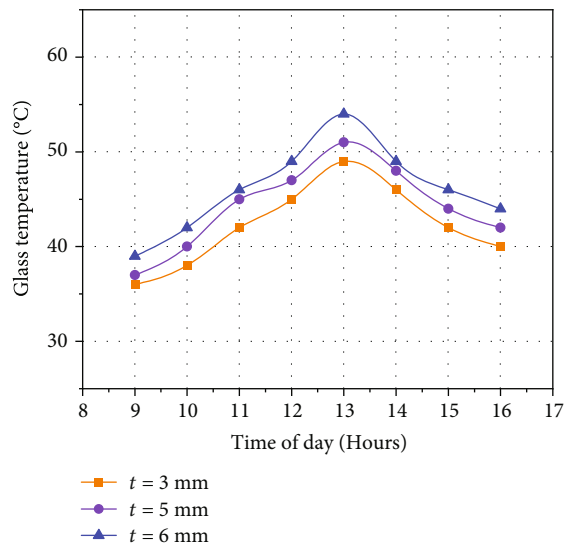

Figure 5: Time-wise fluctuation of T_G.

maximum T_W and minimum T_G which produces the higher difference between T_W and T_G.

3.4. Hourly Variations of the Yield. The value of EHTC is directly proportional to the T_W so it has a similar curve like a T_W curve. The maximum EHTC of 46.28, 37, and 28.34 W/m^{2}k have been recorded for the CSS at G_t of 3, 5, and 6 mm, respectively. The daily average EHTC of 26.71, 18.76, and 9.81 W/m^{2}k have been calculated for the CSS at G_t of 3, 5, and 6 mm, respectively. The CSS at G_t of 5 and 6 mm reduces the daily average EHTC by 29.74% and 63.27%, respectively, as compared to the CSS at G_t of 3 mm. Figure 6 shows the hourly variations of the yield produced from the CSS at G_t of 3, 5, and 6 mm. The yield produced from the CSS at difference G_t has a similar curve like the EHTC because yield is directly proportional to the EHTC. The maximum hourly yield produced from the CSS at G_t of 3, 5, and 6 mm is 0.76, 0.45, and 0.31 kg, respectively. The daily average yield produced from the CSS at G_t of 3, 5, and 6 mm is 3.15, 1.9, and 1.1 kg, respectively. The CSS at G_t of 5 and 6 mm reduces the daily yield by 40.48% and 65.15%, respectively, as compared to the CSS at G_t of 3 mm. From the yield production, it is clear that the CSS at G_t of 3 mm has maximum yield because of the higher difference between T_W and T_G. This difference between T_W and T_G is called the gradient of temperature. Due to higher temperature difference; the CSS at Gt of 3 mm produced more yield than the CSS at Gt of 5 and 6 mm.

3.5. Thermal Efficiency. Figure 7 shows the thermal efficiency of the CSS at G_t of 3, 5, and 6 mm. The thermal efficiency of the CSS at different G_t has the similar curve like the yield. The maximum thermal efficiency of the CSS at G_t of 3, 5, and 6 mm is 47.33, 32.86, and 23.87%, respectively. The daily average thermal efficiency of the CSS at G_t of 3, 5, and 6 mm is 30.71, 18.35, and 11.25%, respectively. The CSS at G_t of 5 and 6 mm reduces the daily average thermal efficiency by 40.25% and 63.37% as compared to the CSS at G_t of 3 mm.

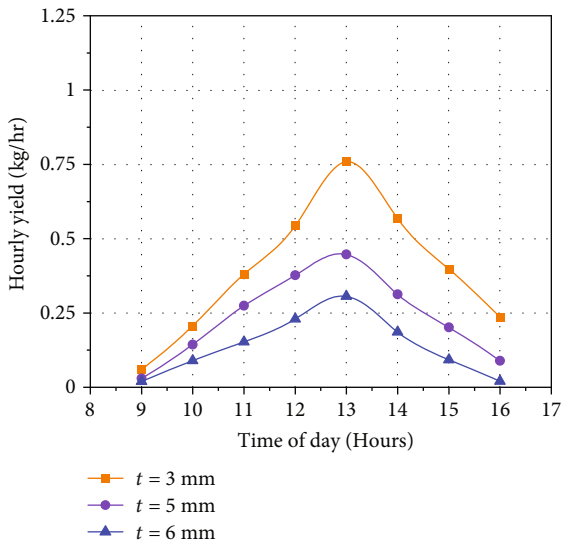

Figure 6: Time-wise fluctuation of yield.

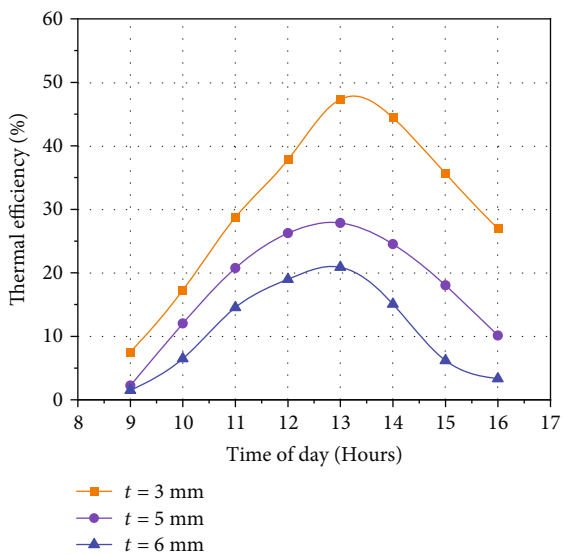

Figure 7: Time-wise fluctuation of thermal efficiency.

The thermal efficiency of the system mostly depends on the yield produced from the CSS. In this experiment, the yield produced from the CSS is maximum in the case of G_t of 3 mm, so thermal efficiency of the system is higher in the case of G_t of 3 mm.

The thermal efficiency of the CSS is given by [23–25]

$$\eta_{\text{passive}} = \frac{\sum \dot{m}_{ew} L}{\sum I(t) A_s \times 3600} \times 100. \quad (1)$$

3.6. Exergy Efficiency. Figure 8 shows the exergy efficiency of the CSS at G_t of 3, 5, and 6 mm. The exergy efficiency of the CSS at different G_t has the similar curve like the thermal efficiency. The maximum hourly exergy efficiency of the CSS at G_t of 3, 5, and 6 mm is 4.72, 2.62, and 1.93%, respectively. The daily average exergy efficiency of the CSS at G_t of 3, 5, and 6 mm is 2.46, 1.38, and 0.84%, respectively. The CSS at G_t of 5 and 6 mm reduces the daily average exergy efficiency by 44.01% and 65.81%, respectively, as compared to the CSS at G_t of 3 mm. The exergy efficiency of the system mostly depends on the yield produced from the CSS. In this research, the maximum exergy efficiency was calculated for the CSS at G_t of 3 mm. The performance of the CSS at G_t of 3 mm is higher, so exergy efficiency is higher at the CSS at G_t of 3 mm.

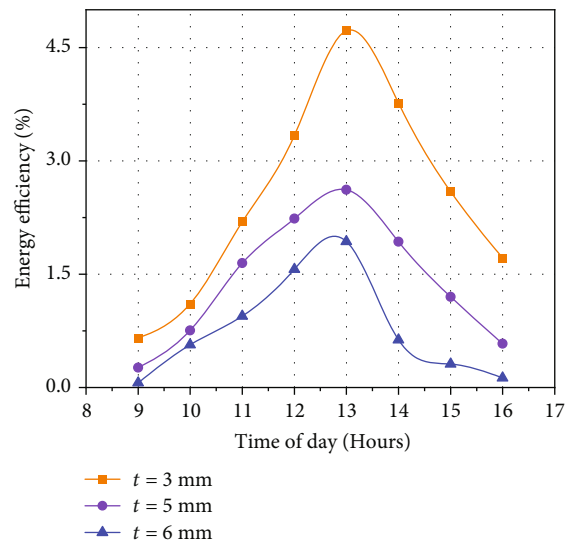

Figure 8: Time-wise fluctuation of exergy efficiency.

The time-wise fractional exergy of evaporation and convection between $T_{s.w}$ and $T_{c.c}$ for the CSS at G_t of 3, 5, and 6 mm is calculated using equations (10) and (11). It is found that fractional exergy of evaporation of the CSS at G_t of 3 mm is higher than that of the CSS at G_t of 5 and 6 mm. The maximum hourly fractional exergy of evaporation of 96.1, 96, and 95.9% has been calculated for the CSS at G_t of 3, 5, and 6 mm, respectively. During the experimentation, it is found that the evaporation rate and water temperature of the CSS at G_t of 3 mm are higher as compared to those of the CSS at G_t of 5 and 6 mm. So time-wise fractional exergy of evaporation of the CSS at G_t of 3 mm is higher than that of CSS at G_t of 5 and 6 mm. It is also found that fractional exergy of convection of the CSS at G_t of 5 mm is higher than that of the CSS at G_t of 3 and 6 mm. The maximum hourly fractional exergy of convection was calculated to be 9.4, 8.6, and 8.4% for the CSS at G_t of 3, 5, and 6 mm, respectively. The reason for maximum fractional exergy of convection for the CSS at G_t of 3 mm is the operating temperature of the G_t.

The EHTC starting from basin of the CSS to the glass cover is computed by [39–41]

$$h_{e,w-g} = 16.273 \times 10^{-3} \times h_{c,w-g} \left[\frac{P_w - P_{gi}}{T_w - T_{gi}} \right]. \quad (2)$$

The convective heat transfer coefficient starting from the basin of the CSS to the glass cover is computed by [39–41]

$$h_{c,w-g} = 0.884\left[\left(T_w - T_{gi}\right) + \frac{\left(P_w - P_{gi}\right)\left(T_w + 273\right)}{\left(268.9 \times 10^{-3} - P_{\mathrm{w}}\right)}\right]. \quad (3)$$

Partial vapour pressure at the basin T_{W} is computed by [39–41]

$$P_w = \exp\left(25.317 - \frac{5144}{273 + T_w}\right). \quad (4)$$

Partial vapour pressure at the T_{G} is computed by [39–41]

$$P_{gi} = \exp\left(25.317 - \frac{5144}{273 + T_{gi}}\right). \quad (5)$$

The thermal efficiency of the CSS is computed as [39–41]

$$\eta_{\mathrm{passive}} = \frac{\sum \dot{m}_{ew} L}{\sum I(t) A_s \times 3600} \times 100. \quad (6)$$

The exergy efficiency of the CSS is computed by [39–41]

$$\eta_{\mathrm{overall,exe}} = \frac{\sum \mathrm{Ex}_{\mathrm{output}}}{\sum \mathrm{Ex}_{\mathrm{input}}}. \quad (7)$$

The hourly exergy output is computed by [39–41]

$$\mathrm{Ex}_{\mathrm{output}} = \frac{m_{ew} L_{fg}}{3600} \times \left[1 - \frac{T_a}{T_w}\right]. \quad (8)$$

The hourly exergy input is computed by [39–41]

$$\mathrm{Ex}_{\mathrm{input}} = A_w I'(t) \times \left[1 - \frac{4}{3}\left(\frac{T_a}{T_s}\right) + \frac{1}{3}\left(\frac{T_a}{T_s}\right)^4\right]. \quad (9)$$

The fractional exergies for evaporation and convection are calculated using equations (10) and (11) and are as follows [42]:

$$F_{e,bw-ig} = \frac{\mathrm{Ex}_{e,bw-ig}}{\mathrm{Ex}_{ti}}, \quad (10)$$

$$F_{c,bw-ig} = \frac{\mathrm{Ex}_{c,bw-ig}}{\mathrm{Ex}_{ti}}. \quad (11)$$

3.7. Comparisons of Present Result and Similar Studies. Table 2 gives the several studies previously carried out by researchers on the thickness of the glass cover of solar stills. It also shows the results obtained on the productivity of pure water and the thermal efficiency of the stills tested, and it was noticed that energy efficiency varies between 17 and 42%, and it is found that the present results vary between 11.25 and 30.71%. We draw the attention that some research does not calculate either energy efficiency or exergy efficiency. Comparing the efficiencies, it is found that the CSS with 3 mm gives a good value in both types of efficiencies [38].

Table 2: Summary of various researchers on the glass cover thickness.

Ref. no.	Glass cover thickness	Energy efficiency	Exergy efficiency
[28]	4 mm	-	-
	8 mm	-	-
	12 mm	-	-
[29]	3.5 mm	21.42%	-
	4 mm	28.09%	-
[30]	3.18 mm	26.22%	-
	4.76 mm	29.28%	-
	6.35 mm	18.95%	
[31]	3 mm	32-34%	-
	4 mm	34-36%	
	5 mm	30-32%	-
	6 mm	26-28%	-
[32]	4 mm		-
	8 mm	-	-
	>8 mm + air film	-	-
	12 mm	-	-
	>12 mm + air film	-	-
[33]	4 mm	27%	-
	5 mm	22%	-
	6 mm	17%	-
[34]	2 mm	45-50%	-
	3 mm	40-45%	-
	4 mm	30-35%	-
	5 mm	30%	-
	6 mm	25-30%	-
	7 mm	20-25%	-
	8 mm	15-20%	
[35]	4 mm	-	-
	6 mm	-	-
[37]	2 mm	-	-
	6 mm	-	-
	10 mm	-	-
	14 mm	-	-
	18 mm	-	-
[38]	4 mm	-52.7%	-
	8 mm + air film		-
Our current work	3 mm	30.71%	2.46%
	5 mm	18.35%	1.38%
	6 mm	11.25%	0.84%

4. Conclusion

Based on the investigational outcome on the CSS, the following conclusions are arrived at.

(i) The CSS at G_t of 3, 5, and 6 mm has a yield of 3.15, 1.9, and 1.1 kg, respectively. The CSS at G_t of 3 mm produced the 40.48% and 65.15% higher yield than the CSS at G_t of 5 and 6 mm, respectively.

(ii) The thermal and exergy efficiencies of 30.71, 18.35, and 11.25% and 2.46, 1.38, and 0.84% have been obtained for the CSS at G_t of 3, 5, and 6 mm, respectively.

(iii) The thermal efficiency of the CSS is higher in the case of CSS at G_t of 3 mm. The thermal efficiency of the CSS at G_t of 3 mm is 40.25% and 63.37% higher as compared to that of the CSS at G_t of 5 and 6 mm, respectively.

(iv) The exergy efficiency of the CSS is higher in the case of CSS at G_t of 3 mm. The exergy efficiency of the CSS at G_t of 3 mm is 44.01% and 65.81% higher as compared to that of the CSS at G_t of 5 and 6 mm, respectively.

Nomenclature

G_t: Glass thickness
CSS: Conventional solar still
T_W: Water temperature
T_G: Glass temperature
EHTC: Evaporative heat transfer coefficient.

Data Availability

The data used to support the findings of this study are included within the article.

Conflicts of Interest

The authors declare that they have no conflicts of interest.

References

[1] M. H. Ahmadi, M. Ghazvini, M. Sadeghzadeh et al., "Solar power technology for electricity generation: a critical review," *Energy Sci Eng*, vol. 6, no. 5, pp. 340–361, 2018.

[2] A. Naseri, M. Bidi, and M. H. Ahmadi, "Thermodynamic and exergy analysis of a hydrogen and permeate water production process by a solar-driven transcritical CO_2 power cycle with liquefied natural gas heat sink," *Renewable Energy*, vol. 113, pp. 1215–1228, 2017.

[3] A. Naseri, M. Bidi, M. H. Ahmadi, and R. Saidur, "Exergy analysis of a hydrogen and water production process by a solar-driven transcritical CO_2 power cycle with Stirling engine," *Journal of Cleaner Production*, vol. 158, pp. 165–181, 2017.

[4] A. Mohammadi, M. H. Ahmadi, M. Bidi, M. Ghazvini, and T. Ming, "Exergy and economic analyses of replacing feedwater heaters in a Rankine cycle with parabolic trough collectors," *Energy Reports*, vol. 4, pp. 243–251, 2018.

[5] M. Dehghani Madvar, M. Alhuyi Nazari, J. Tabe Arjmand, A. Aslani, R. Ghasempour, and M. H. Ahmadi, "Analysis of stakeholder roles and the challenges of solar energy utilization in Iran," *International Journal of Low-Carbon Technologies*, vol. 13, no. 4, pp. 438–451, 2018.

[6] A. Khatibi, F. Razi Astaraei, and M. H. Ahmadi, "Generation and combination of the solar cells: a current model review," *Energy Sci Eng*, vol. 7, no. 2, pp. 305–322, 2019.

[7] M. H. Ahmadi, A. Baghban, M. Sadeghzadeh et al., "Evaluation of electrical efficiency of photovoltaic thermal solar collector," *Engineering Applications of Computational Fluid Mechanics*, vol. 14, no. 1, pp. 545–565, 2020.

[8] A. Naeimi, M. H. Ahmadi, M. Sadeghzadeh, and A. Kasaeian, "Optimum arrangement of two-stage plug and concentrate recycling RO systems using thermodynamic and exergy analysis," *International Journal of Numerical Methods for Heat & Fluid Flow*, vol. 30, no. 6, pp. 3323–3348, 2019.

[9] S. W. Sharshir, N. Yang, G. Peng, and A. E. Kabeel, "Factors affecting solar stills productivity and improvement techniques: a detailed review," *Applied Thermal Engineering*, vol. 100, pp. 267–284, 2016.

[10] A. Muthu Manokar, D. Prince Winston, A. E. Kabeel, R. Sathyamurthy, and T. Arunkumar, "Different parameter and technique affecting the rate of evaporation on active solar still -a review," *Heat and Mass Transfer*, vol. 54, no. 3, pp. 593–630, 2018.

[11] M. Ashouri, M. H. Ahmadi, M. Feidt, and F. R. Astaraei, "Exergy and energy analysis of a regenerative organic Rankine cycle based on flat plate solar collectors," *Mechanics & Industry*, vol. 18, no. 2, p. 217, 2017.

[12] M. Ashouri, A. M. Khoshkar Vandani, M. Mehrpooya, M. H. Ahmadi, and A. Abdollahpour, "Techno-economic assessment of a Kalina cycle driven by a parabolic trough solar collector," *Energy Conversion and Management*, vol. 105, pp. 1328–1339, 2015.

[13] B. Ghorbani, M. Mehrpooya, and M. Sadeghzadeh, "Developing a tri-generation system of power, heating, and freshwater (for an industrial town) by using solar flat plate collectors, multi-stage desalination unit, and Kalina power generation cycle," *Energy Conversion and Management*, vol. 165, pp. 113–126, 2018.

[14] B. Ghorbani, M. Miansari, S. Zendehboudi, and M.-H. Hamedi, "Exergetic and economic evaluation of carbon dioxide liquefaction process in a hybridized system of water desalination, power generation, and liquefied natural gas regasification," *Energy Conversion and Management*, vol. 205, p. 112374, 2020.

[15] B. Ghorbani, R. Shirmohammadi, and M. Mehrpooya, "Development of an innovative cogeneration system for fresh water and power production by renewable energy using thermal energy storage system," *Sustainable Energy Technologies and Assessments*, vol. 37, 2020.

[16] B. Ghorbani, R. Shirmohammadi, M. Amidpour, F. Inzoli, and M. Rocco, "Design and thermoeconomic analysis of a multi-effect desalination unit equipped with a cryogenic refrigeration system," *Energy Conversion and Management*, vol. 202, p. 112208, 2019.

[17] B. Ghorbani, M. Mehrpooya, and S. A. Mousavi, "Hybrid molten carbonate fuel cell power plant and multiple-effect desalination system," *Journal of Cleaner Production*, vol. 220, pp. 1039–1051, 2019.

[18] M. S. Niasar, B. Ghorbani, M. Amidpour, and R. Hayati, "Developing a hybrid integrated structure of natural gas conversion to liquid fuels, absorption refrigeration cycle and multi effect desalination (exergy and economic analysis)," *Energy*, vol. 189, p. 116162, 2019.

[19] A. Khechekhouche, A. Boukhari, Z. Driss, and N. E. Benhissen, "Seasonal effect on solar distillation in the El-Oued region of south-east Algeria," *International Journal of Energetica*, vol. 2, no. 1, 2017.

[20] A. Khechekhouche, A. B. Kabeel, B. Benhaoua, M. E. H. Attia, and E. M. S. El-Said, "Traditional solar distiller improvement by a single external refractor under the climatic conditions of the El Oued region, Algeria," *Desalination and Water Treatment*, vol. 177, pp. 23–28, 2020.

[21] A. Johnson, L. Mu, Y. H. Park et al., "A thermal model for predicting the performance of a solar still with Fresnel lens," *Water*, vol. 11, no. 9, p. 1860, 2019.

[22] A. Khechekhouche, B. Boubaker, and Z. Driss, "Solar distillation between a simple and double-glazing," *Revue de mécanique*, vol. 2, 2018.

[23] M. M. Morad, H. A. M. El-Maghawry, and K. I. Wasfy, "Improving the double slope solar still performance by using flat-plate solar collector and cooling glass cover," *Desalination*, vol. 373, pp. 1–9, 2015.

[24] T. Prem kumar, S. Moulieswaran, and S. Pradeep, "Effect of glazing and cooling on solar waste water still," *International Journal of Research and Analytical Reviews*, vol. 6, no. 1, pp. 927–932, 2019.

[25] B. T. Nguyen, "Factors Affecting the Yield of Solar Distillation Systems and Measures to Improve Productivities," in *Desalination and Water Treatment*, IntechOpen, 2018.

[26] D. Bechki, H. Bouguettaia, J. Blanco-Galvez et al., "Effect of partial intermittent shading on the performance of a simple basin solar still in South Algeria," *Desalination*, vol. 260, no. 1-3, pp. 65–69, 2010.

[27] R. Cherraye, B. Bouchekima, D. Bechki, H. Bouguettaia, and A. Khechekhouche, "The effect of tilt angle on solar still productivity at different seasons in arid conditions (South Algeria)," *International Journal of Ambient Energy*, vol. 41, pp. 1–7, 2020.

[28] H. N. Panchal and P. K. Shah, "Effect of varying glass cover thickness on performance of solar still: in a winter climate conditions," *International Journal of Renewable Energy Research*, vol. 1, pp. 212–223, 2011.

[29] J. S. Gawande and L. B. Bhuyar, "Effect of glass cover thickness on the performance of stepped type solar still," *International Journal of Innovative Science and Research Technology*, vol. 1, pp. 19–26, 2013.

[30] M. K. Boodhan and I. Haraksingh, "An investigation into the effect on the productivity of cascade-type solar distillation systems with varying cover thicknesses and still orientations under tropical Caribbean climatic conditions," *Desalination and Water Treatment*, vol. 55, no. 12, pp. 3295–3302, 2014.

[31] R. Bakari, R. J. A. Minja, and K. N. Njau, "Effect of glass thickness on performance of flat plate solar collectors for fruits drying," *Journal of Energy*, vol. 2014, Article ID 247287, 8 pages, 2014.

[32] A. O. Edeoja, F. Unom, and J. A. Edeoja, "Investigation of the effect of cover thickness on the yield of a single basin solar still under Makurdi climate," *International Journal of Engineering Science Invention*, vol. 14, pp. 131–138, 2015.

[33] H. Panchal, "Performance investigation on variations of glass cover thickness on solar still: experimental and theoretical analysis," *Technol Econ Smart Grids Sustain Energy*, vol. 1, no. 1, p. 7, 2016.

[34] A. Santos and E. Hernandez, "Experimental evaluation of a single slope solar still," *TECCIENCIA*, vol. 12, no. 22, pp. 63–71, 2017.

[35] A. T. Balewa, K. Polytechnic, and F. Polytechnic, "Effect of glass thickness on solar still performance," *Journal of Engineering and Applied Science*, vol. 11, pp. 49–58, 2019.

[36] A. Khechekhouche, Z. Driss, and B. Durakovic, "Effect of heat flow via glazing on the productivity of a solar still," *International Journal of Energetica*, vol. 4, no. 2, pp. 54–57, 2020.

[37] M. Khan and M. Mustafa, "Solar still distillate productivity enhancement by using reflector and design optimization," *Innovative Energy & Research*, vol. 8, 2019.

[38] A. Khechekhouche, B. Benhaoua, A. M. Manokar, A. E. Kabeel, and R. Sathyamurthy, "Exploitation of an insulated air chamber as a glazed cover of a conventional solar still," *Heat Transfer-Asian Research*, vol. 48, no. 5, pp. 1563–1574, 2019.

[39] A. M. Manokar, D. P. Winston, J. D. Mondol, R. Sathyamurthy, A. E. Kabeel, and H. Panchal, "Comparative study of an inclined solar panel basin solar still in passive and active mode," *Solar Energy*, vol. 169, pp. 206–216, 2018.

[40] A. Khechekhouche, B. Benhaoua, M. Manokar, R. Sathyamurthy, A. E. Kabeel, and Z. Driss, "Sand dunes effect on the productivity of a single slope solar distiller," *Heat and Mass Transfer*, vol. 56, no. 4, pp. 1117–1126, 2020.

[41] M. M. Thalib, A. M. Manokar, F. A. Essa, N. Vasimalai, R. Sathyamurthy, and F. P. G. Marquez, "Comparative study of tubular solar stills with phase change material and nano-enhanced phase change material," *Energies*, vol. 13, no. 15, p. 3989, 2020.

[42] S. Nazari, M. Bahiraei, H. Moayedi, and H. Safarzadeh, "A proper model to predict energy efficiency, exergy efficiency, and water productivity of a solar still via optimized neural network," *Journal of Cleaner Production*, vol. 277, 2020.

Hindawi
International Journal of Photoenergy
Volume 2021, Article ID 6619138, 8 pages
https://doi.org/10.1155/2021/6619138

Research Article

Effect of Design Parameters on Fresh Water Produced from Triangular Basin and Conventional Basin Solar Still

A. Rajendra Prasad,[1] Ravishankar Sathyamurthy,[2] M. Sudhakar,[1] B. Madhu,[3] D. Mageshbabu,[3] A. Muthu Manokar,[4] and Ali J. Chamkha[5,6]

[1]*Department of Mechanical Engineering, Sri Sairam Engineering College, Chennai, 600045 Tamil Nadu, India*
[2]*Department of Mechanical Engineering, KPR Institute of Engineering and Technology, Arasur, Coimbatore, 641407 Tamil Nadu, India*
[3]*Department of Mechanical Engineering, Velammal Institute of Technology, Chennai, Tamil Nadu, India*
[4]*Department of Mechanical Engineering, B. S. Abdur Rahman Crescent Institute of Science and Technology, Chennai, 600048 Tamil Nadu, India*
[5]*Faculty of Engineering, Kuwait College of Science and Technology, Kuwait, Kuwait*
[6]*Institute of Theoretical and Applied Research (ITAR), Duy Tan University, Hanoi 100000, Vietnam*

Correspondence should be addressed to Ali J. Chamkha; alichamkha@duytan.edu.vn

Received 19 December 2020; Revised 3 February 2021; Accepted 16 February 2021; Published 2 March 2021

Academic Editor: Hafiz Muhammad Ali

Copyright © 2021 A. Rajendra Prasad et al. This is an open access article distributed under the Creative Commons Attribution License, which permits unrestricted use, distribution, and reproduction in any medium, provided the original work is properly cited.

This paper reported the experimental testing of a triangular and conventional basin solar still (TBSS and CBSS). Solar basin and absorber are made of glass and a polyethylene cover, respectively, with an area of 0.25 m^2. Square and triangular absorber with the same area of 0.25 m^2 with square and triangular glass cover for condensation was fixed. Experimentations were conducted during the month of December 2018, and different natural criteria such as intensity, wind speed, and surrounding ambient temperatures were considered. Also, the modified model was compared to the CBSS on its performance and efficiency characteristics. The experimental results also revealed that the temperature of the water inside the TBSS was higher as compared with that of the CBSS. The daily yield obtained from CBSS and TBSS was found to be 2.7 and 3.2 kg/m^2, respectively. Also, the daily efficiency of the TBSS was improved by 11.36% than the CBSS.

1. Introduction

Renewables appear to be the one of the source which is inexhaustible, clean, ecofriendly, and cost economic. Also, it appears to be the competitive energy among the other nonrenewable energy sources. Due to their abundance and its potential to use in the globe, they differ from the use of fossil fuel. Renewables will not even produce any kind of greenhouse gases which normally affect the climate which includes the reduction in annual rainfall and increased ambient temperature [1–4].

The utilization of solar energy in the distillation process appears to be an economical method to produce fresh water [5–8]. Manokar et al. [9] reviewed the different types of techniques employed in pyramidal solar still (PSS) for fresh water improvement. The different heat exchange mechanism employed in solar still for enhanced fresh water was reviewed by Kabeel et al. [10]. Similarly, Sathyamurthy et al. [11] surveyed the different geometries employed in cover and absorber of solar still for enhanced yield. The factors that affect the performance of PSS with a triangular basin and cover were experimentally studied by Sathyamurthy

et al. [12]. Two different parameters, namely controlling the depth of water and cover cooling techniques, were employed to achieve optimum yield. Essa et al. [13] studied a solar still and augmented the yield using a coffee-based colloid. The use of acrylic material as cover material in the PSS was analyzed by Manokar et al. [14].

Kumar et al. [15] used a double collector cover in the PSS. Their results exhibited that double collector cover reduces the thermal efficiency of the PSS as the air gap between the collector cover increased the cover temperature. Nayi [16] made a comprehensive review of the PSS. Experimental studies on the PSS with phase change materials (PCM) were carried out by Sathyamurthy et al. [17, 18]. Kumar et al. [19, 20] carried out theoretical and experimental studies on PSS integrated with an inclined solar still for enhancing fresh water. Kabeel et al. [21] used TiO_2 nanoparticles in black paints and coated in the absorber material of the triangular PSS. On the same PSS, Nagarajan et al. [22] theoretically studied the effect of glass cooling using a DC powered fan.

The performance of triangular solar still (TSS) in two different directions was experimentally analyzed by Rubio-Cerda et al. [23]. It was reported that the performance of the TSS at glass cover facing the east-west direction was higher as compared to the TSS at glass cover facing north-south direction. Varying water depths in the TSS were reported by Ahsan et al. [24]. The maximum yield of 1.6 and 1.55 kg/m^2 was obtained from water depth of 1.5 and 2.5 cm, respectively. A comparison between PSS and CSS was hypothetically studied by Fath et al. [25]. The annual yield produced from the CSS was 1532.7 L and PSS was 1510.5 L. It was reported that both CSS and PSS produced the nearly same daily yield of about 2.6 L. The performance of the PSS using fan was augmented the yield by 25% as compared to the conventional PSS by Taamneh and Taamneh [26]. The PSS with a fan has produced the maximum yield of 3 kg per day, whereas PSS without fan has produced a maximum yield of 2.5 L per day. Kabeel et al. [27] made a comparative study of conventional PSS and modified PSS basin with V-corrugated absorber surface and PCM. It was reported that modified PSS with PCM produced a daily yield of 6.6 kg, and conventional PSS has a daily yield of 3.5 L. Abdelal and Taamneh [28] introduced a novel composite absorber plate integrated PSS. It was reported that PSS with 5% CNT-coated plate has a maximum daily production of 3.3 kg/m^2, whereas the black painted plate has yield of 1.73 kg/m^2. Various existing solar still designs such as concave [29], spherical [30], hemispherical [31, 32], vertical [31–36], inverted absorber [37–40], tubular [41], pyramid [42], inclined [43–45], and hybrid solar still [46] are reviewed.

From the various review of literature, it is found that the use of triangular basin/absorber and single-slope triangular cover is not extensively studied. Various criteria such as water temperature, glass temperature, yield, evaporative, and convective heat transfer coefficient (EHTC and CHTC) have been studied in detail from the TBSS and CBSS. The present study is aimed at improving the fresh water produced from a triangular basin with a single-slope arrangement. An experimental investigation is carried out to study the obtained fresh water produced from the modified absorber and condensing cover of the TBSS.

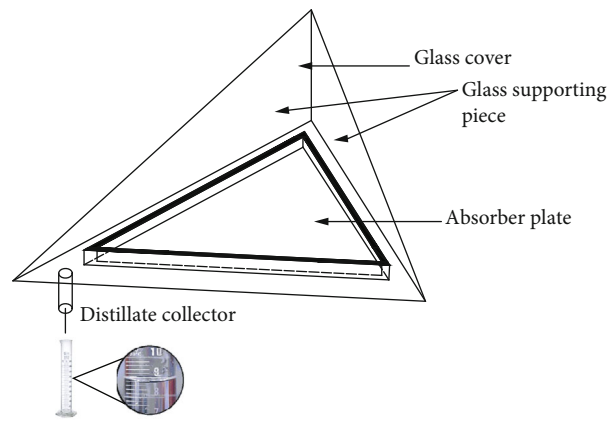

Figure 1: Graphical representation of TBSS.

2. Experimentation

Figure 1 shows the graphical representation of the TBSS with an absorber plate made of a triangular section. Figure 2 shows the schematic diagram of the CBSS and TBSS. It consists of a triangular basin with an area of 0.25 m^2. The dimensions of the conventional basin type solar still are 0.5 m long and 0.5 m wide with higher end wall height of 0.2 m. Similarly, to have equivalent basin area, a triangular basin with sides of 0.57 m each forms a equilateral triangle, and the basin height is 0.2 m. Two triangular supporting pieces are kept vertical in the absorber, while the cover material is made of polyethylene sheet, which transmits the solar radiance. The sea water is fed into the absorber using a plastic hose, and the flow is controlled using a flow control valve. The evaporated water from the absorber gets condensed in the cover and glides through the smooth inclined surface to the distillate collector and collected in a calibrated flask. Insulation are provided at the bottom and side walls of the solar still to prevent the loss of heat. For comparison and experimental validation, a CBSS with a basin area of 0.25 m^2 is fabricated and tested for the same outdoor experimental condition. The flow of sea water into the basin is under control using a control valve. At each interval of evaporation from the upper surface of the water, fresh sea water is fed into the basin to maintain the stable water depth. The whole experiment is fabricated and researched in conditions of Chennai, India. Testing is conducted from 8 a.m. to 6 p.m. during the month of December 2018, while the covers of TBSS and CBSS are facing south direction. On a triangular and conventional basin solar still, four sensors each on the basic elements are placed, and the average values are taken. The water depth inside the TBSS and CBSS is measured on an hourly basis, and sea water is feed into the basin for maintaining stable water depth. Table 1 shows the details of instruments, range, accuracy, and error. The elemental temperatures of the TBSS and CBSS, namely, water, glass, and basin temperature, are measured using PT100 type thermocouple, whereas the wind

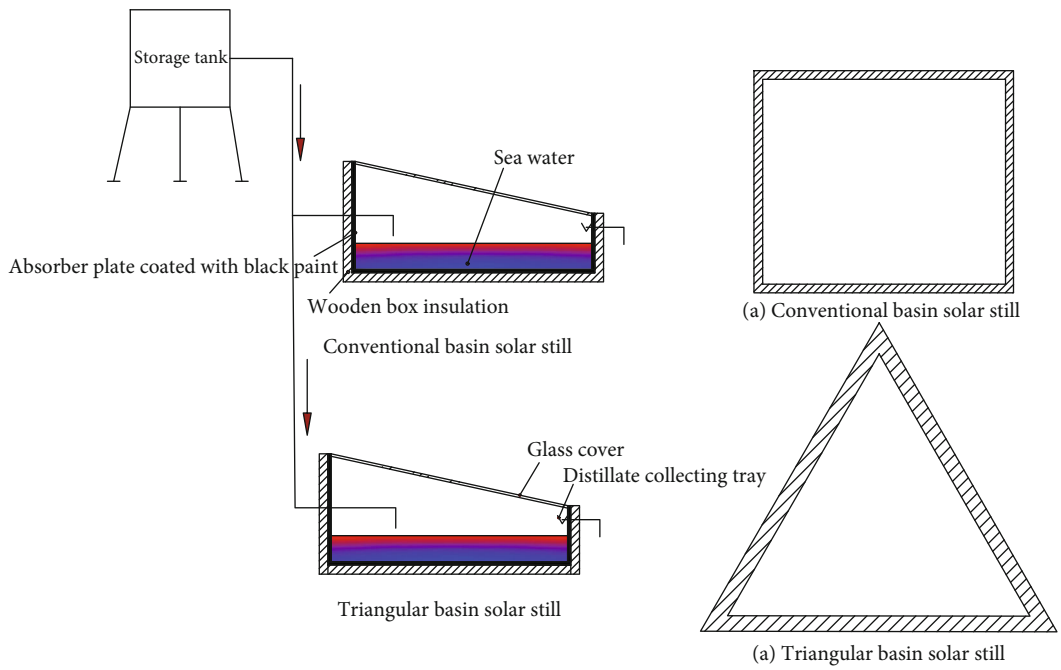

Figure 2: Schematic diagram of conventional and triangular basin solar still.

Table 1: Range, accuracy, error, and instruments used in the study.

Instrument	Range	Accuracy	Error
Temperature sensor (PT-100 type)	0-500°C	±0.1°C	±1.5%
Distillate collecting flask	0-2000 ml	±10 ml	±1.5%
Wind velocity meter	0-45 m/s	±0.1 m/s	±3%
Solar power meter	0-3500 W/m^2	±10 W/m^2	±3.5%

velocity and solar radiance are measured using anemometer and solar power meter, respectively. On an hourly basis, temperatures, solar intensity, and distillate collected are measured.

The daily efficiency of TBSS and CBSS is the ratio of the product of latent heat of vaporization and the amount of accumulated potable water produced to the accumulated solar intensity for the entire day.

3. Uncertainty

The instruments used in the experiments produce some possible errors which is determined in the form of uncertainty. The uncertainties produced during the experiments from the instruments is tabulated in Table 1. It is defined as the ratio of smallest amount to the least value of output. The uncertainty produced by the calibrated flask in collecting the distilled water depends on the amount of water collected in the flask. It is mathematically expressed as

$$R_m = \sqrt{\left(\frac{\partial m}{\partial h} R_h\right)^2}. \quad (1)$$

For determining the uncertainty of TBSS and CBSS daily efficiency, the amount of water collected in the calibrated flask and solar radiation falling on the glass surface and is mathematically expressed as

$$R_\eta = \sqrt{\left(\frac{\partial \eta}{\partial m} R_m\right)^2 + \left(\frac{\partial \eta}{\partial I(t)} R_{I(t)}\right)^2}. \quad (2)$$

Using Equation (1), the uncertainties of distilled water collected from the calibrated flask, solar radiation, wind velocity, and temperature were calculated as 1.5, 3.5, 3, and 1.5%, respectively. Similarly, using (2), the calculated uncertainty of daily efficiency is found as 2.1%.

4. Results and Discussion

The fluctuation in solar intensity, basin, water, and glass temperature of the CBSS and TBSS is shown in Figure 3. The experiments were conducted for the December 2018 (30 days), and the best readings are taken for the analysis. The improvement in performance and efficiency of renewable energy system depends on external input parameters such as solar intensity, ambient temperature, and wind velocity.

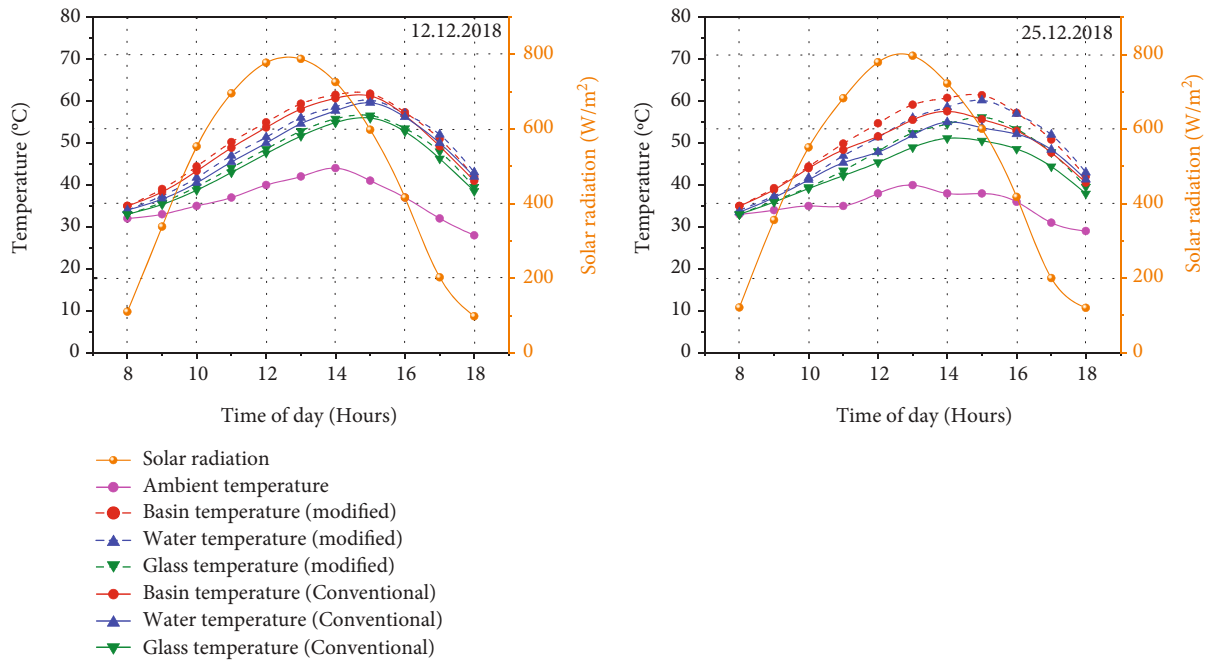

Figure 3: Variations in solar intensity, basin, water, and glass temperature of CBSS and TBSS on 12.12.2018 and 25.12.2018.

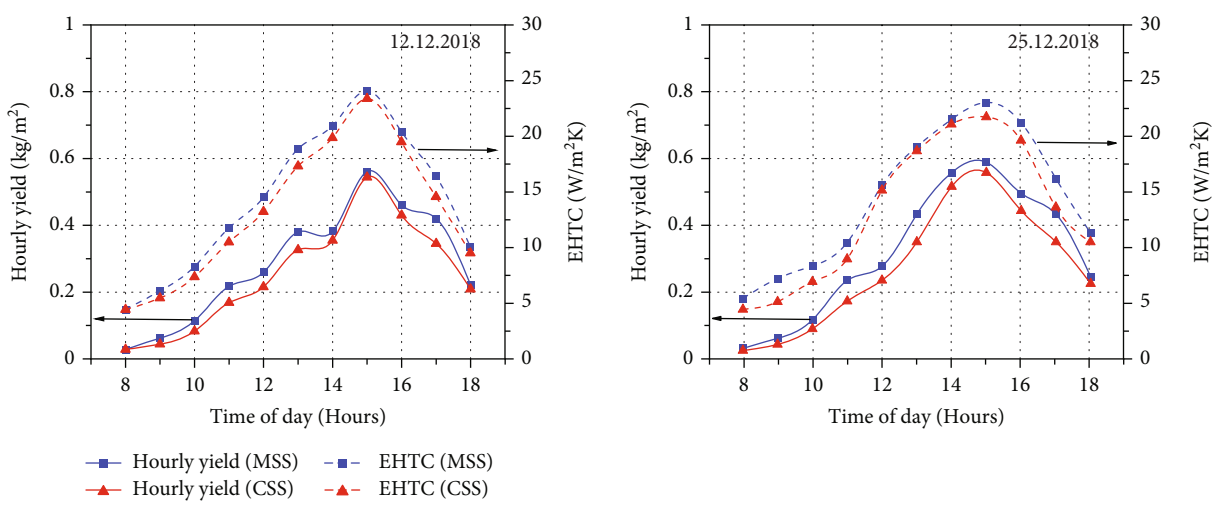

Figure 4: Variations in yield and EHTC from CBSS and TBSS.

With continuous solar intensity as heat input, the elements of the TBSS and CBSS such as water, glass, and basin temperature rise. As time varies, the solar intensity varies by reaching its peak during the midnoon. The whole experiment was conducted during the bright sky condition. The peak solar radiation recorded during the experiments on 12.12.2018 and 25.12.2018 were 778 and 797 W/m^2 while the ambient temperature recorded for the corresponding experiments was 42 and 40°C, respectively. It can be noticed that the maximum temperature occurs at 15 : 00 Hrs. The maximum temperature of the water using TBSS is found as 60.4°C, whereas the temperature of the water using conventional is 58.3°C. The water temperature peaks at 15 : 00 Hrs; as the heat energy is stored in the water as sensible heat and during the lower sun shine hours, the energy is liberated. Also, it is clearly evident that the maximum exposure area of water with solar radiation is the cause for higher temperature in the modified solar still with triangular basin than conventional basin type solar still. Similarly, the cover glass temperature of TBSS is higher as compared to that of CBSS. Due to higher evaporation from the basin, the vapor gets accumulated in the glass cover which possibly increase the temperature of cover from the modified triangular basin solar still. The maximum temperature difference between water and glass is found as 3.6°C and 3.2°C for TBSS and CBSS.

The peak glass temperature of the TBSS and CBSS are found as 56.1 and 50.5°C on 25.12.2018, respectively. There is a maximum temperature difference between water and

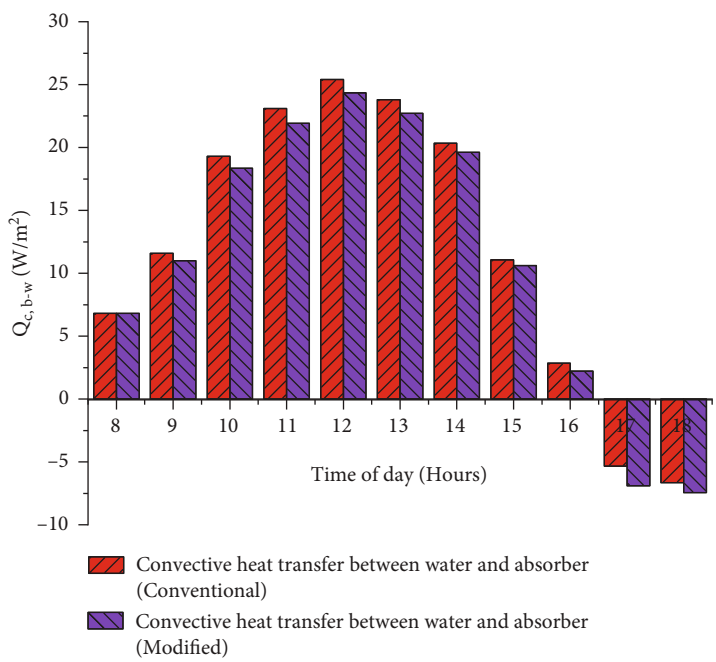

Figure 5: Variations in CHTC between water and basin of CBSS and TBSS.

Table 2: Comparison of yield and thermal efficiency from the CBSS and TBSS.

Date of experiment	Daily yield (kg/m^2)		Daily efficiency (%)		Total solar radiation (W/m^2)	Improvement in yield (%)
	MSS	CSS	MSS	CSS		
12.12.2018	3.24	2.82	38.28	33.32	5303	12.96
15.12.2018	3.35	2.84	38.79	32.88	5412	15.22
19.12.2018	3.12	2.74	37.24	32.70	5250	12.17
25.12.2018	3.41	2.91	39.24	33.49	5445	14.66

glass on 25.12.2018 using TBSS, and CBSS is found as 4 and 3.1°C, respectively. The increase in temperature of the water is due to the maximum absorption of solar radiance with the modified cover surface, which enhanced the evaporation and condensation rate inside the closed chamber. During the experiments, it is found that the elemental temperatures, such as basin, water, and glass, are higher using the TBSS compared to that of CBSS.

Similarly, the variations in yield and EHTC using the correlation from Appendix of the CBSS and TBSS for two different experimental days are shown in Figure 4. It can be seen that the evaporation rate is enhanced using the modified absorber geometry inside the TBSS. The maximum EHTC from the TBSS and CBSS are found as 24.3 and 23.2 W/m^2 K, respectively. On the other hand, the maximum distilled water produced from the TBSS and CBSS is found to be 0.56 and 0.54 kg/m^2, respectively. The increase in freshwater yield is due to the effect of higher evaporation with higher water temperature within the modified basin. There is an increase of about 3.7% in the maximum productivity, and an increase of about 12.96% is observed in the total productivity of freshwater produced. On average, freshwater produced from the TBSS is improved by 12% than the CBSS.

The increase in output is due to the effect of a lower CHTC rate between water and basin (Figure 5). The CHTC between water and basin is higher in the case of the conventional basin, whereas, with the modified basin, the CHTC reduces. During the absence of solar radiation, the CHTC has a negative impact on the modified basin as the rate of CHTC is higher as compared to that of the conventional basin. A comparison of daily productivity and daily efficiency of the TBSS and CBSS during the experimental days is tabulated in Table 2. It is known that the daily yield from the TBSS and CBSS was found as 3.12-3.41 and 2.74-2.91 kg/m^2, respectively. There is an improvement in yield of about 12.96–15.22% using the TBSS than the CBSS. It is also seen that the daily efficiency of the CBSS using a square absorber is lower as compared to that of TBSS using a triangular absorber. The daily efficiency of TBSS and CBSS ranges from 37.24 to 39.24 and from 32.7 to 33.49%, respectively.

The various published work related to our testing is provided in Table 3. From the table, it has been identified that PSS integrated with inclined solar still provided the maximum yield of 7.52 kg/m^2, and triangular PSS coated with TiO_2 nanoparticle has a yield of 6.6 kg/m^2. According to

Table 3: Comparison of present testing with previously published work.

S. No	Author name	Experimentation	Yield	Location
1	Kumar et al. [19, 20]	PSS integrated with an inclined solar still	7.52 kg/m^2	Chennai, India
2	Kabeel et al. [21]	Triangular PSS coated with TiO2 nanoparticle	6.6 kg/m^2	Chennai, India
3	Ahsan et al. [24]	Experimentation on TSS by varying water depth	1.6 kg/m^2	Japan
4	Taamneh and Taamneh [26]	The PSS with fan	3 L	Jordan
5	Kabeel et al. [27]	Modified PSS basin with V-corrugated absorber surface and PCM	6.6 kg/m^2	Tanta, Egypt
6	Abdelal and Taamneh [28]	Novel composite absorber plate integrated PSS	3.3 kg/m^2	Jordan
7	Kabeel et al. [47]	Tubular solar still using NPCM	5.62 kg/m^2	Chennai, India
8	Kabeel [29]	Concave wick	4.1 L/m^2	Tanta, Egypt
9	Dhiman [30]	Spherical solar still	2.75 kg/m^2	India
10	Ismail [48]	Hemispherical solar still transportable type	5.7 L/m^2	Saudi Arabia
11	Arunkumar et al. [49]	Hemispherical solar still	4200 mL/m^2	Coimbatore, India
12	Minasian and Al-Karaghouli [33]	Floating vertical solar still	5000 mL/m^2	Baghdad
13	Boukar and Harmim [31]	Vertical solar still	2.3 kg/m^2	Adrar
14	Tanaka [32]	Multi effect vertical diffusion solar still	13.3 kg/m^2	Fukuoka, Japan
16	Boukar and Harmim [35]	One sided vertical solar still	1.2 kg/m^2	Adrar, Algeria
17	El-Sebaii [36]	Vertical solar still	4.2 kg/m^2	Tanta, Egypt
18	Abdul-Wahab and Al-Hatmi [37]	Inverted absorber solar still with refrigeration cycle	10.08 kg/day	Muscat, Sultanate of Oman
19	Abdul-Wahab and Al-Hatmi [38]	Inverted absorber solar still with refrigeration cycle	10.08 kg/day	Muscat, Sultanate of Oman
20	Present study	TBSS	3.2 kg/m^2	Chennai, India

Ahsan et al. [24], TSS produced a yield of 1.6 kg/m^2, but our work has produced maximum productivity of 3.2 kg/m^2. The present TBSS has produced 50% higher productivity as compared to that of Ahsan et al. [24].

5. Conclusions

The present experimental investigation was conducted in the climatic situation of Chennai, India, and the following conclusions were arrived from the experimental results:

(i) Water temperature from the TBSS with the triangular basin was increased by about 12% when compared to the CBSS

(ii) The maximum total yield produced from the TBSS and CBSS was found to be 3.24 and 2.82 kg/m^2 while the total productivity using modified absorber was improved by 12.96% than CBSS

(iii) The increased yield of freshwater was higher in the case of TBSS, and it was mainly due to its exposure area and the condensing cover area with the solar radiance

(iv) The daily thermal efficiency of the overall system using TBSS and CBSS was found as 39.24 and 33.29%, respectively.

Appendix

The EHTC from saline water to glass is calculated by [50, 51]

$$h_{e,w-g} = 16.273 \times 10^{-3} \times h_{c,w-g} \left[\frac{P_w - P_{gi}}{T_{b.w} - T_{gi}} \right]. \quad \text{(A1)}$$

The CHTC from the saline water to the glass is calculated by [50, 51]

$$h_{c,w-g} = 0.884 \left[\left(T_{b.w} - T_{gi} \right) + \frac{\left(P_w - P_{gi} \right) \left(T_{b.w} + 273 \right)}{\left(268.9 \times 10^{-3} - P_w \right)} \right]. \quad \text{(A2)}$$

Partial vapor pressure at the water is calculated by [50, 51]

$$P_w = \exp \left(25.317 - \left(\frac{5144}{273 + T_{b.w}} \right) \right). \quad \text{(A3)}$$

Partial vapor pressure at the glass is calculated by [50, 51]

$$P_{gi} = \exp \left(25.317 - \left(\frac{5144}{273 + T_{gi}} \right) \right). \quad \text{(A4)}$$

The energy efficiency of the TBSS and CBSS is estimated as [50, 51]

$$\eta_{passive} = \frac{\sum \dot{m}_{ew} \times L}{\sum I(t) A_s \times 3600} \times 100, \quad \text{(A5)}$$

where h is the latent heat of vaporization (kJ/kg) and $I(t)$ is the solar intensity (W/m^2).

The latent heat of vaporization is mathematically expressed by

$$h_{fg} = 10^3 \left[2501.9 - 2.40706 T_w + 1.192217 \times 10^{-3} T_w - 1.5863 \times 10^{-5} T_w\right], \quad \text{(A6)}$$

where T_w is the temperature of water (°C).

Nomenclature

TBSS: Triangular basin solar still
CBSS: Conventional basin solar still
PSS: Pyramidal solar still
EHTC: Evaporative heat transfer coefficient
CHTC: Convective heat transfer coefficient
TSS: Triangular solar still

Data Availability

Will be made available on request.

Conflicts of Interest

The authors declare that they have no conflicts of interest.

References

[1] A. Vedrtnam, M. P. Upadhyay, and K. Kalauni, "Experimental and theoretical studies of the heat transfer characteristics of the lab-scale sensible heat storage system," *International Journal of Energy for a Clean Environment*, vol. 20, no. 2, pp. 167–193, 2019.

[2] N. V. Ogueke, M. C. Njoku, and E. E. Anyanwu, "Design, construction, and testing of a cylindrical solar water heater," *International Journal of Energy for a Clean Environment*, vol. 10, no. 1-4, pp. 57–72, 2009.

[3] H. Agrawal, V. Yadav, Y. Kumar, and A. Yadav, "Comparison of experimental data for sensible and latent heat storage materials for late-evening cooking based on a dish-type solar cooker," *International Journal of Energy for a Clean Environment*, vol. 15, no. 1, pp. 47–72, 2014.

[4] A. Kumar and A. Yadav, "Experimental investigation of a desiccant air conditioning system based on solar-powered composite desiccant bed heat exchanger," *International Journal of Energy for a Clean Environment*, vol. 18, no. 1, pp. 79–97, 2017.

[5] B. Madhu, B. E. Balasubramanian, A. E. Kabeel et al., "Experimental investigation on the effect of sensible heat energy storage in an inclined solar still with baffles," *Desalination and Water Treatment*, vol. 116, pp. 49–56, 2018.

[6] R. Sathyamurthy and E. El-Agouz, "Experimental analysis and exergy efficiency of a conventional solar still with Fresnel lens and energy storage material," *Heat Transfer—Asian Research*, vol. 48, no. 3, pp. 885–895, 2019.

[7] G. B. Balachandran, P. W. David, A. B. P. Vijayakumar, A. E. Kabeel, M. M. Athikesavan, and R. Sathyamurthy, "Enhancement of PV/T-integrated single slope solar desalination still productivity using water film cooling and hybrid composite insulation," *Environmental Science and Pollution Research*, vol. 27, no. 26, pp. 32179–32190, 2019.

[8] A. Khechekhouche, B. Benhaoua, A. M. Manokar, A. E. Kabeel, and R. Sathyamurthy, "Exploitation of an insulated air chamber as a glazed cover of a conventional solar still," *Heat Transfer—Asian Research*, vol. 48, no. 5, pp. 1563–1574, 2019.

[9] A. M. Manokar, Y. Taamneh, A. E. Kabeel, R. Sathyamurthy, D. P. Winston, and A. J. Chamkha, "Review of different methods employed in pyramidal solar still desalination to augment the yield of freshwater," *Desalination and Water Treatment*, vol. 136, pp. 20–30, 2018.

[10] A. E. Kabeel, T. Arunkumar, D. C. Denkenberger, and R. Sathyamurthy, "Performance enhancement of solar still through efficient heat exchange mechanism - a review," *Applied Thermal Engineering*, vol. 114, pp. 815–836, 2017.

[11] R. Sathyamurthy, D. G. Harris Samuel, P. K. Nagarajan, and T. Arunkumar, "Geometrical variations in solar stills for improving the fresh water yield—a review," *Desalination and Water Treatment*, vol. 57, no. 45, pp. 21145–21159, 2016.

[12] R. Sathyamurthy, H. J. Kennady, P. K. Nagarajan, and A. Ahsan, "Factors affecting the performance of triangular pyramid solar still," *Desalination*, vol. 344, pp. 383–390, 2014.

[13] F. A. Essa, A. H. Elsheikh, A. A. Algazzar et al., "Eco-friendly coffee-based colloid for performance augmentation of solar stills," *Process Safety and Environmental Protection*, vol. 136, pp. 259–267, 2020.

[14] A. Muthu Manokar, Y. Taamneh, A. E. Kabeel et al., "Effect of water depth and insulation on the productivity of an acrylic pyramid solar still - an experimental study," *Groundwater for Sustainable Development*, vol. 10, p. 100319, 2020.

[15] S. A. Kumar, P. S. Mohan Kumar, R. Sathyamurthy, and A. M. Manokar, "Experimental investigation on pyramid solar still with single and double collector cover—comparative study," *Heat Transfer—Asian Research*, vol. 49, no. 1, pp. 103–119, 2020.

[16] K. Nayi and K. V. Modi, "Pyramid solar still: a comprehensive review," *Renewable and Sustainable Energy Reviews*, vol. 81, pp. 136–148, 2018.

[17] R. Sathyamurthy, P. K. Nagarajan, H. Kennady, T. S. Ravikumar, V. Paulson, and A. Ahsan, "Enhancing the heat transfer of triangular pyramid solar still using phase change material as storage material," *Frontiers in Heat and Mass Transfer (FHMT)*, vol. 5, no. 1, p. 3, 2014.

[18] R. Sathyamurthy, P. K. Nagarajan, J. Subramani, D. Vijayakumar, and K. M. A. Ali, "Effect of water mass on triangular pyramid solar still using phase change material as storage medium," *Energy Procedia*, vol. 61, pp. 2224–2228, 2014.

[19] P. N. Kumar, D. G. Harris Samuel, P. K. Nagarajan, and R. Sathyamurthy, "Theoretical analysis of a triangular pyramid solar still integrated to an inclined solar still with baffles," *International Journal of Ambient Energy*, vol. 38, no. 7, pp. 694–700, 2016.

[20] P. N. Kumar, A. M. Manokar, B. Madhu et al., "Experimental investigation on the effect of water mass in triangular pyramid

solar still integrated to inclined solar still," *Groundwater for Sustainable Development*, vol. 5, no. 2, pp. 29–234, 2017.

[21] A. E. Kabeel, R. Sathyamurthy, S. W. Sharshir et al., "Effect of water depth on a novel absorber plate of pyramid solar still coated with TiO_2 nano black paint," *Journal of Cleaner Production*, vol. 213, pp. 185–191, 2019.

[22] P. K. Nagarajan, S. A. El-Agouz, T. Arunkumar, and R. Sathyamurthy, "Effect of forced cover cooling technique on a triangular pyramid solar still," *International Journal of Ambient Energy*, vol. 38, no. 6, pp. 597–604, 2016.

[23] E. Rubio-Cerda, M. A. Porta-Gándara, and J. L. Fernandez-Zayas, "Thermal performance of the condensing covers in a triangular solar still," *Renewable Energy*, vol. 27, no. 2, pp. 301–308, 2002.

[24] A. Ahsan, M. Imteaz, U. A. Thomas, M. Azmi, A. Rahman, and N. N. Daud, "Parameters affecting the performance of a low cost solar still," *Applied Energy*, vol. 114, pp. 924–930, 2014.

[25] H. E. Fath, M. El-Samanoudy, K. Fahmy, and A. Hassabou, "Thermal-economic analysis and comparison between pyramid-shaped and single- slope solar still configurations," *Desalination*, vol. 159, no. 1, pp. 69–79, 2003.

[26] Y. Taamneh and M. M. Taamneh, "Performance of pyramid-shaped solar still: experimental study," *Desalination*, vol. 291, pp. 65–68, 2012.

[27] A. E. Kabeel, M. A. Teamah, M. Abdelgaied, and G. B. A. Aziz, "Modified pyramid solar still with v-corrugated absorber plate and PCM as a thermal storage medium," *Journal of Cleaner Production*, vol. 161, pp. 881–887, 2017.

[28] N. Abdelal and Y. Taamneh, "Enhancement of pyramid solar still productivity using absorber plates made of carbon fiber/CNT-modified epoxy composites," *Desalination*, vol. 419, pp. 117–124, 2017.

[29] A. E. Kabeel, "Performance of solar still with a concave wick evaporation surface," *Energy*, vol. 34, no. 10, pp. 1504–1509, 2009.

[30] N. K. Dhiman, "Transient analysis of a spherical solar still," *Desalination*, vol. 69, no. 1, pp. 47–55, 1989.

[31] M. Boukar and A. Harmim, "Parametric study of a vertical solar still under desert climatic conditions," *Desalination*, vol. 168, pp. 21–28, 2004.

[32] H. Tanaka, "Experimental study of vertical multiple-effect diffusion solar still coupled with a flat plate reflector," *Desalination*, vol. 249, no. 1, pp. 34–40, 2009.

[33] A. N. Minasian and A. A. Al-Karaghouli, "Floating vertical solar still for desalination of marsh water," *Renewable Energy*, vol. 2, no. 6, pp. 631–635, 1992.

[34] M. Boukar and A. Harmim, "Development and testing of a vertical solar still," *Desalination*, vol. 158, no. 1-3, p. 179, 2003.

[35] M. Boukar and A. Harmim, "Performance evaluation of a one-sided vertical solar still tested in the Desert of Algeria," *Desalination*, vol. 183, no. 1-3, pp. 113–126, 2005.

[36] A. A. El-Sebaii, "Parametric study of a vertical solar still," *Energy Conversion and Management*, vol. 39, no. 13, pp. 1303–1315, 1998.

[37] S. A. Abdul-Wahab and Y. Y. Al-Hatmi, "Study of the performance of the inverted solar still integrated with a refrigeration cycle," *Procedia engineering*, vol. 33, pp. 424–434, 2012.

[38] S. A. Abdul-Wahab and Y. Y. Al-Hatmi, "Performance evaluation of an inverted absorber solar still integrated with a refrigeration cycle and an inverted absorber solar still," *Energy for Sustainable Development*, vol. 17, no. 6, pp. 642–648, 2013.

[39] S. A. Abdul-Wahab, A. M. Al-Damkhi, H. Al-Hinai, R. Dev, and G. N. Tiwari, "Experimental study of an inverted absorber solar still," *Desalination and Water Treatment*, vol. 19, no. 1-3, pp. 249–254, 2012.

[40] E. Shanazari and R. Kalbasi, "Improving performance of an inverted absorber multi-effect solar still by applying exergy analysis," *Applied Thermal Engineering*, vol. 143, pp. 1–10, 2018.

[41] M. M. Thalib, A. M. Manokar, F. A. Essa, N. Vasimalai, R. Sathyamurthy, and F. P. Garcia Marquez, "Comparative study of tubular solar stills with phase change material and nano-enhanced phase change material," *Energies*, vol. 13, no. 15, p. 3989, 2020.

[42] A. M. Manokar, D. P. Winston, R. Sathyamurthy, A. E. Kabeel, and A. R. Prasath, "Experimental investigation on pyramid solar still in passive and active mode," *Heat and Mass Transfer*, vol. 55, no. 4, pp. 1045–1058, 2019.

[43] A. M. Manokar, M. Vimala, D. P. Winston, R. Sathyamurthy, and A. E. Kabeel, "Effect of Insulation on Energy and Exergy Effectiveness of a Solar Photovoltaic Panel Incorporated Inclined Solar Still—An Experimental Investigation," in *Solar Desalination Technology. Green Energy and Technology*, A. Kumar and O. Prakash, Eds., pp. 275–292, Springer, Singapore, 2019.

[44] A. M. Manokar, M. Vimala, R. Sathyamurthy, A. E. Kabeel, D. P. Winston, and A. J. Chamkha, "Enhancement of potable water production from an inclined photovoltaic panel absorber solar still by integrating with flat-plate collector," *Environment, Development and Sustainability*, vol. 22, no. 5, pp. 4145–4167, 2020.

[45] Y. Taamneh, A. M. Manokar, M. M. Thalib, A. E. Kabeel, R. Sathyamurthy, and A. J. Chamkha, "Extraction of drinking water from modified inclined solar still incorporated with spiral tube solar water heater," *Journal of Water Process Engineering*, vol. 38, p. 101613, 2020.

[46] A. E. Kabeel, R. Sathyamurthy, S. A. El-Agouz, A. M. Manokar, A. Tripathi, and G. B. Abdelaziz, "Experimental investigation of a hybrid setup for distilled water and power production," *Desalination and Water Treatment*, vol. 162, pp. 30–36, 2019.

[47] A. E. Kabeel, R. Sathyamurthy, A. M. Manokar, S. W. Sharshir, F. A. Essa, and A. H. Elshiekh, "Experimental study on tubular solar still using graphene oxide nanoparticles in phase change material (NPCM's) for fresh water production," *Journal of Energy Storage*, vol. 28, p. 101204, 2020.

[48] B. I. Ismail, "Design and performance of a transportable hemispherical solar still," *Renewable Energy*, vol. 34, no. 1, pp. 145–150, 2009.

[49] T. Arunkumar, R. Jayaprakash, D. Denkenberger et al., "An experimental study on a hemispherical solar still," *Desalination*, vol. 286, pp. 342–348, 2012.

[50] G. N. Tiwari and S. A. Lawrence, "New heat and mass transfer relations for a solar still," *Energy Conversion and Management*, vol. 31, no. 2, pp. 201–203, 1991.

[51] G. N. Tiwari, V. Dimri, and A. Chel, "Parametric study of an active and passive solar distillation system: energy and exergy analysis," *Desalination*, vol. 242, no. 1-3, pp. 1–18, 2009.

Hindawi
International Journal of Photoenergy
Volume 2021, Article ID 6630140, 12 pages
https://doi.org/10.1155/2021/6630140

Research Article

Numerical Study on the Thermal Performance of Trombe Wall for Passive Solar Building in Semiarid Climate

Maher Dhahri,[1,2] **Nima Khalilpoor**,[3] **Hana Aouinet**,[4] **Alibek Issakhov**,[5] **Habib Sammouda**,[2] **and Sampath Emani**[6]

[1]*Higher Institute of Agricultural Sciences of Chott Mariem, University of Sousse, BP No. 47, 4042 Sousse, Tunisia*
[2]*Laboratory of Energy and Materials (LabEM) (LR11ES34), High School of Sciences and Technology of Hammam Sousse, Sousse University, BP, 4011 Hammam Sousse, Tunisia*
[3]*Department of Energy Engineering, Graduate School of the Environment and Energy, Science and Research Branch, Islamic Azad University, Tehran, Iran*
[4]*Higher Private School of Engineering and Applied Techniques (IHE-ESPITA), Sousse, Tunisia*
[5]*Faculty of Mechanics and Mathematics, Department of Mathematical and Computer Modelling, Al-Farabi Kazakh National University, Almaty, Kazakhstan*
[6]*Chemical Engineering Department, Universiti Teknologi PETRONAS, Bandar Seri Iskandar, Perak D.R., Malaysia*

Correspondence should be addressed to Nima Khalilpoor; nimakhalilpoor@gmail.com

Received 2 November 2020; Revised 12 January 2021; Accepted 8 February 2021; Published 1 March 2021

Academic Editor: Hafiz Muhammad Ali

Copyright © 2021 Maher Dhahri et al. This is an open access article distributed under the Creative Commons Attribution License, which permits unrestricted use, distribution, and reproduction in any medium, provided the original work is properly cited.

The largest amount of energy in buildings is consumed to provide heating, cooling, and ventilation. Therefore, a practical solution such as using renewable energy sources can be considered to reduce energy costs and pollutants. In addition, architecture principles must be varied to utilize passive solar energy and also to reduce energy losses. In this research, a numerical study is presented to investigate the thermal behavior of TW-FR (Trombe wall placed in a fenestrated room) in the semiarid region of Tunisia. Computational fluid dynamic (CFD) simulation of fluid flow and heat transfer shows good agreement with published data in literature. The thermal comfort level was calculated according to ASHRAE (55-2013). The results show that (i) the normal Trombe wall cannot assure a satisfactory comfort level even in summer conditions and a higher vertical temperature gradient can take a value of 15°C, and the Trombe wall is shown to be more efficient in heating mode in the studied semi-arid region compared to cooling; (ii) the operative temperature for the coldest winter is between 17.85 and 19.85°C. The air temperature gradient in the comfort ranges between the head and feet is 2.3°C; and (iii) the Trombe wall is an excellent solution for Sousse city weather; it is suggested that the passive system (TW-FR) will be examined for a whole year to have a precise evaluation of its efficiency.

1. Introduction

The applications of renewable energies have fascinated the interest of many architects and engineers in recent days [1, 2]. Several researches have shown the potential of using solar energy for satisfying energy demands of buildings [3–5] and industries [6] to alleviate the pollutant emission crisis [7, 8].

A thermal mass storage that comprised of external glazing, dampers, and vent in order to provide required heating, cooling, and ventilation passively is so-called Trombe wall [9]. In winters, air enters into the cavity through a low vent. The temperature of the air is raised in the wall and transferred to the room through the cavity due to buoyancy effect. In summers, the Trombe wall is performing similar to solar chimney since the low glazing vent will be closed and the high vent is opened [10].

A set of instructions are provided for the Trombe wall design based on experimental and numerical investigations.

In the first look, the Trombe wall is a promising approach to save energy and to maintain the indoor air quality. Experimental study of room equipped with Trombe wall is offered by [11] where they studied house natural ventilation in arid climate of Yazd, Iran, experimentally by studying different types of fins, namely, brass, copper, and aluminum. The results approved that using thermal fins enhanced the energy-saving efficiency of the Trombe wall by 3% and improved its natural convection heat transfer rate by 6% inside the channel.

Dong et al. presented a new configuration for the Trombe wall by installing an absorbent plate between the glass cover and the thermal storage wall and examined it in Harbin, China [12]. It was shown that this novel layout increased the thermal efficiency by 50% compared to traditional Trombe wall. Abbassi and Dehmani introduced internal thermal fins into a Trombe wall [13]. Wu et al. proposed a 2-dimensional model on air filtration and thermal performance of a PC-Trombe wall [14]. The authors reported that increasing the solar radiation had positive effect on the thermal efficiency and ambient temperature. On the other hand, the air inlet temperature and ambient wind velocity was decreased. Recently, Abdeen et al. carried out an investigation on the heat transfer and air flow of a Trombe wall under quasistate situation in a moderate typical winter week in Alexandria, Egypt [15].

Computational fluid dynamics (CFD) is a viable solution to evaluate the flow behavior and thermal conditions of different systems [16]. In buildings, CFD can be extensively used to analyze energy consumption and to model the system with respect to real values. Risberg et al. simulated the heat supply through ventilation ducts placed at the ceiling in Swedish houses with passive house standards [17].

Bajc et al. presented a 3D CFD modeling and analyzed temperature distribution in the Trombe wall and in the adjacent room in a moderate climate [18]. The authors optimized the Trombe applying various types of glassing on the outer side of the wall and reported that the Trombe wall could be a practical solution for use in Belgrade region.

Overall, it can be understood from the previously discussed publications that the Trombe wall has promising potential to be used in buildings in order to maintain desirable heating and cooling rates. Monitoring the preceding studies showed that there is no comprehensive study on evaluation of thermal comfort in a building where the Trombe wall was installed in semiarid climate.

The application of the Trombe wall in Tunisia is still uncommon due to the lack of information about energy performance and construction details that do not persuade the stake holders to implement this system. This research has this target to display the effect of the space air flow pattern of Trombe wall installed in a fenestrated room.

2. Numerical Analysis

2.1. Mathematical Model. The simulations are implemented in ANSYS CFX (15.0). The continuity (Equation (1)), momentum (Equation (2)), and energy (Equation (3)) equations applied to the model are as follows [19]:

$$\frac{\partial \rho}{\partial t} + \frac{\partial}{\partial x_i}\left(\rho u_j\right) = 0, \tag{1}$$

$$\rho \frac{\partial u}{\partial t} + \rho(u.\nabla)u = \nabla\left[-pl + (\mu + \mu_{\mathrm{T}})\left(\nabla u + (\nabla u)^T\right) - \frac{2}{3}\left((\mu+\mu_{\mathrm{T}})(\nabla.u)l - \frac{2}{3}\rho kl\right)\right] + F, \tag{2}$$

$$\frac{\partial \rho}{\partial t}(\rho C_{\mathrm{a}} T) + \frac{\partial}{\partial x_j}\left(\rho u_j C_{\mathrm{a}} T\right) - \frac{\partial}{\partial x_j}\left(k\frac{\partial T}{\partial x_j}\right) = S_{\mathrm{T}}, \tag{3}$$

where C_{a} indicates the water specific heat, k shows the thermal conductivity, μ is the dynamic viscosity, and ρ denotes density.

The turbulence kinetic energy (k) and its dissipation rate (ε) can be calculated as follows [20]:

$$\frac{\partial}{\partial t}(\rho k) + \frac{\partial}{\partial x_i}(\rho k U_i) = \frac{\partial}{\partial x_j}\left[\left(\mu + \frac{\mu_t}{\sigma_k}\right)\frac{\partial k}{\partial x_j}\right] + G_k + G_{\mathrm{b}} - \rho\varepsilon - Y_{\mathrm{M}} + S_k,$$

$$\frac{\partial}{\partial t}(\rho \varepsilon) + \frac{\partial}{\partial x_i}(\rho \varepsilon U_i) = \frac{\partial}{\partial x_j}\left[\left(\mu + \frac{\mu_{\mathrm{t}}}{\sigma_3}\right)\frac{\partial \varepsilon}{\partial x_j}\right] + C_{1\varepsilon}\frac{\varepsilon}{k}(G_k + C_{3\varepsilon}G_{\mathrm{b}}) - C_{2\varepsilon}\rho\frac{\varepsilon^2}{k} + S_\varepsilon, \tag{4}$$

where G_k indicates the turbulence kinetic energy associated with gradients of the mean velocity and G_{b} refers to the turbulence kinetic with regard to buoyancy. Y_{M} is the fluctuating dilatation, σ_k and σ_ε are the Prandtl numbers, and $C_{1\varepsilon}$, $C_{2\varepsilon}$, and $C_{3\varepsilon}$ are constants.

Compared to other turbulence models, the $k-\varepsilon$ model is less nonlinear and has simple convergence that makes it simple to provide a suitable initial guess.

The turbulent viscosity, ν_{t}, is obtained as

$$\nu_{\mathrm{t}} = C_\mu \frac{k^2}{\varepsilon}, \tag{5}$$

where C_μ is a constant.

The values of $C_{1\varepsilon}$, $C_{2\varepsilon}$, C_μ, σ_k, and σ_ε are

$$\begin{aligned} C_{1\varepsilon} &= 1.44, \\ C_{2\varepsilon} &= 1.92, \\ C_\mu &= 0.09, \\ \sigma_k &= 1.0, \\ \sigma_\varepsilon &= 1.3, \end{aligned} \tag{6}$$

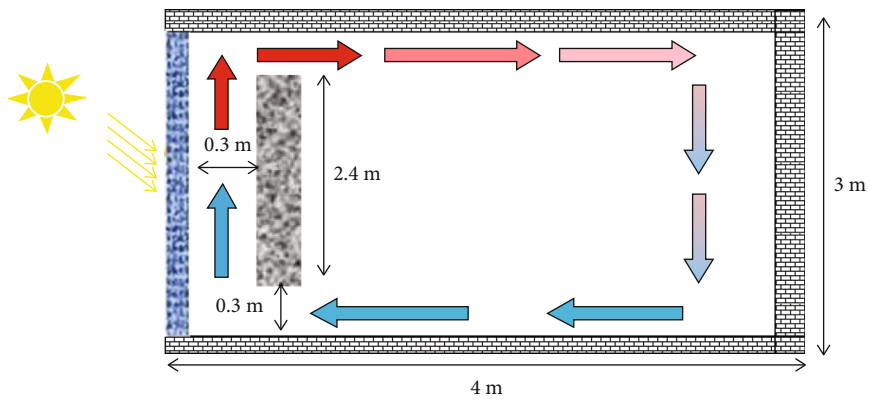

Figure 1: Physical model of the Trombe wall system.

Table 1: Summary of the boundary conditions.

Element	T (°C)	Type of radiation	Heat flux (W/m^2) Heat flux coefficient (W/m^{2}K)
Floor	30°C	Not transparent	—
Roof	45°C	Not transparent	250 (w/m^{2}k)
Glazing	45°C	Transparent	—
Trombe wall	—	Not transparent	800 (w/m^2)
Front wall	45°C	Not transparent	250 (w/m^{2}k)
Other wall	Adiabatic	Not transparent	—

2.2. Mesh Independence Study and Boundary Conditions. The model of passive house with Trombe wall is a simple room with the Trombe wall on its south side and has a dimension of height × length × width of $3 \times 4 \times 4\,\mathrm{m}^3$. The Trombe wall is characterized by 0.3 m for the thickness, 0.3 m for air gap, and 2.4 m for height. The room is vacant and just heated by direct sunlight. The physical model of the system is exposed in Figure 1. The boundary condition details are summarized in Table 1.

The whole domain is modeled with a structured rectangular mesh in ANSYS, and the simulations were performed in CFX 15.0. The used turbulence model as discussed above was $k - \varepsilon$. It is assumed that a steady-state condition was executed. The independence of grid has been established. Six cases of meshes are tested, 62908, 112356, 132804, and 164388. From the velocity results showed in Figure 2, grid size and cell number independency happened after the mesh N°5 and it has been shown that continuing the computation after this mesh (N°5 (cells 132804)) just prolonged the computation and it is performed only for accuracy purposes.

2.3. Climatic Data of the Town of Sousse. The town of Sousse (35° 49′ 34″ north, 10° 38′ 24″ east) is placed at 143 km from Tunis, at the south, and an altitude of 25 m. In summer, the temperatures surpass 43°C in the shade, and the relative humidity is about 67%. In addition, the outside temperature frequently differs between 10°C and 20°C in the winter at day time and can drop less than 1°C at night with inadequate and uneven rain.

3. Results

Many cases were studied in order to examine the heating/-cooling potential of a Trombe wall system. In particular, we considered two different modes: the first is the coldest winter day in the year (28/12/2019), and the second is a hot summer day in the same year (21/07/2019). Climatic conditions for Sousse (2019) are expressed in Table 2. The results are illustrated in a vertical plane at the center of the building. The results obtained are presented in figures with different values of the solar chimney depth in order to see the influence on the thermal efficiency of the system.

3.1. Validation of Computational Methods. To validate the mathematical model, the numerical results obtained by CFD are compared with the results of a traditional TW under the same conditions of the experimental studies [21]. The comparison of energy efficiencies of the Trombe walls for different solar radiation intensities was carried out between CFD results and experimental data and is shown in Figure 3. To evaluate the results, the relative error is used as an indicator. The RE between CFD and experimental results is calculated by

$$\mathrm{RE} = \left| \frac{X_{\mathrm{exp}} - X_{\mathrm{CFD}}}{X_{\mathrm{exp}}} \right| \times 100. \tag{7}$$

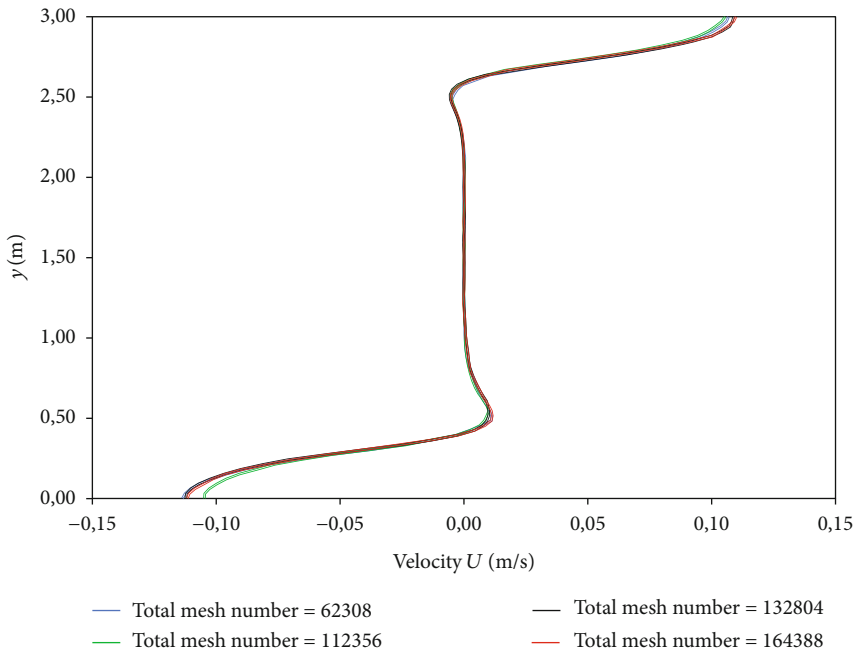

Figure 2: Model grid independency test.

Table 2: Climatic conditions for Sousse (2019).

Sumer day (21/07/2019)		Winter day (28/12/209)	
T (°C)	V (m/s)	T (°C)	V (m/s)
45	6.94	14.43	3.6

As shown in Figure 3, a perfect agreement between the results obtained from the model and the published results is observed and the highest value of RE is 7.29%.

3.2. Hot Summer Day. A typical hot day in summer (July) is selected, and simulation is performed under steady-state conditions. Figure 4 shows the temperature field in the room in the section located at ($Z = 2$ m). Due to buoyancy, the cold air spreads at the floor level. This cold airflow is like a jet and persuades the surrounding air; the Trombe wall could reduce indoor air temperature on average of 6.1°C. In this case, the air temperature gradient between a horizontal plane at 0.2 m and the floor is 7°C which is very high, and this zone is warmer, and an overheating phenomenon in the room is also observed.

Figure 5 shows the raw velocity vector map after passing the glass cover; solar energy here has the first interaction with the system TW-FR. In the first hand, the solar energy is absorbed by the Trombe wall. As a result, by conduction, this energy is moved through the wall and the remaining is moved to the air in the channel by convection. The air moves from the bottom to the top of the channel caused by the chimney effect.

The highest air velocity is about 0.5 m/s. According to [22], we observed that the air velocity in the region occupied by the middle section of the domain is not exceeding 0.17 m/s and this is between the comfort ranges. This condition that the average state air velocity is below 0.2 m/s made the greatest situation for human comfort. According to [22], the velocities between 0.18 and 0.24 m/s are perceivable but still in the comfort zone in summer.

3.3. Cold Winter Day. In this section, the simulations are prepared for a typical winter day at the month of January. Figure 6 shows the temperature field in the room at ($z = 2$ m). Even though the radiation is very high at this day, it is sufficient to transfer the air in the channel. The average temperature for the central point of the room is 18.46°C. The higher temperature in the room is around 20°C, and the minimum is about 10°C. The internal temperature offered higher values than external temperature getting the difference of 6.45°C. It can be concluded from the simulations that the temperature inside reached higher temperature compared to outside in a large zone of the system which is a negative result and will drive the heat flux from inside of the room to ambient. This can see obviously the high temperatures near the wall.

Figure 7 shows that the maximum velocities are positioned near the roof and floor. This flow causes a temperature gradient between regions. A small vortex is produced at the corner close to the room outlet. Reverse flow patterns were strong near floor. A relatively small recirculation zone was created, and a flow was observed. We observed also that the air flow is characterized by a strong turbulence near the floor and roof. High air velocities existed; the highest velocity is about 0.34 m/s. The air velocity in the region where it is thought that will be occupied (the mid region of the domain)

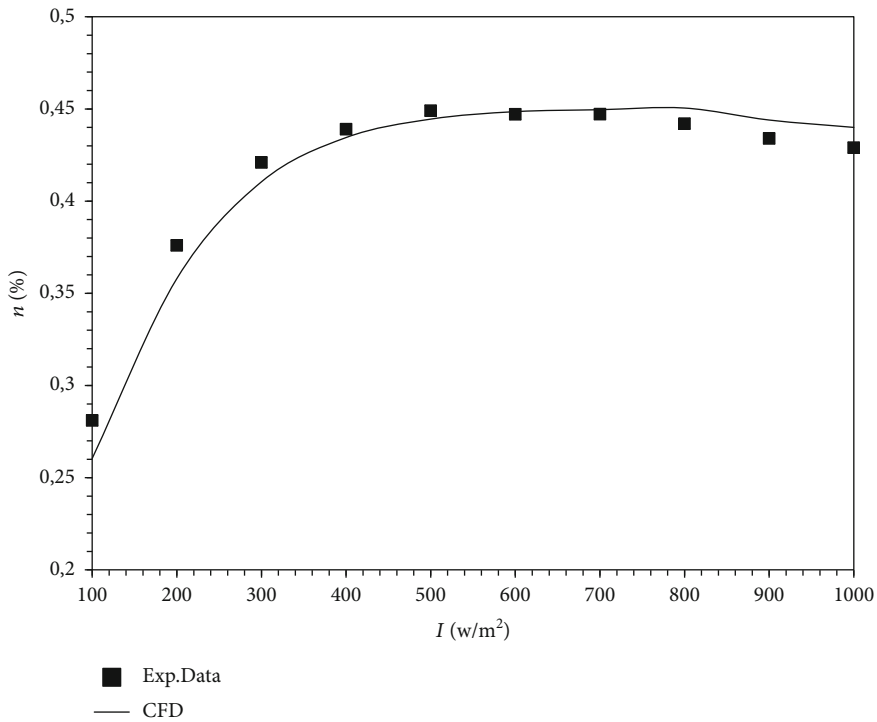

Figure 3: Comparison of thermal efficiency.

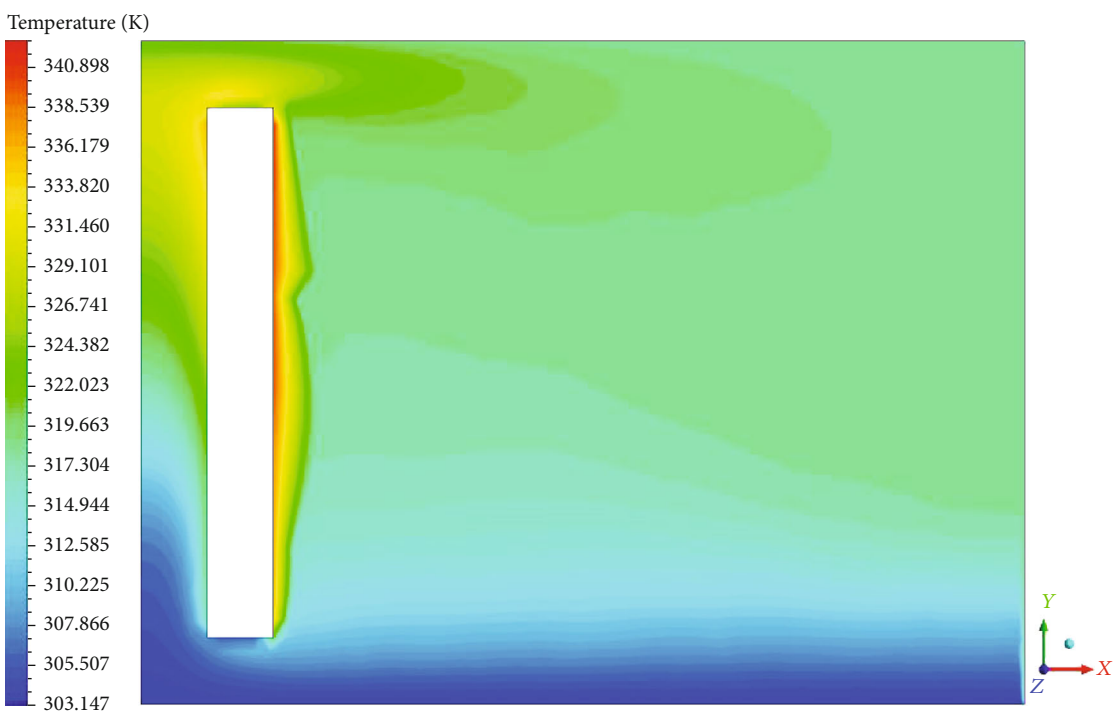

Figure 4: Temperature contour on plane $z = 2$ m in the case of summer hot day.

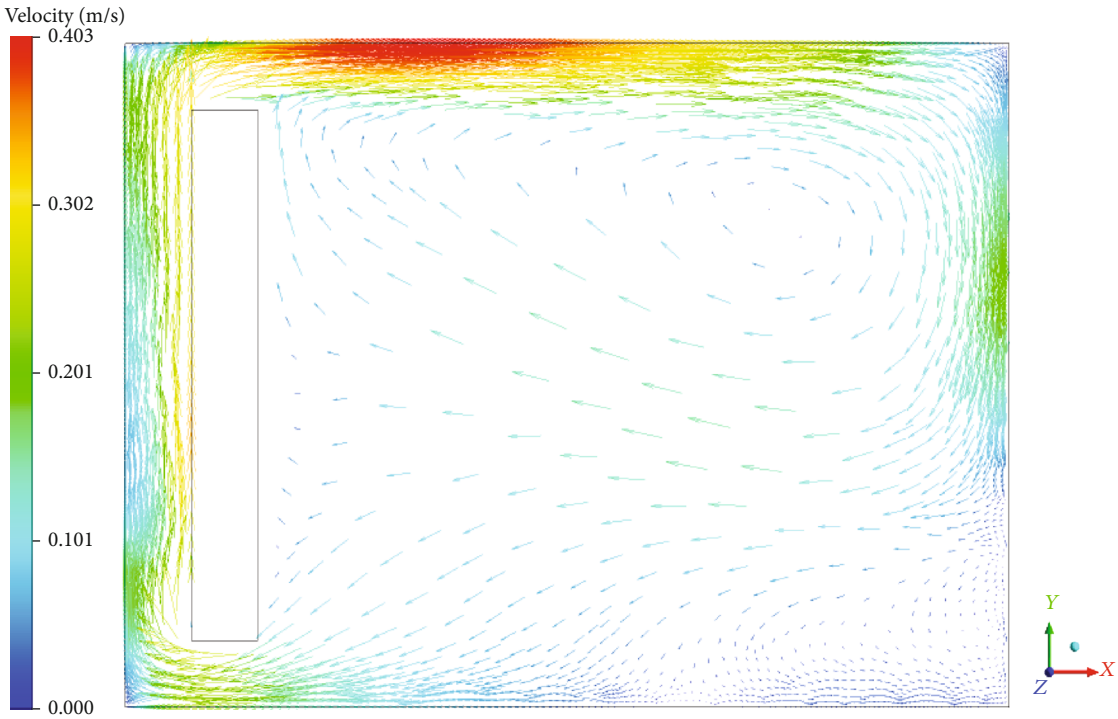

Figure 5: Vector velocity on plane $z = 2$ m in the case of summer hot day.

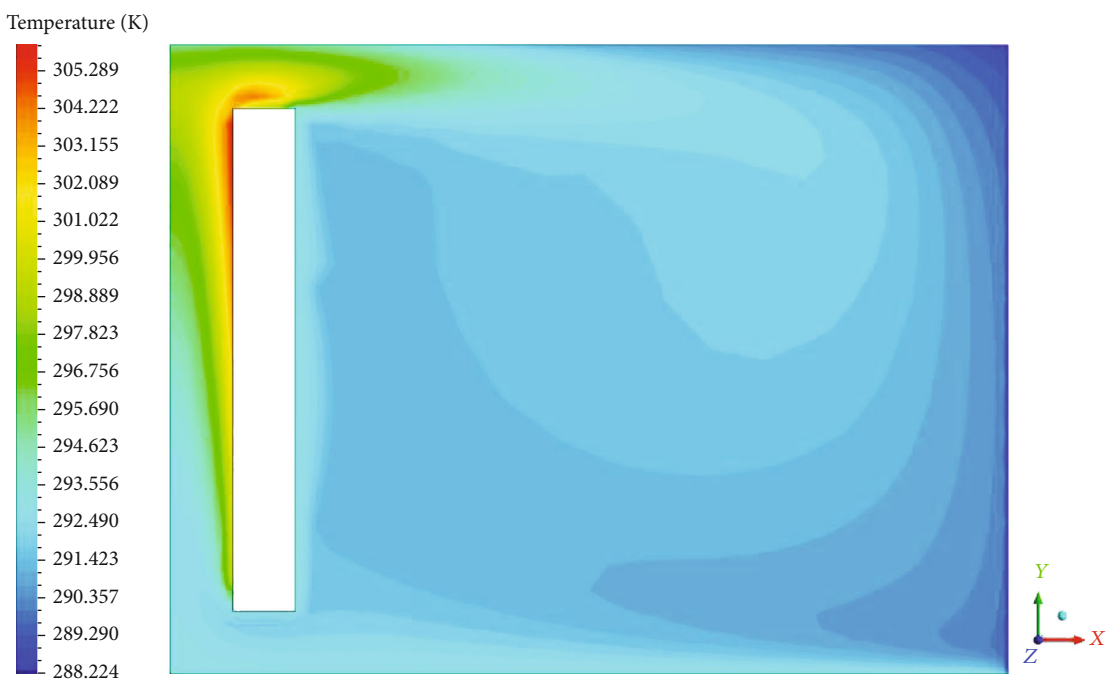

Figure 6: Temperature contour on plane $z = 2$ m in the case of the winter coldest day.

is not exceeding 0.21 m/s. According to [22], this result is between the comfort zones.

The numerical distribution of pressure (Figures 8 and 9) is completely hydrostatic and also slightly small compared to atmospheric pressure particularly in the lower part of the Trombe wall due to the loss at the inlet restriction. A slight difference in distribution of pressure is appreciated between the air gap and the room, mainly in areas of low inlet and outlet pressure of Trombe wall.

The turbulent kinetic energy is discussed in Figures 10 and 11. At the input side, viscosity degraded the turbulent kinetic energy. Since there is no speed gradient nor k

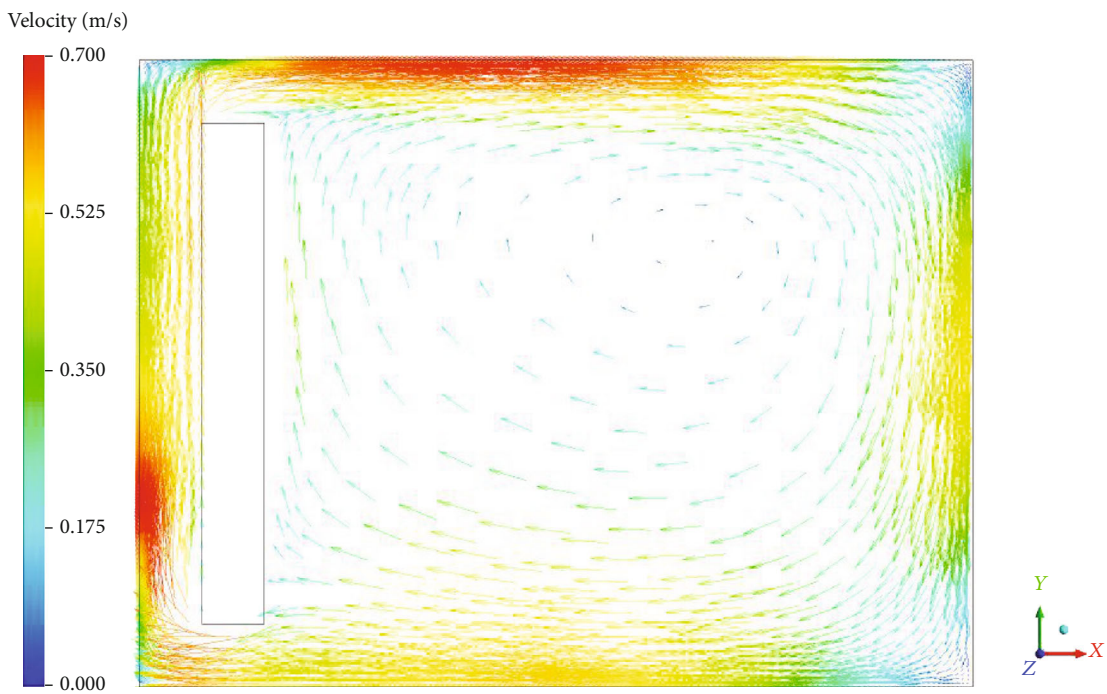

Figure 7: Vector velocity on plane z = 2 m in the case of the winter coldest day.

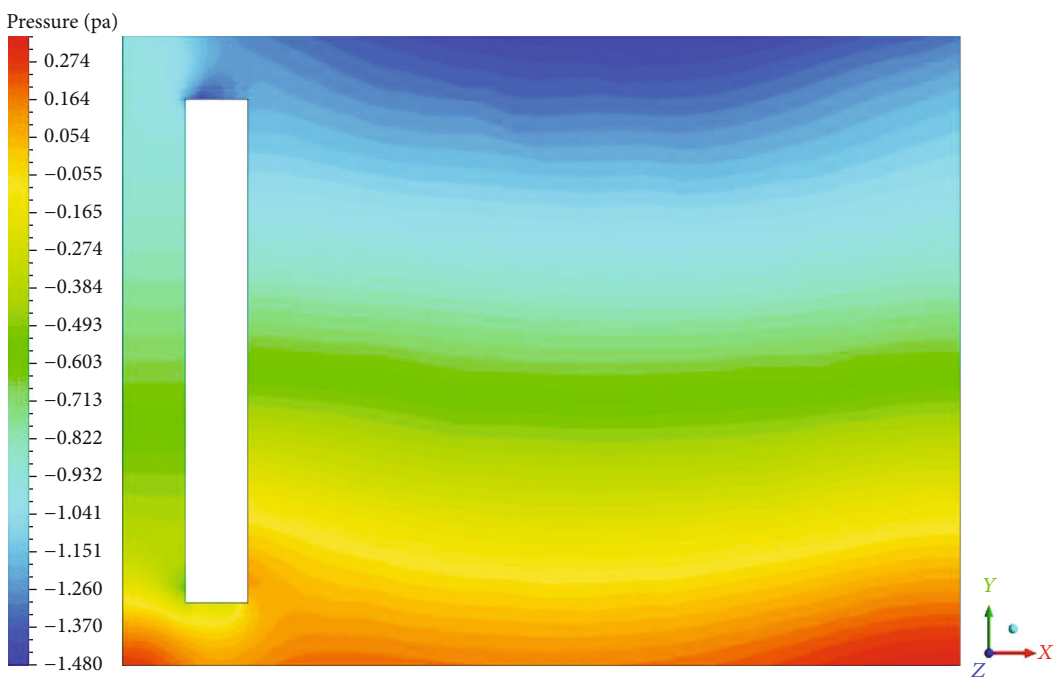

Figure 8: Pressure map in the plane $z = 2$ m in the case of the winter coldest day.

gradient, a balance is achieved between the convection heat transfer and dissipation rate in the transport equation.

4. Discussion

The most cited technique in the literature to explain the indoor thermal comfort in buildings is according to Fanger's comfort model [23], which is also used in [22, 24]. Where the thermal comfort is frequently examined inside the occupied zone, the volume occupants normally use is the volume enclosed by two horizontal planes, one 0.1 m above floor level and the other 2.0 m above floor level. The local discomfort can be classified generally as per the following according to the current standards and *ASHRAE Fundamentals Handbook*.

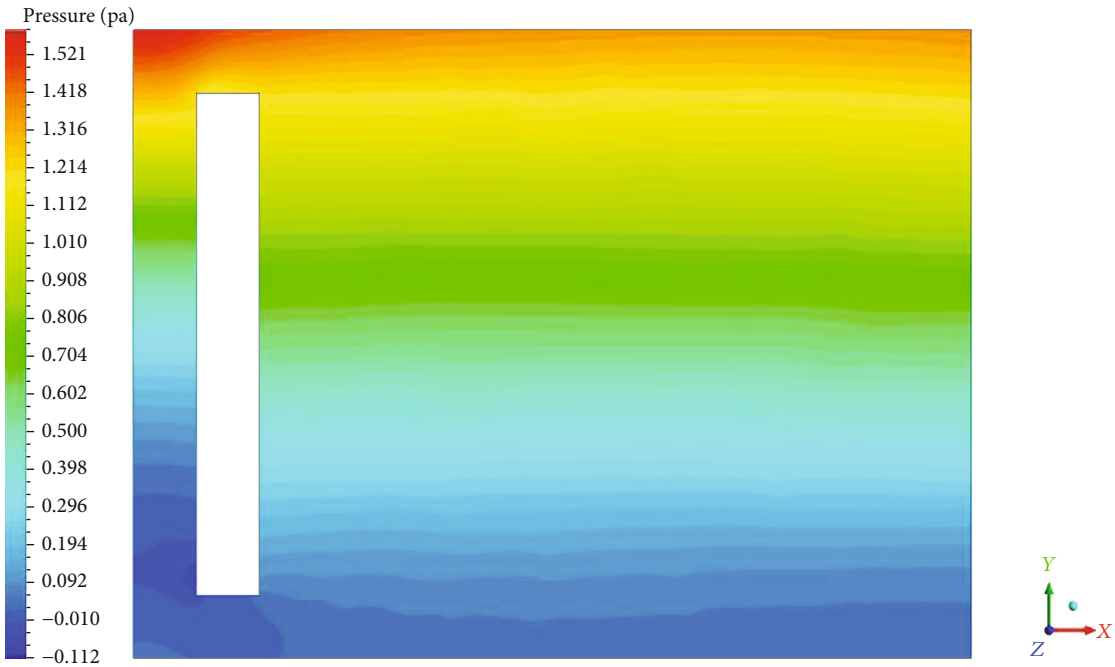

Figure 9: Pressure map in the plane $z = 2$ m in the case of summer hot day.

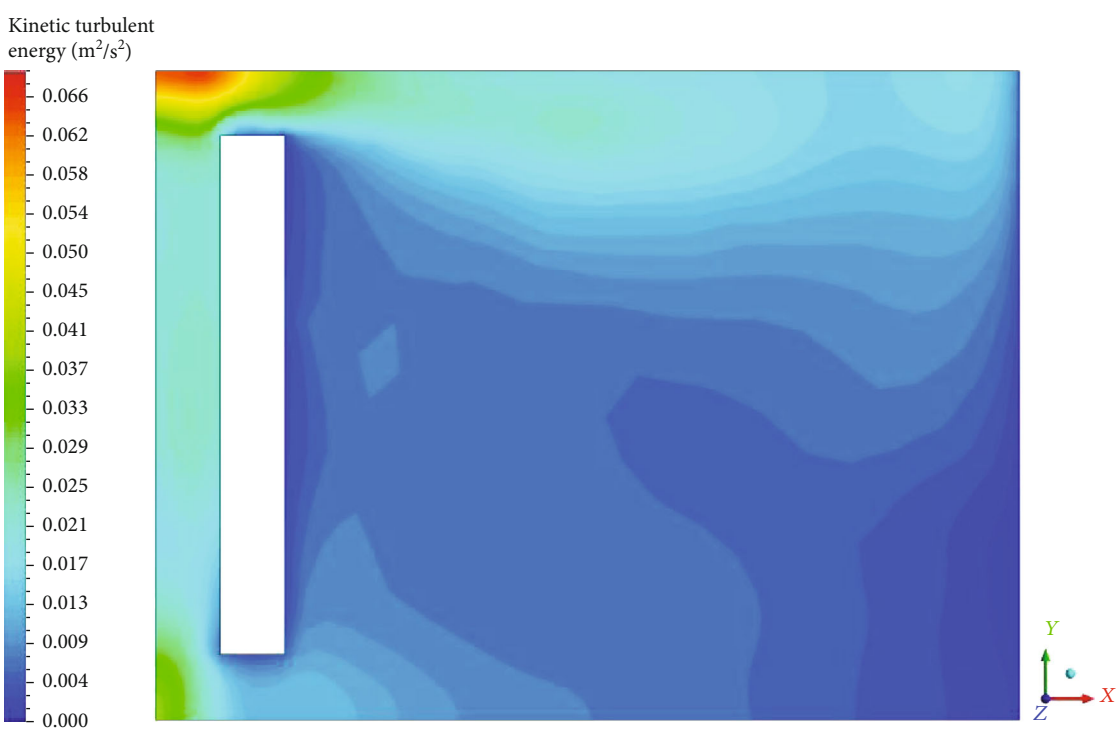

Figure 10: Turbulent kinetic energy in the case of summer hot day.

4.1. Operative Temperature. It can be defined by the uniform temperature of a pretend black enclosure in which a person would exchange the same amount of heat by radiation and convection as in an actual nonuniform environment. It is calculated according to

$$T_{op} = \frac{T_r + T_a\sqrt{10v}}{1 + \sqrt{10v}} \text{ if } v > 10 \text{ m/s},$$
$$T_{op} = \frac{T_r + T_a}{2} \text{ if } v \leq 0.1 \text{ m/s}, \quad (8)$$

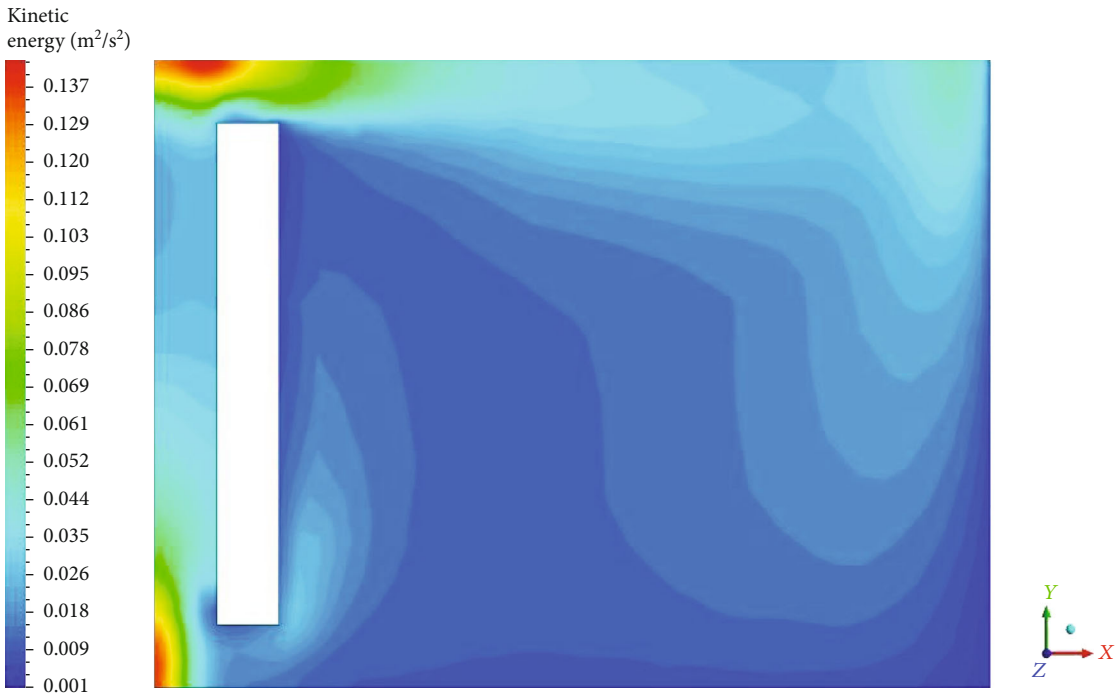

Figure 11: Turbulent kinetic energy in the case of winter coldest day.

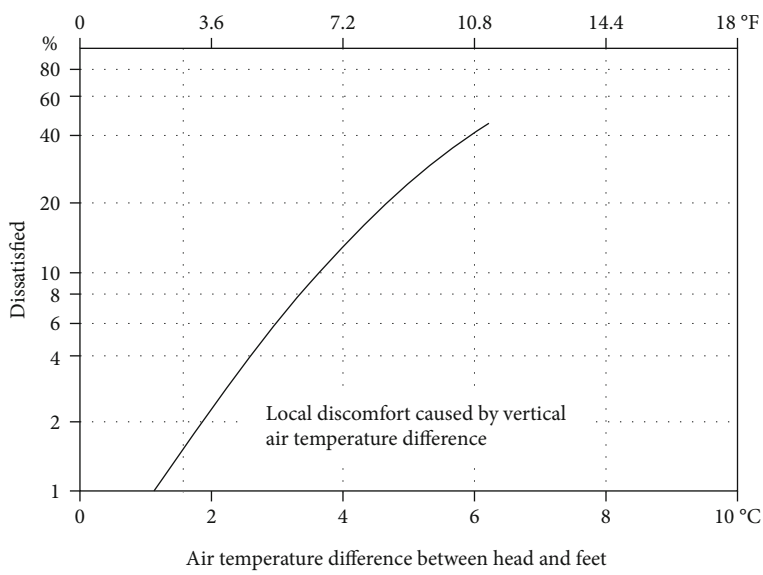

Figure 12: Local thermal discomfort caused by vertical temperature differences [22].

where T_a is the ambient air temperature, T_r the radiation temperature, and v the air velocity.

4.2. Vertical Air Temperature Difference. Thermal discomfort may happen as a result of thermal stratification. Figure 12 demonstrates the estimated value of dissatisfied people with respect to air temperature gradient where the ankle level is colder than the head level.

The thermal comfort for room equipped with a Trombe wall was considered under the coldest winter day and the hot summer day. The main parameter shown in the figures was the operative temperature. The hot summer day gave a bad thermal comfort, and the temperature difference over the entire room is small. The operative temperatures were around 29-44°C in the horizontal plane (Figure 13). The numerical results also show higher vertical temperature gradients which can take a value of 15°C (Figure 14); the results show also that operative temperature in the room is not within the comfort range. This demonstrates that the normal Trombe wall cannot assure a satisfactory comfort level even

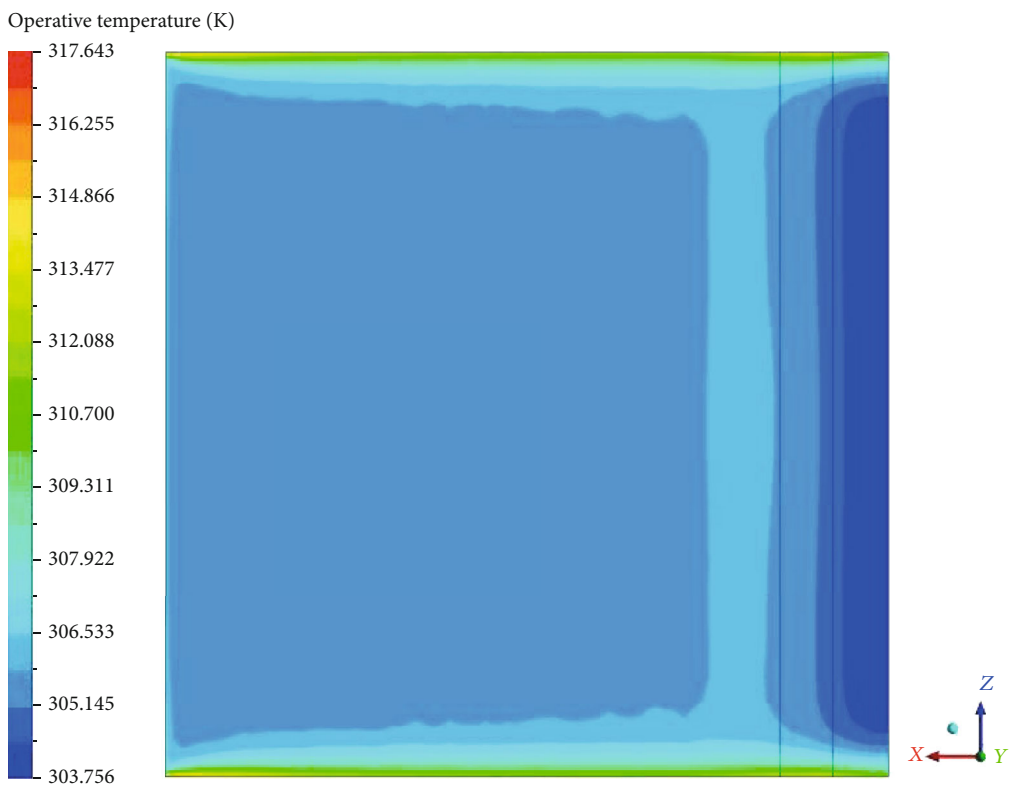

Figure 13: Operative temperature distribution at 0.1 m above the floor in a summer day.

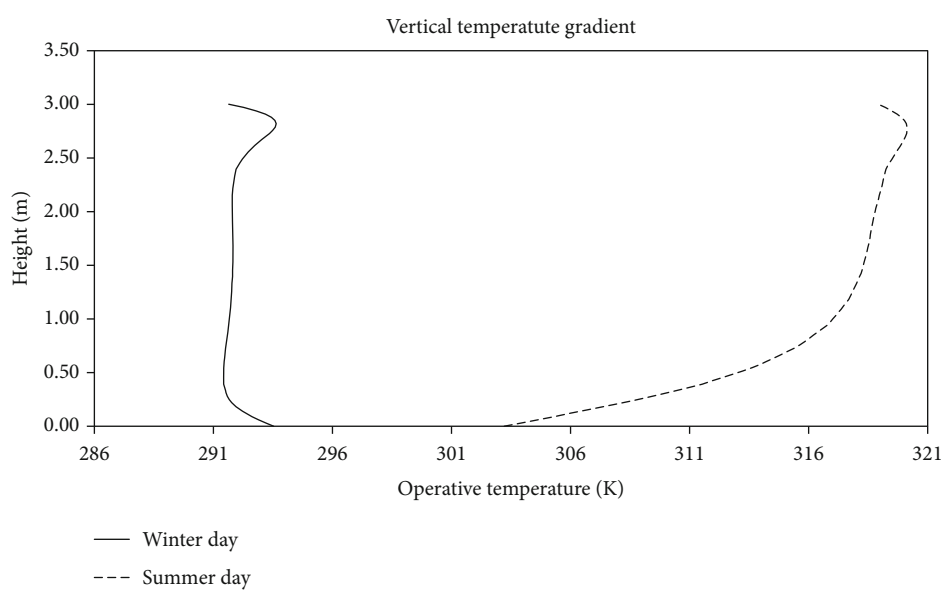

Figure 14: Vertical operative temperature gradient at the line ($x = 2$ m and $z = 2$ m).

in summer conditions. In this case, the air temperature gradient between head level and ankle level is 10°C which exceeds 3°C and the discomfort is sensed because the head level is warmer than the ankle level according to [22]. As a result, the typical Trombe wall cannot reduce the effect of heating in the summer season. Consequently, heating seasons in Tunisia should introduce some modification in the Trombe wall like the use of a water tank, which is part of the building's wall or it must ventilate the room with air circulation open.

This case of the coldest winter day (Figure 15) shows the most irregular distribution, and the vertical temperature gradients in the occupied zone are fewer than 2.5°. The operative

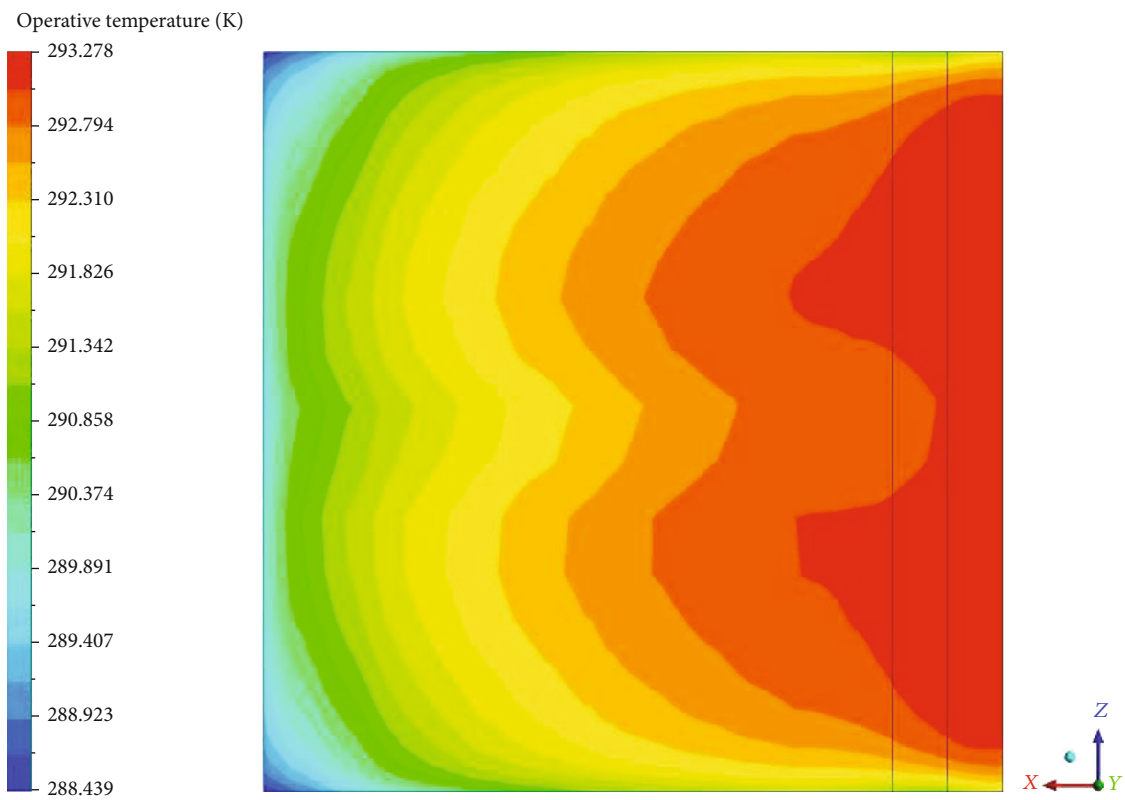

Figure 15: Operative temperature distribution at 0.1 m above the floor in winter.

temperature for the coldest winter is between 17.85 and 19.85°C. The air temperature gradient between the head and feet is 2.3°C. Based on [22], this is between the comfort ranges and 5% of occupants are dissatisfied by the vertical air stratification.

5. Conclusion(s)

The following remarks can be concluded from this study:

(i) The CFD simulation is able to provide accurate air temperature and velocity distributions inside the building room

(ii) It was observed from the simulations that installing the Trombe wall can highly influence the temperature distribution inside the modeled house for Sousse city weather information

(iii) It was shown that installing the Trombe wall had significant influence on the temperature of the room that it was kept around 20°C in winter conditions

(iv) However, in summer conditions, a normal Trombe wall can be considered an additional source of heating for the building

(v) The typical Trombe wall cannot reduce the effect of heating in the summer season. Consequently, during hot seasons in Tunisia, some modifications in the Trombe wall should be introduced

Nomenclature

t:	Time (s)
k:	Turbulent kinetic energy (m^2/s^2)
l:	Turbulent mixing length (m)
i, j:	Cartesian coordinate index
C_a:	Constant pressure specific heat (J/kgK)
T:	Temperature (K)
K:	Thermal conductivity (w/mK)
g:	Gravity acceleration (m/s^2)
F:	Body force (N/m^3)
CFD:	Computational fluid dynamics
$C_{1\varepsilon}, C_{2\varepsilon}$:	Constants
$C_{3\varepsilon}, C_\mu$:	Constants
G_b:	Buoyancy kinetic energy ($kg/m\,s^3$)
G_k:	Velocity gradients turbulent kinetic energy (kg/ms^3)
μ_t:	Effective viscosity (m^2/s)
Y_M:	Contribution of the fluctuating dilatation in compressible turbulence to the overall dissipation rate ($kg/m\,s^2$)
S_k, S_ε:	Mass source (kg/m^3)
C_p:	Specific heat (J/kgK)
L:	Characteristic length (m)
Pr:	Prandtl number

Gr: Grashof number
T_r: Radiation temperature (K)
T_a: Ambient temperature (K).

Greek Symbols

$\sigma_k, \sigma_\varepsilon$: Turbulent Prandtl
ν: Kinematic viscosity (m^2/s)
α: Thermal diffusivity (m^2/s)
β: Thermal expansion coefficient (K^{-1})
ε: Turbulent dissipation rate (m^2/s^3)
k: Turbulent kinetic energy (m^2/s^2)
δ_{ij}: Kronecker delta.

Data Availability

Data are available on request.

Conflicts of Interest

The authors declare that they have no conflicts of interest.

References

[1] M. el Haj Assad, M. H. Ahmadi, M. Sadeghzadeh, A. Yassin, and A. Issakhov, "Renewable hybrid energy systems using geothermal energy: hybrid solar thermal–geothermal power plant," *International Journal of Low-Carbon Technologies*, 2020.

[2] M. Ghazvini, M. Sadeghzadeh, M. H. Ahmadi, S. Moosavi, and F. Pourfayaz, "Geothermal energy use in hydrogen production: a review," *International Journal of Energy Research*, vol. 14, pp. 7823–7851, 2019.

[3] M. H. Ahmadi, M. Ghazvini, M. Sadeghzadeh et al., "Solar power technology for electricity generation: a critical review," *Energy Science & Engineering*, vol. 6, no. 5, pp. 340–361, 2018.

[4] M. Sadeghzadeh, M. H. Ahmadi, M. Kahani, H. Sakhaeinia, H. Chaji, and L. Chen, "Smart modeling by using artificial intelligent techniques on thermal performance of flat-plate solar collector using nanofluid," *Energy Science & Engineering*, vol. 7, no. 5, pp. 1649–1658, 2019.

[5] A. B. Baci, M. Salmi, Y. Menni, S. Ghafourian, M. Sadeghzadeh, and M. Ghalandari, "A new configuration of vertically connecting solar cells: solar tree," *International Journal of Photoenergy*, vol. 2020, 8 pages, 2020.

[6] M. H. Ahmadi, A. Baghban, M. Sadeghzadeh et al., "Evaluation of electrical efficiency of photovoltaic thermal solar collector," *Engineering Applications of Computational Fluid Mechanics*, vol. 14, no. 1, pp. 545–565, 2020.

[7] M. H. Ahmadi, M. Dehghani Madvar, M. Sadeghzadeh, M. H. Rezaei, M. Herrera, and S. Shamshirband, "Current status investigation and predicting carbon dioxide emission in Latin American countries by connectionist models," *Energies*, vol. 12, no. 10, p. 1916, 2019.

[8] M. H. Rezaei, M. Sadeghzadeh, M. Alhuyi Nazari, M. H. Ahmadi, and F. R. Astaraei, "Applying GMDH artificial neural network in modeling CO2 emissions in four nordic countries," *International Journal of Low-Carbon Technologies*, vol. 13, no. 3, pp. 266–271, 2018.

[9] M. Hordesiki, *Dictionary of Energy Efficiency Technologies*, The Fairmont Press, Inc., 1st ed edition, 2004.

[10] G. Gan, "A parametric study of Trombe walls for passive cooling of buildings," *Energy and Buildings*, vol. 27, no. 1, pp. 37–43, 1998.

[11] M. Rabani and M. Rabani, "Heating performance enhancement of a new design Trombe wall using rectangular thermal fin arrays: an experimental approach," *Journal of Energy Storage*, vol. 24, p. 100796, 2019.

[12] J. Dong, Z. Chen, L. Zhang, Y. Cheng, S. Sun, and J. Jie, "Experimental investigation on the heating performance of a novel designed Trombe wall," *Energy*, vol. 168, pp. 728–736, 2019.

[13] F. Abbassi and L. Dehmani, "Experimental and numerical study on thermal performance of an unvented Trombe wall associated with internal thermal fins," *Energy and Buildings*, vol. 105, pp. 119–128, 2015.

[14] S.-Y. Wu, L. Xu, and L. Xiao, "Air purification and thermal performance of photocatalytic-Trombe wall based on multiple physical fields coupling," *Renewable Energy*, vol. 148, pp. 338–348, 2020.

[15] A. Abdeen, A. A. Serageldin, M. G. E. Ibrahim, A. El-Zafarany, S. Ookawara, and R. Murata, "Experimental, analytical, and numerical investigation into the feasibility of integrating a passive Trombe wall into a single room," *Applied Thermal Engineering*, vol. 154, pp. 751–768, 2019.

[16] M. Dhahri and H. Aouinet, "CFD investigation of temperature distribution, air flow pattern and thermal comfort in natural ventilation of building using solar chimney," *World Journal of Engineering*, vol. 17, no. 1, pp. 78–86, 2020.

[17] D. Risberg, M. Risberg, and L. Westerlund, "Investigation of thermal indoor climate for a passive house in a sub-Arctic region using computational fluid dynamics," *Indoor and Built Environment*, vol. 28, no. 5, pp. 677–692, 2019.

[18] T. Bajc, M. N. Todorović, and J. Svorcan, "CFD analyses for passive house with Trombe wall and impact to energy demand," *Energy and Buildings*, vol. 98, pp. 39–44, 2015.

[19] M. Dhahri and H. Aouinet, "Hydrodynamics in two-phase turbulent boundary layers," *Journal of Applied Fluid Mechanics*, vol. 11, no. 1, pp. 55–63, 2018.

[20] D. Maher, A. Hana, and H. Sammouda, "Numerical approximation of air flow, temperature distribution and thermal comfort in buildings," *Scientific African*, vol. 8, article e00353, 2020.

[21] S. Duan, C. Jing, and Z. Zhao, "Energy and exergy analysis of different Trombe walls," *Energy and Buildings*, vol. 126, pp. 517–523, 2016.

[22] American Society of Heating, Refrigerating, Air-Conditioning Engineers, and American National Standards Institute, *Thermal Environmental Conditions for Human Occupancy*, vol. 55, American Society of Heating, Refrigerating and Air-Conditioning Engineers, 2004.

[23] P. O. Fanger, *Thermal comfort. Analysis and applications in environmental engineering*, Danish Technical Press, Copenhagen, 1970.

[24] P. Lenzuni, D. Freda, and M. del Gaudio, "Classification of thermal environments for comfort assessment," *The Annals of Occupational Hygiene*, vol. 53, no. 4, pp. 325–332, 2009.

Hindawi
International Journal of Photoenergy
Volume 2021, Article ID 6675720, 13 pages
https://doi.org/10.1155/2021/6675720

Research Article

Efficient Topology for DC-DC Boost Converter Based on Charge Pump Capacitor for Renewable Energy System

Muhammad Zeeshan Malik,[1] **Vineet Tirth**,[2,3] **Amjad Ali**,[4] **Ajmal Farooq**,[5] **Ali Algahtani**,[2,3] **Rajesh Verma**,[6] **Saiful Islam**,[7] **Kashif Irshad**,[4] **and Ahmed N. Abdalla**[8]

[1]*Faculty of Automation, Huaiyin Institute of Technology, Huai'an, 223003 Jiangsu, China*
[2]*Mechanical Engineering Department, College of Engineering, King Khalid University, Abha 61411, Saudi Arabia*
[3]*Research Center for Advanced Materials (RCAMS) King Khalid University, P.O. Box 9004, Abha 61413, Saudi Arabia*
[4]*Centre of Research Excellence in Renewable Energy (CoRE-RE), King Fahd University of Petroleum and Minerals, Dhahran 31261, Saudi Arabia*
[5]*Department of Electrical Engineering, University of Engineering & Technology Mardan, Pakistan*
[6]*Electrical Engineering Department, College of Engineering, King Khalid University, Abha, 61411 Asir, Saudi Arabia*
[7]*Civil Engineering Department, College of Engineering, King Khalid University, Abha, 61411 Asir, Saudi Arabia*
[8]*Faculty of Electronic Information Engineering, Huaiyin Institute of Technology, Huai'an, Jiangsu, China*

Correspondence should be addressed to Muhammad Zeeshan Malik; malik4one@yahoo.com

Received 13 October 2020; Revised 21 December 2020; Accepted 5 February 2021; Published 15 February 2021

Academic Editor: Francesco Riganti-Fulginei

Copyright © 2021 Muhammad Zeeshan Malik et al. This is an open access article distributed under the Creative Commons Attribution License, which permits unrestricted use, distribution, and reproduction in any medium, provided the original work is properly cited.

In an attempt to meet the global demand, renewable energy systems (RES) have gained an interest in it due to the availability of the resources, especially solar photovoltaic system that has been an importance since many years because of per watt cost reduction, improvement in efficiency, and abundant availability. Photovoltaic system in remote and rural areas is very useful where a grid supply is unavailable. In this scenario, power electronic converters are an integral part of the renewable energy systems particularly for electronic devices which are operated from renewable energy sources and energy storage system (fuel cell and batteries). In this article, a new topology of charge pump capacitor (CPC) which is based on high voltage gain technique DC-DC boost converter (DCBC) with dynamic modeling is proposed. To testify the efficacy of the introduced topology, a prototype has been developed in a laboratory, where input was given 10VDC and 80VDC output voltage achieved at the load side. Furthermore, the experimental result shows that the voltage stress of MOSFET switches is very less in comparison with the conventional boost converter with the same parameters as the proposed converter.

1. Introduction

Solar photovoltaic (PV) that has a tremendous potential to generate electricity directly from the sunlight is considered as a means of powering the future with clean and environment friendly renewable sources [1–3]. However, photovoltaic panels, batteries, and fuel cell output voltage are less. To overcome this issue, DC-DC boost converter is installed to step up the low input voltage to require higher output voltage gain as depicted in Figure 1 [4]. The world surpasses in an approximation of 900 million mobile devices with over 500 million users in 2019. With higher energy demand and increasing prices of conventional electricity, it becomes a challenge for the telecommunication service providers to maintain their existing infrastructure as well as to expand it in many rural locations where access to conventional electricity is not east due to many reasons. Due to technological development in renewable energy technologies specifically solar and wind, this proved as an economical and reliable sources to power the telecom systems in remote locations

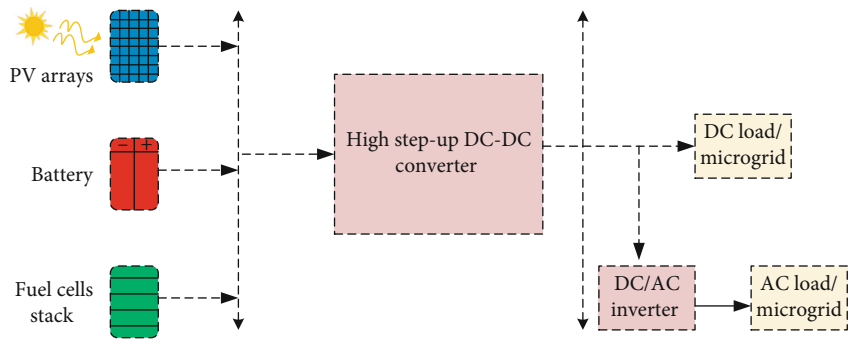

Figure 1: Renewable energy system [4].

Figure 2: Solar remote power station [5].

where conventional grid access is unavailable or difficult to provide, as well as solar power can provide the protection to the defense communication system from any damage or cyberattack as compared to the electric grid as shown in Figure 2 [5]. Therefore, it is significant to use PV technology (off-grid, on-grid, and remote solar power station). In this scenario, a high step-up boost converter has an important part [6, 7]. In literature, many types of boost converter introduced to attain the step-up voltage at the load [8]. These converters are operated with very high duty cycle which caused to increase the converter losses; also, many circuit components occur to reduce the overall system efficiency [9]. In the high PWM signal, MOSFET switches cause the malfunction because of short conduction time [10, 11]. Compared with a classical buck, boost, and buck-boost circuits, transformer-based converters can achieve higher conversion ratios with lower losses [12, 13]. The same feature applies to converters with coupled inductors [14].

The turn's proportion of the transformer or the coupled inductors helps realize higher stepping ratios [15, 16].

DC to DC boost converter with coupled inductor [17, 18] and active clamp flyback converter in [19], the main limitation of these converters is the problems related to the transformer. The massive turn's ratio and high-voltage isolation requirements increase the leakage inductance and parasitic capacitance of the winding. At switching instants, the transformer parasitic will result in high voltage spikes across the switches [20]. The voltage and current spikes lead to increased losses and reduced reliability and may damage circuit components [21–23]. A study of some DC-DC converter is discussed in detailed [24]. It described that full-bridge converter can be more efficient. The disadvantage of this design is that the soft switchings are hard to achieve. In this converter, there is no suitable value for the snubber capacitors for the whole operation range. Furthermore, in this converter, it needs an output inductor, which can cause voltage spike at diodes. [25].

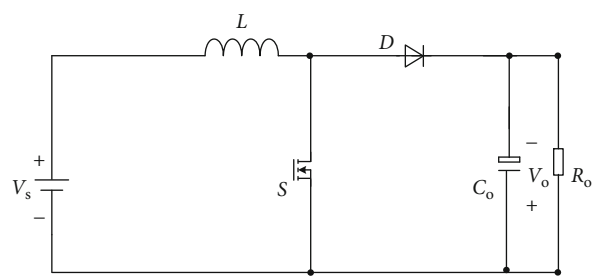

Figure 3: Conventional boost converter [27].

Finally, DC-DC converter with transformer design is presented in the literature, and the cons of this converter including core losses in the transformer can be significantly high, and the design of winding for transformer is complicated; also, efficiency is low and price is high. Switching semiconductor devices have exacerbated this issue as higher transformer core loss at high switching frequencies make it difficult to size the transformer while simultaneously increasing power density appropriately. Additionally, the inherent mutual coupling effect between adjacent transformer windings makes these topologies less suited to multi-input or multioutput type of applications [26–28]. However, this problem can only be addressed by connecting snubber circuits to the switches or by utilizing the transformer parasitic as a resonant tank and operating these converters as resonant soft-switched converters.

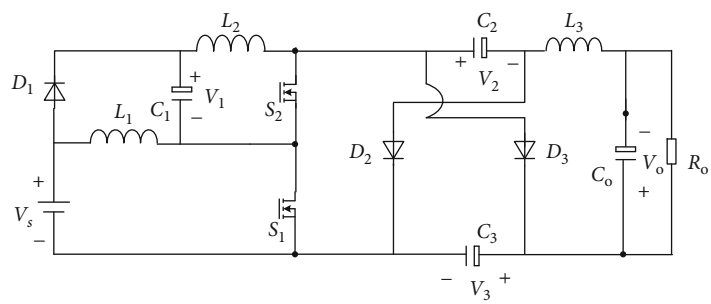

Figure 4: Proposed converter.

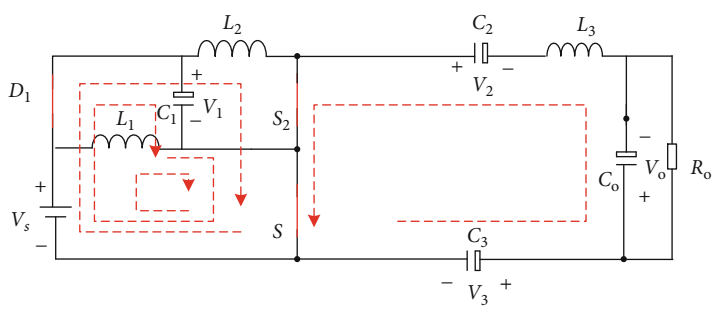

Figure 5: State I.

2. Related Work

2.1. The Principle of Boost Converter Circuits. The popular and generally used converters are the conventional DC-DC boost converters. The fundamental thought of these conventional boost converter circuits governed by splitting the input DC voltage with a precise PWM signal to produce an anticipated voltage at the load side. The PWM signal of conventional boost converters generally kept at a constant rate. Figure 3 illustrates the conventional DC-DC boost converter circuit [27]. These circuits are modest in assembly but undergo from some limits avoiding their usage in high-power applications. For the higher DC voltage conversion ratio, conventional converters work with higher duty cycle, which results in increasing the losses in the circuit components and tend to degrade the overall system efficiency [29, 30]. The higher duty cycle may also cause failure in switches due to the short conduction time [31].

$$M = \frac{1}{1-D} Vs, \tag{1}$$

$$V_{S-\text{tress}} = V_0. \tag{2}$$

In Eqs. (1), (2) where D is the duty ratio of the active switch, however, the actual conversion ratio is much lower when the effect of inductor equivalent series resistance R_L, diode forward voltage drop V_D, diode forward resistance R_d, switch on-state resistance R_{on} is accounted [28]. The effect of all these nonidealities is that the voltage gain from input to output is rarely more than 1.5 to 2.

3. The Proposed Method

3.1. The Circuit Description. This paper presents new DC-DC boost converters based on the charge pump capacitor for high voltage gain. The feature combination of CPC-DCBC with voltage multiplier cell (CPC) does not exist in any available high voltage gain topologies of DC-DC converter. The main advantage of the introduced topology is it has the capability to achieve high voltage gain without working at higher duty ratio.

The essential features of the proposed converters are proved experimentally in the laboratory with low switching losses and single stage without high-current chopping. Construction of the recommended converter is given in Figure 4, where V_s. is an input voltage, four capacitors (C_1, C_2, C_3, and C_0), two MOSFET switches (S_1 ad S_2), inductors (L_1, L_2, and L_3), and diodes (D_1, D_2, and D_3). The presented topology operates in continuous conduction mode (CCM), where all components work in idle condition.

4. The Operating Principle

4.1. State I (t_0-t_1). In this state, as depicted in Figure 5, when switches S_1 and S_2 are on, diode D_1 works in forward biased, and diodes D_2 and D_3 work in reverse biased, respectively. Inductor L_1 increase by input voltage and inductor current increases linearly at the same time (V_s) established across the inductor L_2 and the inductor current increases linearly, respectively. In this state, capacitors V_{C1} and V_{C2} work in series resultant capacitor voltage of $V_{C1} + V_{C2} = 2V_{C2}$ inductor L_3 decrease by $2V_{C2} - V_0$ and

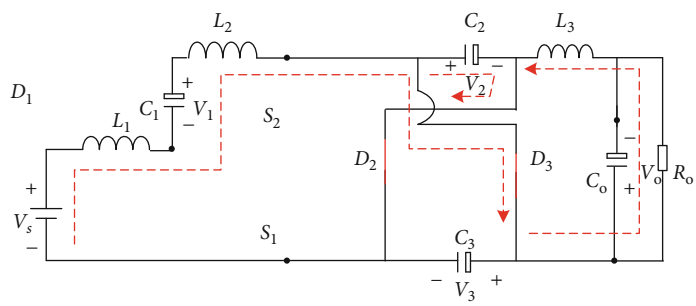

Figure 6: State II.

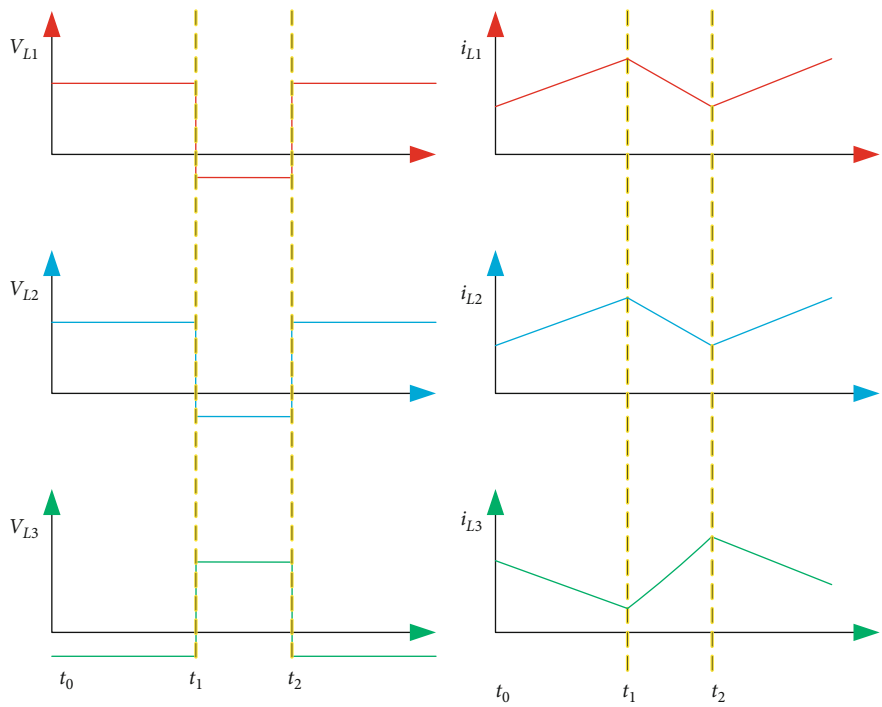

Figure 7: Steady state.

their current decrease in this state. This state is derived in Eqs. (3)-(8).

$$V_1 = V_s, \tag{3}$$

$$i_{L1} = i_{L1-t_0} + \frac{V_s}{L_1} t, \tag{4}$$

$$i_{L2} = i_{L2-t_0} + \frac{V_s}{L_2} t \tag{5}$$

$$i_{L3} = i_{L3-t_0} + \frac{2V_{c2} - V_0}{L_3} t, \tag{6}$$

$$i_{Q1,2} = i_{L1} + i_{L2} + i_{L3}, \tag{7}$$

$$i_{\text{in}} = i_Q - i_{L3}. \tag{8}$$

4.2. State II (t_1-t_2). In this state, as depicted in Figure 6, when both the semiconductor switches S_1 and S_2 are turned off, diode D_1 is reverse biased. The current across the inductor L_1 discharged to the load by $2V_s - V_{c2}$.In the same time inductor, L_2 also released to load the same as inductor L_1 and the voltage across inductor L_3 charged to load by $V_{C2} - V_0$. In this state, inductors i_{L1} and i_{L2} decrease linearly and i_{L3} increases respectfully; this state is derived Eqs. (9)-(13).

$$i_{L1} = i_{L1-t_1} \frac{2V_s - V_{c2}}{L_1} t, \tag{9}$$

$$i_{L2} = i_{L2-t_1} \frac{2V_s - V_{c2}}{L_2} t, \tag{10}$$

$$i_{L3} = i_{L3-t_1} \frac{V_{c2} - V_0}{L_3} t, \tag{11}$$

$$i_Q = 0, \tag{12}$$

$$i_{\text{in}} = i_{L2}. \tag{13}$$

Table 1: Power/component.

Power (W)	Components
P_{L1}	L_1
P_{L2}	L_2
P_{L3}	L_3
P_{C1}	C_1
P_{C2}	C_2
P_{C3}	C_3
P_{C0}	C_0
P_{D1}	D_1
P_{D2}	D_2
P_{D3}	D_3
P_{S1}	S_1
P_{S2}	S_2
$P_{S'1}$	S_1'
$P_{S'2}$	S_2'

5. Proposed Converter Voltage Conversion Ratio

At the proposed converter inductors L_1, L_2, and L_3, applying volt second balance method in each state, the connection between the proposed converters is given below in Eqs. (14)-(20). Steady-state behavior of inductor voltage and their currents are depicted in above Figure 7.

$$V_{L1} = V_s, \tag{14}$$

$$V_{L2} = V_s, \tag{15}$$

$$V_{L3} = 2V_{c2} - V_0, \tag{16}$$

$$V_{L1} = 2V_s - V_{c1}, \tag{17}$$

$$V_{L2} = 2V_s - V_{c2}, \tag{18}$$

$$V_{L3} = V_{c2} - V_0, \tag{19}$$

$$G = \frac{V_0}{V_s} = 2\frac{1+D}{1-D}. \tag{20}$$

Voltage stress across the MOSFET switch in Eqs. (21)-(24)

$$V_{S1,2} = \frac{1}{3.2}V_0, \tag{21}$$

$$V_{D1(\text{stress})} = V_1 = -V_{c1} = -V_s, \tag{22}$$

$$V_{D2(\text{stress})} = V_2 = -V_{c2} = -\frac{2V_s}{1-D}, \tag{23}$$

$$V_{D3(\text{stress})} = V_3 = -V_{c3} = -\frac{2V_s}{1-D}. \tag{24}$$

5.1. Proposed Converter Power Loss Analysis. Total power loss in converter is equal to losses in each component of converter Table 1.

$$\begin{aligned} P_{\text{loss}} = {} & P_{L1} + P_{L2} + P_{L3} + P_{C1} + P_{C2} + P_{C3} + P_{C0} \\ & + P_{D1} + P_{D2} + P_{D3} + P_{S1} + P_{S2} + P_{S'1} + P_{S'2}. \end{aligned} \tag{25}$$

$$\begin{aligned} P_{L1} &= I_{L1(\text{rms})}^2.R_{L1}, \\ P_{L2} &= I_{L2(\text{rms})}^2.R_{L2}, \\ P_{L3} &= I_{L3(\text{rms})}^2.R_{L3}, \\ P_{C1} &= I_{C1(\text{rms})}^2.R_{C1}, \\ P_{C2} &= I_{C2(\text{rms})}^2.R_{C2}, \\ P_{C3} &= I_{C3(\text{rms})}^2.R_{C3}, \\ P_{C0} &= I_{C0(\text{rms})}^2.R_{C0}, \\ P_{D1} &= I_{D1(\text{rms})}^2.R_{D1}, \\ P_{D1} &= I_{D1(\text{rms})}^2.R_{D1}, \\ P_{D2} &= I_{D2(\text{rms})}^2.R_{D2}, \\ P_{D3} &= I_{D3(\text{rms})}^2.R_{D3}, \\ P_{S1} &= I_{s1(\text{rms})}^2.R_{Ds(\text{on})1}, \\ P_{S2} &= I_{s2(\text{rms})}^2.R_{Ds(\text{on})2}, \\ P_{S'1} &= \frac{1}{2}\left[V_{S1(\max)}.I_{S1(\max)}.f_s.(t_r + t_f)\right], \\ P_{S'2} &= \frac{1}{2}\left[V_{S2(\max)}.I_{S2(\max)}.f_s.(t_r + t_f)\right], \end{aligned} \tag{26}$$

$V_{S1(\max)}$ = maximum voltage stress of S_1, $I_{S1(\max)}$ = maximum current stress of S_1, f_s = switching frequency, t_r = rise time of MOSFET switch, and t_f = fall time of MOSFET switch.

$$I_{L1(\text{rms})} = \sqrt{I_{L1(\text{avg})}^2 + \left(\frac{\Delta I_{L1}/2}{\sqrt{3}}\right)^2}. \tag{27}$$

Similarly, for $I_{L2}(\text{rms})$ and $I_{L3}(\text{rms})$,

$$\begin{aligned} I_{c1(\text{rms})} &= \frac{I_{C1(\max)}}{\sqrt{3}} = \frac{\Delta I_{L1}/2}{\sqrt{3}}, \\ I_{c2(\text{rms})} &= I_{C3(\text{rms})} = \frac{\Delta I_{L2}/2}{\sqrt{3}}, \\ I_{c0(\text{rms})} &= \frac{\Delta I_{L3}/2}{\sqrt{3}}, \\ I_{D1(\text{rms})} &= \sqrt{D}(I_s - I_{L1}), \\ I_{D2(\text{rms})} &= I_{D3(\text{rms})} = \sqrt{1-D}.(I_{L1}), \\ I_{s1(\text{rms})} &= \sqrt{D}.I_{L1}, \\ I_{s2(\text{rms})} &= \sqrt{D}.I_{L2}. \end{aligned} \tag{28}$$

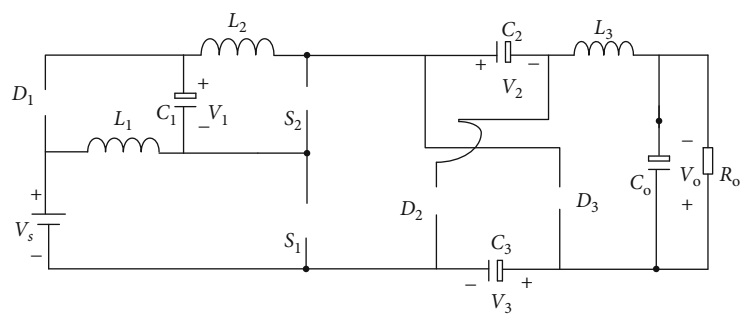

Figure 8: $D_1 T_s - > T_s$

5.2. DCM Analysis of Proposed Converter. Discontinuous conduction mode (DCM) occurs in switching ripples in inductor current is too large which causes reverse current to flow in the diodes. As we know, didoes can conduct in reverse current so converter goes in DCM mode.

DCM mode commonly occurs in converter which has a single quadrant switch. The condition for CCM operation is that average value of conductor should be greater than half of the peak to peak ripples. Converter can go into DCM as given below.

For CCM mode,

$$I_{L(\text{avg})} > \frac{\Delta I_L}{2} = > 2I_{L(\text{avg})} > \Delta I_L. \tag{29}$$

For DCM mode,

$$I_{L(\text{avg})} < \frac{\Delta I_L}{2} = > 2I_{L(\text{avg})} < \Delta I_L. \tag{30}$$

In between the above two conditions is the boundary B/W CCM and DCM which is given by

$$I_{L(\text{avg})} = \frac{\Delta I_L}{2} = > 2I_{L(\text{avg})} = \Delta I_L, \tag{31}$$

In proposed converter, we have three inductors. For CCM inductors, value can be obtained for CCM mode below.

$$\begin{aligned} L_{1(\min)} = L_{2(\min)} &= \frac{DV_s}{2f_s I_{L(\text{avg})}}, \\ L_{3(\min)} &= \frac{D(2V_{c2} - V_0)}{2f_s I_{L3(\text{avg})}}. \end{aligned} \tag{32}$$

As the energy release path from inductor L_3 is discharged by switches S_1 and S_2, these switches are bidirectional, so there is no DCM mode in inductor L_3 due to ripples in current. In simple word, ripples increase in I_{L3} do not cause DCM because MOSFET switches S_1 and S_2 conduct the reverse current. However, value of inductor L_3 should be greater enough to avoid the current reversal problem.

An increase of ripple current theory in inductors L_2 and L_2 causes DCM mode as the freewheeling diodes D_2 and D_3 cannot conduct the reverse current. Hence, for DCM, there is a 3rd stage in proposed converter which D_2 and D_3 also of along with other switching components as shown in below Figure 8.

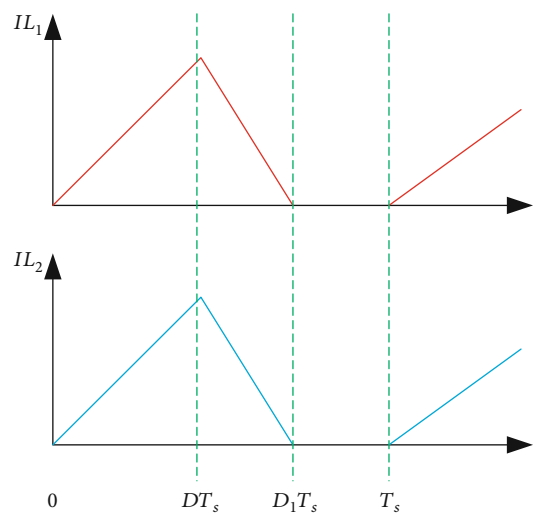

Figure 9: Steady state.

So in DCM operation of proposed converter, there are three switching states in each switching period. State I and state II are the same as CCM mode, and state III is given below when all switches are off.

$$\begin{aligned} IL_1 = IL_2 &= 0, \\ VL_1 = VL_2 &= 0, \\ VL_3 = V_3 - V_0 &- VD_2. \end{aligned} \tag{33}$$

As we know, $V_3 = V_2$ and $V_s = V_1$, so

$$VL_3 = 2V_2 - 2V_s - V_0. \tag{34}$$

Current through inductors L_1 and L_2 is given below steady state Figure 9.

In DCM mode, DC conversion ratio is given by

$$M = \frac{V_0}{V_s} = f(D.D_1) = f\left(D.I_{L(\text{avg})}.L.T_s\right). \tag{35}$$

After applying voltage second balance law on all inductors, we get

$$V_2 = V_3 = \frac{2D_1}{D_1 - D} V_s,$$
$$M = \frac{V_0}{V_s} = \frac{(2D_1)(D + 2 - D_1) - (2D_1 - 2)(D_1 - D)}{D_1 - D},$$
$$D_1 = \frac{2L_1 - D}{DV_s.T_s}. \tag{36}$$

5.3. Dynamic Modeling for the Presented Converter. For dynamic modeling, ripples of inductor current and voltage ripples of capacitor are assume very less. The equivalent circuit of presented converter is shown below in Figure 10 derived from Figure 5.

Subsequently, applying circuit theory in Figure 7, this derived in Eq. (37).

$$\begin{bmatrix} \dot{i}_{L1} \\ \dot{i}_{L2} \\ \dot{i}_{L3} \\ \dot{V}_{c1} \\ \dot{V}_{c2} \\ \dot{V}_{c3} \\ \dot{V}_{c4} \end{bmatrix} = \begin{bmatrix} 0 & 0 & 0 & \frac{-(1-u)}{L_1} & 0 & 0 & 0 \\ 0 & 0 & 0 & 0 & \frac{u}{L_2} & -\frac{u}{L_2} & 0 \\ 0 & 0 & 0 & 0 & \frac{u}{L_3} & \frac{-1}{L_3} & -\frac{1}{L_3} \\ \frac{(1-u)}{C_1} & 0 & 0 & 0 & 0 & 0 & 0 \\ 0 & \frac{u}{C_2} & -\frac{1}{C_2} & 0 & 0 & 0 & 0 \\ 0 & \frac{-u}{C_3} & -\frac{1}{C_3} & 0 & 0 & 0 & 0 \\ 0 & 0 & 0 & 0 & -\frac{u}{C_4} & -\frac{1}{C_4} & -\frac{1}{R_L C_4} \end{bmatrix} \cdot \begin{bmatrix} i_{L1} \\ i_{L2} \\ i_{L3} \\ V_{c1} \\ V_{c2} \\ V_{c3} \\ V_{c4} \end{bmatrix} + \begin{bmatrix} \frac{u}{L_1} \\ \frac{1+u}{L_2} \\ -\frac{1}{L_3} \\ 0 \\ 0 \\ 0 \\ 0 \end{bmatrix} [e_t]. \tag{37}$$

Equation (37) can be written as Eq. (38) without considering losses.

$$\dot{x}(t) = A(u)x(t) + B(u)e(t), \tag{38}$$

where $x_{(t)} = [i_{L1}, i_{L2}, i_{L3}, V_{c1}, V_{c2}, V_{c3}, V_{c4}]^T \in R^7$ is the normal value of state vector, $A_{(u)}$ is a matrix in $R^{7\times7}$, and $B_{(u)}$ is a vector in R^7; $V_s \in R$ = input voltage, whereas resistive load is R_L and u is a function of switch S with the binary value, which is [0, 1]. This means that when the switch value is [0], the switch is off, and when the value is [1], the switch is on. The above equation is based on nonlinear, and matrix $A_{(u)}, B_{(u)}$ is based on control signal of $u_{(t)} \in R$. The linearisation process method obtained the proposed converter behavior to small perturbations around an operation point. Therefore, the nominal steady-state operating system of the proposed converter can be written by setting (8),$AX + BE = 0$ and can be written as shown in Eqs. (49)-(55).

The voltage across the capacitor is

$$V_{c1} = Vs, \tag{39}$$

$$V_{c2} = \frac{2}{1-D} Vs, \tag{40}$$

$$V_{c3} = \frac{2}{1-D} Vs, \tag{41}$$

$$V_{c4} = 2\frac{1+D}{1-D} Vs, \tag{42}$$

Current across the inductor is

$$i_{L1} = \frac{V_s}{(1-D)^4 R_L}, \tag{43}$$

$$i_{L2} = \frac{V_s}{(1-D)^4 R_L}, \tag{44}$$

$$i_{L3} = \frac{V_s}{(1-D)^2 R_L}, \tag{45}$$

where V_s = DC input voltage and D = duty cycle of the switch S, $\tilde{u}$ = small − signal perturbations to the nominal dusty cycle D, and $\tilde{e}$ = to the nominal input voltage V_s to the nominal input voltage, so we can write the relationship between voltage and duty cycle as below (46), (47).

$$e(t) = E + \tilde{e}, \tag{46}$$

$$u(t) = U + \tilde{u}, \tag{47}$$

where $\tilde{e} << E$ and $\tilde{u} << D$, so we can also write as (48), (49).

$$X(t) = X + \tilde{x}, \tag{48}$$

$$V_0(t) = V_0 + \tilde{v}_0. \tag{49}$$

After substituting Eqs. (39)-(45) and (46), (47) into Eq. (40), we can derive linear mode after assuming that the

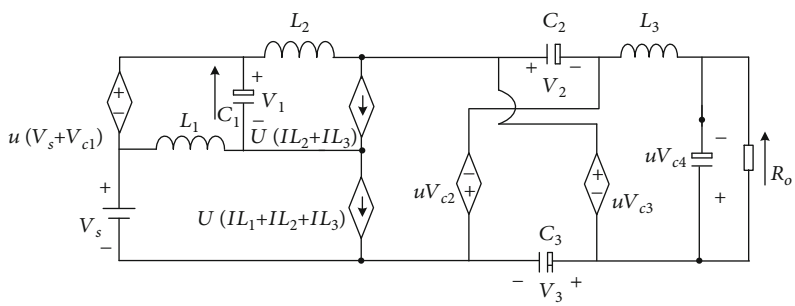

Figure 10: Average equivalent circuit.

perturbations are less enough and nonlinear terms can be avoided so that we can write Eq. (50).

$$\begin{bmatrix} \dot{\widetilde{i_{L1}}} \\ \dot{\widetilde{i_{L2}}} \\ \dot{\widetilde{i_{L3}}} \\ \dot{\widetilde{V_{c1}}} \\ \dot{\widetilde{V_{c2}}} \\ \dot{\widetilde{V_{c3}}} \\ \dot{\widetilde{V_{c4}}} \end{bmatrix} = \begin{bmatrix} 0 & 0 & 0 & \frac{-(1-u)}{L_1} & 0 & 0 & 0 \\ 0 & 0 & 0 & 0 & \frac{u}{L_2} & -\frac{u}{L_2} & 0 \\ 0 & 0 & 0 & 0 & \frac{u}{L_3} & \frac{-1}{L_3} & -\frac{1}{L_3} \\ \frac{(1-u)}{C_1} & 0 & 0 & 0 & 0 & 0 & 0 \\ 0 & \frac{u}{C_2} & -\frac{1}{C_2} & 0 & 0 & 0 & 0 \\ 0 & \frac{-u}{C_3} & -\frac{1}{C_3} & 0 & 0 & 0 & 0 \\ 0 & 0 & 0 & 0 & -\frac{u}{C_4} & -\frac{1}{C_4} & -\frac{1}{R_L C_4} \end{bmatrix} \begin{bmatrix} \widetilde{i_{L1}} \\ \widetilde{i_{L2}} \\ \widetilde{i_{L3}} \\ \widetilde{V_{c1}} \\ \widetilde{V_{c2}} \\ \widetilde{V_{c3}} \\ \widetilde{V_{c4}} \end{bmatrix} + \begin{bmatrix} Vs & \\ \frac{2}{(1-D)L_2} Vs & \frac{u}{L_1} \\ \frac{2}{(1-D)L_2} Vs & \frac{1+u}{L_2} \\ 2\frac{1+D}{(1-D)L_3} Vs & -\frac{1}{L_3} \\ \frac{V_s}{(1-D)^4 R_{Lc1}} & 0 \\ \frac{V_s}{(1-D)^4 R_{Lc2}} & 0 \\ \frac{V_s}{(1-D)^2 R_{Lc3}} & 0 \end{bmatrix} \begin{bmatrix} \tilde{u} \\ \tilde{e} \end{bmatrix}. \tag{50}$$

Equation (50) can be written as Eq. (51).

$$\dot{x}(t) = Ax(t) + Bv(t), \tag{51}$$

where $x_{(t)} \in R^7$ is the state vector, $A \in R^{7\times7}$ and B are constant matrix in $R^{7\times2}$, R^2 is vector of input voltage, and $V_{(t)} = [\tilde{u}\tilde{e}]$. When the perturbation input voltage is neglected $\tilde{e} = 0$,so matrix B can be removed and written as (62).

$$\begin{bmatrix} \dot{\widetilde{i_{L1}}} \\ \dot{\widetilde{i_{L2}}} \\ \dot{\widetilde{i_{L3}}} \\ \dot{\widetilde{V_{c1}}} \\ \dot{\widetilde{V_{c2}}} \\ \dot{\widetilde{V_{c3}}} \\ \dot{\widetilde{V_{c4}}} \end{bmatrix} = \begin{bmatrix} 0 & 0 & 0 & \frac{-(1-u)}{L_1} & 0 & 0 & 0 \\ 0 & 0 & 0 & 0 & \frac{u}{L_2} & -\frac{u}{L_2} & 0 \\ 0 & 0 & 0 & 0 & \frac{u}{L_3} & \frac{-1}{L_3} & -\frac{1}{L_3} \\ \frac{(1-u)}{C_1} & 0 & 0 & 0 & 0 & 0 & 0 \\ 0 & \frac{u}{C_2} & -\frac{1}{C_2} & 0 & 0 & 0 & 0 \\ 0 & \frac{-u}{C_3} & -\frac{1}{C_3} & 0 & 0 & 0 & 0 \\ 0 & 0 & 0 & 0 & -\frac{u}{C_4} & -\frac{1}{C_4} & -\frac{1}{R_L C_4} \end{bmatrix} \begin{bmatrix} \widetilde{i_{L1}} \\ \widetilde{i_{L2}} \\ \widetilde{i_{L3}} \\ \widetilde{V_{c1}} \\ \widetilde{V_{c2}} \\ \widetilde{V_{c3}} \\ \widetilde{V_{c4}} \end{bmatrix} + \begin{bmatrix} Vs \\ \frac{2}{(1-D)L_2} Vs \\ \frac{2}{(1-D)L_2} Vs \\ 2\frac{1+D}{(1-D)L_3} Vs \\ \frac{V_s}{(1-D)^4 R_{Lc1}} \\ \frac{V_s}{(1-D)^4 R_{Lc2}} \\ \frac{V_s}{(1-D)^2 R_{Lc3}} \end{bmatrix} [\tilde{u}]. \tag{52}$$

6. Results and Discussions

6.1. Simulation Results and Discussion. Figures 11(a) and 11(b) presented simulation results of proposed topology and conventional boost converter. These simulation results performed in Matlab Simulink at the same parameters, as

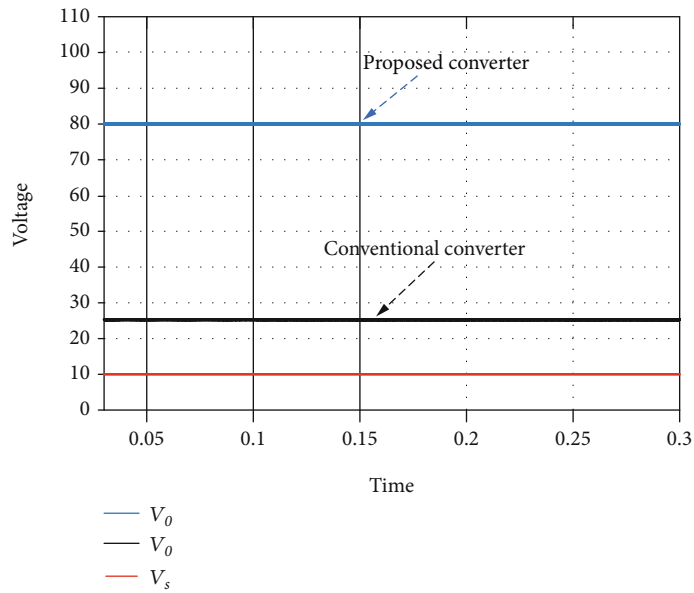

(a)

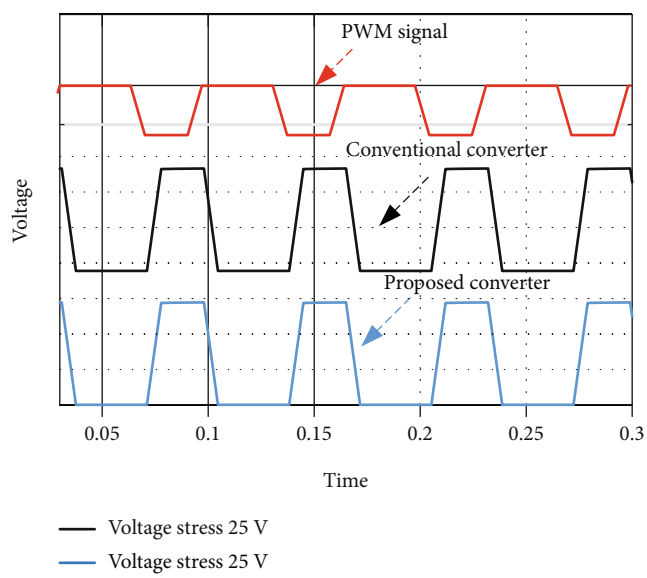

(b)

Figure 11: Proposed converter simulation results.

shown. Figure 11(a) shows the simulation results of both the conventional boost converter and proposed CPC converter, where input voltage given to both the converters is the same 10 V, and it can be seen that the output voltage of the proposed converter is higher as compared to conventional converter, which is 80 V as compared to 25 V output voltage of conventional boost converter, which is very low. In Figure 11(b), we can see that the voltage stress of the traditional boost converter is the same as output voltage, as mentioned in Eq. (2). Still, the voltage stress of the recommended converter CPC topology is very less. From simulation results, it is very clear that the presented converter contains many pros as compared to conventional converter, such as high voltage gains and lower semiconductor switching stress, as shown in Figure 11(b). In traditional boost converter, if we

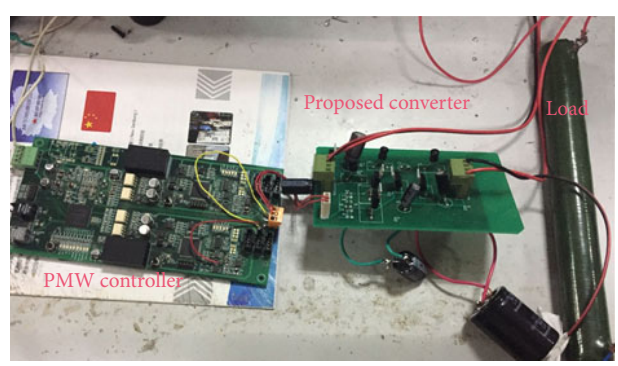

Figure 12: Experimental prototype of presented converter.

Table 2: Component type and cost.

Components	Symbol	Component type	Cost ($)	Model number
Inductors ($L_{1,2,3}$)	L	Passive	0.15/piece	
Capacitor ($C_{1,2,3,4}$)	C	Passive	$0.20-$1/piece	
Resistor	R	Passive	$14-$20/piece	
MOSFET ($S_{1,2}$)	S	Active	$0.22-$0.24/piece	IRFZ46N
Diodes ($D_{1,2,3}$)	D	Active	$0.21-$0.24/piece	MUR860

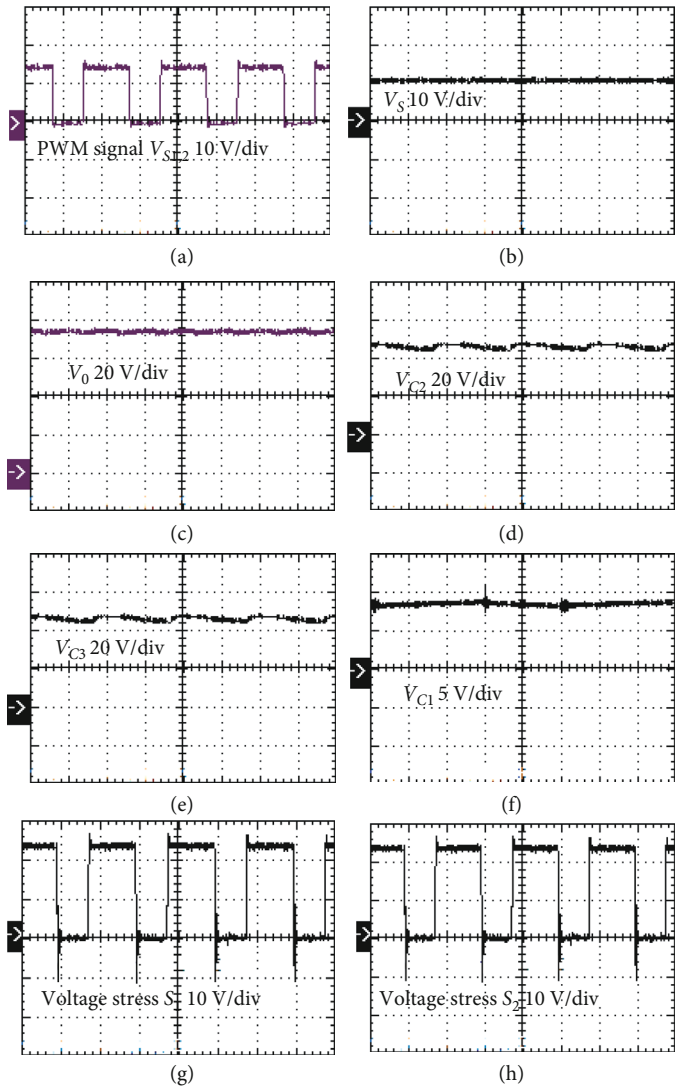

Figure 13: Proposed converter experimental results.

give 10 V as an input voltage to achieve the output voltage according to proposed topology from the conventional boost converter, it shall be operated at higher of duty ratio, which will result in increasing the component losses connected with the circuit and will degrade the overall system efficiency. The higher duty cycle could cause failure or malfunctioning of the switches because of the short conduction time.

6.2. Experimental Results and Discussion. To validate the operation principle and investigate the efficacy of the recommended CPC converter topology, a lab-scale prototype was developed with the circuit parameters: $V_S = 10$ V; $V_0 = 80$ V; switching frequency = 100 kHz; L_1, L_2, and $L_3 = 220\,\mu$H; load = 200 Ω; C_1, C_2, C_3, and $C_0 = 440\,\mu$F, 840 μF, 840 μF, and 420 μF, respectively, as shown in Figure 12, and proposed converter component types and cost are presented in Table 2. The experimental results of the recommended CPC converter are depicted in Figure 13, where the duty cycle of the suggested CPC topology is set at $D = 0.6$, and it works in CCM mode. Figure 13(a) depicted switching signals

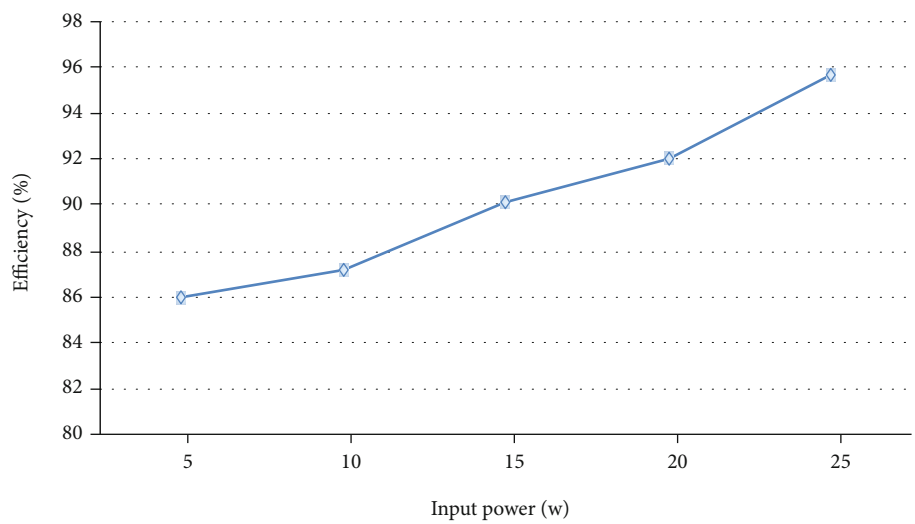

Figure 14: Efficiency graph.

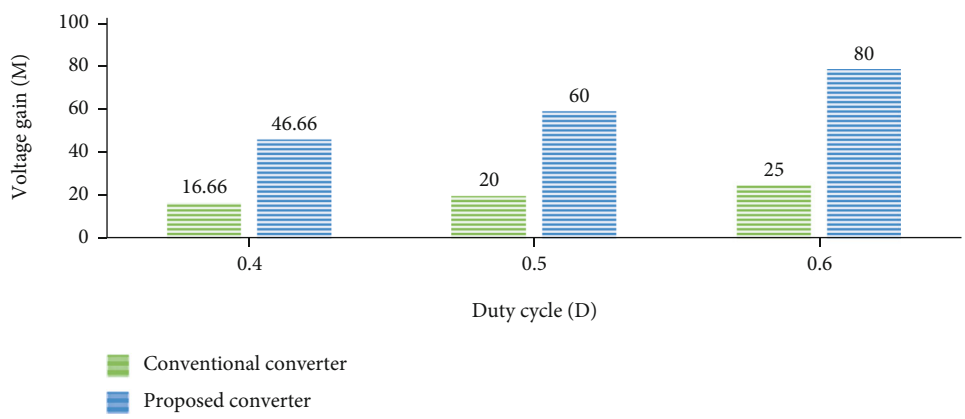

Figure 15: Voltage gain graph.

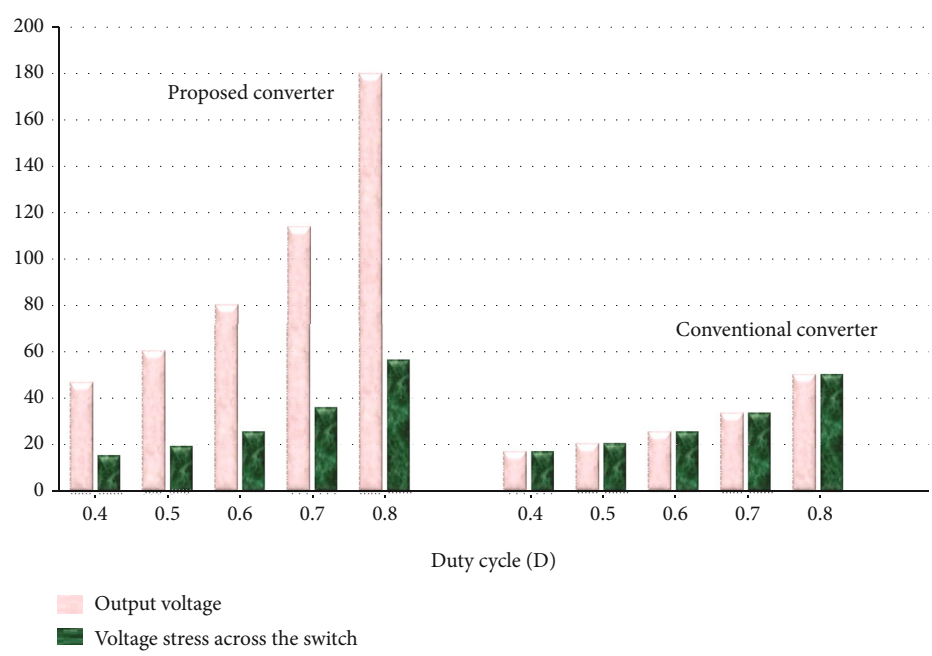

Figure 16: Switching stress graph.

of the anticipated converter, and Figure 13(b) depicted input voltage Vs. Figure 13(c) depicted where we can observe that the output voltage V_0 presented converter is around 78 V, which is very close to the voltage gain equation of the recommended converter. From output voltage, it is vibrant that the recommended converter CPC topology has achieved high voltage gain without higher duty ratio.

Figures 13(d) and 13(e) show the waveform of capacitor voltage V_{C2} and V_{C3} which is 49 V, respectively, which are also very close to the capacitors of Eqs. (40), (41). Figure 13(f) depicted voltage across the capacitor V_{C1} which is 10 V, which is equal to the input voltage. Furthermore, Figures 13(g) and 13(h) depicted voltage stress across the MOSFET switches S_1 and S_2 which are 25 V of each. So, it is testified that the recommended CPC converter topology can get high voltage gain at the load side with monomer switching stress.

The proposed converter efficiency vs. the traditional boost converter were observed at different load at input and output terminals in which input voltage and current and output voltage current were measured with a tool, and supported handling data by following the Eq. (53) were performed in Matlab Simulink.

$$\eta = \frac{V_0 * I_0}{V_{\text{in}} * I_{\text{in}}}. \tag{53}$$

The proposed converter efficiency graph is portrayed in Figure 14, and it can be observed that the maximum efficiency achieved by the proposed CPC topology is 95.68% at 25 W input power and 85.98% minimum efficiency at 5 W input. Thus, it is clear that the recommended CPC topology has shown an excellent efficiency with high voltage gain. Figure 15 shows the output voltages at altered duty cycles, where it can be simply observed that at any duty cycle, recommended converter achieved high voltage at the output in response to the conventional converter. Furthermore, in Figure 16, the switching stress and output voltage across the MOSFETs of recommended CPC converter and traditional boost converter are illustrated, where we can witness that at 0.4, 0.5, and 0.6 duty ratio levels, voltage gain of the proposed converter is very high and switching stress is low as compared to traditional boost converter, and the voltage gain is equal to voltage stress across the MOSFET switch.

7. Conclusions

Renewable energy systems are needed in order to meet the increasing demand of the global energy consumption, and power electronic converters are an important module in such systems. This paper presents new DC-DC boost converters based on the charge pump capacitor (CPC). The feature combination of CPC-DCBC with voltage multiplier cell attains high output voltage gain with lesser switching stress. After simulation and experimental results, it is evidenced that the CPC-DCBC proposed topology could achieve high output voltage without working at an extremely duty cycle with excellent efficiency. The presented converter topology is applicable where a grid supply is unavailable and the source appliances generally run at high current with low input voltage, whereas their output load requirement is low current with high output voltage. for example, remote telecommunication system, off-grid solar system, and defense communication system. It also has the following advantages over traditional DC-DC boost converter:

(i) It operates at a lower duty cycle, which reduces the losses linked with the components installed in circuit and improves its efficiency

(ii) Less number of components, which reduce the risk of malfunctioning across the components and can, therefore, achieve higher voltage gain with very less voltage stress

(iii) Fewer switch utilization because of low voltage stress across them, which tends to reduce the active switch cost

(iv) Smaller inductor size because of less energy volume, which reduces the cost and size of the converter

Data Availability

The raw data used for this proposed work have been cited in the manuscript. Moreover, the derived data supporting the findings of this study have been graphically depicted and are available with the corresponding author on request.

Conflicts of Interest

The authors declare that there is no conflict of interest regarding the publication of this paper.

Acknowledgments

Authors thankfully acknowledged the support and funding provided by the Scientific Research Deanship, King Khalid University, Kingdom of Saudi Arabia, for the Large Research Group under the grant number R.G.P2./82/41.

References

[1] M. Sahoo and K. S. Kumar, "High gain step up DC-DC converter for DC micro-grid application," in *7th International Conference on Information and Automation for Sustainability*, pp. 1–5, Colombo, Sri Lanka, 2014.

[2] A. Naderi and K. Abbaszadeh, "High step-up DC–DC converter with input current ripple cancellation," *IET Power Electronics*, vol. 9, no. 12, pp. 2394–2403, 2016.

[3] A. A. A. Freitas, F. L. Tofoli, E. M. Sá Júnior, S. Daher, and F. L. M. Antunes, "High-voltage gain dc–dc boost converter with coupled inductors for photovoltaic systems," *IET Power Electronics*, vol. 8, no. 10, pp. 1885–1892, 2015.

[4] L. Kouchachvili, W. Yaïci, and E. Entchev, "Hybrid battery/supercapacitor energy storage system for the electric vehicles," *Journal of Power Sources*, vol. 374, pp. 237–248, 2018.

[5] S. Chakrabarti and S. Chakrabarti, "Rural electrification programme with solar energy in remote region-a case study in an island," *Energy Policy*, vol. 30, no. 1, pp. 33–42, 2002.

[6] S.-W. Lee and H.-L. Do, "High step-up coupled-inductor cascade boost DC–DC converter with lossless passive snubber," *IEEE Transactions on Industrial Electronics*, vol. 65, no. 10, pp. 7753–7761, 2018.

[7] D. Thenathayalan, C. Lee, and J.-H. Park, "High-order resonant converter topology with extremely low-coupling contactless transformers," *IEEE Transactions on Power Electronics*, vol. 31, no. 3, pp. 2347–2361, 2015.

[8] A. Tomaszuk and A. Krupa, "Step-up DC/DC converters for photovoltaic applications–theory and performance," *Electrical Review*, vol. 89, pp. 51–57, 2013.

[9] T. Kim, D. Feng, M. Jang, and V. G. Agelidis, "Common mode noise analysis for cascaded boost converter with silicon carbide devices," *IEEE Transactions on Power Electronics*, vol. 32, no. 3, pp. 1917–1926, 2016.

[10] H. Wang and Z. Li, "A PWM LLC type resonant converter adapted to wide output range in PEV charging applications," *IEEE Transactions on Power Electronics*, vol. 33, no. 5, pp. 3791–3801, 2017.

[11] H. Wu, X. Zhan, and Y. Xing, "Interleaved LLC resonant converter with hybrid rectifier and variable-frequency plus phase-shift control for wide output voltage range applications," *IEEE Transactions on Power Electronics*, vol. 32, no. 6, pp. 4246–4257, 2017.

[12] M. Z. Malik, A. Ali, Q. Xu, and G. Chen, "A new quadratic boost converter with voltage multiplier cell: an analysis and assessment," *International Journal of Smart Home*, vol. 10, no. 8, pp. 281–294, 2016.

[13] A. Haque, A. Alshareef, A. I. Khan, M. M. Alam, V. S. B. Kurukuru, and K. Irshad, "Data description technique-based islanding classification for single-phase grid-connected photovoltaic system," *Sensors*, vol. 20, no. 11, p. 3320, 2020.

[14] M. Z. Malik, H. Chen, M. S. Nazir et al., "A new efficient step-up boost converter with CLD cell for electric vehicle and new energy systems," *Energies*, vol. 13, no. 7, article 1791, 2020.

[15] M. Z. Malik, Q. Xu, A. Farooq, and G. Chen, "A new modified quadratic boost converter with high voltage gain," *IEICE Electronics Express*, vol. 14, no. 1, 2017.

[16] M. Z. Malik, A. Farooq, A. Ali, and G. Chen, "A DC-DC boost converter with extended voltage gain," *MATEC Web of Conferences*, vol. 40, article 07001, 2016.

[17] J. Leyva-Ramos, R. Mota-Varona, M. G. Ortiz-Lopez, L. H. Diaz-Saldierna, and D. Langarica-Cordoba, "Control strategy of a quadratic boost converter with voltage multiplier cell for high-voltage gain," *IEEE Journal of Emerging and Selected Topics in Power Electronics*, vol. 5, no. 4, pp. 1761–1770, 2017.

[18] J. R. Garcia-Sanchez, E. Hernandez-Marquez, J. Ramirez-Morales et al., "A robust differential flatness-based tracking control for the 'MIMO DC/DC boost converter–inverter–DC motor' system: experimental results," *IEEE Access*, vol. 7, pp. 84497–84505, 2019.

[19] S. Malek, "A new nonlinear controller for DC-DC boost converter fed DC motor," *International Journal of Power Electronics*, vol. 7, no. 1/2, pp. 54–71, 2015.

[20] A. Richelli, L. Colalongo, S. Tonoli, and Z. M. Kovacs-Vajna, "A 0.2–1.2 V DC/DC boost converter for power harvesting applications," *IEEE Transactions on Power Electronics*, vol. 24, no. 6, pp. 1541–1546, 2009.

[21] M. Maalandish, S. H. Hosseini, S. Ghasemzadeh, E. Babaei, R. Shalchi Alishah, and T. Jalilzadeh, "Six-phase interleaved boost DC/DC converter with high-voltage gain and reduced voltage stress," *IET Power Electronics*, vol. 10, no. 14, pp. 1904–1914, 2017.

[22] M. S. B. Ranjana, N. S. Reddy, and R. K. P. Kumar, "A novel high gain floating output DC-DC multilevel boost converter for fuelcell applications," in *2014 International Conference on Circuits, Power and Computing Technologies [ICCPCT-2014]*, pp. 291–295, Nagercoil, India, 2014.

[23] T. Roy Choudhury and B. Nayak, "Comparative steady state analysis of boost and cascaded boost converter with inductive esr losses & capacitor current behaviour," *International Journal of Power Electronics and Drive Systems (IJPEDS)*, vol. 7, no. 1, p. 159, 2016.

[24] H. Ardi, A. Ajami, F. Kardan, and S. N. Avilagh, "Analysis and implementation of a nonisolated bidirectional DC–DC converter with high voltage gain," *IEEE Transactions on Industrial Electronics*, vol. 63, no. 8, pp. 4878–4888, 2016.

[25] S. B. Mahajan, P. Sanjeevikumar, P. Wheeler, F. Blaabjerg, M. Rivera, and R. Kulkarni, "X-Y converter family: a new breed of buck boost converter for high step-up renewable energy applications," in *2016 IEEE International Conference on Automatica (ICA-ACCA)*, pp. 1–8, Curico, Chile, 2016.

[26] M. Lotfi Nejad, B. Poorali, E. Adib, and A. A. Motie Birjandi, "New cascade boost converter with reduced losses," *IET Power Electronics*, vol. 9, no. 6, pp. 1213–1219, 2016.

[27] M. Z. Malik, A. Ali, and D. Kumar, "A two cascaded boost converter with high voltage gain module," *International Journal of Computer and Electrical Engineering*, vol. 9, no. 2, pp. 476–483, 2017.

[28] A. Farooq, Z. Malik, D. Qu, Z. Sun, and G. Chen, "A three-phase interleaved floating output boost converter," *Advances in Materials Science and Engineering*, vol. 2015, Article ID 409674, 8 pages, 2015.

[29] F. Akar, Y. Tavlasoglu, E. Ugur, B. Vural, and I. Aksoy, "A bidirectional nonisolated multi-input DC–DC converter for hybrid energy storage systems in electric vehicles," *IEEE Transactions on Vehicular Technology*, vol. 65, no. 10, pp. 7944–7955, 2015.

[30] I.-M. Pop-Calimanu, S. Lica, S. Popescu, D. Lascu, I. Lie, and R. Mirsu, "A new hybrid inductor-based boost DC-DC converter suitable for applications in photovoltaic systems," *Energies*, vol. 12, no. 2, p. 252, 2019.

[31] J. Sun, X. Ding, M. Nakaoka, and H. Takano, "Series resonant ZCS–PFM DC–DC converter with multistage rectified voltage multiplier and dual-mode PFM control scheme for medical-use high-voltage X-ray power generator," *IEE Proceedings - Electric Power Applications*, vol. 147, no. 6, pp. 527–534, 2000.

Hindawi
International Journal of Photoenergy
Volume 2021, Article ID 6648739, 10 pages
https://doi.org/10.1155/2021/6648739

Research Article

Study on the Influence of Light Intensity on the Performance of Solar Cell

Zhe Li,[1] Jian Yang,[1] and Pouya Asareh Nejad Dezfuli[2]

[1]*Xingtai Power Supply Branch, State Grid Hebei Electric Power Co., Ltd., Xingtai 054000, China*
[2]*Chemical Engineering Department, Amirkabir University of Technology (AUT), Mahshahr, Iran*

Correspondence should be addressed to Jian Yang; xt_yangj2@163.com and Pouya Asareh Nejad Dezfuli; asareh.p@aut.ac.ir

Received 26 November 2020; Revised 29 December 2020; Accepted 20 January 2021; Published 1 February 2021

Academic Editor: Hafiz Muhammad Ali

Copyright © 2021 Zhe Li et al. This is an open access article distributed under the Creative Commons Attribution License, which permits unrestricted use, distribution, and reproduction in any medium, provided the original work is properly cited.

In order to solve the problem that the influence of light intensity on solar cells is easily affected by the complexity of photovoltaic cell parameters in the past, it is proposed based on the influence of light intensity on the power generation performance of solar cells. By analyzing the electrical performance parameters of photovoltaic cell trough solar energy and determining the influencing factors, discarding other weakly related parameters, and designing targeted research programs, according to the study of the impact of light intensity and temperature on the battery temperature changes, the performance of photovoltaic power generation was understood. The output voltage and current of the maximum power point were obtained. By analyzing its relationship with influencing factors, the impact analysis on the power generation performance of photovoltaic cells was realized. The experimental results show that the open circuit voltage, short-circuit current, and maximum output power of solar cells increase with the increase of light intensity. Therefore, it can be known that the greater the light intensity, the better the power generation performance of the solar cell.

1. Introduction

enewable energy generally includes solar energy, wind energy, water energy, biomass energy, marine energy, tidal energy, and geothermal energy [1, 2]. Among these renewable energy sources, solar energy is rich in resources and can radiate to every corner of the earth. Therefore, solar energy is recognized as one of the most potential energy for large-scale development and utilization in this century. It is proposed in document [3–5] that increasing the development and utilization of solar energy resources can not only alleviate the pressure of economic growth on the environment and ecology to a great extent but also slow down the high-speed consumption of fossil energy, which is of far-reaching significance for the clean and sustainable development of energy [6, 7]; the research on solar energy utilization technology began in the 1960s; after decades of development, photovoltaic and photothermal application technologies have matured and are now in the stage of commercial application [8]. Among them, the commercial solar water heater is widely used, with an efficiency of 60-70%. In some optical devices, solar cells, thermoelectric conversion systems, or spacecraft thermal control systems, radiation is the main heat transfer or energy conversion method. The special radiation characteristics generated when light is incident on the surface of periodic microstructures can effectively meet the industrial needs of this type of system [9].

Traditional fuel energy is declining day by day, and at the same time, there are about 2 billion people in the world who do not have normal energy supply. Searching for new energy has become an urgent issue facing mankind. With its unique advantages, solar energy has become the focus of attention. Because solar power has the advantages of cleanliness, safety, and resource versatility and adequacy that are unmatched by thermal power, hydropower, and nuclear power, solar power is considered to be the most important energy source in the 21st century. At present, there are two main methods to study the performance of solar photovoltaic cells: numerical simulation and finite element analysis. Kohan et al. established a three-dimensional numerical model of photovoltaic modules

and TEG devices [10]. The purpose is to study the performance of a hybrid photovoltaic+TEG power generation system with a thermoelectric generator installed on the back of the photovoltaic module. The model ignores the complexity of the internal structure of the device and regards the device as a uniform medium, and the power output is modeled as an internal energy sink. The finite volume method is used to solve the control energy equation. The results show that under certain environmental conditions, a hybrid system can generate more electric energy than pure photovoltaic power generation. However, due to the insufficient temperature difference of the TEG plant, the increase is very small. In addition, the existence of triethylene glycol may have an adverse effect on the cooling of photovoltaic modules. Zandi and Razaghi et al. studied flat perovskite solar cells by a three-dimensional finite element method [11]. In order to fully characterize the proposed device, a hybrid optoelectronic modeling method is used. Compared with the experimental results, the accuracy of the model is verified. In this new structure, when the thickness of $CH_3NH_3SnI_3$ is 200 nm, the power conversion efficiency (PCE) increases from 14.32% to 15.32%. The short-circuit current j (SC) is improved by coating a 40 nm MGF (2) layer on the surface of PSC as an antireflection layer. The influence of periodic corrugated back and reflector on PSC is considered. The PCE of the new two-layer active PSC structure is up to 17.5% because of the periodic corrugation and the reflector replacing the flat back and the reflector, respectively.

In recent years, with the support of industrial policies and financial support, the application of the photovoltaic system has gradually begun to meet the conditions for large-scale commercial development. It can be predicted that the cost of photovoltaic power generation has significantly decreased. Although it is still higher than the traditional power generation mode, with the continuous development of technology, the new energy with solar energy as the main body will become the main body of energy supply in the future, which cannot be compared with and replaced by other renewable energy sources [12]. Most research activities at home and abroad focus on the research and development of parabolic cylindrical mirrors and Fresnel lens condenser systems. But the parabolic cylindrical surface and Fresnel lens surface are difficult to process, the precision is low, the cost is high, and the product life is short. It is not easy to popularize and apply. The constant voltage electronic load is used to simulate the function of battery charging; that is, the voltage at both ends of the load is stable and unchanged, and the generated current that changes with the light intensity at different times is released through the electronic load circuit to obtain the process of receiving light. In the application research of solar cells, it is very important to study the light intensity for the power generation performance of solar cells. In the previous research methods, due to the influence of various parameters of photovoltaic cells, it consumes too much useless electric energy and thermal energy and costs too much, and the overall cost performance of the research method is low. In view of this situation, a new research method of the influence of light intensity on the performance of solar cells is proposed.

2. Study on the Influence of Light Intensity on the Performance of Solar Cell

2.1. Determine the Influencing Factors of Photovoltaic Cell Power Generation Performance. The manufacturing methods of photovoltaic cells vary, but there are mainly the following types: monocrystalline silicon cell, polycrystalline silicon cell, amorphous silicon cell, chromium telluride cell, Gu selenium copper cell, etc. [13]. Table 1 shows the types and characteristics of common photovoltaic cells.

Based on the characteristics of different types of photovoltaic cells mentioned above, it is determined that monocrystalline silicon photovoltaic cells are mostly used in trough solar energy. Under the condition of constant light intensity, the photocurrent produced by the solar cell does not change with time. Therefore, it can be equivalent to an ideal constant current source [14]. Part of the photogenerated current flows into the load R_0 of the external circuit, which is defined as the current I_0, forming the terminal voltage U_0 at both ends of the external circuit; I_d is the dark current, which is opposite to the photogenerated current. When the voltage is positively biased to the equivalent diode of the PN junction, the current will be generated; due to the contact between the front electrode and the back electrode, and the material itself having a certain resistivity, it is not allowed to flow into the external circuit in the middle to avoid the introduction of additional resistance; it can be regarded as a series resistance R_1 in the equivalent circuit; in the equivalent circuit, a parallel resistance R_1 is often used, because in the process of making the battery, leakage will occur on the edge of the battery, and the metal leakage will be caused by tiny cracks and scratches when making the metalized electrode, which will lead to a part of the electric abortion that should have passed through the load. The phenomenon of short-circuit can be improved by using resistance to equivalent this phenomenon. To sum up, the solar cell can be equivalent to a single diode five-parameter circuit model. The five parameters are the photovoltaic cell current I_{ph}, the equivalent diode reverse saturation current I_c, the junction capacitance C_0, the series resistance R_1, and the parallel resistance R_2.

According to the circuit principle and Shockley's diffusion theory, the $I-V$ equation of photovoltaic cells can be obtained. As shown below,

$$I_0 = I_{\mathrm{ph}} - I_c\left\{\exp\left[\frac{q(V+R_1I_0)}{n\kappa T}\right]-1\right\} - \frac{V+R_1I_0}{R_2}. \quad (1)$$

In the formula, q represents the electronic charge (1.6×10^{-19} C), n represents the diode factor (value range is 1-5), κ represents the Boltzmann constant (1.38×10^{-23} J/K), and T represents the absolute temperature.

According to the current-voltage relationship of the working state of photovoltaic cells in Formula (1), the factors describing the power generation performance of slot solar photovoltaic cells, namely, the main parameters of photovoltaic cells, are determined as follows.

Open circuit voltage: the voltage at the output when the photovoltaic cell circuit disconnects the load.

Table 1: Types and characteristics of common photovoltaic cells.

Type	Monocrystalline silicon	Polysilicon	Amorphous silicon
Photoelectric conversion efficiency	12%~17%	10%~15%	6%~8%
Service life	15-20 years	15-20 years	5-20 years
Average price	Expensive	More expensive	Cheaper
Stability	Good	Good	Poor (attenuated)
Colour	Black	Navy blue	Brown
Main features	The photoelectric conversion efficiency is higher than other types of batteries, with high reliability and relatively high cost	Stable and reliable operation, low cost, can be widely used, but compared with monocrystalline silicon, the conversion efficiency is lower	Low price, mostly used in calculators, electronic watches, etc., with the lowest conversion efficiency

Short-circuit current: the current flowing through the short contact when the output terminal of photovoltaic cells is short-circuited.

Curve factor (also called filling factor): in order to correct the difference between the ideal photovoltaic cell volt-ampere characteristic curve and the actual photovoltaic cell, curve factor [15] is introduced. Define the curve factor as

$$\chi = \frac{I_{p\ \max} \times U_{p\ \max}}{I_{sc} \times U_{oc}} = \frac{P_{\max}}{I_{sc} \times U_{oc}}. \quad (2)$$

In the formula, I_{sc} represents short-circuit current, U_{oc} represents open circuit voltage, $P_{\max}$ represents maximum power, $I_{p\ \max}$ represents optimal working current, $U_{p\ \max}$ represents optimal working voltage, and $I_{p\ \max}$ represents optimal working current. The ideal curve factor of battery characteristics is 1. Generally, the curve factor is between 0.5 and 0.8.

Conversion efficiency: under standard test conditions, the ratio of the maximum output power when the external circuit of the photovoltaic cell is connected to the optimal load to the solar incident operation. The standard test conditions for determining the influence factors and determining the influence of light intensity on the power generation performance of slot solar photovoltaic cells are as follows: the solar spectrum distribution and the ambient temperature are 25 ± 1°C when the atmospheric quality is AM1.5 [16].

2.2. Research Scheme Design of the Influence of Light Intensity on the Power Generation Performance of Photovoltaic Cells. Based on the solar energy storage and heating system of the 12th Five-Year Plan National Science and Technology project, this paper studies the influence of light intensity on the power generation performance of solar cells under constant resistance load. The schematic diagram of slot solar energy heat storage and heating system is as shown in Figure 1 [17].

In Figure 1, the mark 1 indicates solar photovoltaic panel, 2 indicates automatic power switching device, 3 indicates 220 V AC household power supply, and 4 indicates far-infrared heating soft plate and pebble thermal reservoir. The trough type solar photovoltaic power generation heat storage and heating system refers to the photovoltaic cell as the power source, as the energy conversion carrier to convert direct current into heat energy, which is the far-infrared thermal fiber soft board with constant resistance value, which stores the heat energy in the indoor floor tiles or the heat storage medium pebble layer under the floor [18]. The heating form is to store the heat energy in the daytime and release the heat energy at night. In order to reduce the self-loss of the inverter device, the photovoltaic cell is directly connected with the heating load in the working process of the photovoltaic cell, which is energy delay utilization, electrothermal integration, and effective energy conversion technology [19].

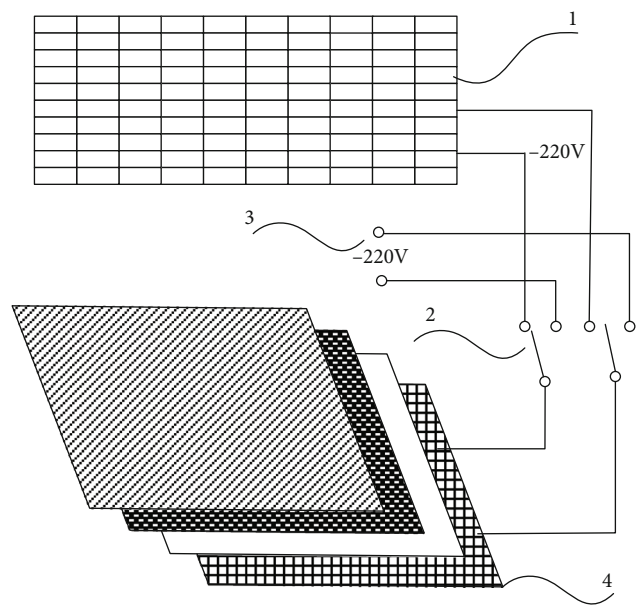

Figure 1: Schematic diagram of heat storage and heating system for photovoltaic power generation.

In order to simulate the working state of the residential trough solar photovoltaic power supply system, the same type of polysilicon photovoltaic cell module and its matching far-infrared thermal fiber soft board with constant resistance value are used [20]. The technical parameters of polysilicon PV modules used in the impact study are shown in Table 2.

In order to obtain the power generation performance data of photovoltaic cells under different light intensity, the research data were tested in a certain area for six consecutive months and measured in half an hour from 8.00 a.m. every

Table 2: Technical parameters of polysilicon photovoltaic cell module.

Type	Project	Parameter
Working parameters	Peak power P/W	245 W
	Maximum working voltage U/V	30.2 V
	Maximum working current I/A	8.13A
	Open circuit voltage U/V	37.5 V
	Short-circuit current I/A	8.68A
Temperature coefficient	Standard operating temperature (°C)	46 ± 2
	Peak power temperature coefficient (%/°C)	-0.45
	Open circuit voltage temperature coefficient (%/°C)	-0.37
	Temperature coefficient of short-circuit current (%/°C)	0.06
Operating conditions	Reverse current	Do not load an external voltage greater than the open circuit voltage
	Front maximum static load	2400 Pa
	Maximum static load on opposite side	2400 Pa

day. Research data were obtained such as photovoltaic cell temperature, photovoltaic cell surface light intensity, photovoltaic cell output voltage, and current.

For the measurement of the temperature of photovoltaic cells, the actual power generation of photovoltaic cells depends not only on the solar radiation absorbed and transmitted but also on the actual operating temperature of photovoltaic cells. When the rated temperature is increased by 1°C, the output of photovoltaic cells will be reduced by about 0.5% of the rated capacity. Therefore, it is necessary to determine the actual operating temperature of photovoltaic cells in a day. A RC-4 temperature recorder is used to measure the temperature of photovoltaic cells. In order to measure the temperature of photovoltaic cells more accurately, temperature sensors are pasted on the surface and back of photovoltaic cells.

For the measurement of light intensity on the surface of the photovoltaic cell module, a Tm-207 solar power meter was used to measure the light intensity on the surface of photovoltaic cells. Five light intensity values are quickly measured each time, which are the light intensity values of four corners and their centers of the photovoltaic panel, and then, the average value is the light intensity of the photovoltaic panel surface.

For the measurement of output voltage and current of the photovoltaic cell module, in this test, a DC voltmeter and a DC ammeter are used to measure the output voltage and current of photovoltaic cells at the same time [9].

Based on the above research scheme, the influence of different light intensities on the performance of solar cell power generation is studied.

2.3. Calculation of Incident Angle and Surface Radiation. During the outdoor operation of photovoltaic cells, with the rotation of the earth and the rotation around the sun, the solar direction on the surface of photovoltaic cells changes at all times, so it is necessary to calibrate the different positions of the sun. The angle of intersection between the sun's light and the equatorial plane is the declination angle of the sun, which is represented by ω. In the northern hemisphere of the earth, the change range of solar declination angle ω is ±23°27'. According to Cooper's equation,

$$\omega = 23.45 \sin\left[\frac{360}{365}(284 + n)\right]. \tag{3}$$

In the formula, n represents the number of days from January 1 of any year [10]. The angle between the sun's rays and the sun's rays projected on the ground is the sun's height angle, which is expressed by γ. The angle between the projection of the sun's horizontal plane and the true north direction is the sun's azimuth, which is represented by β. When the earth rotates, the sun's altitude angle and azimuth angle will change accordingly; that is, the sun's time angle λ will be considered:

$$\lambda = \nu T. \tag{4}$$

In the formula, ν represents the earth's rotation velocity $(15°/h)$ and T represents the time from noon (defined as positive in the morning and negative in the afternoon) [11]. Define ϕ as the local latitude, and calculate the solar altitude angle γ and solar azimuth angle β:

$$\gamma = \arcsin\left(\sin\phi \sin\omega + \cos\phi \cos\lambda\right), \tag{5}$$

$$\beta = \arccos\frac{\sin\gamma \sin\phi + \cos\phi \cos\phi \cos\lambda}{\cos\gamma \cos\phi}. \tag{6}$$

The solar radiation angle on the surface of photovoltaic cells is different with different tilt angles. According to the research of scholars, the radiation quantity of an inclined plane can be divided into three parts: direct solar radiation quantity, ground reflected solar radiation quantity, and scattering radiation quantity. It is assumed that the sky scattering radiation quantity is evenly distributed. According to this characteristic, many scholars also put forward different models and different calculation methods

for sky scattering. Based on the research models of various researchers, the hay model is used to calculate the radiation intensity and radiation amount on various inclines. The hay model is shown in the following formula:

$$H_S = H_z + H_f + H_t. \tag{7}$$

In the formula, H_S represents the total radiation of the inclined plane, H_z represents the direct radiation of the inclined plane, H_f represents the reflected radiation of the ground, and H_t represents the scattered radiation of the sky. The calculation formulas of the direct radiation quantity of the inclined plane, the reflection radiation quantity of the ground, and the sky scattering radiation quantity are as follows:

$$H_z = H_1 + K_1, \tag{8}$$

$$K_1 = \frac{\cos(\sigma - \psi) - \cos\omega \sin\lambda + \pi/180\omega \cdot \sin(\sigma - \psi) \cdot \sin\omega}{\cos\sigma \cos\omega \sin\lambda + \pi/180\omega \cdot \sin\sigma \sin\omega}, \tag{9}$$

$$H_f = \frac{\mu}{2} H(1 - \cos\psi), \tag{10}$$

$$H_t = H_2 \left[\frac{H_1}{H_0} K_1 + \frac{1}{2}(1 + \cos\psi)\left(1 - \frac{H_1}{H_0}\right) \right]. \tag{11}$$

In the above formula, H_1 represents the horizontal direct radiation amount, K_1 represents the ratio of the inclined plane direct radiation amount to the horizontal plane direct radiation amount, σ represents the local latitude, ψ represents the tilt angle of the battery board, μ represents the ground reflection coefficient, H represents the total horizontal radiation amount, H_2 represents the horizontal plane scattering radiation amount, and H_0 represents the total horizontal plane solar radiation amount outside the atmosphere. Different angles and different light intensities have different effects on the performance of solar cells. When the light is radiated to the photovoltaic cell material, some of the incident light is reflected or scattered on the surface, and some of it is absorbed by the photovoltaic cell. Assuming the incident light energy is G, the light energy at the distance L from the surface

$$G_0 = G \cdot \exp(-\rho L). \tag{12}$$

ρ in the formula represents the absorption coefficient of crystalline silicon in photovoltaic cells. The absorption coefficient of crystalline silicon material is larger than $10^5\,\mathrm{cm}^{-1}$. Therefore, it can absorb most of the solar energy. The light absorbed by the crystal silicon cell makes the electrons with lower energy in silicon jump to a higher energy level. When the transition takes place in the conduction band or valence band, there are no excess nonequilibrium carrier electrons or holes, only the energy is exchanged with the lattice, and finally, the light energy is converted into heat energy. Only the photon whose energy is larger than the forbidden bandwidth is absorbed; it is possible to make the electron transition from the valence band to the conduction band and produce the electron-hole pair. Therefore, the absorption of light leads to the generation of unbalanced carriers, the increase of total carrier concentration, and conductivity. The photovoltaic effect occurs in crystalline silicon solar cells. When the external circuit is turned on, the current is generated. The condition for the above reaction is that the incident light energy is larger than the bandgap width M of the crystalline silicon battery, according to the formula

$$\frac{Bv}{\xi} = Bf > M. \tag{13}$$

In the formula, B represents Planck constant, v represents light speed, ξ represents light wavelength, and f represents light frequency. Only the incident light whose wavelength is less than ξ can be absorbed by the photovoltaic cell. In conclusion, in the study of the influence of light intensity on the power generation performance of solar cells, the incident angle of light and the absorption of light by solar cells need to be considered [12].

Table 3: Output voltage and current data of maximum power point under different light intensities.

Light power (W/m^2)	Voltage (V)	Electric current (A)	Light power (W/m^2)	Voltage (V)	Electric current (A)
50	170	0.6	450	350	5.5
100	270	1.8	500	329	6.5
150	340	1.4	550	352	6.4
200	348	1.7	650	346	5.8
250	346	2.3	700	348	6.4
300	324	3.3	750	363	6.7
400	349	4.5	800	375	7.2

2.4. Qualitative Study on Power Generation Performance of Trough Solar Photovoltaic Cells

2.4.1. Light Affects the Output Characteristics of Photovoltaic Cells. Under the same temperature of different light intensities, the test output characteristics of crystalline silicon solar cells are shown in Table 3. It can be seen from the table that with the change of light intensity, the output voltage V_m and current I_A at the maximum power point of the trough solar photovoltaic cell change.

Know from Table 3 that with the increase of light intensity from $50\,W/m^2$ to $800\,W/m^2$, the maximum power point output current of the photovoltaic cell increases linearly from less than 1 A to more than 7 A. When the light intensity reaches $150\,W/m^2$, the output voltage of the maximum power point of the photovoltaic cell quickly climbs from 200 V to about 300 V. when the light intensity is greater than $200\,W/m^2$, with the increase of the light intensity, the voltage is approximately the same, and it fluctuates at about 340 V.

Based on the above data, the influence of light on the performance of solar cells is analyzed by using the determined influence factors. Under different light intensities, the total energy of light on the battery board is different. The short-

Table 4: Temperature, output voltage, and current of the photovoltaic cell.

Temperature range of photovoltaic cell	Average output voltage	Average output current
24~28	31.36	5.71
32~36	30.21	5.55
40~44	29.35	5.41
48~52	28.90	5.33
56~60	27.67	5.13

circuit current of crystalline silicon solar cells is closely related to the incident photon energy. Therefore, the quantum efficiency/collection efficiency (QE) is defined to characterize the relationship between the photocurrent and the incident light on the surface of crystalline silicon solar cells. QE is an energy function, which is usually expressed by internal quantum efficiency, that is, the ratio of the number of photogenerated carriers that contribute to the short-circuit current to the number of photons absorbed by the battery. Therefore, with the increase of light intensity, the number of effective carriers increases. When the crystalline silicon solar cell is short-circuited, the measured current is the short-circuit current.

For the short-circuit current, it can be seen from the above data that the short-circuit current of the battery increases linearly with the increase of the light intensity; for the open circuit voltage, when the temperature of the photovoltaic panel is constant, the short-circuit current of the panel increases linearly with the increase of the light intensity, and the open circuit voltage of the panel increases logarithmically. After calculation, the curve factor is between 0.71 and 0.82.

2.4.2. Temperature Affects the Output Characteristics of Photovoltaic Cells. The light intensity loading on the panel will cause its own temperature change. Therefore, the light intensity on the surface of the PV module and the corresponding output voltage and current data are analyzed under different temperatures of the PV cell. Due to the packaging of photovoltaic modules, the temperature data of the back surface of the surface muscle area of photovoltaic modules are measured, respectively, and the average value is the photovoltaic panel temperature. Then, the influence of the temperature change of the photovoltaic cell on the output voltage and current is shown in Table 4.

Through the data in Table 3, we can know the relationship between the temperature of the photovoltaic cell itself and the output voltage and current and analyze the photoelectric conversion rate of the photovoltaic cell [13]. The photoelectric conversion rate of the photovoltaic cell is the ratio of the output power of the photovoltaic cell to the total solar radiation power radiated on the surface of the photovoltaic cell:

$$\eta = \frac{P_{\text{out}}}{P_{\text{in}}}. \tag{14}$$

Table 5: Data under different light intensities.

Light intensity	Voltage	Power supply	Input light power	Output power	Conversion rate
183.2	9.60	4.64	304.24	11.99	4.09
232.8	10.5	1.98	381.05	21.29	5.63
313.7	14.6	2.70	513.34	40.25	8.06
359.8	16.40	3098	588.94	48.54	9.4
439.2	20.65	3.78	718.74	78.44	10.91
518.1	22.50	4.15	848.03	92.70	13.45
553.0	25.80	4.76	905.15	122.81	13.57
575.9	27.00	4.98	842.03	95.31	13.46
637.4	28.10	5.12	1043.31	158.45	14.56
718.6	29.25	5.46	1198.45	169.12	14.11

In the formula, P_{out} represents the output power of the cell, P_{in} represents the total solar radiation power projected on the surface of the photovoltaic cell, and η represents the photoelectric conversion rate. Because the influence of the temperature of the photovoltaic cell on its output power and conversion occurs at the same time, the two factors are analyzed together in the subsequent analysis and research.

The output voltage, output current and corresponding input light power, output power, and conversion efficiency of the PV module under the light intensity from small to large are shown in Table 5.

According to the data in Table 5, the output power of photovoltaic cells increases gradually with the increase of light intensity. When the light intensity increases to about 700, the output power tends to be saturated; when the light intensity is greater than 650, the growth rate of P_{out} is less than that of P_{in}. According to the conversion rate formula of photovoltaic cells, the photovoltaic conversion rate of photovoltaic cells will gradually decrease with the increase of light intensity [14].

Through the above research and analysis, it is concluded that the output voltage, current, and photoelectric conversion rate of solar photovoltaic cells are closely related to the light intensity and the cell temperature. For the photovoltaic cells with constant resistance load, the output voltage, current, and output power of the photovoltaic cells decrease obviously with the increase of the temperature of the photovoltaic cells, and the photoelectric conversion rate of the photovoltaic cells shows a linear downward trend.

The temperature of photovoltaic cells has a great negative impact on their power generation performance. Therefore, it is necessary to take cooling measures for photovoltaic cells [15]. For example, the installation mode of solar photovoltaic cells should try to ensure the air circulation on the upper and lower sides of the photovoltaic cells to maintain rapid heat dissipation; when the photovoltaic power station battery panels are arranged in groups, they should be arranged in staggered rows as much as possible.

3. Experimental Study

3.1. Experimental Data Simulation. In the experimental study of the influence of light intensity on the performance of solar

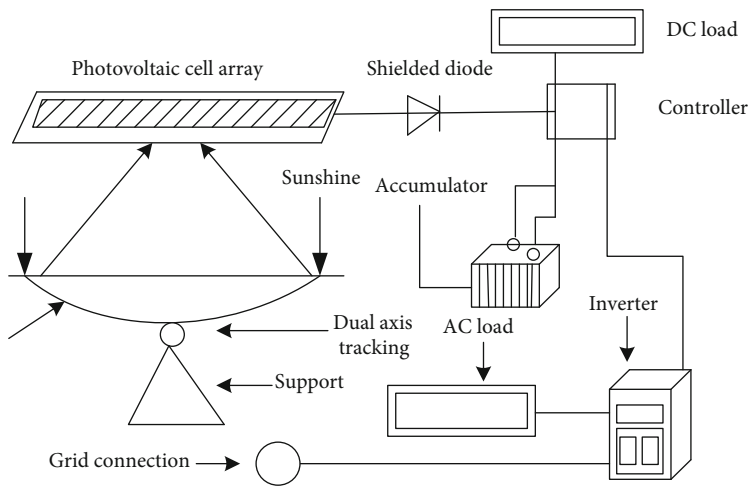

Figure 2: Trough type concentrating photovoltaic power generation system.

Figure 3: Slot collector.

energy generation of trough photovoltaic cells, the trough concentrated photovoltaic power generation system with high cost performance is used, as shown in Figure 2.

The annual total power generation and heat gain are analyzed as experimental research data, and the investment cost of research methods for the influence of different light intensities on the power generation performance of photovoltaic cells is carried out. The trough collector and concentrating photovoltaic cell used in the experiment are shown in Figure 3.

The daylighting area of the trough concentrator is $1.82\,\mathrm{m}^2$, and the volume of the heat storage tank is 80 L. The calculation formula of electric efficiency and thermal efficiency of the trough photovoltaic power generation system is as follows:

$$J_{\mathrm{el}} = \frac{P_{\max}}{W_d \cdot S_m}, \tag{15}$$

$$J_{\mathrm{th}} = \frac{l_m \cdot C_0 \cdot (T_{\mathrm{out}} - T_{\mathrm{in}})}{W_d \cdot S_m}. \tag{16}$$

In the formula, J_{el} represents the electrical efficiency, J_{th} represents the thermal efficiency, $P_{\max}$ represents the maximum output power of the battery array, S_m represents the daylighting area of the trough concentrating mirror, W_d represents the direct solar radiation, l_m represents the mass flow of cooling working fluid water, C_0 represents the specific heat capacity of cooling working fluid at constant pressure under the average temperature, T_{out} represents the outlet temperature of cooling working fluid, and T_{in} represents the inlet of cooling working fluid temperature. In the unit area, according to the light intensity, the energy generation model of the trough solar photovoltaic cell, the electrical energy, and thermal energy coefficient of the trough concentrated photovoltaic power generation system are

$$D_e = J_{\mathrm{el}} \cdot W_d. \tag{17}$$

The calculated monthly power and heat output of the trough type concentrated photovoltaic power generation system are shown in Table 6.

The difference in direct solar radiation per month has an effect on the monthly power output and heat output of solar cells. The higher the direct radiation is, the higher the light intensity is. Because of the different seasons, the light intensity of each month is different. It can be seen from the data in the table that the greater the average direct radiation in

Table 6: Monthly power and heat output of trough type concentrated photovoltaic power generation system.

Month	Monthly average direct radiation (MJ/m^2)	Electric efficiency (%)	Thermal efficiency (%)	Monthly power generation (kW·h)	Monthly heat production (MJ)
January	289.30	4.21	52.7	7.26	148.50
February	301.44	4.25	53.2	7.74	167.92
March	381.53	4.29	51.7	7.64	178.85
April	382.54	4.19	50.9	8.12	195.28
May	364.21	4.23	51.5	6.74	164.52
June	265.36	4.20	51.3	4.25	94.52
July	192.39	4.21	52.4	4.16	88.03
August	211.52	4.16	52.6	3.95	95.26
September	187.36	4.12	53.1	3.84	94.21
October	198.64	4.12	53.9	3.69	117.62
November	238.51	4.16	53.4	4.14	113.25
December	264.84	4.23	53.7	5.38	126.41

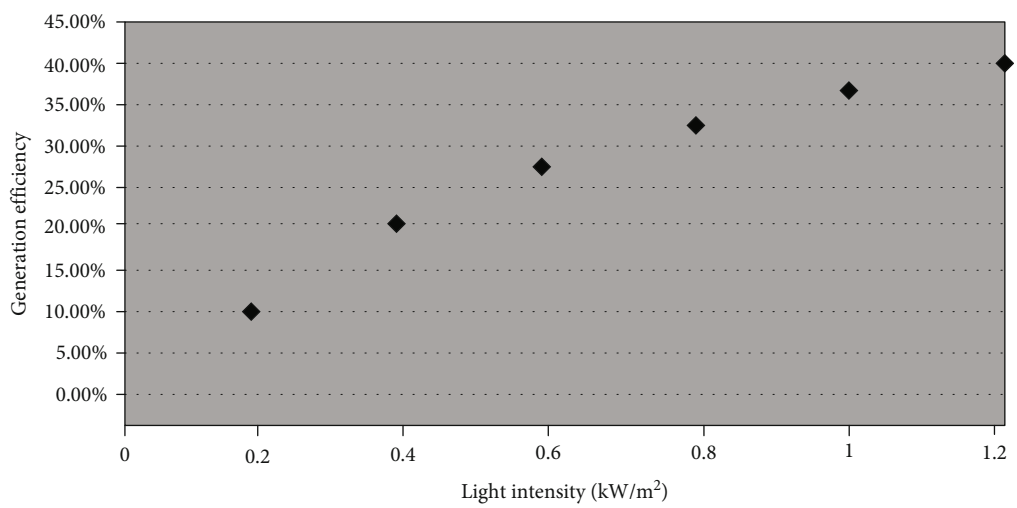

Figure 4: Power generation efficiency of photovoltaic cells.

the current month, the greater the monthly power and heat output of the trough type concentrated photovoltaic power generation system.

Set the light intensity of the six points as 0.2 kW/m^2, 0.4 kW/m^2, 0.6 kW/m^2, 0.8 kW/m^2, 1.0 kW/m^2, and 1.2 kW/m^2, the maximum output power is 20.7 W; the surface light power of the trough solar photovoltaic cell is 297.4 W, and the efficiency of the trough solar photovoltaic cell is 6.96%. Draw the experimental results into the scatter diagram as Figure 4.

Figure 4 shows the power generation efficiency of the trough solar photovoltaic cell. The maximum power generation efficiency of the trough solar photovoltaic cell is 40% when the light intensity is 1.2 kW/m^2. It can be seen that, with the gradual increase of the light intensity, the power generation efficiency of the photovoltaic cell under the research method of the influence of the light intensity designed in this paper on the power generation performance of the trough solar photovoltaic cell is also increased.

3.2. Experimental Results and Analysis of Maximum Output Power. Firstly, the random illumination model is used as the input condition to observe the change of basic parameters I_{SC} and U_{OC}. Then, set the light intensity to 1 kW/m^2, 0.8 kW/m^2, 0.6 kW/m^2, and 0.4 kW/m^2, respectively, and observe the change of the output power curve of the trough solar photovoltaic cells.

It can be seen from Figure 5(a) that the increase of light intensity has an impact on both the short-circuit current and the open circuit voltage, but it has a greater impact on the former, which is consistent with the actual situation, proving the effectiveness of the model established in this paper. As can be seen in Figure 5(b), the change of light intensity has a very obvious effect on the maximum power output of solar cells, and it shows a linear downward trend with the gradual decrease of light intensity. When the light intensity is 1 kW/m^2, the maximum output power is as high as 95 W. When the light intensity is reduced to 0.4 kW/m^2, the maximum output power is also reduced to 57 W. It can

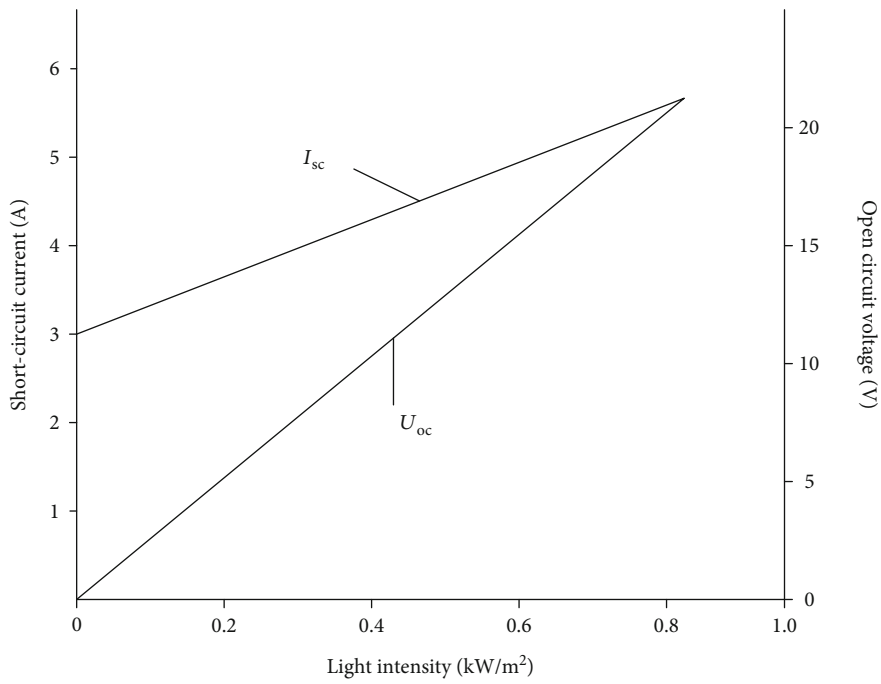

(a) Influence of different illumination on short-circuit current and open circuit voltage

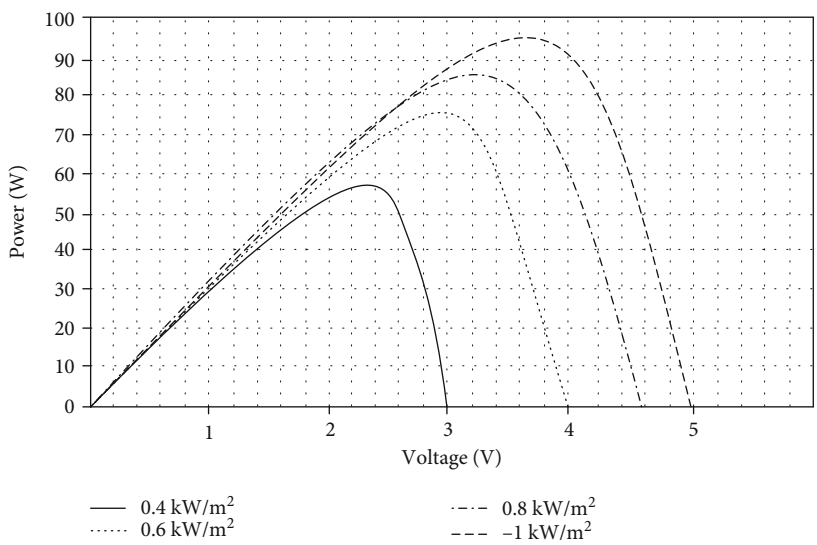

(b) The effect of specific illumination on output power

Figure 5: Effect of light intensity change on output characteristics of maximum utilization of electric energy of photovoltaic cells.

be seen that the light intensity has a certain impact on the power generation performance of trough solar photovoltaic cells, and the lower the light intensity is, the less the power generation capacity is.

4. Conclusion

This paper studies the influence of light intensity on power generation performance of trough solar photovoltaic cells. Through reasonable analysis of the electrical performance parameters of photovoltaic cells, the influencing factors are determined and targeted research and analysis are conducted. It is concluded that when the light intensity gradually increases, the open circuit voltage and short-circuit current of the trough solar photovoltaic cell gradually increase; the open circuit voltage and short-circuit current of the trough solar photovoltaic cell gradually increase. The maximum output power increases with the light intensity, large and enlarged to solve the problems of traditional research methods. With the gradual increase of light intensity, the power generation efficiency of photovoltaic cells under the research method of light intensity on the power generation performance of trough solar photovoltaic cells designed in this paper also increases. Certain help and data support are provided for follow-up research to promote the application and development of solar photovoltaic cells in the future.

Data Availability

The datasets generated during and/or analyzed during the current study are available from the corresponding authors on reasonable request.

Conflicts of Interest

The authors declare that they have no conflicts of interest.

References

[1] A. Z. Sahin, K. G. Ismaila, B. S. Yilbas, and A. Al-Sharafi, "A review on the performance of photovoltaic/thermoelectric hybrid generators," *International Journal of Energy Research*, vol. 44, no. 5, pp. 3365–3394, 2020.

[2] M. H. Ahmadi, A. Baghban, M. Sadeghzadeh et al., "Evaluation of electrical efficiency of photovoltaic thermal solar collector," *Engineering Applications of Computational Fluid Mechanics*, vol. 14, pp. 545–565, 2020.

[3] Y. Wu, Z. Wang, M. Liang et al., "Influence of nonfused cores on the photovoltaic performance of linear triphenylamine-based hole-transporting materials for perovskite solar cells," *ACS Applied Materials & Interfaces*, vol. 10, no. 21, pp. 17883–17895, 2018.

[4] Y. Lu, G. Li, Y. G. Akhlaghi et al., "Effect of grid and optimization on improving the electrical performance of compound parabolic concentrator photovoltaic cells," *Solar Energy*, vol. 196, pp. 607–615, 2020.

[5] M. Zamen, A. Baghban, S. M. Pourkiaei, and M. H. Ahmadi, "Optimization methods using artificial intelligence algorithms to estimate thermal efficiency ofPV/T system," *Energy Sci. Eng.*, vol. 7, no. 3, pp. 821–834, 2019.

[6] P. Zhang, Z. Ling, G. Chen, and B. Wei, "Influence of thermal annealing-induced molecular aggregation on film properties and photovoltaic performance of bulk heterojunction solar cells based on a squaraine dye," *Frontiers of Materials Science*, vol. 12, no. 2, pp. 139–146, 2018.

[7] C.-C. Chang, W. J. M. Kort-Kamp, J. Nogan et al., "High-temperature refractory metasurfaces for solar thermophotovoltaic energy harvesting," *Nano Letters*, vol. 18, no. 12, pp. 7665–7673, 2018.

[8] M. A. M. Ramli and H. R. E. H. Bouchekara, "Estimation of solar radiation on PV panel surface with optimum tilt angle using vortex search algorithm," *IET Renewable Power Generation*, vol. 12, no. 10, pp. 1138–1145, 2018.

[9] Y. Wang, Y. Zhang, G. Lu et al., "Reconstructing space- and energy-dependent exciton generation in solution-processed inverted organic solar cells," *ACS Applied Materials & Interfaces*, vol. 10, no. 16, pp. 13741–13747, 2018.

[10] H. R. F. Kohan, F. Lotfipour, and M. Eslami, "Numerical simulation of a photovoltaic thermoelectric hybrid power generation system," *Solar Energy*, vol. 174, pp. 537–548, 2018.

[11] S. Zandi and M. Razaghi, "Finite element simulation of perovskite solar cell: a study on efficiency improvement based on structural and material modification," *Solar Energy*, vol. 179, pp. 298–306, 2019.

[12] S. Yoon, S. H. Lee, J. C. Shin et al., "Photoreflectance study on the photovoltaic effect in InAs/GaAs quantum dot solar cell," *Current Applied Physics*, vol. 18, no. 6, pp. 667–672, 2018.

[13] O. Kaspi, A. Yosipof, and H. Senderowitz, "Pv analyzer: a decision support system for photovoltaic solar cells libraries," *Mol. Inform.*, vol. 37, no. 9-10, p. 1800067, 2018.

[14] Y. Liu, P. Cheng, T. Li et al., "Unraveling sunlight by transparent organic semiconductors toward photovoltaic and photosynthesis," *ACS Nano*, vol. 13, no. 2, pp. 1071–1077, 2019.

[15] L. R. Diaz, B. Cocilovo, A. Miles, W. Pan, P.-A. Blanche, and R. A. Norwood, "Optical and mechanical tolerances in hybrid concentrated thermal-PV solar trough," *Optics Express*, vol. 26, no. 10, pp. A602–A608, 2018.

[16] F. Yang, F. Yang, G. Wang, T. Kong, H. Wang, and C. Zhang, "Effects of water temperature on tissue depletion of florfenicol and its metabolite florfenicol amine in crucian carp (_Carassius auratus gibelio_) following multiple oral doses," *Aquaculture*, vol. 515, p. 734542, 2020.

[17] Z. Wu, Y. Liu, and X. Jia, "A novel hierarchical secret image sharing scheme with multi-group joint management," *Mathematics*, vol. 8, no. 3, p. 448, 2020.

[18] H. Cheng and Y. Liu, "An improved RSU-based authentication scheme for VANET," *Journal Internet Technology*, vol. 21, pp. 1137–1150, 2020.

[19] N. Gao, B. Cheng, H. Hou, and R. Zhang, "Mesophase pitch based carbon foams as sound absorbers," *Materials Letters*, vol. 212, pp. 243–246, 2018.

[20] N.-S. Gao, X.-Y. Guo, B.-Z. Cheng, Y.-N. Zhang, Z.-Y. Wei, and H. Hou, "Elastic wave modulation in hollow metamaterial beam with acoustic black hole," *IEEE Access.*, vol. 7, pp. 124141–124146, 2019.

Hindawi
International Journal of Photoenergy
Volume 2020, Article ID 6644796, 15 pages
https://doi.org/10.1155/2020/6644796

Research Article

Investigation of the Soan River Water Quality Using Multivariate Statistical Approach

Zakaullah and Naeem Ejaz

Department of Civil Engineering, University of Engineering and Technology, Taxila, Pakistan

Correspondence should be addressed to Zakaullah; engrzaka@gmail.com

Received 7 November 2020; Revised 23 November 2020; Accepted 3 December 2020; Published 21 December 2020

Academic Editor: Hafiz Muhammad Ali

Copyright © 2020 Zakaullah and Naeem Ejaz. This is an open access article distributed under the Creative Commons Attribution License, which permits unrestricted use, distribution, and reproduction in any medium, provided the original work is properly cited.

Evaluating the quality of river water is a critical process due to pollution and variations of natural or anthropogenic origin. For the Soan River (Pakistan), seven sampling sites were selected in the urban area of Rawalpindi/Islamabad, and 18 major chemical parameters were examined over two seasons, i.e., premonsoon and postmonsoon 2019. Multivariate statistical approaches such as the Spearman correlation coefficient, cluster analysis (CA), and principal component analysis (PCA) were used to evaluate the water quality of the Soan River based on temporal and spatial patterns. Analytical results obtained by PCA show that 92.46% of the total variation in the premonsoon season and 93.11% in the postmonsoon season were observed by only two loading factors in both seasons. The PCA and CA made it possible to extract and recognize the origins of the factors responsible for water quality variations during the year 2019. The sampling stations were grouped into specific clusters on the basis of the spatiotemporal pattern of water quality data. The parameters dissolved oxygen (DO), biochemical oxygen demand (BOD), chemical oxygen demand (COD), turbidity, and total suspended solids (TSS) are among the prominent contributing variations in water quality, indicating that the water quality of the Soan River deteriorates gradually as it passes through the urban areas, receiving domestic and industrial wastewater from the outfalls. This study indicates that the adopted methodology can be utilized effectively for effective river water quality management.

1. Introduction

Rivers convey water and minerals to territories all around the earth. They have a significant influence on the hydrological cycle and serve as drainage outlets for runoff. Unsafe drinking water and inadequate sanitary conditions are associated with infectious diseases such as cholera, diarrhea, dysentery, and polio which significantly affect human health. According to the World Health Organization (WHO), at least two billion people worldwide use drinking water from a contaminated source containing human excreta [1]. In the last decades, research has revealed that developing countries have been able to control waterborne diseases to some extent through the development of sustainable natural resources, especially water resources, out of concern for the improvement of public health. However, challenges to achieving this workable goal remain, due to the increase in demand for water and the reduction of water availability resulting from escalating population growth and increased financial stability [2].

Many developing and developed countries are facing degradation of freshwater resources over the last decades up to an alarming situation mainly due to rapid regional development especially in underdeveloped countries and agricultural runoff from fields containing fertilizers and pesticides [3, 4]. The use of agricultural chemical manures and municipal water influence the water quality significantly [5, 6].

As the quality of water is important for human health and ecological systems, its deteriorating quality in developing countries has caused detrimental health impacts such as diarrhea, poor oral hygiene, hepatitis, anemia, and dental caries [7]. Research has revealed that the quality of existing water resources has been deteriorating rapidly with ever increasing urbanization, massive industrialization, agricultural expansion, inadequate management of domestic, industrial and

urban wastes, eroded soil, and transportation infrastructures in recent decades [8–10].

Giri and Singh [11] reported that the escalation of urbanization and industrial development near water tributaries has led to river degradation, water effluence, and disintegration of natural ecological integrity. In most developing countries, the massive contamination of tributaries due to the point source pollution containing harmful chemicals is a major issue and has been widely observed [12, 13]. The utilization of water has been escalating at more than double the increase in population in the recent era. Globally, approximately six billion people are impounding 54% of all the open freshwater contained in streams, lakes, and natural springs [14].

Waterways play a significant role in incorporating and arranging the landscape and in influencing the environmental condition. They are the prime variables in controlling the global water cycle and behave as active elements which carry nutrients and contaminants. In Pakistan, the increasing pace of urbanization and industrialization has caused the severe decline of flora and fauna in the river basin due to the mismanagement of water reservoirs. In particular, untreated sewage, agricultural runoff, and industrial effluents have resulted in a considerable deterioration in water quality. The population residing near rivers has to use this water for many purposes including domestic uses and drinking. Similarly, the quality of surface water is declining due to human development, industrialization, agricultural inputs, transportation, urbanization, animal and human excretions, and domestic waste. Variation in the quality and amount of stream water as a result of characteristic and anthropogenic impacts is generally observed in different waterways throughout the world [15].

Water quality assessment is the most widely accepted way forward for identification of biological issues pertaining to river environment, and fluctuations in the environmental key indicators due to seasonal and time variation are quite helpful for analysis of the contamination level [16].

According to a report published by the Asia Foundation [17], almost 95% of the water in Pakistan is utilized for agronomic practices, which compensate 60% of its population engaged in agriculture and livestock, while 80% of the exports depend upon agribusiness. Despite the fact that Pakistan has the world's largest glaciers, it is nevertheless counted among the world's 36 most water-stressed countries. Due to an escalation in population growth as well as to strained relations with the neighboring country concerning transboundary issues of water management, the water situation in the country has become critical, both with respect to its impending waterfront and sustainability, as the demand for water is expected to exceed supply.

The release of sewage water into the water bodies is the primary source of water pollution whereas the secondary source of contamination is the discharge of toxic chemicals from industrial effluents and agricultural nonpoint sources into the water bodies [18]. Low dissolved oxygen problem in the River Ravi (Pakistan) was identified by [19, 20] due to discharge of very high biochemical oxygen demand (BOD) loadings from several wastewater outfalls and surface drains. They also identified concentrations of unionized ammonia (NH_3) higher than its permissible toxicity levels. Fecal coliforms were also found higher than the recreational and irrigation water quality standards [21]. In particular, in low flow conditions, the water quality of the river does not meet the desired standards for any of its beneficial uses, including fishery, irrigation, recreation, and drinking.

The people frequently suffer from waterborne diseases because of using contaminated drinking water. About 30% of all reported diseases and 40% of deaths in the Pakistan are attributed to fecal contamination of drinking waters [22]. In Pakistan, the main causes of waterborne diseases are contaminated drinking water, lack of sanitary facilities at treatment plants, and release of industrial effluents and domestic sewage into the water bodies [23].

The PCA approach was successfully utilized to interpret a large and complex data matrix for the investigation of water quality of the Açude da Macela reservoir for consumption of the local community and agriculture purposes [24]. Different multivariate integrated techniques were applied to classify the various sampling sites according to spatial and temporal characteristics for the investigation of water quality of Qiandao Lake in China. The results obtained from this study reveal that CA, discriminant analysis (DA), and PCA are valuable tools for water resource management [25].

The Soan River is among those waterways where housing developments have been established along the banks. According to [26] about 5.5 million residents of Rawalpindi/Islamabad discharge municipal sewage into the Soan River. Due to encroachment along the riverbanks, the ecosystem and surface runoff have drastically affected the pollution levels of the river. Due to the inadequate drainage of wastewater into the river, an excessive increase of heavy metals and nutrients in river water above the national standards has been observed [26].

The aim of this study was to investigate the possible major pollution sources affecting water quality in the urban area of the Soan River by using multivariate statistical approaches through Pearson's correlation, CA, and PCA with the objective of providing support for environmental executives in order to enable them to make better decisions regarding action plans.

2. Materials and Methods

2.1. Description of Study Area. The Soan River is a minor tributary of the Indus River. The origin of the Soan River is the southwestern range of the Murree hills, which are located at longitude $71^\circ 45'$ to $73^\circ 35'$E and latitude $32^\circ 45'$ to $33^\circ 55'$N and passes through the Rawalpindi, Attock, and Jehlum districts of Punjab (Pakistan). The total length of the Soan River is 272 km, and it drains a total catchment area of 11,085 km^2. Nallah Lai, a drainage channel which originates from the area of the Margalla hills, ultimately falls into this river by draining wastewater into the river near the Soan bus bay. This river provides its water to the Simly Dam which is located in Islamabad and is the largest drinking water reservoir for the Islamabad Capital Territory and its adjacent areas. Agricultural lands are also located along the river, and the use of herbicides and insecticides is common in these farming areas

[27]. The main sources of water in the Soan River basin are precipitation, streamflow, and snow melting found in the Murree region. However, this basin is water deficient, as most of the area is covered and underlain by the rocks of tertiary age. The Ling stream from Lithar and Kahuta joins the Soan River near Sihala before Kaak bridge. The Kaak bridge was constructed over this river at the Islamabad Highway. Furthermore, two more streams near this bridge join the Soan River. One stream is the Korang River, and the other is the Lei stream. After following about 16 km distance upstream of Kalabagh in the southwest direction, the Soan River joins the Indus River [27, 28].

The mean temperature of the river ranges from a minimum of 3°C in winter to a maximum of 45°C in summer. In summer, the river flow decreases, whereas in the monsoon season (July-September), heavy rain results in flash flooding, which causes increased runoff. The river passing through residential societies is contaminated by the dumping sites of the surrounding area. Furthermore, construction waste is also poured into the river and has been since the formation of private housing societies nearby. There are also some industries constructed along the left bank of the river, and these directly pour their effluents into the river without any treatment [29]. This surface water also recharges the ground water aquifer of the region. The average annual rainfall in the study area varies from 250 to 1800 mm from north to southwest. The maximum rainfall occurs during July-September, whereas the minimum takes place in the months of November-December [30].

2.2. Sample Collection and Chemical Analysis. The most critical and polluted urban reach of the Soan River from downstream of Simly Dam (Chakian Bridge) Islamabad to the Bahria Town Phase-VIII Rawalpindi was identified by reconnaissance survey, and seven sampling sites were selected according to natural conditions and industrial zone as well as human activities along the river banks. The water samples were collected for two seasons (premonsoon in the month of May 2019 and postmonsoon in the month of November 2019) from a depth of 0.3 m in clean and sterilized plastic sample bottles of 1.5 L. The water samples collected from the field were placed in an insulated cool box and transported as soon as possible to the PCRWR Water Quality Lab Islamabad and stored at 4°C until they were analyzed [31]. The water quality parameters, their units, and methods of analysis are described in Table 1. The locations of selected sites as shown in Figure 1 were recorded (latitudinal and longitudinal position) using a handheld GPS (Global Positioning System) unit.

2.3. Pearson Correlation Matrix. Pearson correlation matrix is widely employed to evaluate the relationship between the variables of any data set. If the correlation coefficient exists between 1 and -1; it indicates that the strongest relationship may be positive or negative between two parameters, and if it is zero, there will be no correlation between them at a significant level of $p < 0.05$ (Kumar et al., 2006). Pearson's correlation matrix measures the strength, direction, and probability of the linear association between two interval or ratio variables.

2.4. Cluster Analysis (CA). CA enables the researcher to arrange the water samples into groups resulting in high interval homogeneity (within clusters) and high external heterogeneity (between clusters). In CA, a tree-like diagram known as a dendrogram is created, and it summarizes the clusters by significantly decreasing the dimensions of the primary dataset. Euclidean distance is widely used to evaluate the sampling stations which can be characterized by the discrepancy present in the statistical analysis of the data.

The CA approach through the Ward linkage method was used collectively for clustering to classify the samples for investigation of water quality characteristics of the Mahitsy Commune, Central Highland of Madagascar [32]

2.5. Principal Component Analysis (PCA). PCA is a dimension reduction analytical method which reduces a large number of variables into a lower number of factors. It is normally used for data formation and for attaining qualitative inductive data about possible contamination causes. An eigenvalue in the PCA approach shows the significance of any factor, and the factors having higher eigenvalues greater than 1 or equal to 1 are considered the most significant factors as endorsed by [33]. A scree plot is a diagram in the PCA multivariate technique whose Y-axis represents the eigenvalues and whose X-axis shows the number of factors. The point where the gradient of the curve clearly levels off (the elbow) shows the number of factors to be created by the data analysis.

According to the literature review, the PCA has been widely used to determine latent contamination causes, without changing the original characteristics of the variables and by reducing the dimensions of data with negligible loss of primary data and by grouping multiple variables with respect to their geography [8, 34–36].

3. Results and Discussion

3.1. Data Processing and Statistical Analyses of Water Quality Parameters. To evaluate the collected river water quality dataset consistently at different sampling stations, multivariate statistical techniques were employed through Pearson's correlation, CA, and PCA. All statistical computations in the present study were rendered using Microsoft Excel 2016 and IBM SPSS 22.

The statistical description of mean value, range, and standard deviation of selected water quality parameters at seven stations of the Soan River collected during premonsoon and postmonsoon seasons (2019) are provided in Table 2.

The values of measured parameters EC, pH, alkalinity as $CaCO_3$, HCO_3, Ca, Cl^-, hardness, Mg, Na, K, SO_4, NO_3, and TDS are generally within the recommended range at all stations during both seasons, but there is significant change of measured values of DO, BOD, COD, and turbidity.

Lower concentration of DO was observed during both seasons at stations S-4 to S-7 at downstream as compared to upstream stations S-1 and S-2 due to large amounts of organic waste originating from domestic waste and industrial waste water entering into the Soan River containing plenty of biodegradable material causing increase in oxygen demand, and DO is depleted steadily. Lower concentration of DO

Table 1: Water quality parameters, abbreviations, units, and analytical methods used for analysis.

Sr. no.	Parameters	Units	Analysis method
1	pH	pH unit	pH meter, Hanna Instruments, model 8519, Italy
2	Electrical conductivity (EC)	μS/cm	EC meter, Hach-44600-00, USA
3	Turbidity (Turb.)	NTU	Turbidity meter, LaMotte, model 2008, USA
4	Alkalinity as $CaCO_3$	ppm	2320 standard method (1992)
5	Bicarbonates (HCO_3)	ppm	2320 standard method (1992)
6	Calcium (Ca)	ppm	3500 Ca-D standard method (1992)
7	Chloride (Cl^-)	ppm	Titration assembly argentometric method APHA (1998)
8	Hardness (hard.)	ppm	EDTA titration, standard method (2012)
9	Magnesium (Mg)	ppm	Flame photometer
10	Potassium (K)	ppm	Flame photometer
11	Sodium (Na)	ppm	Flame photometer
12	Sulphate (SO_4)	ppm	Spectrophotometric
13	Nitrate (NO_3)	ppm	Spectrophotometric
14	Total dissolved solids (TDS)	ppm	2540C, standard method (2012)
15	Biological oxygen demand (BOD)	ppm	Manometric pressure measurement method by Lovibond BOD system
16	Chemical oxygen demand (COD)	ppm	Lovibond COD reactor and photometer
17	Dissolved oxygen (DO)	ppm	DO meter method, model Jenway 970
18	Total suspended solids (TSS)	ppm	Oven dry method

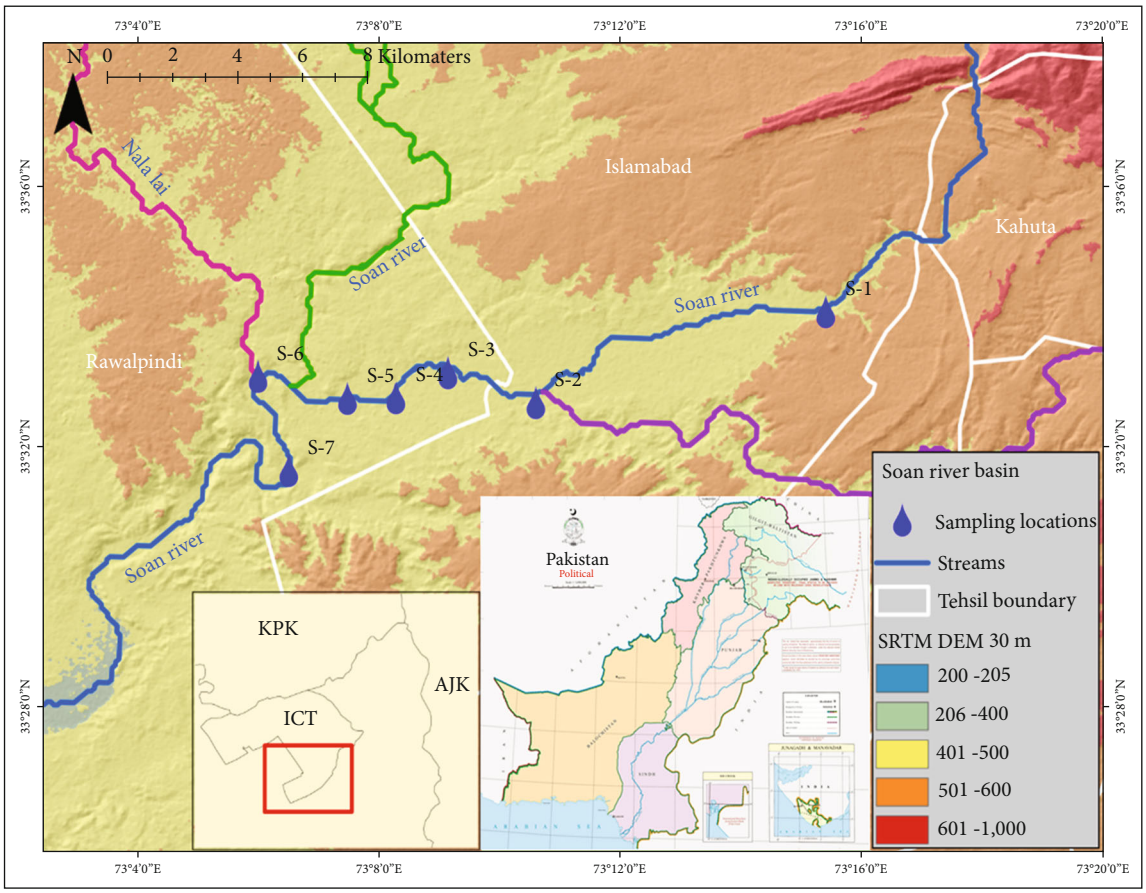

Figure 1: Map of the study area showing water quality monitoring stations.

Table 2: Statistical analysis of water quality parameters of the Soan River (premonsoon and postmonsoon seasons 2019).

	Stations	EC	pH	Turbidity	Alkalinity	HCO_3	Ca	Cl	Hard.	Mg	K	Na	SO_4	NO_3	TDS	DO	BOD	COD	TSS
Premonsoon season	S-1	426	8.3	2.7	1.80	180	40	24	170	17	2.1	36	25	0.4	234	5.7	10	16	10
	S-2	541	7.55	6.8	2.00	200	44	36	170	15	6.3	50	30	1.7	325	5.5	15	25	20
	S-3	576	7.52	2.9	2.20	220	32	36	180	24	7.0	55	35	4.7	317	5.3	20	32	10
	S-4	754	6.65	63	3.00	300	40	18	200	24	8.2	90	40	12	415	2.1	87	420	142
	S-5	799	6.97	6.7	3.30	330	40	48	240	34	8.1	88	45	1.7	439	3.4	55	185	20
	S-6	1109	7.52	18	4.50	450	60	60	370	53	17.0	78	65	2.8	665	3.5	50	118	60
	S-7	1329	7.64	15.1	4.70	550	55	72	470	78	21.0	90	90	3.2	797	3.9	58	133	50
	Mini-	426.00	6.65	2.70	1.80	180.00	32.00	18.00	170.00	15.00	2.10	36.00	25.00	0.40	234.00	2.10	10.00	16.00	10.00
	Maxi-	1329.00	8.30	63.00	4.70	550.00	60.00	72.00	470.00	78.00	21.00	90.00	90.00	4.70	797.00	5.70	87.00	420.00	142.00
	Mean	790.57	7.45	16.46	3.07	318.57	44.43	42.00	257.14	35.00	9.96	69.57	47.14	3.79	456.00	4.20	42.14	132.71	44.57
	Std. deviation	325.05	0.52	21.34	1.17	138.01	9.73	19.29	117.43	22.88	6.61	22.24	22.89	3.87	203.18	1.34	28.14	141.92	47.18
	PSQCA/NEQS standards	NGVS	6.5-8.5	<5	NGVS	NGVS	NGVS	250	500	NGVS	NGVS	NGVS	NGVS	10	1000	5	80	150	200
Postmonsoon season	S-1	371	7.6	105	1.30	130	28	14	132	15	3.2	23	26	2.7	204	4.5	80	142	270
	S-2	403	7.3	82	1.22	122	28	22	140	17	4.8	25	34	3.7	222	4.2	102	190	210
	S-3	415	7.18	75	1.30	130	40	19	140	10	4.6	32	32	4.5	228	3.7	90	163	225
	S-4	445	7.01	67	1.40	140	40	26	150	12	5.3	35	34	6.1	245	3.5	95	170	190
	S-5	872	6.9	58	2.80	280	60	77	270	29	10.0	63	37	2.1	480	2.3	110	300	170
	S-6	1342	6.77	25	4.30	430	116	89	400	27	26.0	100	72	17	738	1.7	123	381	82
	S-7	550	6.85	45	1.80	180	44	29	190	19	6.8	37	32	8.2	303	3.3	97	177	130
	Mini-	371	6.77	25	1.20	122	28	14	132	10	3.2	23	26	2.1	204	1.7	80	142	82
	Maxi-	1342	7.6	105	4.30	430	116	89	400	29	26	100	72	17	738	4.5	123	381	270
	Mean	628.29	7.09	65.29	2.02	201.71	50.86	39.43	203.14	18.43	8.67	45.00	38.14	6.33	345.71	3.31	99.57	217.57	182.43
	Std. deviation	358.46	0.29	25.95	1.15	114.86	30.70	30.35	99.38	7.21	7.94	27.59	15.30	5.14	197.12	1.00	13.94	88.3	62.30
	PSQCA/NEQS standards	NGVS	6.5-8.5	<5	NGVS	NGVS	NGVS	250	500	NGVS	NGVS	NGVS	NGVS	10	1000	5.00	80	150	200

NGVS: no guideline value set; NEQS: National Environmental Quality Standards; PSQCA: Pakistan Standards and Quality Control Authority.

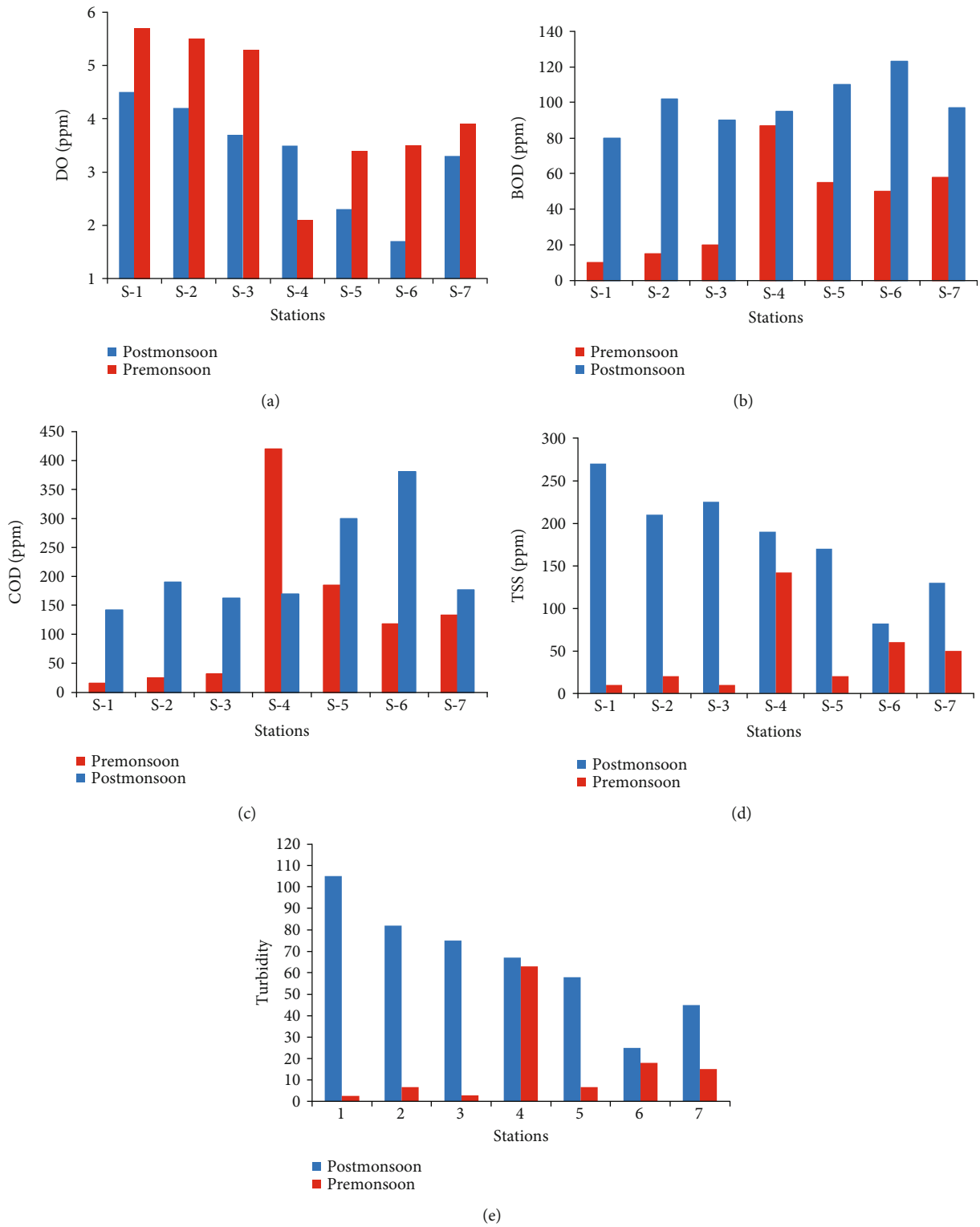

Figure 2: (a–e) Comparison between premonsoon and postmonsoon water quality variations in the Soan River: (a) dissolved oxygen (DO), (b) biochemical oxygen demand (BOD), (c) chemical oxygen demand (COD), (d) total suspended solids (TSS), and (e) turbidity.

shows river pollution. Figure 2(a) shows that the impact of the wastewater discharge on DO sag is extended to the subsequent stations, i.e., S-6 and S-7. Also, from Figure 2(a), it is evident that DO concentration is higher in the month of May (i.e. premonsoon) due to the impact of early rainfall events during these months, while the DO levels are low, with an exception of S-4, in postmonsoon samples due to dry weather flow conditions that prevail right after the monsoon

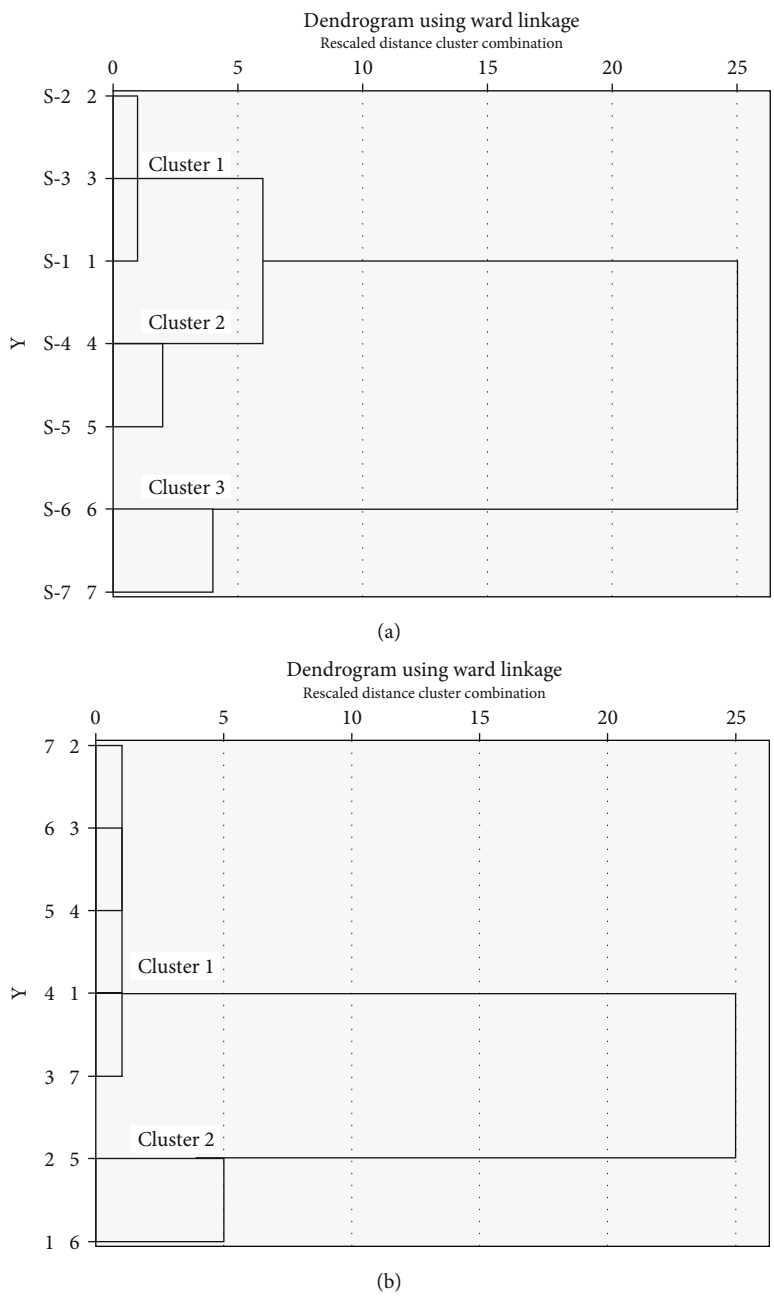

Figure 3: (a) Dendrogram of cluster analysis for sampling stations according to surface water quality parameters of the Soan River (premonsoon). (b) Dendrogram of cluster analysis for sampling stations according to surface water quality parameters of the Soan River (postmonsoon).

in the study area. Figure 2(b) manifest higher BOD values observed against the lower values of DO at downstream stations due to industrial and populated accommodations. Low concentration level of BOD indicates that the river water is free from biological pollution [37] whereas high BOD is harmful for aquatic life as it deteriorates the DO level [38]. Observed COD concentrations show a similar pattern. High COD value (i.e., 2 times of BOD) at S-5 directs towards the possibility of industrial wastewater discharge that contains nonbiodegradable organics [39]. TSS and turbidity levels are fairly correlated in Figures 2(d) and 2(e), and their higher values in postmonsoon samples manifest the presence of urban and agricultural runoffs with higher sediment loads.

3.2. Spatiotemporal Variance of Water Quality Parameters by Cluster Analysis (CA). According to Ashfaq et al. [30], there are high spatial and temporal variations of rainfall in the Soan Basin containing about 70% rainfall during the monsoon season (July to September) and the remaining 30% falls in spring and winter seasons. The hierarchical CA technique was used for the assessment of similarity among the sampling sites. A dendrogram was plotted based upon the chemical

Table 3: Pearson's correlation matrix (premonsoon).

	EC	pH	Turbidity	Alkalinity	HCO_3	Ca	Cl^-	Hard.	Mg	K	Na	SO_4	NO_3	TDS	DO	BOD	COD	TSS
EC	1																	
pH	-0.196	1																
Turbidity	0.200	-0.69	1															
Alkalinity	0.984**	-0.241	0.227	1														
HCO_3	0.998**	-0.17	0.187	0.985**	1													
Ca	0.752	0.163	-0.02	0.637	0.761*	1												
Cl^-	0.855*	0.115	-0.32	0.826*	0.853*	0.706	1											
Hard.	0.972**	0.038	0.032	0.942**	0.977**	0.821*	0.901**	1										
Mg	0.968**	0.009	0.019	0.932**	0.974**	0.846*	0.900**	0.992**	1									
K	0.982**	-0.114	0.137	0.950**	0.970**	0.760*	0.877**	0.969**	0.959**	1								
Na	0.769*	-0.747	0.564	0.794*	0.764*	0.415	0.464	0.611	0.636	0.673	1							
SO_4	0.985**	-0.073	0.100	0.945**	0.985**	0.844*	0.883**	0.989**	0.993**	0.979**	0.686	1						
NO_3	0.081	-0.721	0.921**	0.085	0.058	-0.07	-0.395	-0.097	-0.073	0.049	0.484	0.005	1					
TDS	0.997**	-0.143	0.166	0.976**	0.992**	0.764*	0.871*	0.980**	0.970**	0.990**	0.723	0.987**	0.04	1				
DO	-0.544	0.816*	-0.808*	-0.612	-0.542	-0.11	-0.11	-0.36	-0.363	-0.43	-0.903**	-0.421	-0.69	-0.493	1			
BOD	0.597	-0.792*	0.821*	0.636	0.595	0.257	0.151	0.421	0.435	0.489	0.926**	0.496	0.719	0.547	-0.984**	1		
COD	0.276	-0.835*	0.927**	0.322	0.275	0.001	-0.21	0.084	0.097	0.161	0.750	0.166	0.848*	0.222	-0.929**	0.933**	1	
TSS	0.328	-0.662	0.989**	0.357	0.315	0.06	-0.20	0.168	0.148	0.271	0.623	0.227	0.886**	0.299	-0.841*	0.854*	0.912**	1

*Correlation is significant at the 0.05 level (2-tailed). **Correlation is significant at the 0.01 level (2-tailed).

Table 4: Pearson's correlation matrix (postmonsoon).

	EC	pH	Turbidity	Alkalinity	HCO_3	Ca	Cl	Hard.	Mg	K	Na	SO_4	NO_3	TDS	DO	BOD	COD	TSS
EC	1																	
pH	-0.697	1																
Turbidity	-0.812*	0.957**	1															
Alkalinity	0.999**	-0.681	-0.800*	1														
HCO_3	0.999**	-0.681	-0.800*	1.000**	1													
Ca	0.978**	-0.695	-0.830*	0.976**	0.976**	1												
Cl	0.960**	-0.710	-0.758*	0.956**	0.956**	0.893**	1											
Hard.	0.999**	-0.707	-0.823*	0.999**	0.999**	0.976**	0.957**	1										
Mg	0.828*	-0.567	-0.612	0.832*	0.832*	0.696	0.904**	0.836*	1									
K	0.972**	-0.648	-0.806*	0.969**	0.969**	0.990**	0.874*	0.970**	0.704	1								
Na	0.995**	-0.720	-0.823*	0.992**	0.992**	0.986**	0.954**	0.992**	0.784*	0.971**	1							
SO_4	0.927**	-0.611	-0.776*	0.917**	0.917**	0.965**	0.812*	0.921**	0.605	0.985**	0.933**	1						
NO_3	0.759*	-0.621	-0.803*	0.756*	0.756*	0.854*	0.565	0.765*	0.364	0.873*	0.769*	0.893**	1					
TDS	1.00**	-0.697	-0.812*	0.999**	0.999**	0.978**	0.960**	0.999**	0.828*	0.972**	0.995**	0.926**	0.759*	1				
DO	-0.938**	0.866*	0.890**	-0.931**	-0.931**	-0.911**	-0.955**	-0.938**	-0.794*	-0.868*	-0.951**	-0.812*	-0.659	-0.938**	1			
BOD	0.895**	-0.769*	-0.832*	0.874*	0.874*	0.851*	0.903**	0.894**	0.802*	0.868*	0.888**	0.861*	0.661	0.895**	-0.884**	1		
COD	0.978**	-0.667	-0.758*	0.970**	0.970**	0.930**	0.980**	0.974**	0.867*	0.931**	0.970**	0.894**	0.652	0.978**	-0.925**	0.940**	1	
TSS	-0.820*	0.920**	0.986**	-0.810*	-0.810*	-0.825*	-0.756*	-0.834*	-0.657	-0.823*	-0.818*	-0.793*	-0.825*	-0.820*	-0.852*	-0.768*	0.860*	1

*Correlation is significant at the 0.05 level (2-tailed); **Correlation is significant at the 0.01 level (2-tailed).

analysis of all selected sites that grouped these sites into three and two clusters during premonsoon and postmonsoon seasons, respectively, as shown in Figures 3(a) and 3(b).

In the premonsoon season, Cluster 1 contains the stations S-1, S-2, and S-3. The primary land uses around these stations include agriculture and newly developed neighborhoods with less number of residents. Therefore, the pollution levels were found to be lower than in the other stations; it is also evident from high DO levels for these stations in Figure 3(a). Cluster 2 comprises S-4 and S-5 that passes through the developed part of the city receiving large volumes of domestic and industrial wastewaters. High pollution levels during the premonsoon, with high BOD, COD, and low DO levels, can also be seen in Figure 2. The land use is the same in the catchment area of these two stations. Other sources of contamination to this part of the river (S-4 and S-5) are open dumping of solid waste from slaughterhouses and some low-income residential neighborhoods without having a proper solid waste collection and disposal mechanism. Cluster 3 consists of two highly polluted stations at the downstream of the river, i.e., S-6 and S-7. There are two main reasons of such as high pollution (also see Figure 3) at these stations in the premonsoon monitoring: (i) at S-6, the river water is completely mixed with the industrial wastewater discharge from S-5—the meandering river morphology between S-5 and S-6 justifies this mixing length during relatively higher velocities in premonsoon period; (ii) S-6 is the confluence point of Nallah Lai that discharges large volumes of untreated municipal wastewater from Rawalpindi city into the Soan River; and (iii) continuing meandered river morphology covers a mixing length and shows high pollution levels at S-7.

In the postmonsoon period, the river primarily behaves like a sewage drain flowing at very low velocity. Therefore, only two clusters are formed for this monitoring survey, and the cluster configuration differs due to the low flow regime in the river. Cluster 1 contains five stations, i.e., S-1, S-2, S-3, S-4, and S-7. The primary reason for having these stations in a single cluster is the similar DO and COD values obtained at these stations (see Figures 2(a) and 2(c)). Relatively higher DO levels at S-4 and S-7 (i.e., >3 ppm) can be attributed to the sampling errors as the samples were obtained from the river bank, where complete mixing of the wastewater could not have been achieved yet. Cluster 2 contains S-5 add S-6 that shares the similar characteristics as already discussed above. The primary reason for having different clusters is the changing flow pattern in both the seasons that resulted in velocity variations, changing mixing lengths, and absence of nonpoint sources during the postmonsoon period.

The results reveal that the CA technique is a useful approach for the classification of river water at temporal and spatial scales. Therefore, the selection of critical sampling points and the respective costs incurred on future monitoring strategies should be minimized.

3.3. Pearson's Correlation Matrix. Pearson's correlation matrix was prepared, and the correlation coefficient (r) was applied to check the possible relationship among the chemical parameters of the water quality for the Soan River. According to guidelines established by Cohen [40], there is a strong correlation if the value of the Pearson coefficient (r) is $0.75 \leq r < 1$. Several significant positive strong correlations and few negative correlations were found among some of the parameters which are presented in Tables 3 and 4.

In the premonsoon season, results revealed that most of the parameters show a significant positive correlation, as given below in Table 3:

(i) EC with alkalinity, HCO_3, hardness, Mg, K, SO_4, and TDS ($r > 0.9$)

(ii) Turbidity with NO_3, COD, and TSS ($r > 0.9$)

(iii) Alkalinity with HCO_3, hardness, Mg, K, SO_4, and TDS ($r > 0.9$)

(iv) HCO_3 with hardness, Mg, K, SO_4, and TDS ($r > 0.9$)

(v) Cl^- with hardness, Mg, K, and SO_4 ($r > 0.9$)

(vi) K and Mg with SO_4 and TDS ($r > 0.9$)

(vii) TSS with NO_3 ($r > 0.9$)

(viii) SO_4 with TDS ($r > 0.9$)

(ix) BOD with COD ($r > 0.9$)

Alkalinity in water exists due to the presence of bicarbonate (HCO_3^-), carbonate (CO_3^-), and hydroxide (OH^-) of elements such as Ca, Mg, Na, K, and NH_3 while hardness is primarily associated with the presence of carbonates and bicarbonates of Ca and Mg. TDS commonly contains inorganic salts having cations (Ca, Mg, K, and Na) and anions (CO_3, HCO_3, Cl, and SO_4). Therefore, TDS are highly correlated with alkalinity, hardness, cations, and anions. EC is essentially a measure of TDS and so was found highly correlated with all these parameters with an R value higher than 0.9. Similarly, turbidity is a measure of TSS. In raw wastewater, COD contains both the soluble and particulate forms of organic matter. Therefore, turbidity was found to be highly correlated with TSS and COD. NO_3 values are very small (i.e., 3.8 ppm in Table 1) in untreated wastewater due to the absence of nitrification process. So, the main reason of this correlation is the similar trend of the NO_3 values as of TSS, turbidity, and COD. COD was found highly correlated with the BOD and can be used as a monitoring parameter to avoid the long 5-day BOD test. All the other high correlations found reflect the relationships between alkalinity, hardness, TDS, cations, and anions that have already been described above. TDS and EC are quick tests and can be used to monitor the rest of the parameters using regression equations; the correlation relationship was detected as a strong negative between Na and DO, and DO with COD and BOD ($r > -0.9$). The former makes clear sense as there is essentially no relationship between Na and DO in the river water. DO should have a strong correlation with BOD; the reason for not obtaining a strong correlation between these parameters can be attributed to limited data and sampling errors. No significant correlation of pH was observed with any element in the river water, while there is a slightly negative correlation with other

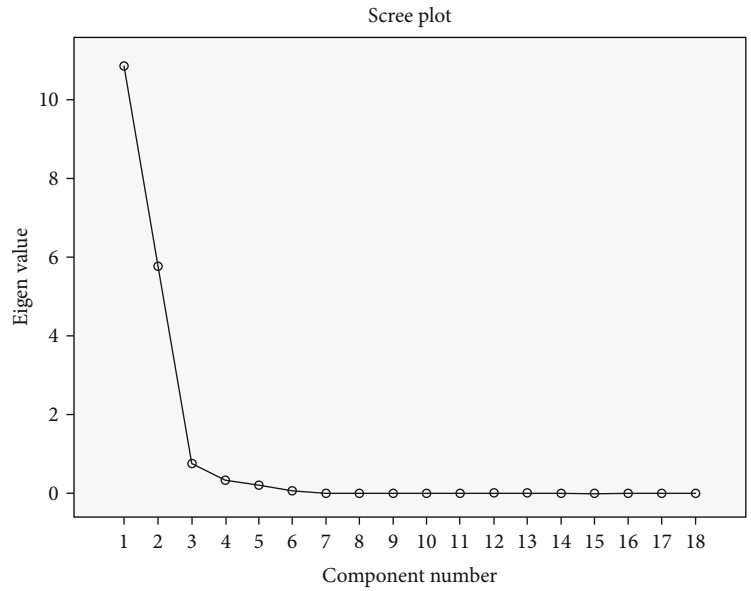

(a) Premonsoon season

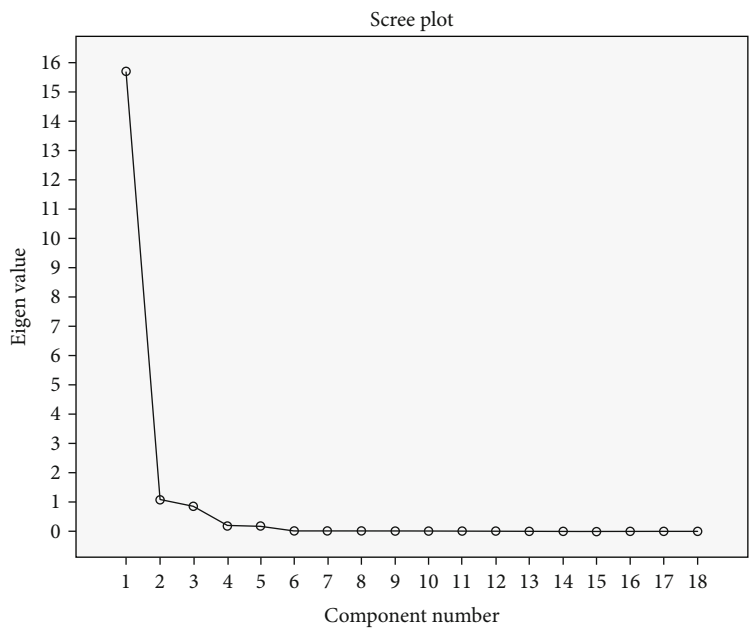

(b) Postmonsoon season

Figure 4: (a, b) Scree plot of the eigenvalues for principal components.

parameters like BOD, COD, TSS, NO_3, and turbidity. The analysis of the results shows that these water quality parameters cannot be controlled by a single specific factor because they have different pollution sources. Overall, divergent results revealed that common sources are not always linked with significant correlations among each other.

In Table 4, the postmonsoon results revealed that most of the parameters show a significant positive correlation as follows:

(i) EC with alkalinity, HCO_3, hardness, K, Cl^-, Ca, Na, SO_4, COD, and BOD ($r > 0.9$)

(ii) EC with TDS which has strong correlation ($r = 1$)

(iii) TSS with turbidity with NO_3 ($r > 0.9$)

(iv) Alkalinity with HCO_3, hardness, K, Na, SO_4, COD, and TDS ($r > 0.9$)

(v) HCO_3 with Ca, Cl^-, K, Na, hardness, K, SO_4, COD, and TDS ($r > 0.9$)

(vi) Cl^- with hardness, Mg, Na, TDS, Ca, COD, and BOD ($r > 0.9$)

(vii) K and Mg with Na, SO_4, and TDS ($r > 0.9$)

Table 5: Principal components, loading factors, eigenvalues, and variance.

Premonsoon season			Postmonsoon season		
Parameters	Components		Parameters	Components	
	PC-1	PC-2		PC-1	PC-2
EC	0.97	0.24	EC	0.85	0.53
pH	0.01	-0.86	pH	-0.34	-0.83
Turbidity	-0.03	0.95	Turbidity	-0.42	-0.88
Alkalinity as $CaCO_3$	0.94	0.29	Alkalinity as $CaCO_3$	0.85	0.51
Bicarbonate	0.97	0.23	Bicarbonate	0.85	0.51
Calcium	0.82	-0.07	Calcium	0.75	0.63
Chloride	0.94	-0.25	Chloride	0.90	0.39
Hardness	0.99	0.04	Hardness	0.84	0.54
Mg	0.99	0.04	Mg	0.89	0.19
K	0.97	0.15	K	0.75	0.61
Na	0.62	0.71	Na	0.82	0.56
SO_4	0.99	0.12	SO_4	0.68	0.63
Nitrate (NO_3)	-0.14	0.90	Nitrate (NO_3)	0.35	0.84
TDS	0.98	0.19	TDS	0.85	0.53
DO	-0.33	-0.91	DO	-0.74	-0.61
BOD	0.40	0.91	BOD	0.73	0.57
COD	0.05	0.99	COD	0.89	0.43
TSS	0.10	0.93	TSS	-0.45	-0.86
Eigenvalues	10.86	5.77	Eigenvalues	15.67	1.08
% explained variance	60.35	32.11	% explained variance	87.1	6.01
% cumulative variance	60.35	92.46	% cumulative variance	87.1	93.11

(viii) NO_3 with SO_4 ($r > 0.9$)

(ix) SO_4 with TDS ($r > 0.9$)

It is pertinent to mention here that a significant negative correlation of DO and TSS with all other parameters was observed except for turbidity and pH due to the low flow regime in the river. Discussion on the premonsoon period stated above explains the reasons of the strong correlations between hardness, alkalinity, TDS, EC, cations, and anions for postmonsoon sampling as well. Similar to the premonsoon period, the negative correlation between DO and BOD (and COD) during postmonsoon is due to data limitations and sampling errors. For remaining parameters, this finding validates that there is practically no correlation between DO and other parameters, except TSS that sometimes are organic in nature and contribute to sediment oxygen demand. However, the samples in the present study were not obtained from the bottom, so no such correlation can be established.

3.4. Principal Component Analysis (PCA). The guidelines developed by Kaiser [41] for the PCA technique were followed to determine the significant relationships among the selected sites in order to identify the physiochemical properties of the water quality parameters; the loading factors were calculated and classified as "strong," "moderate," and "weak" corresponding to absolute loading values of >0.75, 0.50-0.75, and 0.30-0.50, respectively. In order to understand the underlying data structure, scree plot graphs are used for configuring the principal components to be retained based on the eigenvalues. The scree plot also provides the percentage variances explained for each component and provides an indication on how the principal components were obtained [42].

As shown in Figures 4(a) and 4(b), there is a definite change of slope after the 3rd eigenvalue; only two components were retained. Loading values and the explained variance of two retained PCs are shown in Table 5. Only two PCs have eigenvalues > 1 (Kaiser Normalization) which explain almost 92.46% of the total variance in the water quality dataset during the premonsoon season in the water quality dataset whereas 93.11% of the total variance was described during the postmonsoon season, which is prescribed by only two factors in both seasons due to eigenvalues greater than 1. The variables having eigenvalues lower than 1 were ignored due to their low significance [43].

In the premonsoon season, PC-1 recorded 60.35% of the total variance, indicating that high positive loadings of EC, alkalinity, HCO_3, Ca, Cl^-, hardness, Mg, K, SO_4, and TDS were observed. In this factor, there are biogenic and anthropogenic (urban wastewater) pollution sources. PC-2 contributes 32.11% of the total variance and comprises strong positive loading on turbidity, NO_3, BOD, COD, and TSS whereas there is a negative loading on pH and DO

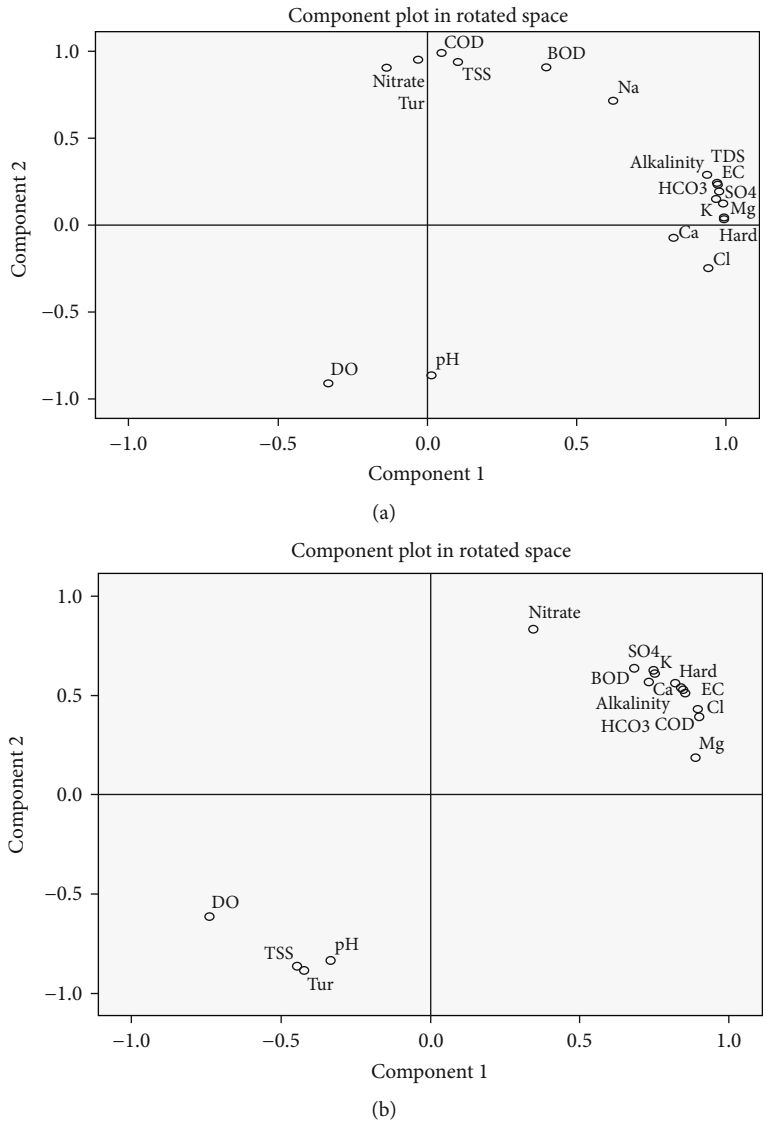

Figure 5: (a) PCA plotting for premonsoon season; (b) PCA plotting for postmonsoon season.

parameters. This PC-2 is associated with the leaching of sewage from urban areas and industrial point-source discharge, agricultural nonpoint sources, and livestock operations [44]. Similarly, during the postmonsoon season, PC-1 contributes 87.10% of the total variance, showing high positive loadings of all parameters except pH, turbidity, DO, and TSS which show negative loadings. From Table 5, it is clear that there is negative loading of DO during both seasons which may be indicative of too much bacteria and an excess amount of BOD (untreated sewage, organic discharges).

The results obtained from PCA identified the major pollution sources of the study area which is mainly due to some natural processes and anthropogenic activities. The discharging untreated urban wastewater into the river constitutes the major point anthropogenic contamination source. The nonpoint source which also contributes immensely in Soan River water contamination is from agricultural activities and livestock farming. The PCA plots of premonsoon and postmonsoon are shown in Figures 5(a) and 5(b).

4. Conclusion

In the present study, multivariate statistical techniques were used for the evaluation of pollution variations and source apportionment due to water contamination in the Soan River. The hierarchical CA technique was used for the assessment of similarity among the sampling sites. A dendrogram was plotted based upon the chemical analysis of all selected sites that grouped these sites into three and two statistical significant clusters during premonsoon and postmonsoon seasons, respectively, as shown in Figures 3(a) and 3(b). The PCA and FA made it possible to extract and recognize the origins of or the factors responsible for water quality variations during the year 2019. The parameters such as DO, BOD, COD, turbidity, and TSS were identified as the most significant parameters contributing to water quality, indicating that the water quality of the Soan River deteriorates gradually from upstream to downstream as it passes through the urban areas, receiving domestic and industrial wastewater from the outfalls.

The results of DO, COD, TSS, and BOD prove that this wastewater requires proper treatment to overcome these indicators of pollution before disposal. Moreover, mismanagement causes solid waste to move down to the drainage system, which results in sewer line blockage and consequently in the spread of various types of diseases-causing organisms.

The sustainable integrated water resource management of rivers should be planned through various approaches such as the treatment of wastewater released from industrial zone and municipal locations. It is recommended that a long-term and continued monitoring program should be established to predict the water quality of the Soan River. This can be achieved by the selection of landfill sites to dump the municipal solid waste, adequate treatment of urban and industrial wastewater before releasing in the river, and improvement of agronomic practices in this area. Furthermore, installing an automatic wireless-sensor networking system for river water quality assessment and forecasting may support the environmental protection authority in the implementation of appropriate action plans.

Data Availability

The data used to support the findings of this study are included in the article.

Conflicts of Interest

The authors declare that they have no conflict of interest regarding the publication of this paper.

Acknowledgments

The authors acknowledge the PCRWR, Ministry of Science and Technology Islamabad, Pakistan, for technical support.

References

[1] WHO, *Drinking water fact sheets*, World Health Oganization (WHO), 2018.

[2] P. Li and H. Qian, "Water resource development and protection in loess areas of the world: a summary to the thematic issue of water in loess," *Environmental Earth Sciences*, vol. 77, no. 24, p. 796, 2018.

[3] O. V. Omonona, J. O. Amah, S. B. Olorunju et al., "Hydrochemical characteristics and quality assessment of groundwater from fractured Albian carbonaceous shale aquifers around Enyigba-Ameri, southeastern Nigeria," *Environmental Monitoring and Assessment*, vol. 191, no. 3, p. 125, 2019.

[4] M. Tripathi and S. K. Singal, "Use of principal component analysis for parameter selection for development of a novel water quality index: a case study of river Ganga India," *Ecological Indicators*, vol. 96, pp. 430–436, 2019.

[5] L. Ali, A. Rashid, S. A. Khattak, M. Zeb, and S. Jehan, "Geochemical control of potential toxic elements (PTEs), associated risk exposure and source apportionment of agricultural soil in southern Chitral, Pakistan," *Microchemical Journal*, vol. 147, pp. 516–523, 2019.

[6] A. Rashid, S. A. Khattak, L. Ali et al., "Geochemical profile and source identification of surface and groundwater pollution of district Chitral, Northern Pakistan," *Microchemical Journal*, vol. 145, pp. 1058–1065, 2019.

[7] M. Memon, M. S. Soomro, M. S. Akhtar, and K. S. Memon, "Drinking water quality assessment in southern Sindh (Pakistan)," *Environmental Monitoring and Assessment*, vol. 177, no. 1-4, pp. 39–50, 2011.

[8] J. Zhao, G. Fu, K. Lei, and Y. Li, "Multivariate analysis of surface water quality in the Three Gorges area of China and implications for water management," *Journal of Environmental Sciences*, vol. 23, no. 9, pp. 1460–1471, 2011.

[9] Y. Ouyang, P. Nkedi-Kizza, Q. T. Wu, D. Shinde, and C. H. Huang, "Assessment of seasonal variations in surface water quality," *Water Research*, vol. 40, no. 20, pp. 3800–3810, 2006.

[10] A. A. Masoud, "Groundwater quality assessment of the shallow aquifers west of the Nile Delta (Egypt) using multivariate statistical and geostatistical techniques," *Journal of African Earth Sciences*, vol. 95, pp. 123–137, 2014.

[11] S. Giri and A. K. Singh, "Risk assessment, statistical source identification and seasonal fluctuation of dissolved metals in the Subarnarekha River, India," *Journal of Hazardous Materials*, vol. 265, pp. 305–314, 2014.

[12] Y. Yi, Z. Yang, and S. Zhang, "Ecological risk assessment of heavy metals in sediment and human health risk assessment of heavy metals in fishes in the middle and lower reaches of the Yangtze River basin," *Environmental Pollution*, vol. 159, no. 10, pp. 2575–2585, 2011.

[13] S. Bhargava, U. Saxena, and A. K. Bhragava, "Some microbiological studies of polluted Kali River water at Meerut," *Biochemical and Cellular Archives*, vol. 9, pp. 155-156, 2009.

[14] WWAP, *Statics on water use. World Water assessment programme*, WWAP, 2012.

[15] N. Gupta, S. M. Nafees, M. K. Jain, and S. Kalpana, "Physicochemical assessment of water quality of river Chambal in Kota city area of Rajasthan state (India)," *Rasayan Journal of Chemistry*, vol. 4, no. 2, pp. 686–692, 2011.

[16] M.-L. Wu, Y. S. Wang, Y. T. Wang et al., "Seasonal and spatial variations of water quality and trophic status in Daya Bay, South China Sea," *Marine Pollution Bulletin*, vol. 112, no. 1-2, pp. 341–348, 2016.

[17] B. Kundi, *Pakistan's water crisis: why a national water policy is needed*, The Asia Foundation, California St., 2017, 9th floor San Francisco, CA 94104.

[18] M. Daud, M. Nafees, S. Ali et al., "Drinking water quality status and contamination in Pakistan," *BioMed Research International*, vol. 2017, 18 pages, 2017.

[19] H. Haider and W. Ali, "Development of dissolved oxygen model for a highly variable flow river: a case study of Ravi River in Pakistan," *Environmental modeling & assessment*, vol. 15, no. 6, pp. 583–599, 2010.

[20] H. Haider and W. Ali, "Calibration and verification of a dissolved oxygen management model for a highly polluted river with extreme flow variations in Pakistan," *Environmental Monitoring and Assessment*, vol. 185, no. 5, pp. 4231–4244, 2013.

[21] H. Haider and W. Ali, "Fecal coliform management using a coupled hydrodynamics and water quality model for the river Ravi in Pakistan," *Pakistan Journal of Engineering and Applied Sciences*, vol. 9, pp. 48–57, 2011.

[22] D. S. Asia, *Water vision 2025, country report, Pakistan, Maharashtra, India, Global Water Partnership*, South Asia Technical Advisory Committee Regional Office, 2000.

[23] I. Hashmi, S. Farooq, and S. Qaiser, "Chlorination and water quality monitoring within a public drinking water supply in Rawalpindi Cantt (Westridge and Tench) area, Pakistan," *Environmental Monitoring and Assessment*, vol. 158, no. 1-4, pp. 393–403, 2009.

[24] C. A. B. Garcia, H. L. Garcia, M. C. S. Mendonça et al., "Assessment of water quality using principal component analysis: a case study of the Açude da Macela–Sergipe–Brazil," *Water Resources*, vol. 7, p. 8, 2017.

[25] Q. Gu, Y. Zhang, L. Ma et al., "Assessment of reservoir water quality using multivariate statistical techniques: a case study of Qiandao Lake, China," *Sustainability*, vol. 8, no. 3, p. 243, 2016.

[26] S. Nazeer, M. U. Khan, and R. N. Malik, "Phytoplankton spatio-temporal dynamics and its relation to nutrients and water retention time in multi-trophic system of Soan River, Pakistan," *Environmental Technology & Innovation*, vol. 9, pp. 38–50, 2018.

[27] S. Nazeer, M. Z. Hashmi, and R. N. Malik, "Heavy metals distribution, risk assessment and water quality characterization by water quality index of the river Soan, Pakistan," *Ecological Indicators*, vol. 43, pp. 262–270, 2014.

[28] F. Iqbal, M. Ali, A. Salam et al., "Seasonal variations of physico-chemical characteristics of river Soan water at Dhoak Pathan bridge (Chakwal), Pakistan," *International Journal of Agriculture and Biology*, vol. 6, no. 1, pp. 89–92, 2004.

[29] M. Aoun Rizvi and A. I. S. Ullah, "A study on the evaluation of water pollution on Soan river Rawalpindi. M.Sc. (Env. Sci.)," in *College of Earth and Environmental Sciences*, University of the Punjab, Lahore, Pakistan: Lahore, 2004.

[30] A. Ashfaq, M. Ashraf, and A. Bahzad, "Spatial and temporal assessment of groundwater behaviour in the Soan Basin of Pakistan. University of Engineering and Technology Taxila," *Technical Journal*, vol. 19, no. 1, p. 12, 2014.

[31] L. S. G. Clesceri, A. E. Greenberg, and A. D. Eaton, *Standard methods for the examination of water and wastewater*, American Public Health Association, Washington, 1998.

[32] M. Rasolofonirina, V. Ramaroson, and S. D. Ravelomanantsoa, "Assessment of nitrate occurrence in the shallow groundwater of Merimandroso area, Analamanga region, Madagascar using multivariate analysis," *American Journal of Water Resources*, vol. 6, no. 1, pp. 39–47, 2018.

[33] S. Shrestha and F. Kazama, "Assessment of surface water quality using multivariate statistical techniques: a case study of the Fuji river basin, Japan," *Environmental Modelling & Software*, vol. 22, no. 4, pp. 464–475, 2007.

[34] W. D. Alberto, D:. María del Pilar, A. María Valeria, P. S. Fabiana, H. A. Cecilia, and B. María de los Ángeles, "Pattern recognition techniques for the evaluation of spatial and temporal variations in water quality. A case study: Suquía River Basin (Córdoba–Argentina).," *Water Research*, vol. 35, no. 12, pp. 2881–2894, 2001.

[35] M. Vega, R. Pardo, E. Barrado, and L. Debán, "Assessment of seasonal and polluting effects on the quality of river water by exploratory data analysis," *Water Research*, vol. 32, no. 12, pp. 3581–3592, 1998.

[36] F. Zhou, G. H. Huang, H. Guo, W. Zhang, and Z. Hao, "Spatio-temporal patterns and source apportionment of coastal water pollution in eastern Hong Kong," *Water Research*, vol. 41, no. 15, pp. 3429–3439, 2007.

[37] D. Saksena, R. Garg, and R. Rao, "Water quality and pollution status of Chambal river in National Chambal sanctuary, Madhya Pradesh," *Journal of Environmental Biology*, vol. 29, no. 5, pp. 701–710, 2008.

[38] O. R. Awofolu, Z. Mbolekwa, V. Mtshemla, and O. S. Fatoki, "Levels of trace metals in water and sediment from Tyume River and its effects on an irrigated farmland," *Water SA*, vol. 31, no. 1, pp. 87–94, 2005.

[39] H. A. Raja and C. A. Shearer, "Freshwater ascomycetes: new and noteworthy species from aquatic habitats in Florida," *Mycologia*, vol. 100, no. 3, pp. 467–489, 2017.

[40] J. Cohen, *Statistical power analysis for the behavioral sciences*, Erlbaum: Hillsdale, Hillsdale, NJ, 2nd edition, 1988.

[41] H. F. Kaiser, "The application of electronic computers to factor analysis," *Educational and Psychological Measurement*, vol. 20, no. 1, pp. 141–151, 2016.

[42] C.-W. Liu, K.-H. Lin, and Y.-M. Kuo, "Application of factor analysis in the assessment of groundwater quality in a Blackfoot disease area in Taiwan," *Science of the Total Environment*, vol. 313, no. 1-3, pp. 77–89, 2003.

[43] J. O. Kim, O. Ahtola, P. E. Spector, and C. W. Mueller, *Introduction to factor analysis: what it is and how to do it*, Sage, 1978.

[44] P. Simeonova, V. Simeonov, and G. Andreev, "Water quality study of the Struma river basin, Bulgaria (1989–1998)," *Open Chemistry*, vol. 1, no. 2, pp. 121–136, 2003.